Metal-free carbon-based oxygen bi-functional electrocatalysts for rechargeable metal-air battery applications

A dissertation submitted in partial fulfilment of the requirements
for the degree of Doctor of Philosophy

Juhun Shin

Department of Chemistry

Supervised by

Prof. Christopher Blackman

Prof. Gopinathan Sankar

Prof. Zheng Xiao Guo

2022

Declaration

I, Juhun Shin, confirm that the work presented in this dissertation is my own. Where information has been derived from other sources, I confirm that this has been indicated accordingly.

Acknowledgements

I would like to express my deepest gratitude to Prof. Chris Blackman for immense support and encouragements in my last years of PhD. Without his influences, I would have had difficulties finishing the project. I would also like to thank Prof. Zheng Xiao Guo, for the early years of PhD and his guidance throughout and Prof. Gopinathan Sankar, for his continuous support as my secondary supervisor.

I would like to acknowledge all my colleagues and collaborators: Prof. Jae Hee Jung, Dr. Gi-Byoung Hwang, Dr. Tingting Zhao, Dr. Jian Guo, Dr. Zhuangnan Li, Dr. Ki Joon Heo, Dr. Martin Rosillo-Lopez, Dr. Guanjie He, Dr. Srinivas Gadipelli, Dr. Yuchen Yang, Dr. Yudao Qin, Dr. Yue Lu, Dr. Yiyun Zhu, Dr. Xiaoyu Han, Dr. Chia-Hao Chang, Dr. Juntao Li, Dr. Xueming Xia, Yuting Yao, Bowen Guan, Suji Im, Jone-Him Tsang, Beatriz-Janeiro Ferraz and all UCL Chemistry technical staffs.

I would like to acknowledge the support by EPSRC (Grant Nos. EP/K021192/1 and EP/L018330/1).

I cannot express enough the never-ending support and love received from my family and I am and always will be grateful. A special thanks to the One on the other side of the world.

And all this was possible because of Your love, grace, and mercy…

Abstract

With rapid advancements in mobile systems and vehicles, there is an increasing expectation of performances for energy storage/conversion devices each year. New technologies such as metal-air batteries and fuel-cells have gained much attention as better substitutes of currently widely used batteries and fossil fuels however it is crucial to improve the sluggish oxygen kinetics occurring on the surface of the electrodes of these devices. Abstaining from using scarce noble-metal containing species, this thesis outlines syntheses and electrocatalytic performances of non-metal carbon-based materials as oxygen electrocatalysts for possible cost-effective cathode candidates in metal-air batteries.

To explore a different synthesis approach of graphene-like carbon material, as to a harsh acid oxidation preparation method, oxygen electrocatalysts were obtained via high temperature (>700 °C) graphitisation of glucose and dicyandiamide. Pores created during polymerisation and the nitrogen species (pyridinic, pyrrolic, and graphitic) increased catalytically active sites on as prepared graphitic carbons. Annealing temperature was varied to study the effect of the ratio of N-dopant species, and the concentration of carbon defects as a function of the annealing temperature.

Increasing the number of active sites whilst preserving electronic conductivity is challenging, but crucial to enhancing electrocatalysts' performances. Heteroatom-doped 'carbon dots', quasi-spherical carbon particles with size of less than 20 nm, were enriched on the surface of graphene substrates to maximise catalytically available active sites.

Embedding carbon dots (with many N and S dopant species) provide many catalytically active sites for each defect site compared to direct heteroatom doping. Dual heteroatom-doped carbon dots embedded graphene catalysts, NS-CD@gf_a900 exhibited significantly high catalytic performances of 7.71 mA cm^{-2} at 1600 rpm and only 0.91 V overpotential for oxygen bi-functional reactions; even close to noble-metal Pt/C and Ir/C counterparts (0.77 V) as a result of the effect of many available catalytic sites and the synergistic behaviour of the dopants to the electronic structures.

An alternative to the traditional method of 2D carbon preparation via exfoliation and oxidation using harsh chemicals is via a bottom-up approach of forming carbon polymers. Pyrene, a polycyclic aromatic carbon with a four fused benzene-ring structure, was rationally selected as the building block for the formation of carbon substrate via a Friedel-Craft acylation mechanism. There was a significant increase in measured pore volume in the nano-range and throughout, compared to other carbon polymers and graphene samples, which can enhance the gas/ion diffusion mechanism. Nitrogen and sulphur doping with high temperature annealing at 900 °C resulted in a highly porous carbon substrate that exhibited comparable electrocatalytic performances to the Pt/C electrocatalyst.

Impact statement

The main research goals of functionalised materials for energy storage/conversion devices should be to minimise the complexity of preparations, associated environmental issues, and the cost of fabrication. Most of all, the current performance of oxygen electrocatalyst materials in metal-air batteries restricts commercialisation of the technology – the highest oxygen conversion levels are limited to scarce noble-metal catalysts such as platinum, ruthenium and iridium. Electrocatalysis requires the catalyst material to be conductive, able to adsorb/desorb molecules with fast conversion at water splitting potential of 1.23 V, and have high stability. Many research articles focus on metal-catalysts (either precious or transition metals) as the activation energy of the oxygen redox reaction is easily met, reaching close to the maximum current density of 5.71 mA cm^{-2} with sufficient number of conversions. Yet, catalyst poisoning and stability issues are typically encountered and require the use of further carbon support/substrate to increase the overall electrode conductivity.

Heteroatom doped (B, N, O, P, S) graphitic carbon substrates with stable porous morphologies and many active sites for oxygen catalytic reactions can be rationally designed to be utilised as metal-free electrocatalysts.

The projects in this thesis concentrate on surpassing performances of current metal-based and non-metal electrode materials but also to provide simple innovative synthesis methods of carbon electrocatalysts for applications such as metal-air batteries and fuel cells. Projects are in chronological order and the obtained insights for each project are described immediately following the project.

CONTENTS

CHAPTER 1 : INTRODUCTION

CHAPTER 2 : EXPERIMENTAL AND CHARACTERISATIONS

CHAPTER 3 : HIGHLY DEFECTIVE AND ACTIVE ELECTROCATALYST VIA HIGH TEMPERATURE POLYMERISATION OF CARBON MONOMER

CHAPTER 4 : UTILISING FUNCTIONALISED CARBON DOTS AS NON-METAL BI-FUNCTIONAL ELECTROCATALYST

CHAPTER 5 : TWO-DIMENSIONAL CARBON SUBSTRATE AS SOLE BI-FUNCTIONAL ELECTROCATALYST; FRIEDEL-CRAFT ASSISTED POLYMERISATION OF PYRENE

List of Figures

List of Tables

List of Abbreviations

2-dimensional (2D)

3-dimensional (3D)

Annealed carbon polymer (GDC)

Annealed graphene oxide (AGO)

Atomic force microscopy (AFM)

Atomic percentage (at. %)

Attenuated total reflectance-infrared spectroscopy (ATR-IR)

Barrett-Joyner-Halenda analysis (BJH)

Brunauer-Emmett-Teller anaylsis (BET)

Carbon dot (CD)

Carbon dot embedded graphene hydrogel (CD@gf)

Carbon nanotubes (CNTs)

Carbon to oxygen ratio (C/O ratio)

Citric acid (CA)

Covalent-organic frameworks (COFs)

Current-resistance (iR)

Cyclic voltammetry (CV)

D and G bands ratio (I_D / I_G)

Deionised water (DI water)

Density functional theory (DFT)

Dichloroethane (DCE)

Dicyandiamide (DCDA)

Electrochemical double layer capacitor (EDLC)

Electron (e^{-})

Electron dispersive X-ray spectroscopy (EDS)

Equivalence (equiv.)

Fast Fourier transform (FFT)

Full width half maximum (FWHM)

Glassy carbon (GC)

Graphene hydrogel (RGel)

Graphene oxide (GO)

Half-wave potential ($E_{1/2}$)

Hydrogen evolution reaction (HER)

Hydrothermally reduced graphene hydrogel (RGel)

Iridium-on-carbon (Ir/C)

Metal-nitrogen-carbon bonds (M-N-C bonds)

Koutecky-Levich relation (K-L relation)

Linear sweep voltammetry (LSV)

Lithium-ion battery (LIB)

Membered-carbon-ring (MB)

Metal-organic-framework (MOF)

Nickel-metal hydride (NiMH)

N, S-doped graphene hydrogel (NS-Gel)

Normal hydrogen electrode (NHE)

Onset potential (E_{onset})

Oxidised pyrene polymer (PyGO)

Oxygen evolution reaction (OER)

Oxygen reduction reaction (ORR)

Platinum-on-carbon (Pt/C)

Polyacrylamide (PAM)

Poly-acrylonitrile (PAN)

Polytetrafluoroethylene (PTFE)

Poly(vinylidene fluoride) (PVDF)

Potential at -3 mA cm^{-2} (E_{-3})

Potential at 10 mA cm^{-2} (E_{10})

Potential difference (ΔE)

Pyrene polymer (PyG)

Quenched solid density functional theory (QSDFT)

Reduced graphene oxide (RGO)

Reduced pyrene polymer (rPyG)

Reversible hydrogen electrode (RHE)

Rotating disk electrode (RDE)

Ruthenium oxide (RuO_2)

Scanning electron microscopy (SEM)

Tetra-chlorinated-pyrene (CPy)

Thermally treated carbon dot embedded graphene hydrogel (CD@gf_aXXXX)

Thermally treated N-doped oxidised pyrene polymer (NPyGO)

Thermally treated N-doped pyrene polymer (NPyG)

Thermally treated N, S-doped graphene hydrogel (NS-Gel_a900)

Thermally treated N, S-doped oxidised pyrene polymer (NSPyGO)

Thermally treated N, S-doped pyrene polymer (NSPyG)

Thiourea (TU)

Transmission electron microscopy (TEM)

Trithiocyanuric acid (TTCA)

X-ray diffraction (XRD)

X-ray photoelectron spectroscopy (XPS)

Zeolitic-imidazolate-framework (ZIF)

Zinc-air battery (ZAB)

. . . Understanding the infinite energy around us . . .

Chapter 1 : Introduction

1.1 Energy storage and conversion

Energy; a manifested property of a substance or a matter that is converted to perform work. Harnessing energy (of any form) has been crucial to mankind from the ancient times. With rapid development of current technologies, the world is significantly enhancing every second – a sustainable system is necessary to maintain the demand. Total energy consumption has inclined ever since the modernisation of the industries; 28,516 TW h^{-1} in 1950 to 173,340 TW h^{-1} in 2019, over 600% increase in total energy consumption in just 70 years[1]. However, despite the advancements on sustainable energy sources, human civilisation still heavily relies on fossil fuels (oil, coal, and natural gases) and combustion methods to harness energy (shown in Figure 1.1)[2]. Considering the serious environmental issues associated with fossil fuels and possible future depletion of fuels, alternative renewable energy sources, featuring energy storage and conversion devices, are necessary to replace conventional processes. Among the existing electrochemical systems, lithium-ion batteries (LIB) have been deployed on many occasions (mostly consumer electronics, and electric vehicles) as the primary energy source with moderate energy density and cyclability[3]. Yet, LIB technology is struggling to keep up with the energy demand with slow improvements in both energy and power densities; not to mention the safety concerns caused by thermal runaways and short-circuits[4]. Hence, new environmental, and sustainable energy storage systems with high energy and power densities are highly desired for the rapid developments.

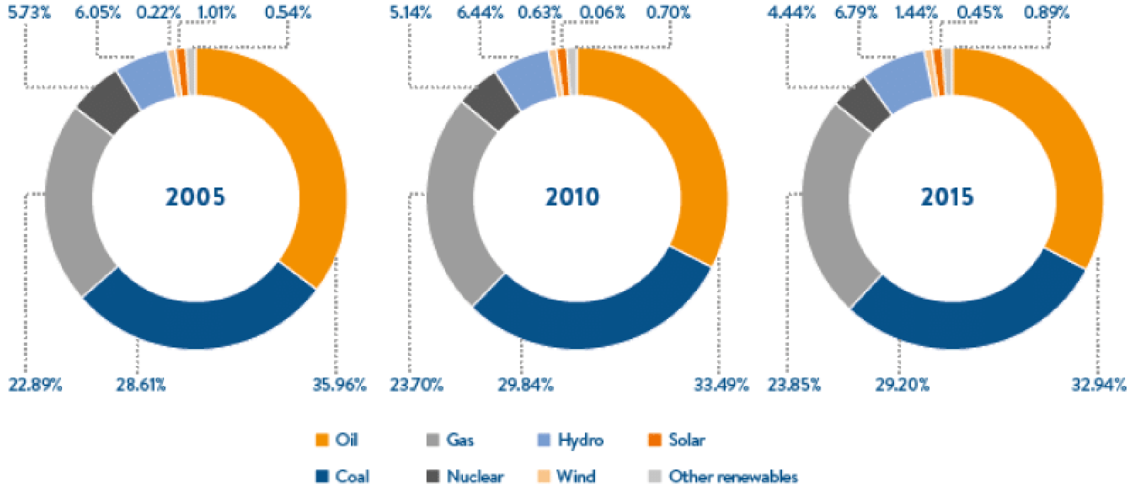

Figure 1.1 Comparative primary energy consumption over the past 10 years[2].

1.1.1 Lithium-ion batteries

With the acknowledgement by the 2019 Nobel prize in chemistry[5], LIB technologies have enabled developments of many applications such as electric vehicles and portable devices. Lithium, the lightest alkali-metal, exhibits high specific energy (available stored energy per unit mass), fast ion mobility, and high working cell voltage making it the most favourable amongst all elements[6].

Typically, a LIB consists of a lithium-rich cathode material, an ion-hosting anode material, and an ion-permeable separator; all wetted by an organic electrolyte to allow ion movements. Both electrodes in typical LIBs are structured either in layers (e.g. $LiCoO_2$ cathode and graphite anode) or porous insertion materials (e.g. $LiFePO_4$ cathode and TiO_2 anode). Charged/discharged state of a LIB is described by the motion of lithium intercalation/deintercalation in-and-out of two differently charged electrodes[7].

Despite the market dominance, chemical limitations of current LIB technology are apparent. With battery over-charge and -discharge, the conventional layer-structured electrodes can have permanent damages (layer expansion/collapsing) caused by over inserted/stripped ions in the electrodes and thermal runaway of a cell can occur[8]. Insertion oxides, 3-dimensional (3D) frameworks, may not have the same deformation issues as the layer-structured electrodes however, porous structures have less sites to accommodate ions and restrict the ion movements (during insertion/extraction) resulting in overall decrease in both energy and power densities than layered-structures[9]. There is a formation of solid electrolyte interphase (SEI) on the surface of the electrodes which is said to stabilise and prevent further decomposition of electrolyte in a cell. Nevertheless, batteries suffer irreversible capacity loss during the first few cycles which may have an influence on the battery lifetime[10-12]. Due to the safety issues of lithium in air, cells are completely sealed and therefore cannot be replenished when dendritic cell failure occurs[13].

The energy density increase in LIBs is mainly achieved by the physical cell capacity/volume increase; in other words, increase in size and weight is inevitable[14, 15].

1.1.2 Supercapacitors

A supercapacitor is a device that can store and release charges at the electrode interfaces rapidly providing high power densities and a prolonged cycle life[16].

Very similar to LIBs, a supercapacitor consists of two electrodes with an ion-permeable membrane immersed in an electrolyte[17]. Depending on the choice of the electrode material and the relative potential, supercapacitors can be classified into two types; an electrostatic double layer capacitor (EDLC) or an electrochemical pseudocapacitor. In EDLCs, which typically use carbon materials as the electrodes, an electrostatic Helmholtz double layer is formed at the electrode-electrolyte interface. Pseudocapacitors on the other hand are based on the electrochemical Faradaic redox reactions; electrosorption on the surface of the electrodes. The rapid charge transfer on the surface of the electrodes delivers necessary power in short-term however suffers from lack of specific energy which is typically a factor of 10 less than that of LIBs[17-21].

Supercapacitors are used in conjunction with LIBs to provide both energy and power for some applications. In recent years, materials for LIBs and supercapacitors are converging with similar properties to increase either energy or power densities[22-25].

1.1.3 Metal-air batteries

Metal-air batteries, electrochemical/electrocatalytic cells utilising ambient air, have intrigued many researchers as a possible solution to both portable and large-scale energy storage due to exceptional energy density compared with LIBs. They are also relatively cheap, safe (in aqueous setup), as well as being environmentally friendly[26-30]. The first attempt to combine oxygen to the electrochemical system was introduced in the 19th century by a French electrical engineer Georges Leclanché using zinc and manganese dioxide on carbon[31].

Different to the conventional intercalation/insertion of ions in a closed cell, the main source of energy, typically oxygen, is supplied from air with constant feedstock. Overall construction includes an anode (a pure single metal plate or sheet), a cathode (air-breathing where oxygen conversion reactions occur), with/without a separator, and an electrolyte saturating the cell. In other words, the theoretical specific energy of a metal-air battery can significantly increase with respect to the density of the anode material used. Typically, metals for the anode-side are alkali (earth) metals, or first row transition metals exhibiting electrochemical responses[28, 29, 32]. Depending on the choice of metal for the anode, metal-air batteries can have either an aqueous system or a non-aqueous cell construction[32]. In an aqueous setup (non-alkali metal), a mechanical replacement of the used metal anode is easily achievable to replenish the cell[26, 27, 33]. Oxygen electrochemical reactions are promoted by the cathode materials where oxygen molecules are either reduced or evolved via catalysis. An air electrode consists of a gas diffusion layer and an active material layer for the catalysis. Between these two boundaries, a hydrophobic binder or a substrate, for instance polytetrafluoroethylene (PTFE), is used making it air-permeable whilst excluding water molecules[34-37]. Single- or bi-functional oxygen reactions determines the principle state of the batteries; either primary or rechargeable air-batteries[26, 30, 38]. The most common exemplary usage of metal-air batteries would be a primary zinc-air battery (ZAB) in hearing aids[39].

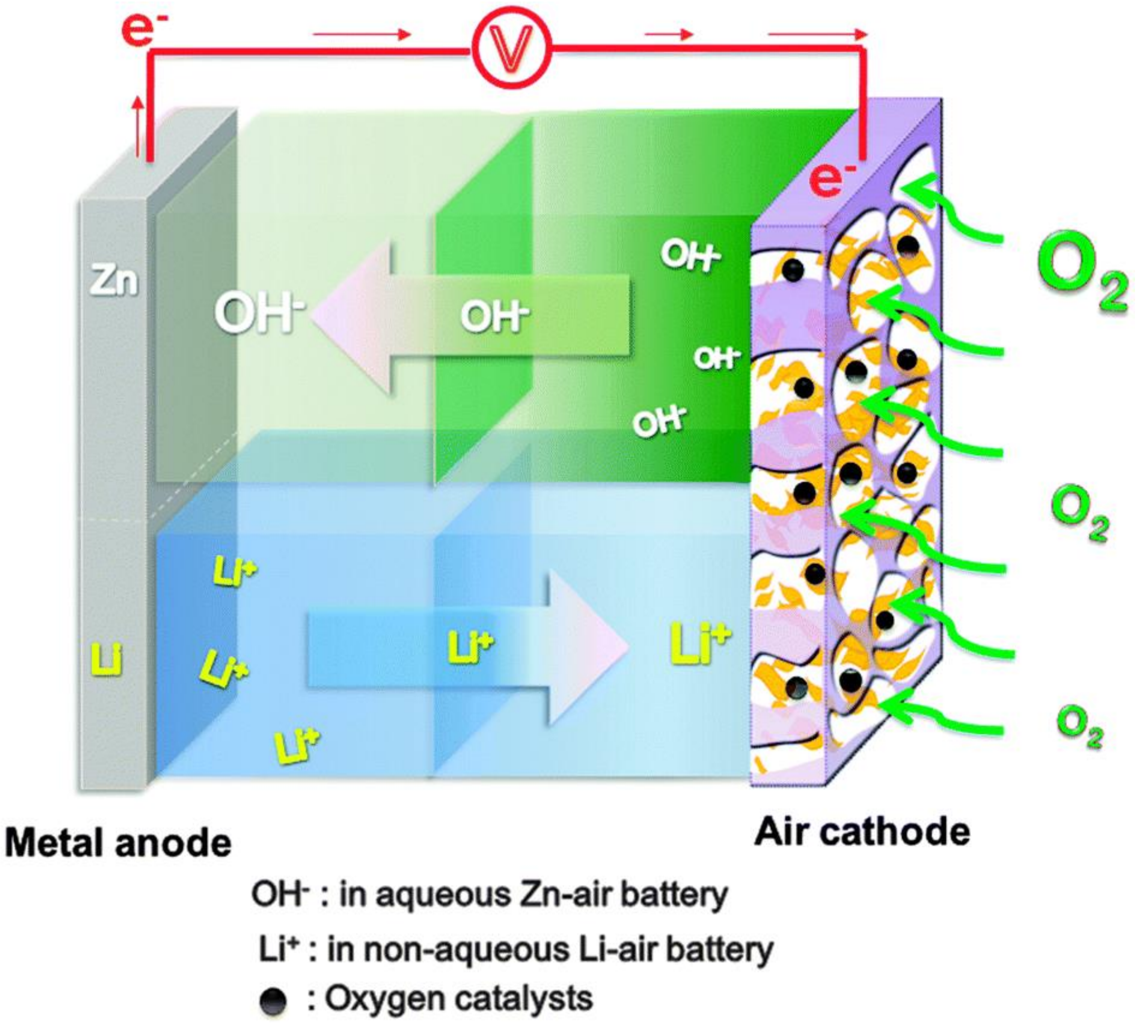

Figure 1.2 Schematic structure of a metal-air battery; a metal anode and an air permeable cathode with active oxygen electrocatalysts[40].

1.1.4 Other energy storage devices

Apart from the above-mentioned systems, other energy storage device designs are available which have been studied elsewhere.

Various metal-ion batteries exist with the same metal ion shuttling charge/discharge mechanisms as the LIBs; these include sodium-ion, potassium-ion, and aluminium-ion batteries. Compared to LIBs, other metal ion batteries lack in energy capacity due to the larger ion size, and stability of materials[41-46].

Some of the most commercially used batteries are nickel-cadmium (Ni-Cd) and nickel-metal hydride (NiMH) batteries[47, 48]. Only proton exchange takes place at the cathode hence structural integrity is high. NiMH batteries can offer the same specific energy as the LIBs at a lower cost. However, drawbacks are high self-discharge and degradation[49].

Fuel cells and electrolysers are electrocatalytic conversion devices with almost identical mechanism as the described cathode reactions in metal-air batteries[50, 51]. These systems are useful as power sources and have higher energy efficiency than fossil fuel combustion. However, the main disadvantage of this particular technology is that electrical energy cannot be stored as in other batteries – instead a physical form of gases needs to be stored for "future" conversions[52].

1.1.5 Comparison of energy storage/conversion devices

Table 1.1 shows a list of commercialised and extensively researched energy storage/conversion devices today in comparison to gasoline - specific energies and power parameters are all theoretical values.

In automotive vehicles, given the mechanical aspects of the combustion engine and the fuel tank, the calculated specific energy of petrol becomes approximately 1700 W h kg^{-1}. Realistically, current battery technologies only achieve specific energy of around 100-150 W h kg^{-1} whereas the metal-air batteries show minimum of 300 W h kg^{-1} of practical energy[53]. Since theoretical energies and power densities are significantly greater than of the metal-ion systems, there are more opportunities to improve the achievable practical densities. The energy value of fuel-cells must also consider the weight of pressurised hydrogen gas cylinders which will be similar or less than of gasoline[54].

Table 1.1 Energy and power comparison of different available energy storage/conversion devices[21, 32, 55-59].

	Nominal cell voltage (V)	**Specific energy (W h / kg)**	**Specific power (W / kg)**	**Cost of metal ($ / kg)**
Li-ion battery	3.2-3.8	200-250	250-340	68
Na-ion battery	3.7	100-130	-	1.7
Ni-MH battery	1.2	120	250-1000	12.3
Supercapacitor	2.3-2.7	1-30	3000-10000	1 (carbon)
Li-air battery	2.91	5200	-	68
Zn-air battery	1.65	1370	100	2.1
Fuel-cell	1.23	33330 (H_2)	450	2500 (10% Pt/C)
Gasoline (fuel)	-	12000	-	1.7

1.2 Rechargeable metal-air battery

In secondary metal-air batteries, two distinct reversible catalysis reactions occur at the surface of the cathode, oxygen reduction reactions (ORR) and oxygen evolution reactions

(OER), allowing the cell to charge and discharge (unlike primary metal-air batteries with a single ORR process). Rechargeable metal-air batteries are feasible next generation batteries to replace LIBs in electric vehicles and portable consumer electronics.

Despite the high energy density as mentioned earlier, possible commercialisation is hindered by technical difficulties of the cell. This includes the complexity of electrocatalysis (bi-functionality of the catalysts), the anode dendrite formation, and diffusion limitations of the cell[32, 60, 61]. Although there are many designs of metal-air batteries, here ZABs have been selected as the basis of the research due to high realistic energy densities, easy set-up, safety, and low-cost construction/operation[62].

The involved chemical reactions in the ZAB (in alkaline conditions) versus normal hydrogen electrode (NHE) are as follows (also illustrated in Figure 1.3)[32, 63]:

Cathode : $O_2 + 2H_2O + 4e^- \rightarrow 4OH^-$ $E_0 = +0.4\ V$

Anode : $Zn \rightarrow Zn^{2+} + 2e^-$

$Zn^{2+} + 4OH^- \rightarrow Zn(OH)_4{}^{2-}$ $E_0 = -1.25\ V$

In aqueous : $Zn(OH)_4{}^{2-} \rightarrow ZnO + H_2O + 2OH^-$

Overall : $2Zn + O_2 \rightarrow 2ZnO$ $E_0 = +1.65\ V$

Side : $Zn + 2H_2O \rightarrow Zn(OH)_2 + H_2$

A side-reaction can also take place at the anode which not only consumes both the electrolyte and the active metal reducing the overall cell capacities, but the converted zinc hydroxide blocks and insulates the surface of the anode slowing the cell kinetics. There is a risk of zincate ion cross-over to the cathode side, driven by the ion concentration. Conversion to ZnO at the cathode side may behave as the resistive component effecting the overall cell performances. In practice, the measured cell voltage is approximately 1.3 V with ohmic losses.

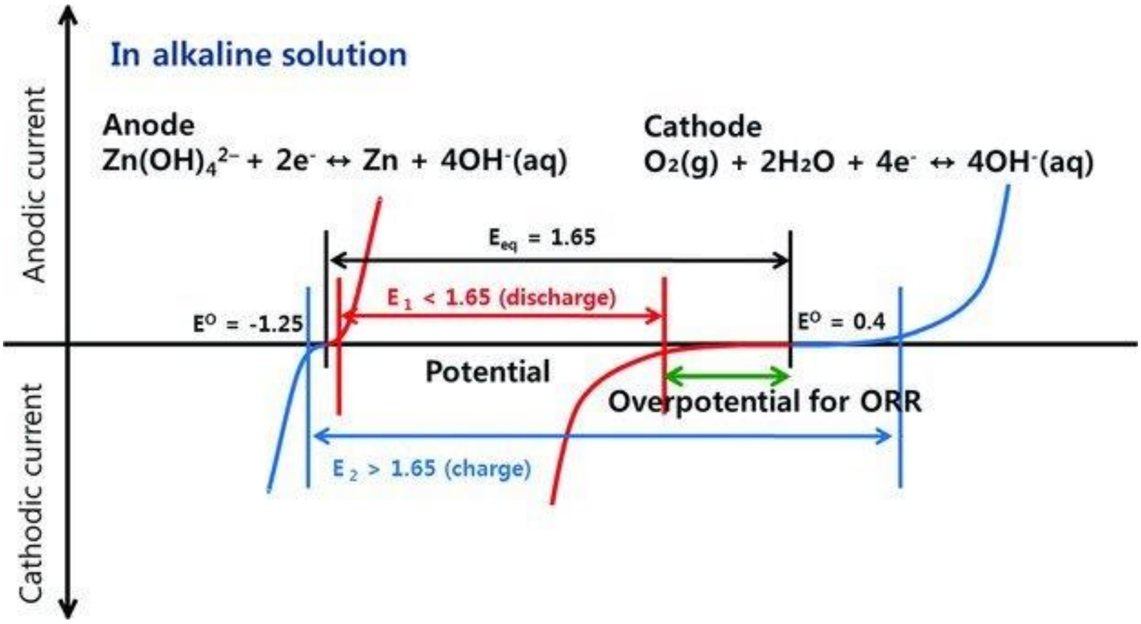

Figure 1.3 Polarisation curve of a ZAB showing differences in the equilibrium potential in an ideal (E_{eq}) and in a realistic discharge (E_1) / charge (E_2) state[32].

1.2.1 Oxygen reactions and mechanisms

The main challenge in a rechargeable metal-air battery lies in the cathode where oxygen adsorption/conversion takes place – ORR whilst discharging, and OER whilst charging. The mechanism takes place at a potential of 1.23 V vs. reversible hydrogen electrode (RHE) where water splitting occurs. However, in real systems, reactions are sluggish and require sacrificial overpotentials. Oxygen electrocatalysis involves a triple phase boundary process; associative/dissociative oxygen adsorption to the surface, oxygen intermediates migrating to diffuse on the surface of the material, and the actual charge transfer across the cell[29].

The overall ORR scheme is as follows[64]:

Acid : $O_2 + 4H^+ + 4e^- \rightarrow 2H_2O$

Alkaline : $O_2 + 2H_2O + 4e^- \rightarrow 4OH^-$

If an oxygen molecule approaches the surface of the catalyst in a perpendicular fashion, one oxygen atom is bound to the surface and an associative 4-electron (4 e^-) transfer process takes place. The oxygen reaction, in alkaline media, can be expressed in detail (where adsorption sites are represented by (*)).

$$O_2 + * \rightarrow {O_2}^*$$

$${O_2}^* + H_2O + e^- \rightarrow OOH^* + OH^-$$

$$OOH^* + e^- \rightarrow O^* + OH^-$$

$$O^* + H_2O + e^- \rightarrow OH^* + OH^-$$

$$\mathrm{O}H^* + e^- \rightarrow OH^- + *$$

Meanwhile, there also can be an associative 2-electron (2 e^-) pathway via the formation of peroxide ions.

$$O_2 + H_2O + 2e^- \rightarrow OOH^- + OH^-$$

$$OOH^- + H_2O + 2e^- \rightarrow 3OH^-$$

The 2 e^- reaction pathway has the same intermediate process up to the formation of OOH^* but instead of O^* species, OOH^- (peroxide) ions are formed, and they desorb from the material surface. These generated peroxide ions can strongly oxidise the active sites and deactivate the catalyst, leading to performance decline[65].

A dissociative mechanism is also possible where both oxygen atoms from the same molecule are adsorbed to the catalyst surface in a parallel manner. This follows two-step 2 e^- pathway however the overall process is the same as the associative 4 e^- transfer.

$$O_2 + 2* \rightarrow 2O^*$$

$$2O^* + 2e^- + 2H_2O \rightarrow 2OH^* + 2OH^-$$

$$2OH^* + 2e^- \rightarrow 2OH^- + 2*$$

The OER process is a direct inverse of the ORR mechanism.

$$4OH^- \rightarrow O_2 + 2H_2O + 4e^-$$

Different OER mechanisms have been proposed depending on the cathode materials used. Commonly, the OER pathway in an alkaline condition can be expressed.

$$* + OH^- \rightarrow OH^* + e^-$$

$$OH^* + OH^- \rightarrow H_2O + O^* + e^-$$

$$O^* + OH^- \rightarrow OOH^* + e^-$$

$$OOH^* + OH^- \rightarrow {O_2}^* + e^-$$

$${O_2}^* \rightarrow O_2 + *$$

The OH^- ions for the initial step originate either from the oxygen reduction process, or directly from the KOH electrolyte in alkaline systems.

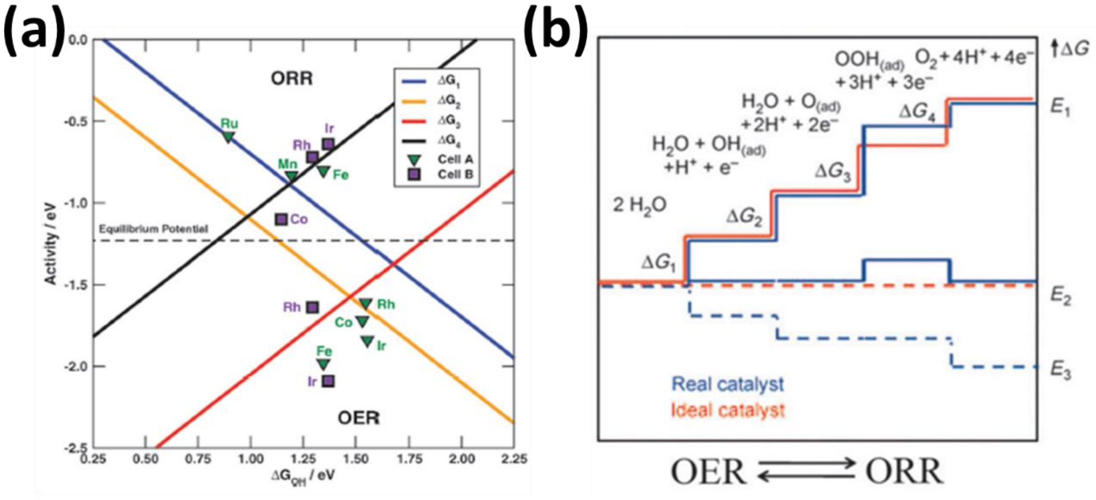

Figure 1.4 (a) Combined volcano plot of materials for ORR and OER and (b) plot of Gibbs free energy of intermediates in oxygen electrocatalysis[66, 67].

These multi-step processes are directly related to the reaction kinetics of the catalyst. Theoretical ORR and OER activities of metal species are shown in the combined volcano plot in Figure 1.4a. The volcano plot shows the free energy of each element directly associated with the oxygen molecule binding strength and the overpotential of reduction/evolution reactions; the intersect of two Gibbs free energy represents the optimum activity, and either side of the peak denote weak/strong adsorption of the oxygen molecule. If the oxygen intermediate is bound to the catalyst surface too weakly (generally shown by low number of electrons transferred), an insufficient number of conversion reactions will take place before the desorption of molecules and hence low activity and increase in possible formation of peroxide ions. On the other hand, if the oxygen intermediate is too strongly attached to the material used, poor activity will be observed again despite the electron transfer number being very close to 4; this is caused by not enough regenerated catalytic sites available for incoming oxygen molecules. This catalyst poisoning leads to dramatic decline in catalytic activity over time[68, 69].

Overpotential is often required to thermodynamically drive the reaction forward. If every conversion step for each oxygen intermediate is equal to 1.23 V vs. RHE, then no overpotential will be required (plotted as red line in the Gibbs free energy plot in Figure 1.4b). Unfortunately, depending on the material used in real systems and associated kinetics, an overpotential is observed for the adsorption/conversion reactions of oxygen species to drive the reaction forward. Generally, the largest Gibbs free energy is observed when the oxygen molecule is first adsorbed to the substrate, and when water molecules are introduced to the 4 e^- reaction mechanism where splitting is required[70]. The energy barrier, ΔG for each reaction, must be overcome for the reaction to proceed. The aim is to minimise the calculated free energies which reduces the ORR/OER potential difference (ΔE) and hence maximises the catalytic activities.

1.2.2 Components of rechargeable metal-air batteries

1.2.2.1 Anode materials

Only zinc metal and its alloys are used in ZABs; zinc is abundant, recyclable, and safe in aqueous conditions compared to lithium[71]. However, as mentioned earlier, a fundamental problem of zinc anode is the spontaneous dissolution of zinc ions in an aqueous electrolyte which leads to self-corrosion. During cell-charge, dendritic crystallisation of zinc may occur on the anode surface rather than ions re-combining to the voids created in the first place. Full dendritic growth over time may puncture the separator in a cell, ultimately causing short circuit[72, 73].

To prevent self-discharge, anode surface coating and ion sputtering have been introduced to shield direct contact of anodic zinc[71, 74]. Conventionally, SEI formation occurs on the surface of electrodes in batteries however in water-containing electrolyte, solid-solid interphase is more desirable to suppress the ion dissolution and dendrite formation. For instance, K. Zhao et al.[75] demonstrated atomic layer deposition of TiO_2 thin film coating to the metallic zinc anode which considerably reduced the amount of hydrogen gas evolution and increased long-term stability at a pH value ≈ 4.

Another method is to dissolve additives/inhibitors to the electrolyte solution. In general, different electrolyte compositions or additives react and bind to the surface of electrodes to restrict irreversible material/electrolyte consumption and dendritic growth of recombined ions. The addition of triethylphosphate in 0.5 M $Zn(CF_3SO_3)_2$ resulted in no change being observed in SEM images before and after 1000 cycles as well as suppressing dendrite formation[76].

In addition to electrode modifications, overall surface area of the anode immersed or in contact with the electrolyte must be increased to maximise the anodic reactions.

1.2.2.2 Electrolyte

Generally, for metal-air batteries, two types of electrolytes are used; an aprotic electrolyte (e.g. for lithium, sodium) or an aqueous cell-construction (e.g. for zinc, aluminium, iron).

For aqueous electrolyte, used in ZABs, either KOH (alkaline) or H_2SO_4/$HClO_4$ (acid) is used[40].

Both aqueous electrolytes are relatively inexpensive compared to non-aqueous electrolyte solutions however, there are still challenges yet to solve[34]. In acidic conditions, degradation and corrosion of the electrode material can occur; suffer from long-term battery performance. Meanwhile, alkaline solutions also face threats from flow-in of ambient CO_2 which undergo a side reaction to generate potassium carbonate. Carbonate poisoning consumes the electrolyte irreversibly to dry the cell and blocks the electrode pores in a similar way to metal dendrites[27]. One way to address this challenge is to use O_2-selective membranes to block CO_2 permeation[77].

Solid polymer electrolytes have been developed to reduce dendritic site formation and electrode dissolution whilst maintaining the overall ion conductivity and transport. Advance of flexible cells is also possible due to possible bending movements of solid polymer electrolytes. Poly(vinylidene fluoride) (PVDF), poly-acrylic acid (PAA), polyacrylamide (PAM) based polymer electrolyte maintained relatively high ionic conductivity (ranging from 0.01 to 0.1 mS cm^{-1})[78-83]; liquid KOH electrolyte ionic conductivity is between 0.56 to 0.62 S cm^{-1}.[84]

1.2.2.3 Cathode materials

The cathode consists of two components; an active catalyst layer and a gas diffusion layer. During electrocatalysis, oxygen undergo gas-solid-liquid triple phase boundaries. To minimise water entering/escaping the cell whilst providing gas diffusion pathways, a hydrophobic binder/paper is used between the two boundaries – e.g. polytetrafluoroethylene (PTFE) or hydrophobic carbon paper[85-89].

Currently, extensive research is focused on the rates of catalytic activities of the cathode materials as the rate of zinc oxidation, and corrosion during discharge are long-term effects. An adequate number of active sites, adsorption/desorption strength, electron pathway, overpotential, and durability are necessary, to be able to carry out ORR and OER effectively. From a materials perspective, cathode materials can be categorised as the following; noble-metal composites and alloys, transition metal containing compounds, non-metallic doped carbon allotropes, and hybrid systems which may include multiple functionalities of the listed complexes. Morphologies may vary from 3-dimensional frameworks to 1-dimensional substrates, amorphous and crystalline (ordered).

1.2.2.3.1 Noble-metal containing catalysts

Noble-metal (precious metal) containing materials have always been the dominant choice for nearly all catalysis reactions including ORR and OER. Very high activities, relative to any other single element, is mostly due to the direct 4 electron pathway[69]. Hence, platinum on carbon (Pt/C) is accepted as the most outstanding benchmark ORR catalyst, whilst for OER it is iridium on carbon (Ir/C) and ruthenium oxide (RuO_2)[90]. Still, commercialisation is hampered by the expensive raw materials and the poor efficiency of these materials in long-term cycles due to poisoning (elements positioned on the sides of the oxygen conversion activity peaks in Gibbs free energy diagram shown in Figure 1.4a). Bi-functionality is also restricted for most of ORR materials caused by the dissolution process in OER potential[91].

Initially, researchers explored the effect of weight percentage of precious metals in Pt/C and Ir/C on the overall catalytic activity to gain general insight and to reduce the overall loading percentage[92, 93]. Studies showed that the exposed surface atoms contribute to the catalysis reaction while, the inner core (surrounded) atoms hardly contributed. In view of this, single crystals, or clusters of Pt and loading of other noble metals have been studied to fine-tune the performances. Sheng et al.[94] reviewed the synthesis of improved carbon supported Pt realized by well-dispersed nanoparticles (< 2 nm) to maximize mass activity.

The surface atom arrangement, together with different shapes, also affect the activity efficiency. Particularly, investigations on various index facets of noble-metal species led Hoshi et al.[95] to a conclusion that the ORR catalytic reactions were orientation dependent; Pt (111) surface exhibited higher ORR activity than the (100) surface.

To reach the maximum potential activity of Pt, different metals and carbonaceous supports were utilized. K Y Cho et al.[96] reported Mo-doped Pd, Pt octahedral shell embedded carbon with less overpotential for the ORR process than of Pt/C. Better electronic conductivity and enhanced stability were seen by the change in electronic structure with the introduced molybdenum. The carbon substrate also provided an active charge transfer mechanism (with the increase in conductivity) as well as intrinsic catalytic properties – active Pt sites are protected by carbon lamination. Pt alloys with different metals (e.g. Ni, Co, Pd, Au), in most cases, enhance the catalytic performances because oxygen molecules are more weakly bound to the surface for the regeneration step[97-99]. Similarly, Ru- or Ir- containing hybrid materials were reported to exhibit improved general OER performances as expected. Kim et al.[100] examined iridium complexes for OERs by structural variations (from nanoparticles to nanoporous morphologies) and proposed that the architecture via fast dealloying of oxygen could lead to an increase in activity stability.

1.2.2.3.2 Transition-metal containing catalysts

In efforts to completely remove precious-metal usage, transition metal complexes, with numerous compositions, have been explored as possible candidates for electrocatalysis. They are highly abundant (which directly leads to manageable costs), have good stability in alkaline systems and fair tolerance in acid electrolyte and have variable electronic states to assist reactions on the surfaces. Although the associated activities are slightly lower, the overall electron transfer number for oxygen reactions can reach very close to 4 (similar to noble-metal group) by altering electron environments with different metallic compositions[101-103].

There are broad number of structures available ranging from layered, spinel, to perovskites; transition-metal oxides, layered double hydroxide, nitrides, and carbides as rising classes of metal catalysts. Especially, the first row of transition metals (e.g. Mn, Fe, Co, Ni) demonstrated reasonable sole ORR or OER capabilities but also very good bifunctional oxygen reaction performances[104-107]. Cobalt containing species, for instance, CoO, Co_3O_4, Co_9S_8, CoP, are known for efficient oxygen electrocatalysis as well as hydrogen evolution (HER), a process which is involved with OER for water splitting[108-111] – this follows the calculated ORR/OER activity from the volcano plot (Figure 1.4).

Multiple metal co-doping (multi-core) can generate hierarchical frameworks with oxygen vacancies which promotes oxygen electrocatalytic reactions. Wang et al.[112] revealed a change in local structure around the transition metal ions with oxygen vacancies/defects favouring oxygen activations. Yin et al.[113] outlined Zn-air batteries and water splitting devices fabrication using NiS_2/CoS_2 porous nanowires; without a conductive substrate, they still showed outstanding OER performance with the lowest overpotential realized on NiS_2/CoS_2-O sites. Bimetallic Ni-Fe complexes have been described several times to have superior intrinsic activities in OER. Gorlin et al.[114] carried out quantitative analyses on various Ni-Fe oxides to derive the OER dynamics. With the assistance of X-ray absorption spectroscopy at Ni and Fe K-edges, they deduced that multiple oxidation states of Ni (+2 to +4) species existed in this well-mixed bimetallic oxyhydroxide. Diminished concentration of Ni^{4+} supported the formation of active sites, which can be described as $Ni^{2+}Fe^{3+}OOH$, to boost the overall Faradaic efficiencies.

Frequently, carbonaceous materials have been used in conjunction with transition-metal-containing complexes. Owing to their physical and electronic properties, deposition of metal complexes or clusters on carbon composites considerably increase both electrical conductivity and stability of the material due to core-metal site shielding provided by the outer layer coating. Defect sites from the carbon medium can either be the anchoring sites for metallic species or become, along with metal centres, catalytically active sites[115-118]. Carbon materials can be used directly (metal growth on the surface during syntheses) or indirectly (addition of carbon substrates to already synthesised metal nanoparticles) in catalyst preparations. Wang et al.[119] fabricated metal-oxide particles on carbon directly for bifunctional oxygen cathodes. They deduced that the impregnated cobalt and cobalt oxide particles on carbon formed Co-N-C bonds, promoting bifunctionality with overpotential between ORR and OER to be only 0.75 V compared to around 1.05 V for Pt/C and Ir/C. Xiao et al.[120] produced iron sulphide decorated N-, S-dual doped polydopamine spheres. The structure exhibited superior ORR capabilities (6.2 mA cm^{-2}), even higher than that of Pt/C in alkaline media, with very promising results in acidic conditions, and good durability. Tong et al.[121] used a direct synthesis approach with prepared GO to form graphene with defects occupied by in-situ formed CoO_x. Abundant oxygen holes and the metal-heteroatom-carbon interaction coupled effects strongly enhanced the activity in alkaline environment.

In particular, the formation of non-precious metal-nitrogen-carbon (M-N-C) bonds, is found to have synergetic effect in oxygen catalysis for providing higher activities. The coordination number of N to metal atoms influences the charge distribution at the M-N-C centres[122]. Various nitrogen-containing compounds can be used to provide similar effect with different porosity; these linkers include phthalocyanine, porphyrin-like, aniline, pyrrole, and ethylenediamine[123-127]. Kim et al.[128] established an experiment where Vulcan (carbon) was enriched with Co_3O_4 nanoparticles followed by polypyrrole coating. This material was then annealed at high temperature to transform Co_3O_4 encapsulated species to CoO phase material. Also, polypyrrole decomposed to become nitrogen doped carbon material with accessible pores for efficient electron transfer whilst preventing particle aggregation during catalysis. Wan et al.[129] suggested a Co-doped carbon preparation method, regulated by selective anions in the reaction. Interestingly, pyrolysis of cobalt in carbon, in the presence of either the nitrate ions or chloride ions, led to distinctive Co site formations. The preferred Co-N-C active sites were selectively constructed on the surface of the carbon layers with chloride ions whereas, nitrate ions were responsible for the encasing of metallic cobalt nanoparticles hindering the catalytic reactions of cobalt. However, it is worth noting that not all M-N-C sites are active towards ORR/OER. Fu et al.[130] demonstrated the pore size effect and the accessibility to M-N-C sites responsible for ORR/OER by varying N-source carbon monomers used in the early stage of the electrocatalyst preparation. Sites located in meso- or micro-pores were able to participate in the conversion reactions whereas the inaccessible moieties deeply buried in bulk remained inactive. This is true to all types of electrocatalysts.

Another popular category of transition-metal-containing material is the metal-organic framework (MOF). MOFs are a highly structured framework consisting of metal ion centres surrounded by coordinated organic linkers in series of arrays (can be classified as polymers). Structures vary depending on the ligand environment; most commonly 2-dimensional planes or porous 3-dimensional networks are formed. Choices of metals and chelating ligands can be easily replaced to design preferred shape, size, and porosity[131]. Generally, MOFs are either embedded on a carbon substrate or pyrolysed in an inert atmosphere to bypass poor conductivity issues and to create more active sites. Sacrificial carbonisation of MOFs results in rational carbon frameworks with M-N-C bonds. This can only occur at annealing temperature of 600 °C or higher (depending on the choice of metal) where bonds between metal species and C-N functional groups break[132]. The advantage of using MOFs is that the skeleton of the framework remains providing a reticulated porous structure to enhance accessibility of catalytic sites[133]. Recently, Gadipelli et al.[134] reported an effective method of synthesizing ORR/OER catalysts by controlling the degree of graphitisation of MOFs with varied metal-ion concentrations. The reduction and evolution reactions were switched by altering the concentration ratio of cobalt and zinc – increasing the zinc moieties for ORR and cobalt for OER. High-temperature annealing process of the frameworks then provided the necessary N-doped carbon structure for the oxygen electrocatalysis to occur. Self-assembly and growth of MOFs were achieved on a 3D microporous polymeric carbon substrate by Jia et al.[135] Solutions of cobalt and 2-methylimidazole were added to cleaned melamine sponge which led to full coverage of surface with needle-like zeolitic-imidazolate-framework (ZIF). The tubular structure exhibited good electrocatalytic activity with high accessible surface area.

1.2.2.3.3 Carbon containing (non-metal) catalysts

Over the last few years, there have been many attempts to utilise carbon materials exclusively as metal-free electrocatalysts rather than as catalyst supports. They offer large surface area per volume, affordability, high abundancy and stability in alkaline systems along with good electrical conductivity (free electron transport across graphitic sp^2 and sp^3 carbon and hence low resistivity); carbon materials are regarded as one of the finest tuneable catalysts[136-138]. Many carbon allotropes have been reviewed as the framework for oxygen electrocatalysis – this includes graphene, carbon nanotubes (CNTs), graphdiynes, graphitic carbon nitrides, and other carbon polymers[139-142]. Yet, this is still restricted to alkaline media due to stability issues in acidic conditions (similar to transition metal group catalysts). Also, pristine carbons, such as untreated graphite, carbon nanotubes, graphene, show almost negligible electrocatalytic activities as there are no catalytically active sites to adsorb and donate electrons in ordered structures[143].

Chemical changes to carbon materials can be made by introducing heteroatoms (B, N, P, S). Either replacing a carbon atom by a heteroatom or having heteroatom functional groups lead to change in electron density population around the region[144, 145]. Nitrogen has been used as an effective dopant due to its similarity to carbon (differs by 1 atomic number), providing easy incorporation into the carbon matrix but with sufficient alteration of electronic behaviour in order to increase catalytic performances. Nitrogen can exist as several species within one single substrate; graphitic (where N is bonded with 3 neighbouring carbons in 6-membered carbon ring (6-MR)), pyridinic (where N is bonded to 2 carbons and sitting on the edge of 6-MR), pyrrolic nitrogen (one of the edges of 5-MR), and amines. These functional groups all have different associated energies toward oxygen electrocatalysis[146-148].

Jiao et al.[149] prepared metal-free heteroatom (B, N, P, O, and S) doped graphene samples to investigate the dopant effect towards ORRs and calculated relative free energies for each active site using Density Functional Theory (DFT) (shown in Figure 1.5). N-doped and B-doped graphene were found to exhibit the highest onset potential with lowest predicted free energy for ORRs followed by P-doping and S-doping. From the free energy diagram, it was clear that the associated energies for all adsorbates on graphitic nitrogen was significantly lower than that of other nitrogen functional groups and therefore is the most active in N-doped graphene for ORRs. However, the nitrogen atom itself in graphitic nitrogen was not regarded as ORR active as the adsorption free energy on the graphitic nitrogen was higher than the energy observed on the carbon next to the nitrogen and OOH and OH cannot chemisorb to the graphitic N. Graphitic carbon substrates (resembling graphene) can be prepared via bottom-up organic polymerisation reactions.

Hierarchical carbon frameworks can be designed from bottom-up polymerisation processes. Preparation methods include thermally-assisted (such as hydrothermal, wet, processes or pyrolysis of carbon, dry process) condensation polymerisations, depositions, and catalyst-assisted coupling reactions. Typically, an aromatic carbon monomer and another organic monomer (both monomers either with/without heteroatom functional groups) are selected for polymerisation. By varying the size and functional groups of organic building units, morphologies and pore sizes can be tailored. Via pyrolysis of trithiocyanuric acid and sucrose, Pei et al.[150] synthesised highly porous and active reversible oxygen electrocatalysts. Pyrolysis mixture consisted silica spheres (as hard template for carbon polymerisation), two monomers, and Teflon to thermally decompose to release HF to etch the SiO_2 in-situ. Macro-pores were evidently introduced by the silica template as well as the micro- and meso-pores from the smaller molecules. With the increase in carbonisation temperature, the relative content ratio of graphitic N increased; along with doped sulphur, the electrocatalytic performances in both ORR and OER were extremely high. N-doped and pure porous carbon frameworks both exhibited lower activities than the N, S-enriched porous carbon – this suggests a synergistic effect when both N and S are doped. Zhao et al.[151] synthesised N-doped few-layer graphdiynes for oxygen electrocatalysis via Suzuki cross-coupling methods. Hexabromobenzene was converted with ethynyl groups (with sp-C) and the polymer was grown on a cupper substrate. By replacing the sp-C with N, the oxygen binding energies observed from sp-hybridised nitrogen atoms (energy values of 2.13 and 2.51 eV) were very close to the optimal energy values for ORRs (between 1.81-2.88 eV) compared to graphitic and pyridinic Ns (3.29 and 3.96 eV)[152] resulting in noticeable catalytic activity increase, comparable to Pt/C.

Similar to MOFs, covalent-organic-frameworks (COFs) gained much attention due to the formation of stable porous 2D/3D crystalline structures. COF formation does not require a metal catalyst in its process which is a major difference compared to many bottom-up carbon polymerisation reactions[153, 154]. Xu et al.[155] assembled a 2D COF with a trianiline compound and exfoliated the stacked 2D COF layers with phytic acid. After further pyrolysis step, prepared carbon sheets exhibited very high electrocatalytic performances due to many N-doped sites with exposed numerous edges.

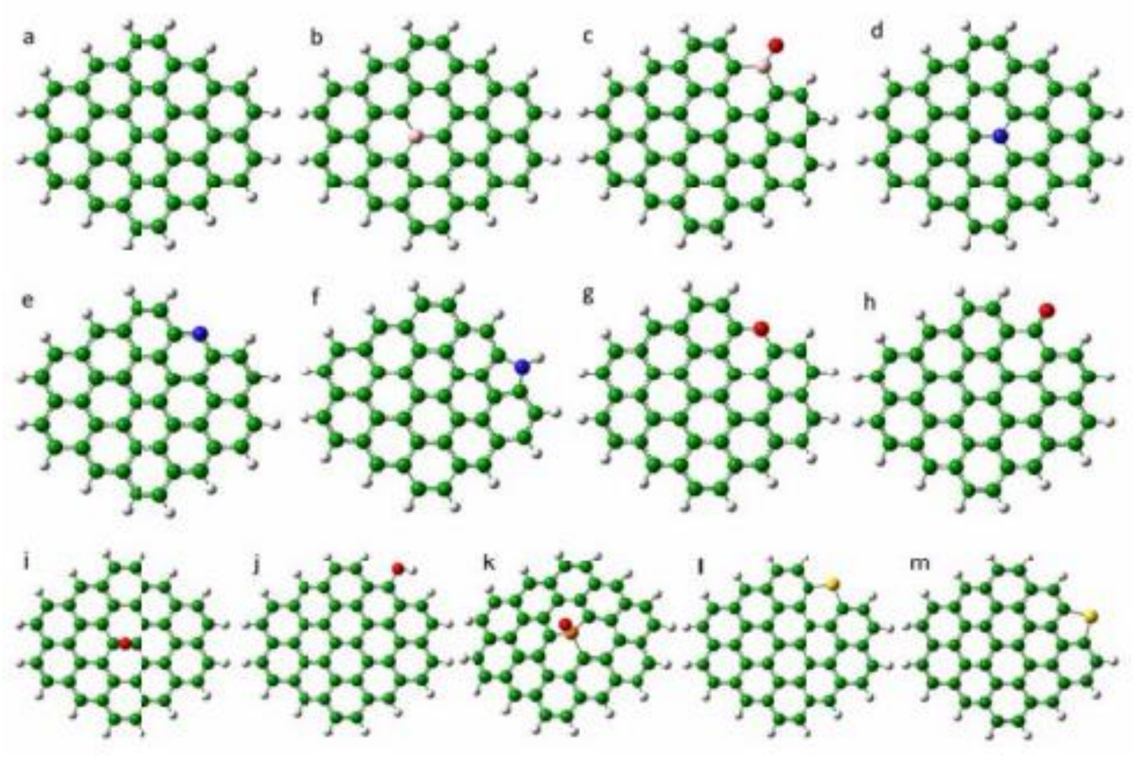

Figure 1.5 Heteroatom-doping configurations on graphene; (a) pure, (b) graphitic B, (c) 2C-B-O type, (d) graphitic N, (e) pyridinic N, (f) pyrrolic N, (g) pyran type O, (h) carbonyl O, (i) epoxy O, (j) hydroxyl O, (k) P-doped, (l) C-S-C type S, and (m) thiophene S graphene [149].

Despite the structural variety and scalability, drawbacks are the use of hard-template for the fabrication of porous media which requires harsh acid etching, use of precious metal catalysts for coupling reactions, and complex multi-step organic reactions for some polymerisation processes; result in expensive raw materials cost, environmental issues, and manufacturing costs.

Overall challenges still remain for metal-free carbon electrocatalysts to be fully utilised as to other precious-metal or transition-metal counterparts – need to reduce the overpotential required for the reactions to occur and the overall 4 e^- oxygen conversion process. In the following chapters, different allotropes and associated synthesis procedures will be introduced to tackle current limitations on kinetics and catalytic behaviours of non-metal electrocatalysts. Electrochemical performances and long-term stability tests are compared with conventional benchmarks to evaluate the materials applicability.

Chapter 2 : Experimental and characterisations

2.1 Annealed carbon polymer

2.1.1 Materials

Glucose (D-(+)-glucose monohydrate, ≥99.5%, Sigma-Aldrich), dicyandiamide (DCDA, 99%, Sigma-Aldrich), graphite (<20 μm, Sigma-Aldrich), sulphuric acid (95-97%, Merck KGaA), phosphoric acid (>85 wt.%, Sigma-Aldrich), potassium permanganate (≥99%, Sigma-Aldrich), hydrogen peroxide (30 wt.%, Sigma-Aldrich), and hydrochloric acid (35%, VWR) were directly used as purchased with no additional treatments or purifications.

2.1.2 Synthesis of annealed carbon polymer (GDC)

All annealed carbon polymer samples (GDCs) were prepared by a single two-step annealing process. In a typical N-doped GDC synthesis, glucose and dicyandiamide were thoroughly mixed in a 1:1 ratio. The powder mix was then transferred to an alumina boat and programmed to anneal first at 300 °C for 3 h under N_2 gas flow (>99.998%, gas flow of 150 SCCM) with 5 °C min^{-1} ramping rate in a sealed horizontal furnace. After conducting the initial polymerisation, the temperature was increased (5 °C min^{-1} temperature ramping rate) to various temperature (700, 800, 900, and 1000 °C) to anneal for 3 h under N_2 flow. Obtained samples were named as GDC_XXXX (where XXXX denote the final target temperature used).

2.1.3 Synthesis of graphene oxide (GO)

Graphene oxide (GO) was synthesised by oxidation of graphite using a reported improved Hummers' method[156]. A mixture of concentrated sulphuric acid and phosphoric acid (9:1 volume ratio) was stirred and cooled to < 5 °C. With vigorous stirring, graphite powder (5 g) was added to the acid mixture. Keeping the temperature below 10 °C, potassium permanganate (6 equiv. wt.) was slowly added. After the addition, the mixture was heated to 50 °C for 24 h. 600 mL of DI water was added carefully with the temperature kept below 80 °C, followed by the addition of approximately 40 mL of hydrogen peroxide solution. The obtained slurry mixture was thoroughly washed in 3.4% HCl then with DI water. GO mixture was freeze-dried in liquid N_2 to obtain light-brown powder.

2.1.4 Synthesis of annealed graphene oxide (AGO)

Similar to GDC samples, GO was annealed at 900 °C for 3 h under N_2 gas flow (150 SCCM) in a sealed horizontal furnace. Samples named as AGO_900.

2.2 Heteroatom-doped carbon dot embedded graphene

2.2.1 Materials

Citric acid (CA, 99%, Sigma-Aldrich), dicyandiamide (DCDA, 99%, Sigma-Aldrich), thiourea (TU, 99%, Sigma-Aldrich), Nafion (5 wt.% in alcohol and water, Sigma-Aldrich), and 20% platinum on carbon black (Pt/C, Alfa Aesar) were directly used as received with no additional modification or treatments.

2.2.2 Synthesis of heteroatom-doped carbon dots (CD)

All carbon dots (CDs) were prepared by a one-pot hydrothermal process. In a typical N-doped CD synthesis, 15 mmol of CA and 15 mmol of DCDA were dissolved in 15 mL of DI water and sonicated (~37 kHz) for 30 min to obtain homogeneous solution. The resulting solution was then transferred into a 50 mL Teflon-lined stainless-steel autoclave and heated at 180 °C for 6 h. Large agglomerated particles were separated using 0.22 μm pore filter membranes (mixed cellulose esters membrane, hydrophilic, MF-Millipore™ Membrane Filter). Afterward, the filtrate was completely dehydrated at 100 °C for 24 h and ground to obtain fine powder. N, S co-doped CDs were prepared only by changing the precursor to TU. Samples were named as N-CD and NS-CD, respectively.

2.2.3 Synthesis of heteroatom-doped CD-embedded graphene hydrogel (CD@gf)

GO was synthesised by oxidation of graphite using a reported improved Hummers' method (detailed in Chapter 2.1.3). The obtained GO powder was added to DI water and ultrasonicated for 2 h to obtain homogeneous GO solution (5 mg mL^{-1}). 20 mg of desired CD (either N- or N, S-doped) was added to 20 mL of GO solution, sonicated for 30 min and was subjected to hydrothermal reaction at 180 °C for 12 h. The resulting reduced GO hydrogel was washed with DI water a few times to separate/remove unreacted CDs and freeze-dried in liquid N_2. Samples were named after the CDs used in the reaction: N-CD@gf, and NS-CD@gf. The hydrogel formed with no CD was named as RGel. The amount of NS-CD used was either halved or doubled to obtain NS-CD@gf (s) and NS-CD@gf (h).

2.2.4 Thermal treatment of CD-embedded graphene hydrogel (CD@gf_aXXXX)

Annealing processes were conducted at various temperature (800, 900, and 1000 °C) for 3 h under N_2 flow with 3 °C min^{-1} temperature ramping rate. Samples were named as CD@gf_aXXXX (where XXXX denote target temperature used).

2.2.5 Synthesis of N, S-doped hydrogel (NS-Gel) and thermal treatment (NS-Gel_a900)

Similar to the preparation of NS-CD@gf, N, S-doped hydrogel was synthesised by using 20 mg of TU instead of CDs (named NS-Gel). The resulting hydrogel was annealed at 900 °C, in same conditions, and was named NS-Gel_a900.

2.3 Pyrene carbon polymer

2.3.1 Materials

Pyrene (98%, Alfa Aesar), chlorine gas (99.9%, CK Special Gases Ltd.), aluminium chloride (99% anhydrous, Acros Organics), nitric acid (65%, Merck KGaA), melamine (99%, Sigma-Aldrich), trithiocyanuric acid (TTCA, 95%, Alfa Aesar), Nafion (5 wt.% in alcohol and water, Sigma-Aldrich), and 20% platinum on carbon black (Alfa Aesar) were directly used in experiments and no additional modification or treatments were made.

2.3.2 Synthesis of tetra-chlorinated-pyrene (CPy)

In a typical process, 2.47 mmol of pyrene was dissolved in 50 mL of dichloroethane (DCE). Chlorine gas was slowly bubbled to the reaction mixture for 1 h. Note. Cl_2 is a toxic gas therefore experiments should always be carried out in a fumehood. The apparatus setup had a trap fitted and the gas-end was connected to a large water tank. The reaction mixture was then heated to 60 °C for 8 h, with constant slow supply of Cl_2 gas. The mixture was washed with DCE several times to remove unreacted species and vacuum-dried to obtain a fine powder.

2.3.3 Friedel-Craft polymerisation of pyrene and CPy (PyG)

1 mmol of pyrene and 1 mmol of CPy were dissolved and stirred in 20 mL of DCE. Then, 2 mmol of anhydrous aluminium chloride was slowly added to the mixture. After the addition, the mixture was refluxed at 80 °C for 8 h. The obtained black/reddish brown mixture was filtered and washed with DCE and methanol to remove unreacted species and $AlCl_3$.

2.3.4 Thermal reduction and exfoliation of PyG (rPyG)

10 mg of PyG was placed in a quartz tube and thermally treated in a vertical furnace in air for 30 mins at 350 °C.

2.3.5 Oxidation process to few-layer PyG (PyGO)

50 mg of PyG was placed in a flask and 10 mL of nitric acid was added slowly under stirring. The volume of acid used was the amount needed to fully wet/disperse the powder. The mixture was refluxed at 80 °C for 8 h with vigorous stirring. The obtained slurry mixture was thoroughly washed with deionised water until pH ~7 and freeze-dried.

2.3.6 N- or N, S- doping of PyG (NPyG/NSPyG)

10 mg of PyG sample was mixed with 100 mg of either melamine or TTCA and then annealed at 900 °C for 3 h under N_2 flow. Samples were denoted as NPyG and NSPyG depending on the dopants. Note. High temperature annealing of doping precursors alone result in full decomposition however with a carbon substrate, chemical reactions take place with the fragments of precursors (formed during decomposition) i.e. elemental doping[151, 157].

2.3.7 N- or N, S- doping of PyGO (NPyGO/NSPyGO)

Similar to the preparation of NPyG and NSPyG, doping of PyGO was achieved by using 10 mg of PyGO instead of PyG.

2.3.8 Thermal reduction of GO (rGO)

Prepared GO was placed in a quartz tube and was subjected to heating at 300 °C in a vertical furnace in air for 30 min to thermally reduce GO. Initial brown colour of GO changed to black fluffy powder.

2.4 Yields

	Precursors	Yield
GDC_700	Glucose – 500 mg DCDA – 500 mg	217 (± 18) mg
GDC_800		167 (± 20) mg
GDC_900		155 (± 14) mg
GDC_1000		121 (± 15) mg
GO	Graphite – 5 g	5.21 (± 0.11) g
AGO_900	GO – 30 mg	8.67 (± 0.07) mg
N-CD	CA – 2.99 g DCDA – 1.31 g	1.43 (± 0.15) g
NS-CD	CA – 2.99 g TU – 1.19 g	1.16 (± 0.13) g
N-CD@gf	GO – 100 mg CD – 20 mg	21.44 (± 0.21) mg
NS-CD@gf		20.35 (± 0.33) mg
RGel	GO – 100 mg	30.04 (± 0.39) mg
N-CD@gf_a900	CD@gf – 30 mg	9.02 (± 0.14) mg
NS-CD@gf_a900		8.73 (± 0.21) mg

	Precursors	**Yield**
CPy	Pyrene – 500 mg	731 (± 25) mg
PyG	Pyrene – 202 mg CPy – 340 mg	470 (± 31) mg
rPyG	PyG – 10 mg	7.41 (± 0.27) mg
PyGO	PyG – 50 mg	29.42 (± 0.75) mg
NPyG	PyG/PyGO – 10 mg melamine/ trithiocyanuric acid – 100 mg	2.89 (± 0.13) mg
NSPyG		2.73 (± 0.26) mg
NPyGO		2.25 (± 0.11) mg
NSPyGO		1.94 (± 0.17) mg

2.5 Structural characterisation

XRD was used for phase identification. Samples were prepared by first grinding the powder sample and packing into a borosilicate capillary tube. Patterns were collected between 2° and 60° using a STOE Stadi-P (Cu Kα radiation, $\lambda = 1.5406$ Å). Chemical composition and chemical bond identification were studied by XPS. Samples were grinded and adhered to a carbon tape on an XPS sample grid. Results were collected using a Thermo Scientific K-alpha (Al source, 1486.6 eV) with flood gun. To obtain repeatable results, 3 regions of each sample was measured and average atomic percentages were calculated. Obtained XPS data were analysed using CasaXPS software and all data were calibrated to the C 1s peak position using adventitious carbon at 285 eV. For each high-resolution elemental scan, FWHMs of all fittings were constrained to have equal contribution to the overall energy fitting. Ratio of 2:1 was applied for the p-orbital splitting. Morphology of materials were determined by SEM and the images were taken using a JEOL JSM-6301F instrument in the secondary electrons imaging mode. Small amount of powder for each sample was adhered to a carbon tape on a SEM sample stud. Morphologies, phases, and elemental composition of materials were also recorded by TEM and EDS on a JEOL JEM 2100 (LaB_6 filament) and an Oxford Instruments X-MaxN 80-T Silicon Drift Detector (SDD) fitted to a TEM machine – EDS images were taken in the dark-field imaging mode. High-resolution TEM images were obtained using a Titan G2 Cube 60-300 instrument at the accelerating voltage of 60 kV – images were acquired from Korea Institute of Science and Technology. All TEM samples were prepared by sonicating small amount in MeOH and depositing on a holey-carbon film coated copper grid. Physical appearance and the atomic thickness of materials were shown by the AFM images and were attained by a Keysight Technologies 5600LS AFM instrument. Attenuated total reflectance infra-red spectra (ATR-IR) were obtained using a Bruker Tensor 27 FTIR spectrometer. Mass spectroscopy data was collected using an Agilent 6510 Q TOF mass spectrometers (ESI). Raman spectroscopy was used to calculate the ratio of D and G bands (I_D/I_G) of carbon samples, out-of-plane and in-plane vibrations of defects/disorder and hybridised carbons. Raman spectra of bulk powder samples were obtained by using a Renishaw Ramascope (514.5 nm laser) in ambient conditions. BET analyses provided information on surface area, pore size distribution, and total pore volume. BET isotherms of nitrogen adsorption–desorption were measured using Quantachrome Autosorb-iQC at 77 K, liquid N_2. Sample mass was greater than 10 mg for all measurements to reduce errors. All recorded BET data were analysed using ASiQwin software – for pore size distribution calculations, QSDFT and BJH methods were applied to measure micro/meso-pores with effects of chemical heterogeneity and surface roughness.

2.6 Electrochemical characterisation

To determine the feasibility of the materials for oxygen electrocatalysis, materials were electrochemically tested in the water splitting region (~1.23 V vs. RHE). All electrochemical tests were carried out at room temperature using Metrohm Autolab PGSTAT302N with a three-electrode system: Ag/AgCl (in saturated KCl) reference electrode, carbon rod as a counter electrode, and a glassy carbon coated working electrode where material of interest was casted on the surface. Aqueous KOH (0.1 M) electrolyte was used and saturated by O_2 (>99.5%) or N_2 (>99.998%) purge prior to the measurements. Bubbling of either O_2 or N_2 was kept the same to maintain saturation. For the preparation of active catalyst, 2 mg of sample was added to 480 µL DI water and 20 µL Nafion mixture and sonicated for 1 h to achieve a homogeneous ink. 5 µL of the ink suspension was drop-casted onto the glassy carbon (GC) tip (3 mm diameter) and dried at 60 °C. Active catalyst loading was fixed to ~0.28 mg cm^{-2} for all samples. Increasing the mass loading generally increases the total charge transferred on the electrode i.e. increase the observed current density. However, with a high mass loading, not all surfaces of the catalyst will participate in the electrochemical reactions (especially with limited RDE-GC tip area)[158]. Fresh electrolyte was used for each batch of experiments to minimise cross-contamination; a separate cell/electrode was used for Pt/C measurements.

Cyclic voltammetry (CV) scans were performed between −0.8 and 0.2 V versus Ag/AgCl with a scan rate of 10 mV s^{-1} for ten cycles. Linear sweep voltammetry (LSV) curves were recorded using a rotating disk electrode (Metrohm) at the potential range of −0.8 to 0.2 V versus Ag/AgCl system with sweeping voltage of 10 mV s^{-1} and varying rotation speed, 400, 800, 1200, 1600, and 2000 rpm, to study ORR capabilities. Electrode rotation is required to constantly feed excess O_2 to the surface of the electrode in an aqueous setup. OER measurements were taken at the potential range of 0.2 to 1.0 V versus Ag/AgCl with rotation speed of 1600 rpm. When compared to literature, standard rotation speed of 1600 rpm was used for both ORR and OER. Measurements were repeated (either 2 or 3 times) for consistency. The effect of current/resistance of the cell was not considered (no iR compensation) in any of the obtained data. From the RDE results, electron transfer number, n, was measured using the K–L relation correlated from the current densities measured. The K–L equations are as follows[159]:

$$\frac{1}{J}=\frac{1}{J_L}+\frac{1}{J_K}=\frac{1}{B\omega^{1/2}}+\frac{1}{J_K}$$

$$B=0.62nFC_0(D_0)^{2/3}\nu^{-1/6}$$

$$J_K=nFkC_0$$

where J is the measured current density (normalised by the geometric area of the electrode), J_L and J_K are diffusion and kinetic limiting current densities, B is the Levich constant determined by the inverse value of the slope of a straight linear fitting of the measured current densities, ω is the angular rotation velocity of the electrode, F is the Faraday constant (96485 C mol^{-1}), C_0 is the O_2 concentration dissolved in KOH solution (1.2 x 10^{-6} mol cm^{-3}), D_0 is the O_2 diffusion coefficient in electrolyte (1.9 x 10^{-5} cm^2 s^{-1}), and v is the kinetic viscosity of the KOH electrolyte solution (0.01 m^2 s^{-1})[160]. A chronoamperometric test was performed at −0.3 V versus Ag/AgCl for ORR and 0.7 V versus Ag/AgCl for OER with constant RDE rotation of 1600 rpm to measure the stability of samples.

The recorded Ag/AgCl reference electrode potentials were converted to RHE potential range using the following relations:

$$E_{RHE} = E_{vs.Ag/AgCl} + 0.197 + 0.059pH$$

$$E_{RHE} = E_{vs.Ag/AgCl} + 0.964$$

Consequently, the RHE conversion is defined by the addition of 0.964 V to measured potentials in 0.1 M KOH systems.

Chapter 3 : Highly defective and active electrocatalyst via high temperature polymerisation of carbon monomer

3.1 Introduction

Advancement of many energy storage and conversion devices evolved from electrochemical setups to electrocatalytic systems[161, 162]. However, the complexity of oxidation/reduction mechanisms (involving electron transfer process at the surface) still limits the full potential of many conversion devices. In terms of material fabrications, graphene or carbon variants have widely been applied either as a conductive substrate for an electrode or as the catalyst/active material due to high electron conductivity, large surface area, tunability, material stability, and cost[163, 164].Many studies demonstrate structural modifications of graphene with either metals or heteroatoms to generate active centres for oxygen electrocatalysis[165, 166]. This is achieved by fine tuning the electronic properties of the graphene surface to be able to donate and/or accept electrons. Elemental doping on graphene occurs at defect sites and around remaining oxygen moieties from post-reduction of graphene oxide. Doping heteroatoms, especially nitrogen, to graphitic carbons has shown remarkable electronic properties toward electrocatalytic reactions with change in electron density and minimal alteration of the structure[149]. Heteroatom-doping can be carried out either in-situ with prepared graphene or via post-treatment with dopant precursors[167, 168]. Neither method can control the doping concentration fully however in-situ method does offer a more even doping distribution throughout the material.

Carbonisation can be easily achieved by annealing monomers at high temperature (>500 °C)[169, 170]. Thermal decomposition and rearrangement of monomers result in more stable and ordered structures as well as elemental doping and effective removal of remaining branched functional groups with an increase in electronic conductivity. As the temperature increases, the carbonisation degree increases. The high-temperature assisted bottom-up approach avoids the use of strong acids/oxidising agents, and the process is less complex to setup[171, 172] compared to hard-template annealing processes and some bottom-up polymerisation methods[173, 174].

In this chapter, annealed carbon polymers were synthesised using readily available organic compounds, glucose and dicyandiamide, to be tested as oxygen electrocatalysts. Material preparation consists of 2-step annealing process; first target temperature to be just enough to decompose the organic compounds in order for the initial polymerisation to take place followed by the desired high temperature carbonisation. Low temperature polymerisation is necessary to maintain the carbonaceous framework at high temperature conditions. A wide range of carbonisation temperature was studied (700-1000 °C) to understand the temperature effect on heteroatom concentration in substrates, defect formations, and electrocatalytic activities.

3.2 Results and discussion

3.2.1 Carbonisation via a single 2-step heat treatment

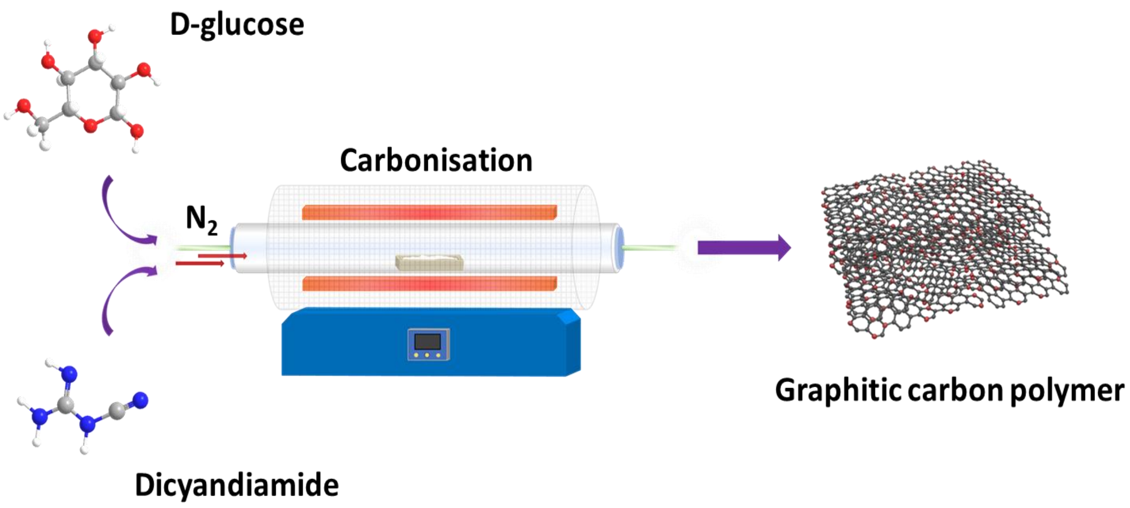

Figure 3.1 Schematic representation of the GDC sample preparation via polymerisation of glucose and DCDA at high temperatures.

The schematic synthesis procedure of annealed carbon polymer (GDC) is illustrated in Figure 3.1. All GDC samples were prepared in a single carbonisation process in bulk with no additional treatments. In a typical reaction, two monomers were dry-mixed and subjected to first annealing process at 300 °C for 3 h under N_2 to carry out bulk polymerisation followed by the high temperature (ranging from 700-1000 °C) carbonisation process. An initial polymerisation step, prior to the high temperature (>700 °C) carbonisation, was necessary to prevent the full decomposition of monomers (decomposition temperatures of glucose and DCDA are ~185 °C and ~255 °C) and to ensure polymerisation processes to take place. Polymerisation steps may include reactions such as amide/imine formations and substitution reactions between O and N groups in glucose and DCDA. The high temperature treatment then removes unreacted/unstable oxygen moieties to improve overall electronic conductivity with the increased carbonisation degree of the material[175, 176].

3.2.2 Structural analyses – 2D carbon polymer with surface defects

Obtained GDC samples (GDC_700, GDC_800, GDC_900, and GDC_1000) were all a few layers 2D sheet-like substrates similar to GO sheets (TEM images shown in Figure 3.2) – AGO sample exhibited many wrinkles and twisted/folded porous 3D structure. Carbonisation temperature changes did not impact the overall structure of GDC samples however, as seen in higher magnification images (Figure 3.3), an increase in surface roughness of GDC_800, GDC_900, and GDC_1000, compared to GDC_700, was shown. This flake-like surface of GDC samples may be due to irregular bonds formed between glucose and DCDA upon annealing in contrast to perfectly arranged honeycomb lattices in graphene. The image contrast of the polymers suggest that the polymer thickness was reduced at temperatures greater than 700 °C with higher degree of exfoliation. Detailed changes in surface morphologies of GDC samples are shown in SEM images in Figure 3.4. A fairly smooth surface was observed for GDC_700 whereas all other samples exhibited surface defects. Occurrence and the size of defects increased with the increase in annealing temperature – in agreement with the high-magnification surface TEM images in Figure 3.3.

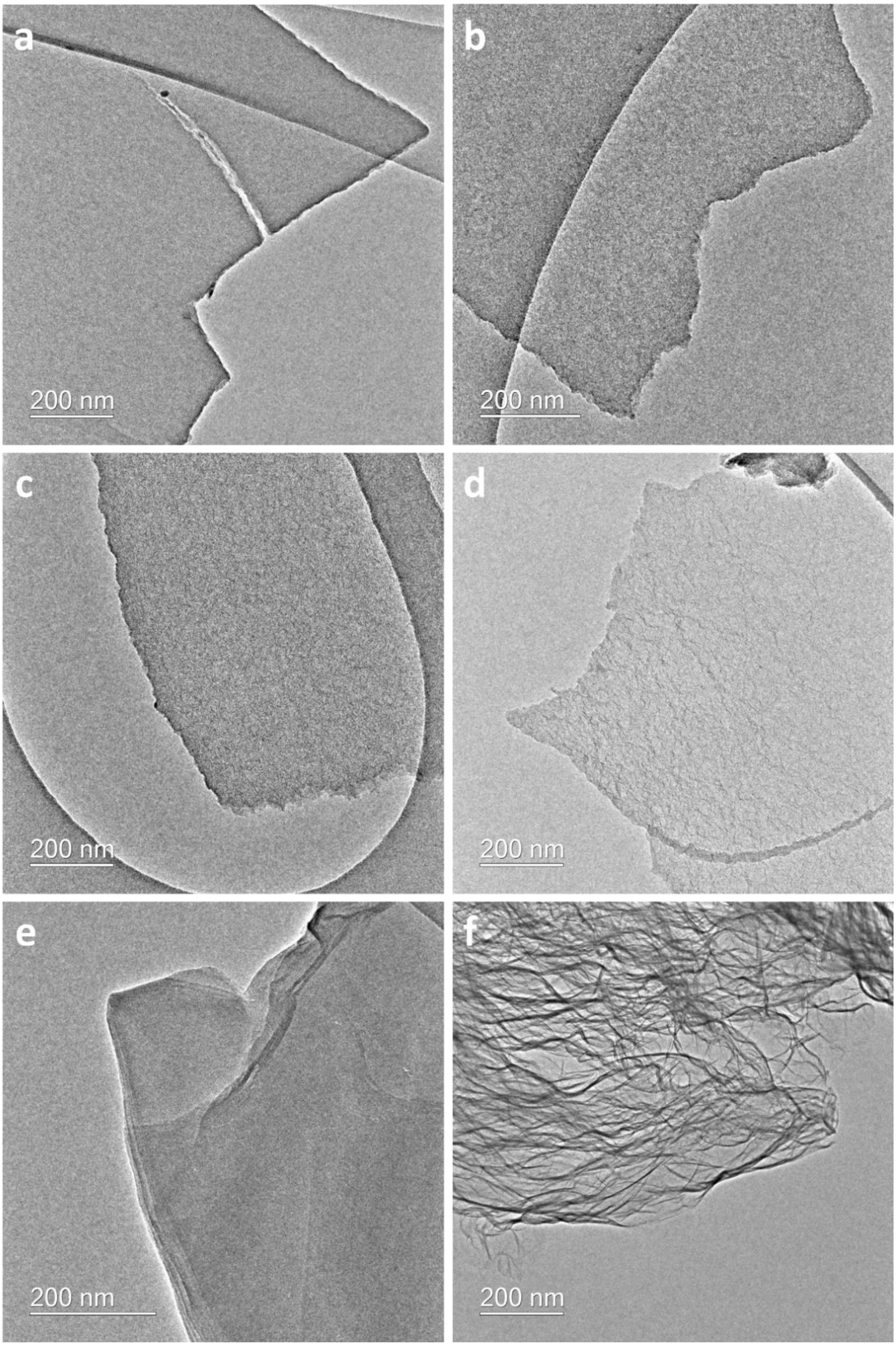

Figure 3.2 TEM images of (a) GDC_700, (b) GDC_800, (c) GDC_900, (d) GDC_1000, (e) GO, and (f) AGO_900.

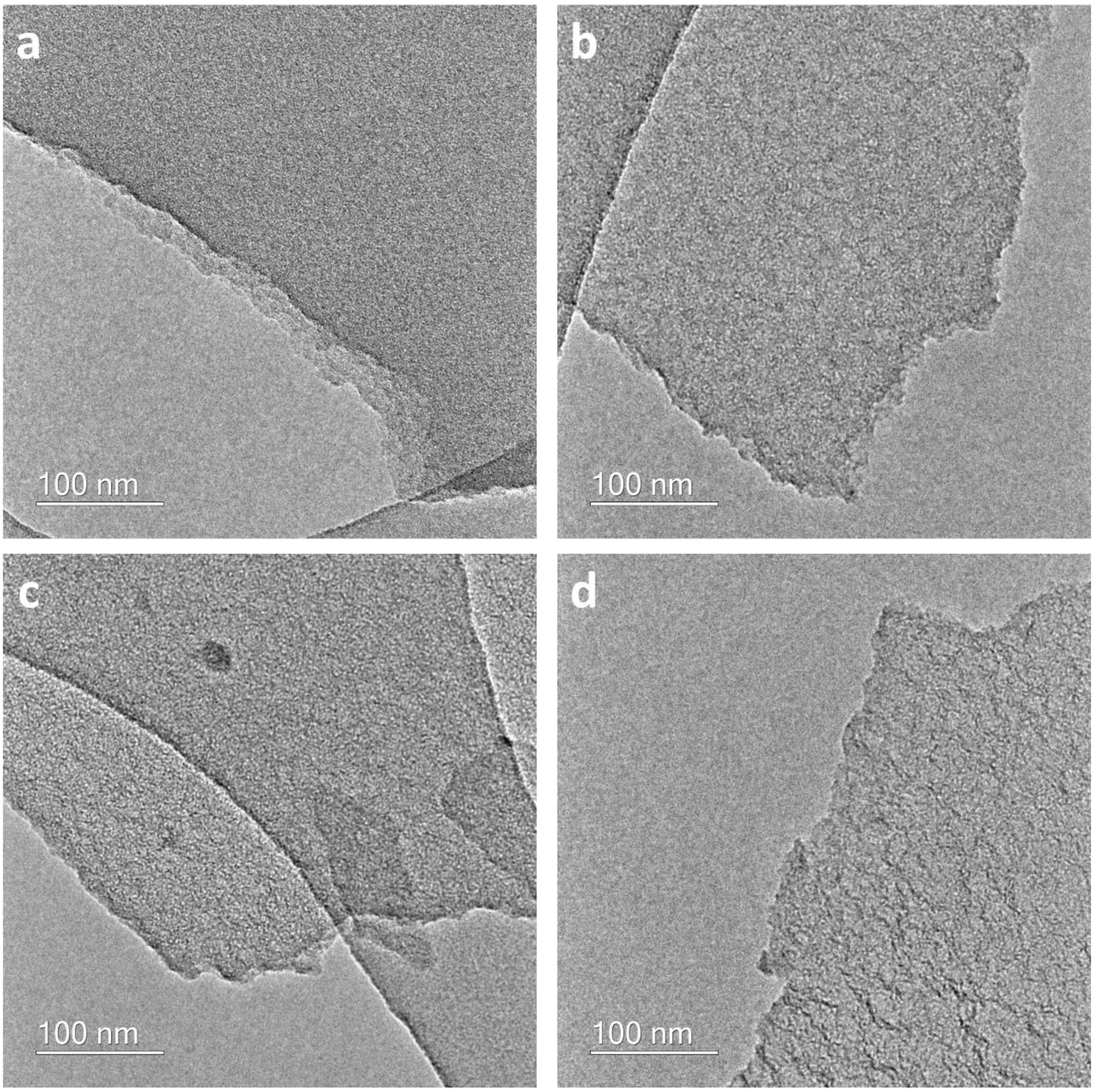

Figure 3.3 High magnification TEM images of (a) GDC_700, (b) GDC_800, (c) GDC_900, and (d) GDC_1000 showing surface roughness.

Surface area and pore sizes/volume is crucial to ORR and OER with oxygen gas diffusion in/out of the materials. BET N_2 adsorption-desorption isotherms provide essential insights to predict both surface and pore structures[177, 178]. The N_2 adsorption-desorption isotherms of all GDC samples were collected under 77 K (shown in Figure 3.5). All isotherms exhibited the shape of Type I BET isotherm with micropores[179, 180] – commonly seen in activated carbons. General increase in both specific surface area and pore volume was observed as the carbonisation temperature increased; the results congruent with TEM and SEM images (Figures 3.2-3.4). 2D-sheet structures of polymers resulted in low surface area and pore volume compared to 3D porous frameworks. Nonetheless, GDC samples displayed increased area and volume than compared to GO. All values from BET results are tabulated in Table 3.1.

All GDC samples exhibited broad (amorphous nature coming from the bulk polymerisation) but distinct graphitic (002)-like peaks in XRD measurements at around 25° (Figure 3.6). Peaks at lower angle, compared to graphite, indicated the increase in interlayer spacing (0.36 nm compared to 0.34 nm of graphite at around 26.5°) due to the formation of fragments and defects at high annealing temperatures. Presence of O and N functional groups (from monomers used) may also contribute to amorphism[181-183]. Higher diffraction peaks, (100), (101) and (004) at 42°, 45° and 55°, were either very weak in signal or not observable for GDC samples.

Raman spectra of graphitic carbon materials exhibit intense peaks at around 1350 and 1600 region, corresponding to the D and G bands[184, 185]. D band is the vibrations measured by the presence of defects and/or disorder in carbonaceous systems and G band is the in-plane vibrations of sp^2 hybridised carbons; the relative D to G ratio (I_D/I_G) provides a rough estimate of the disorder of carbon materials[186, 187].

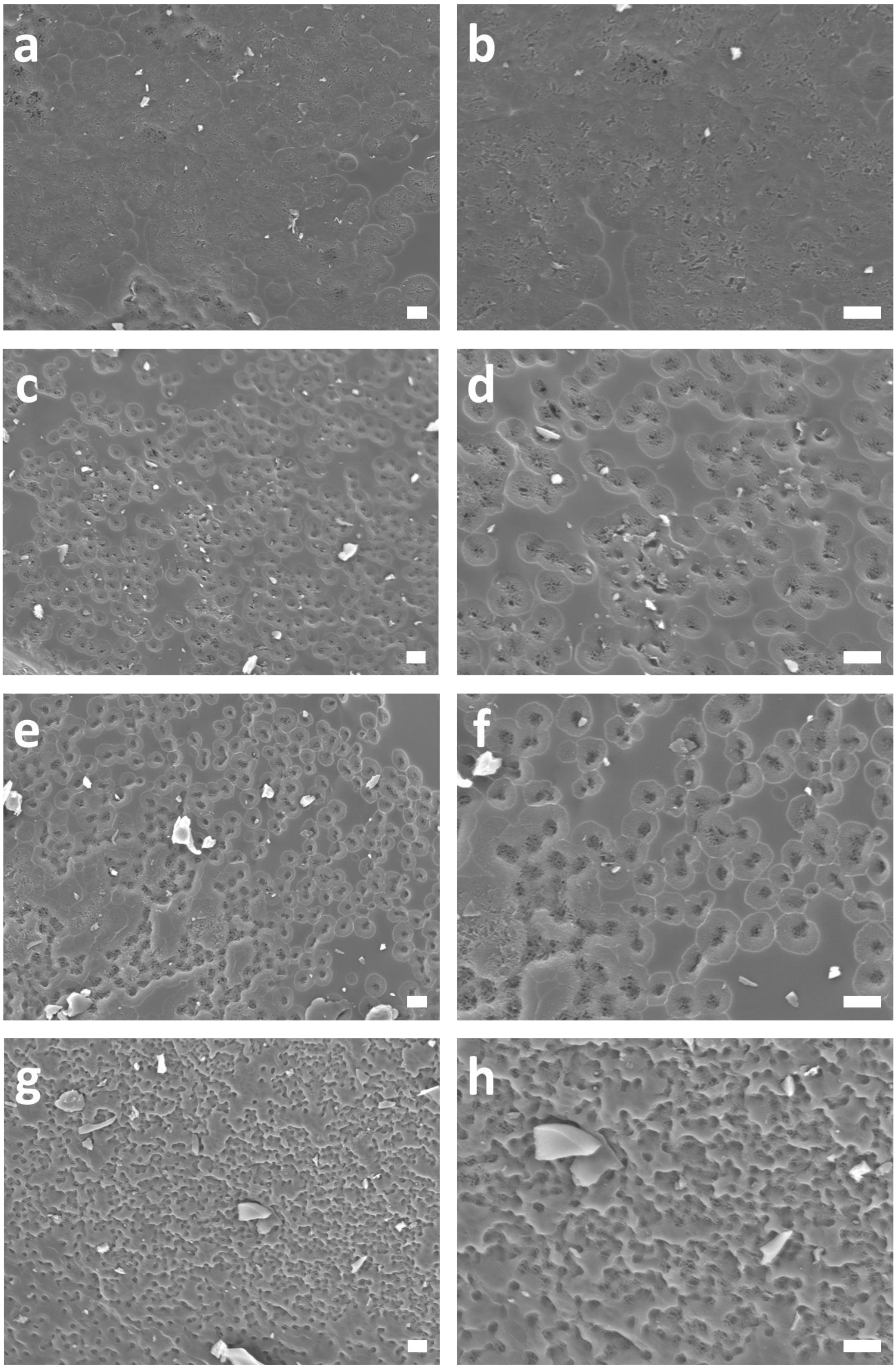

Figure 3.4 Low and high-magnification SEM images of (a),(b) GDC_700, (c),(d) GDC_800, (e),(f) GDC_900, and (g),(h) GDC_1000 showing surface roughness. Scale bar of 1 μm.

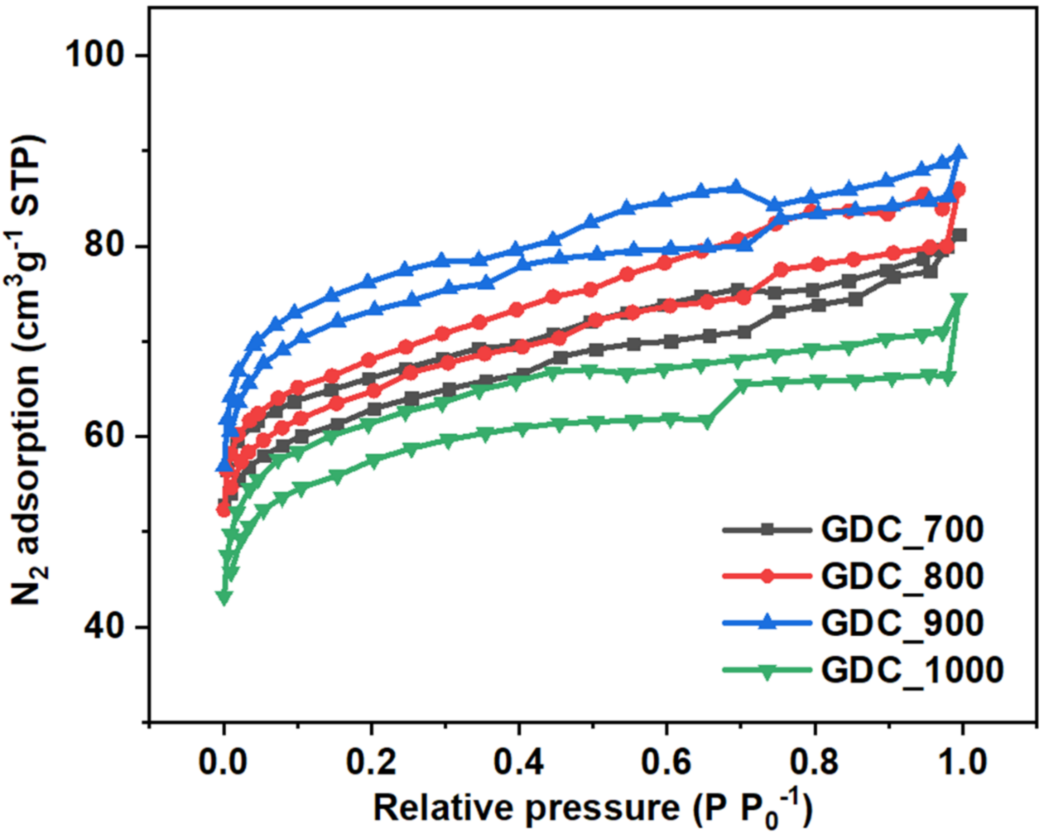

Figure 3.5 N_2 adsorption-desorption isotherms of GDC_700, GDC_800, GDC_900, and GDC_1000.

Table 3.1 The specific surface area and pore volume of GDC samples and GO.

	Specific surface area (m^2 g^{-1})	**Pore volume (cm^3 g^{-1})**
GDC_700	197.05	0.13
GDC_800	206.09	0.13
GDC_900	227.21	0.14
GDC_1000	181.65	0.12
GO	0.06	0.0001

Broad peaks, regions around 2500-3200 cm^{-1}, can be assigned to the combination of 2D, 2D', and D+D' bands typically shown in graphene[184]. With the presence of dopants along with high temperature carbonisation process, the I_D/I_G ratios calculated from the Raman spectra were 0.89, 0.93, 0.92, and 0.92 for GDC_700, GDC_800, GDC_900, and GDC_1000, respectively (Figure 3.7). Close I_D/I_G values of 800-1000 °C samples suggested that there were no major changes to the overall defect chemistry. Typical I_D/I_G ratios of GO and graphite are 0.85 and 0.05. Increased disorder/defects, shown by the high I_D/I_G values of GDC_800, GDC_900, and GDC_1000, describe the increase in surface roughness (shown in TEM images in Figure 3.3 and in SEM images in Figure 3.4).

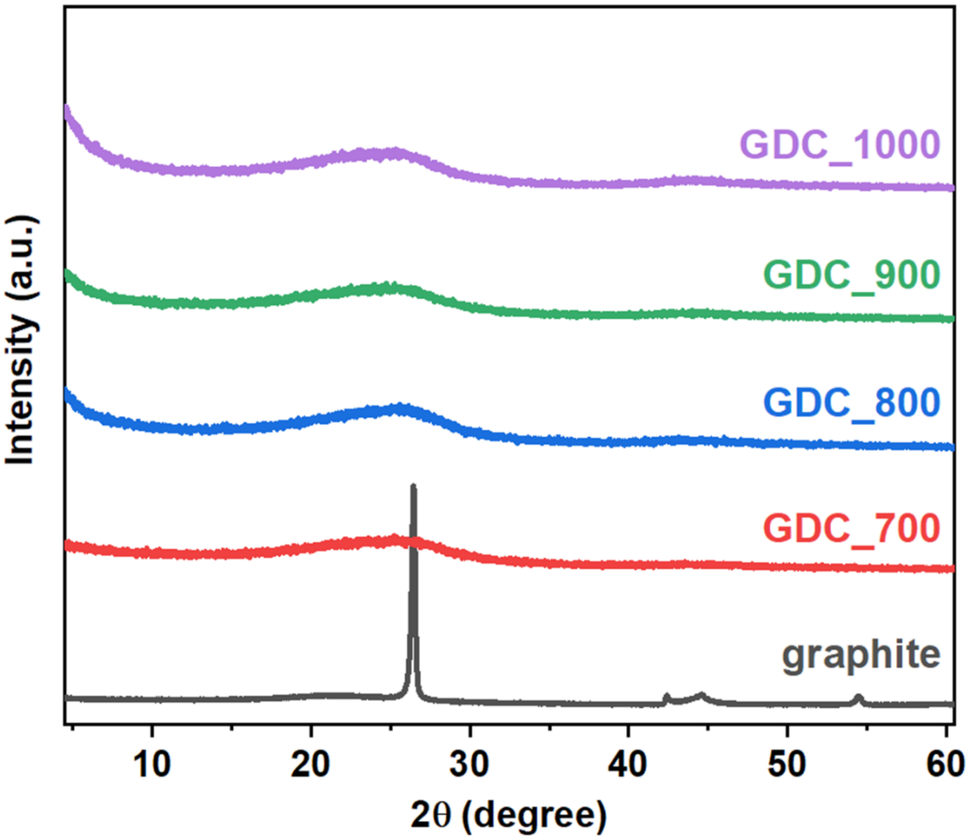

Figure 3.6 XRD patterns of graphite, GDC_700, GDC_800, GDC_900, and GDC_1000.

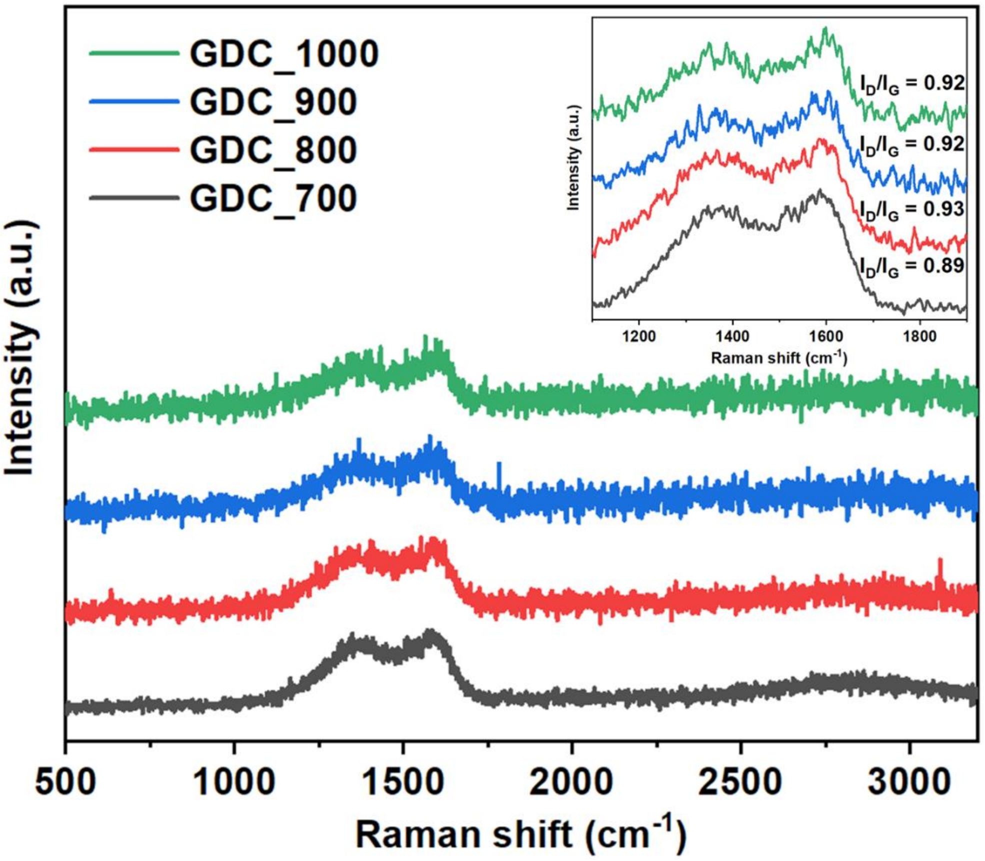

Figure 3.7 Raman spectra of GDC_700, GDC_800, GDC_900, and GDC_1000; the inset is the close-up of D and G band region with relative I_D/I_G ratio.

3.2.3 Chemical analyses – carbonisation and N-doping

Chemical properties of all GDC samples were investigated using XPS technique. The overlay of survey spectra (Figure 3.8) displayed typical N-doped carbon polymer signals with intense C 1s peak. The concentration of N 1s peak decreases with the increase in temperature – this is due to the loss of -NH_2 groups at higher temperature[188]. Aromatic N groups are more stable than the sp^3 hybridised functional groups[189]. No other elements were found during the measurement in all measured 3-regions. Although not absolute values with XPS sensitivity of 0.1 at. %, however, is expected to have little influence on chemical and electrochemical properties of samples.

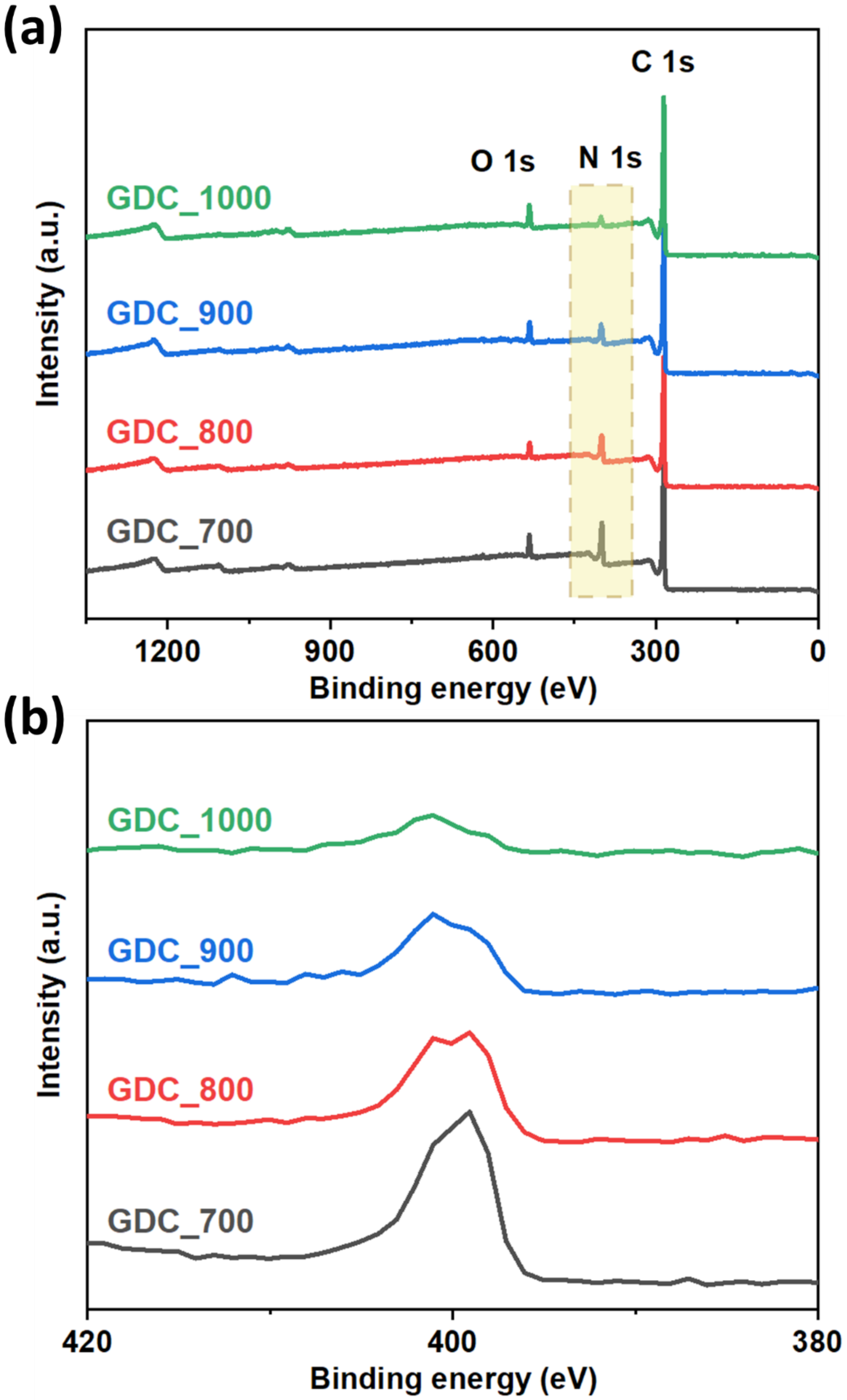

Figure 3.8 (a) XPS survey spectra of GDC_700, GDC_800, GDC_900, and GDC_1000. (b) XPS survey spectra of all GDC samples between 380-420 eV; close-up view of N 1s region.

Table 3.2 XPS elemental composition of GDC samples, GO, and AGO. Survey spectra of each sample were recorded at multiple locations to obtain the average.

	C (at. %)	**N (at. %)**	**O (at. %)**	**Avg. C (at. %)**	**Avg. N (at. %)**	**Avg. O (at. %)**
GDC_700	76.6	17.2	6.2	77.0	17.5	5.5
	77.1	17.8	5.1			
	77.4	17.6	5.0			
GDC_800	82.6	13.2	4.2	82.3	13.6	4.1
	82.1	13.6	4.3			
	82.3	14.0	3.7			
GDC_900	86.4	8.3	5.3	86.8	8.3	4.9
	87.0	8.3	4.7			
	87.1	8.4	4.5			
GDC_1000	90.0	3.7	6.3	90.3	3.9	5.8
	90.0	4.0	6.0			
	90.7	4.1	5.2			
GO	67.4	—	32.6	67.6	—	32.4
	67.6		32.4			
	67.9		32.1			
AGO_900	96.3	—	3.7	97.0	—	3.0
	97.5		2.5			
	97.2		2.8			

A summary of all elemental composition of all GDC samples is presented in Table 3.2. As mentioned earlier, less stable N functional groups were removed resulting drop in N concentration from 17.5% to 3.9% with the increase in annealing temperature - this also resulted in increase in carbonisation degree. High temperature-assisted carbonisation of GDC samples led to significantly lower concentration of oxygen, averaging around 5% compared to 32.4% in GO. High oxidation degree of carbon substrates provides many reaction centres to dope different elements to the material[190, 191] however this is not necessary in GDC samples as catalytically active N sites are already present and the low concentration of O improves the overall electronic conductivity as electrocatalysts[192]. However, values of O of all GDC samples were not as small as 3.0% of AGO_900 with effective eliminations of oxygen functional groups achieved by highly exfoliated graphene layers.

To scrutinise the chemical environment, high resolution XPS elemental spectra of C 1s and N 1s were analysed (Figure 3.9) – all chemical bonds and associated binding energies are tabulated in Table 3.2 and 3.3. In C 1s spectra, C=C, C-O/C-N, C=O/C=N, and π- π* satellite interactions were exhibited at binding energies of around 284.8, 286.1, 288.1, and 290.2 eV, respectively[193]. Binding energies of single- and double-bond O overlap with the energies of single- and double-bond of N; hence the combined fittings. In N 1s spectra, 3 major types of N environments (pyridinic, pyrrolic, and graphitic N) and oxidised N were present at binding energies of around 398.4, 399.6, 400.9, and 403.2 eV[194].

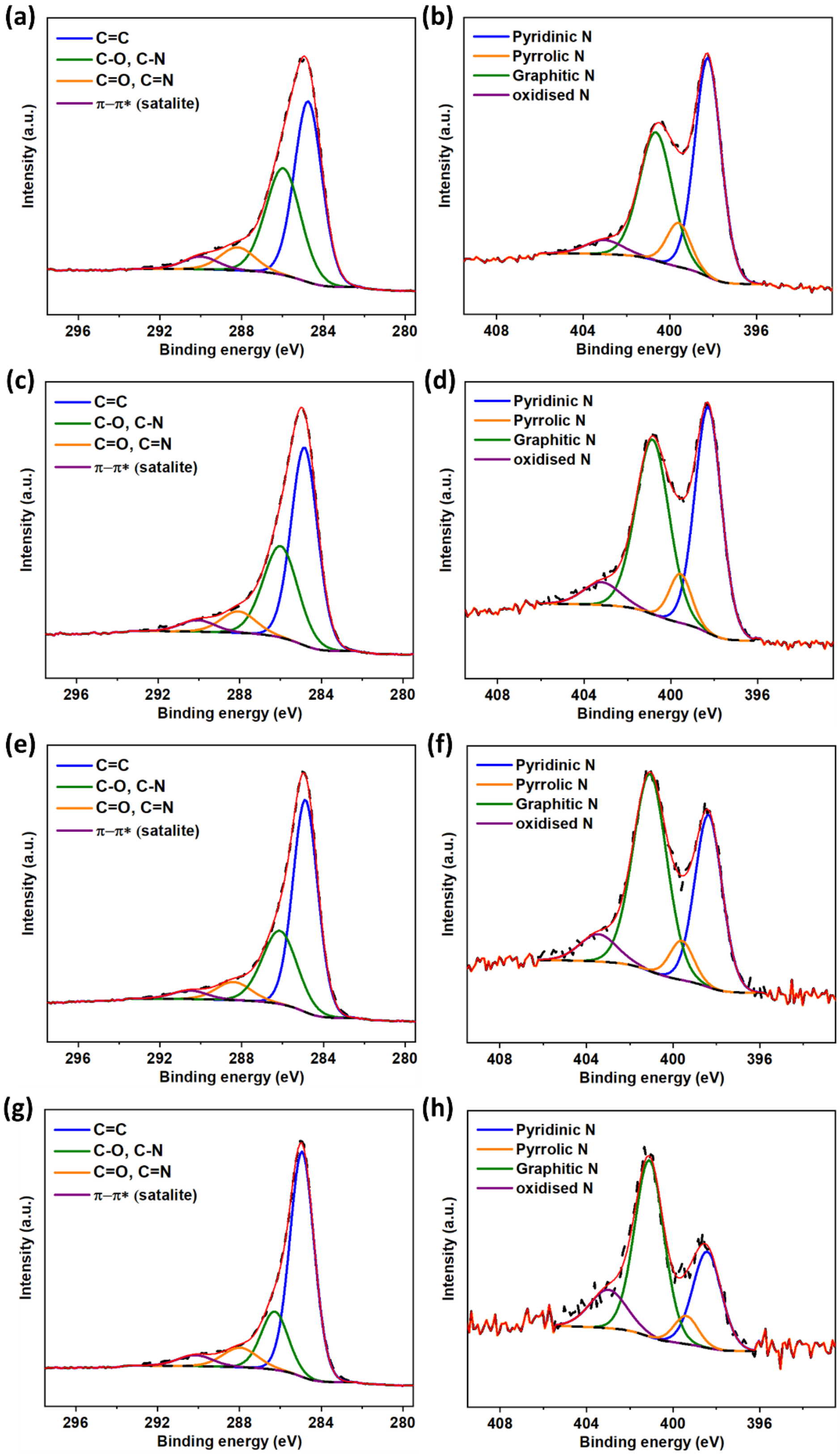

Figure 3.9 High-resolution C 1s and N 1s XPS spectra of (a),(b) GDC_700, (c),(d) GDC_800, (e),(f) GDC_900, and (g),(h) GDC_1000.

Table 3.3 Quantification of XPS deconvoluted C 1s peaks and associated chemical environments.

% of deconvoluted C 1s peak fittings and binding energies				
	C=C	**C-O/C-N**	**C=O/C=N**	**π- π* satellite**
GDC_700	51.2% (284.8 eV)	36.5% (286.0 eV)	8.0% (288.2 eV)	4.3% (290.0 eV)
GDC_800	55.1% (284.8 eV)	32.8% (286.0 eV)	7.9% (288.1 eV)	4.2% (290.1 eV)
GDC_900	60.4% (284.9 eV)	29.0% (286.1 eV)	7.2% (288.4 eV)	3.4% (290.5 eV)
GDC_1000	67.8% (284.9 eV)	19.0% (286.2 eV)	8.4% (288.0 eV)	4.8% (290.2 eV)

Table 3.4 Quantification of XPS deconvoluted N 1s peaks and associated chemical environments.

	% of deconvoluted N 1s peak fittings and binding energies			
	Pyridinic N	**Pyrrolic N**	**Graphitic N**	**Oxidised N**
GDC_700	49.8% (398.2 eV)	9.1% (399.6 eV)	36.5% (400.6 eV)	4.6% (403.0 eV)
GDC_800	43.7% (398.3 eV)	7.9% (399.6 eV)	42.3% (400.8 eV)	6.1% (403.2 eV)
GDC_900	35.4% (398.4 eV)	7.1% (399.6 eV)	50.0% (401.0 eV)	7.5% (403.4 eV)
GDC_1000	27.6% (398.4 eV)	6.7% (399.4 eV)	51.6% (401.1 eV)	14.1% (403.0 eV)

As the carbonisation temperature increased, the C-O/C-N bond contribution (to total C 1s signal intensity) decreased and C=C (a mix energy of sp^3 and sp^2 of aromatic carbon) increased. Although the decrease is observed for the combined C-O and C-N contribution, which occur at the same energy in the C 1s spectrum, the loss is mainly from the removal of pyridinic or sp^3 N, as observed in the decreasing amount observed in the N 1s spectra. This is also confirmed in the O 1s overlay in Figure 3.10 where shape and intensities of all O 1s spectra of all GDC samples remained almost identical. Generally, the oxygen concentration should decrease with respect to increase in annealing temperature due to cleavage of less-stable oxygen functional groups. Here, GDC samples did not follow this trend - it is possible that there was a small oxygen leak during annealing. Also, there might be some oxygen moieties trapped in bulk of GDC samples.

As explained earlier, doping nitrogen to graphitic carbon framework significantly enhances the ability for a metal-free carbon substrate to catalytically reduce oxygen[167]. Especially, it is imperative to maximise the percentage of graphitic N in any graphitic carbon substrates as it provides the most oxygen reactive sites during ORR[149]. At higher temperatures, increased conversion of graphitic N was revealed, reaching up to 51.6% of the total N amount (expected to show improved electrocatalytic performances)[195, 196]. Concentration of pyrrolic N, a nitrogen in a 5-membered aromatic carbon ring structure, was limited to less than 10% and the percentage contribution was very close for each sample. The oxidised N group may have come from polymeric bond between N and O of DCDA and glucose. Since intensities of O energies remain unchanged with ascending temperature, the observed increase in the amount of oxidised N does not necessarily equate to larger population of N-O bond; rather, difference in ratios of the bonds as some pyridinic N centres are removed.

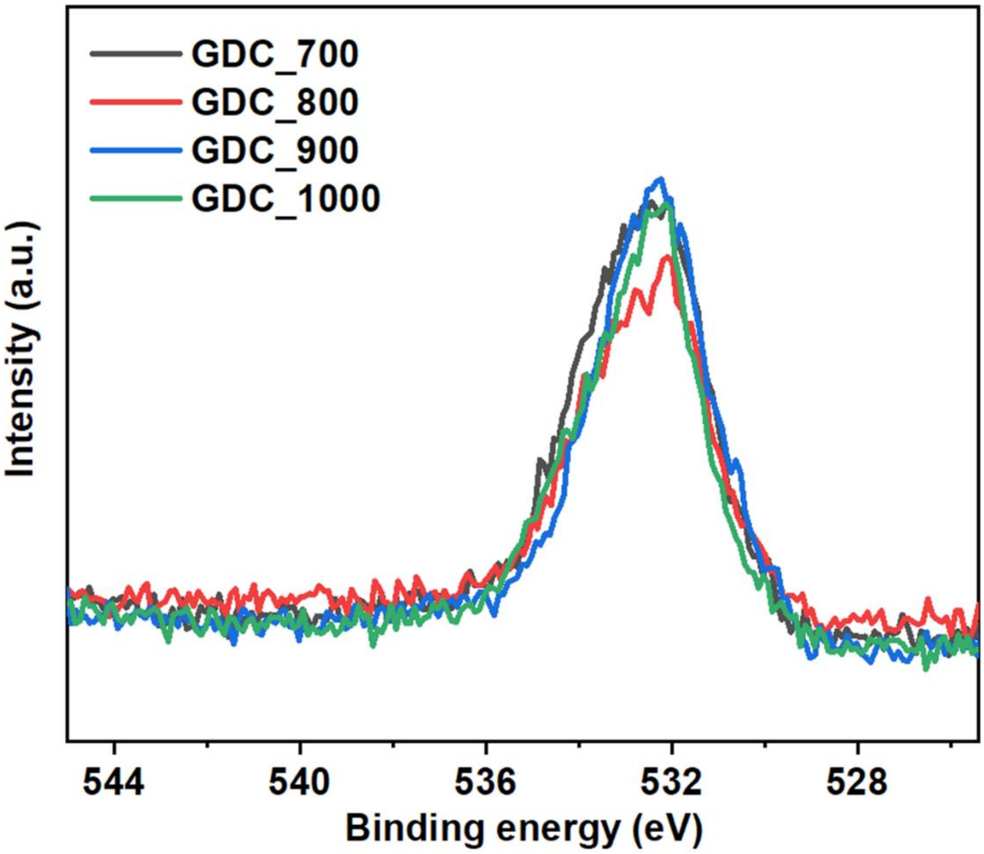

Figure 3.10 Overlay of XPS O 1s spectra of GDC_700, GDC_800, GDC_900, and GDC_1000.

In Figure 3.11, similar to GDC samples, high resolution C 1s scan of AGO_900 exhibited intense carbon-carbon peaks arising from the high aromaticity of graphene. GO displayed completely different peak shape with larger contribution of C-O and C=O from the harsh oxidation step[197, 198]. The oxidation of GO occurs primarily on the surface which can be thermally reduced/eliminated easily upon high temperature annealing to increase electron conductivity and a tuneable bandgap[199]. Since there are no N species present in AGO_900 sample, C-O and C=O peak intensities (usually where C-N and C=N energies overlap) are reduced compared to GDC samples[200].

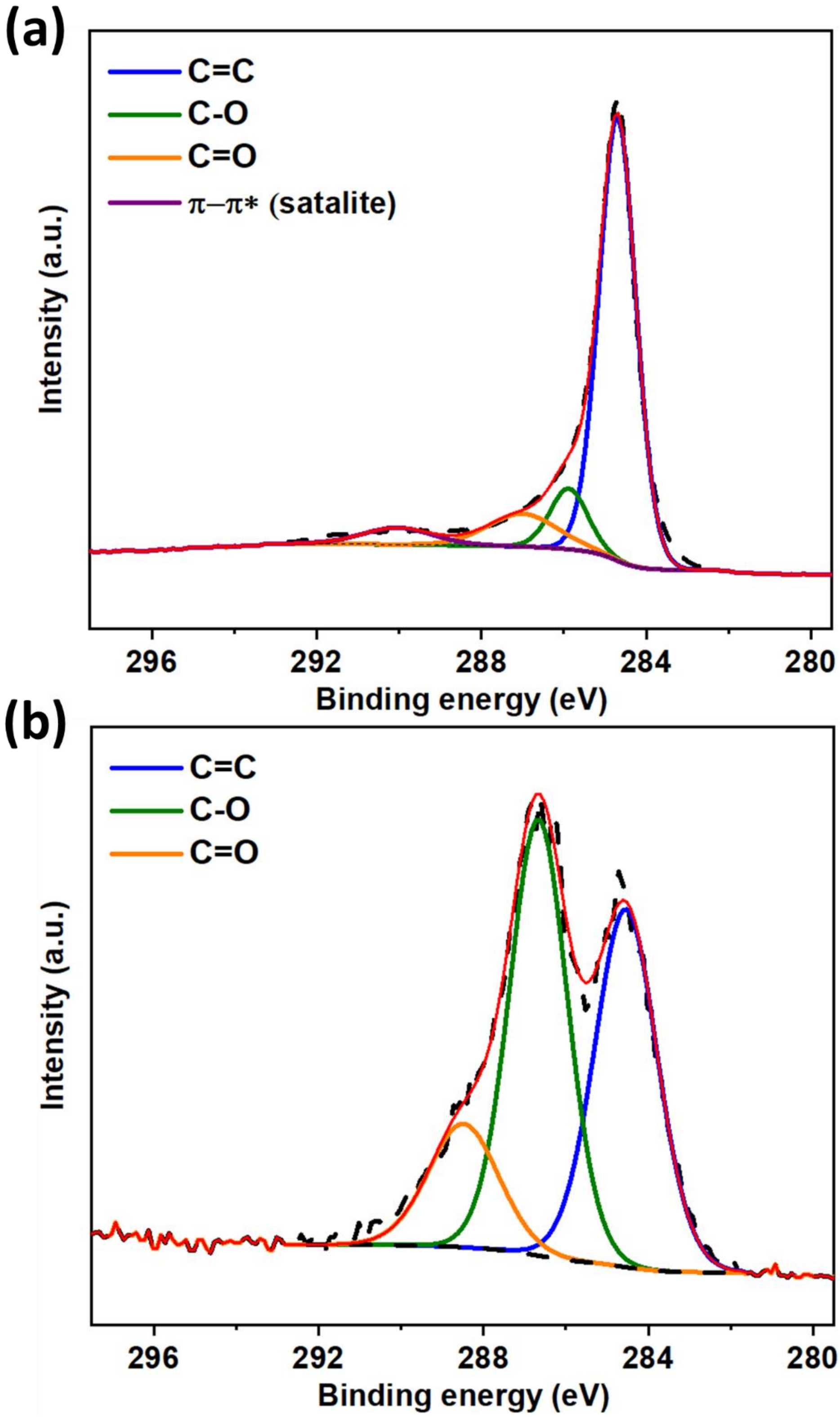

Figure 3.11 High resolution C 1s XPS spectra of (a) AGO_900, and (b) GO.

3.2.4 Electrocatalytic performances of GDC polymers

All samples were directly tested as synthesised to study materials' behaviour under oxygen reactions conditions as possible cathode materials for metal-air batteries. In any electrochemical setups, all electrodes are not in the ideal conditions and a difference in the potential (*iR*) drop can be seen[201]. Electrocatalytic performances of a material can increase up to 20% in value with *iR*-compensation depending on the measured electrode resistance of a cell[202]. However, this contribution is not applied to any of the tests and the results shown are as measured (not *iR*-corrected).

Initially, CV scans were measured in O_2-saturated 0.1 M KOH electrolyte (Figure 3.12). General shapes and depths of the current responses were observed throughout samples. Oxygen reduction peaks were evident at around 0.58 V versus the reversible hydrogen electrode (RHE) suggesting a successful oxygen redox reaction. Compared to other samples, the oxygen redox response of GDC_700 in CV was recorded at a lower potential at around 0.55 V implying lower oxygen electrocatalytic activities. To further investigate the oxygen reduction mechanisms, linear sweep voltammetry (LSV) tests were conducted in 0.1 M KOH with 10 mV s^{-1} at the rotating disk electrode (RDE) rotation speed of 1600 rpm with continuous bubbling of O_2 (Figure 3.13a). The electrocatalytic activity of GDC_700 was noticeably lower than the other 3 GDC samples with the current density reaching 1.88 mA cm^{-2} as expected from the CV measurement. The highest current response was achieved for GDC_900 with ~2.47 mA cm^{-2} followed by GDC_800, then GDC_1000 at 2.34 and 2.28 mA cm^{-2}. Using the K-L equation, the maximum theoretical current density at 1600 rpm (assuming a complete $4e^{-}$ transfer) should be 5.7 mA cm^{-2}, normally achieved by Pt/C[203, 204]. Reduced current responses of GDC samples suggest incomplete/insufficient oxygen conversion reactions taking place on the RDE surface.

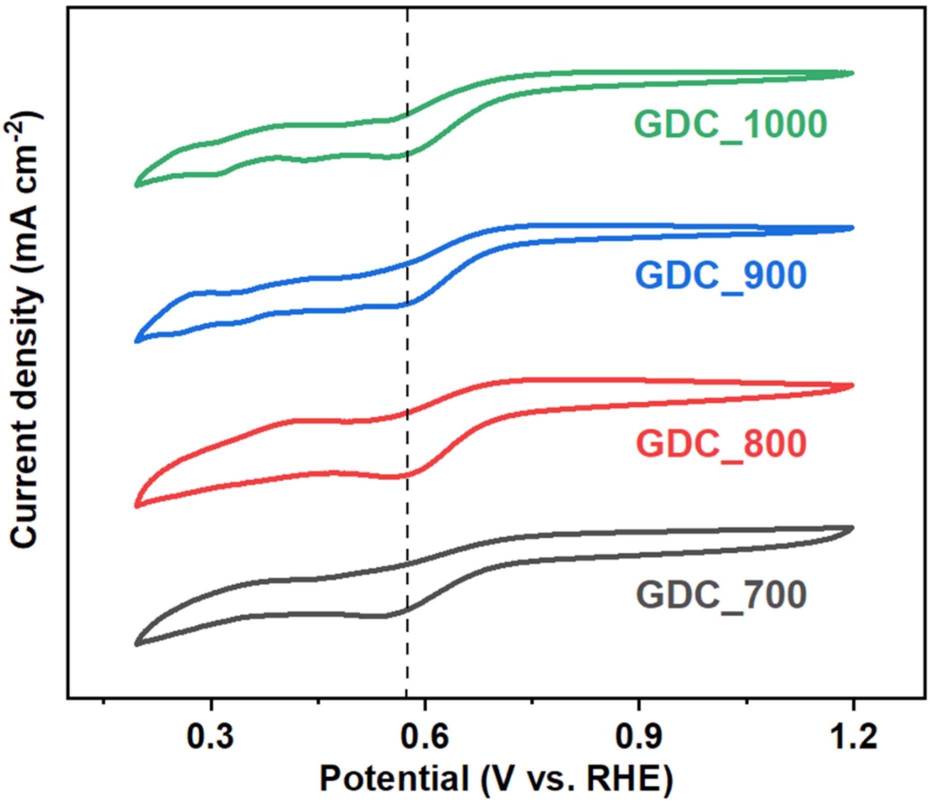

Figure 3.12 CV curves of GDC_700, GDC_800, GDC_900, and GDC_1000 measured in O_2-saturated 0.1 M KOH with the scan rate of 10 mV s^{-1}.

Since all samples were polymerised and carbonised at high temperatures, observed onset potentials (E_{onset}), the point at which oxygen conversion starts to occur, were all roughly at 0.75 V (equating to 480 mV overpotential from 1.23 V vs. RHE for water-splitting). Tafel slopes of the LSVs at 1600 rpm were obtained (Figure 3.13b). The Tafel slope provides kinetics of electrochemical/electrocatalytic reactions in response to change in applied potential and generally is obtained around the E_{onset} value – lower calculated slope value signifies smaller required overpotential[205]. GDC_900 exhibited the lowest Tafel value of 100.1 mV dec^{-1} whereas GDC_700 with the slowest electrocatalytic activities showed the highest value, 129.9 mV dec^{-1}, in accordance with the CV and LSV results.

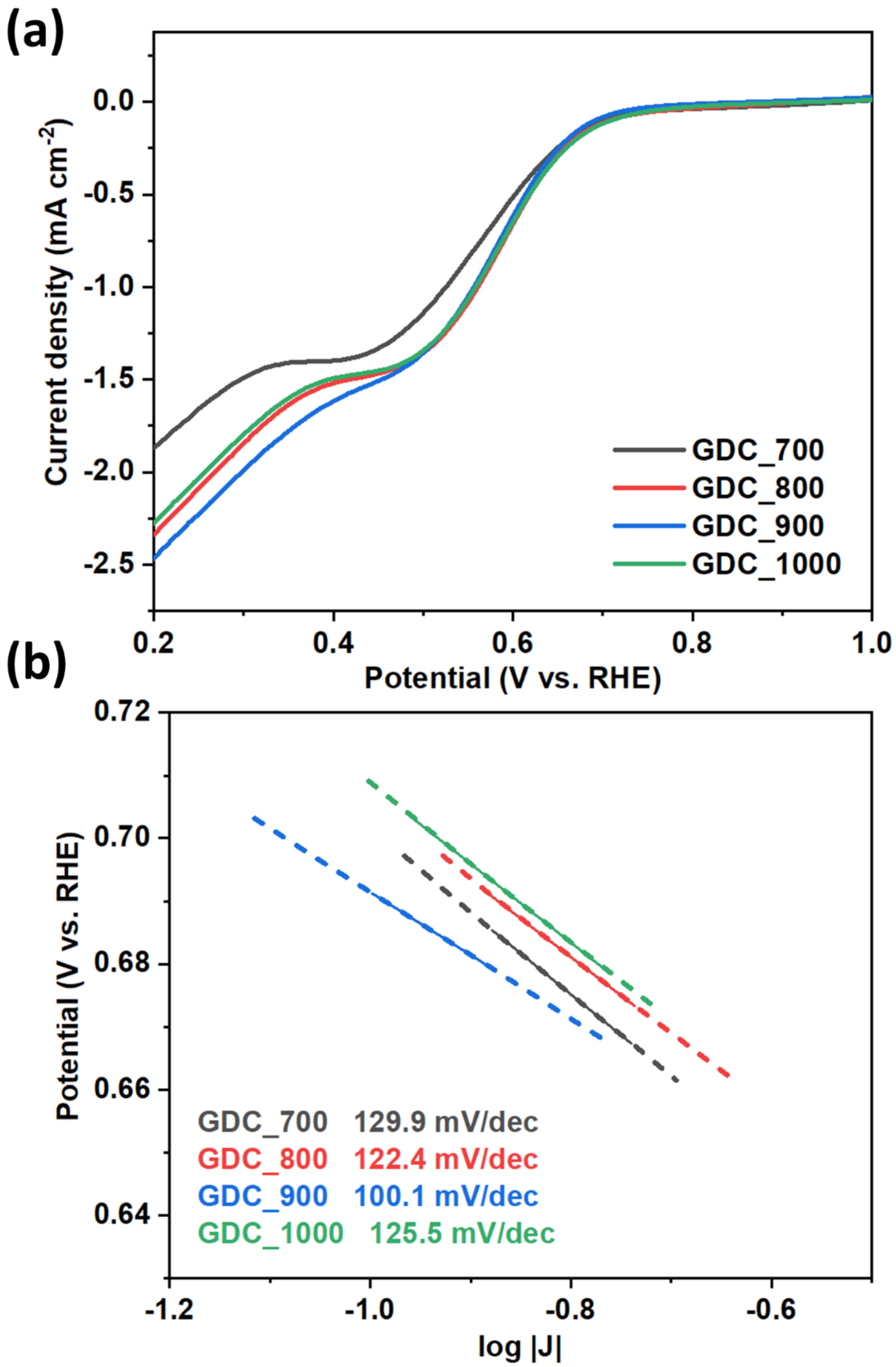

Figure 3.13 (a) Combined LSV curves for ORR of all GDC samples, and corresponding (b) ORR Tafel plots. O_2-saturated 0.1 M KOH electrolyte at 1600 rpm.

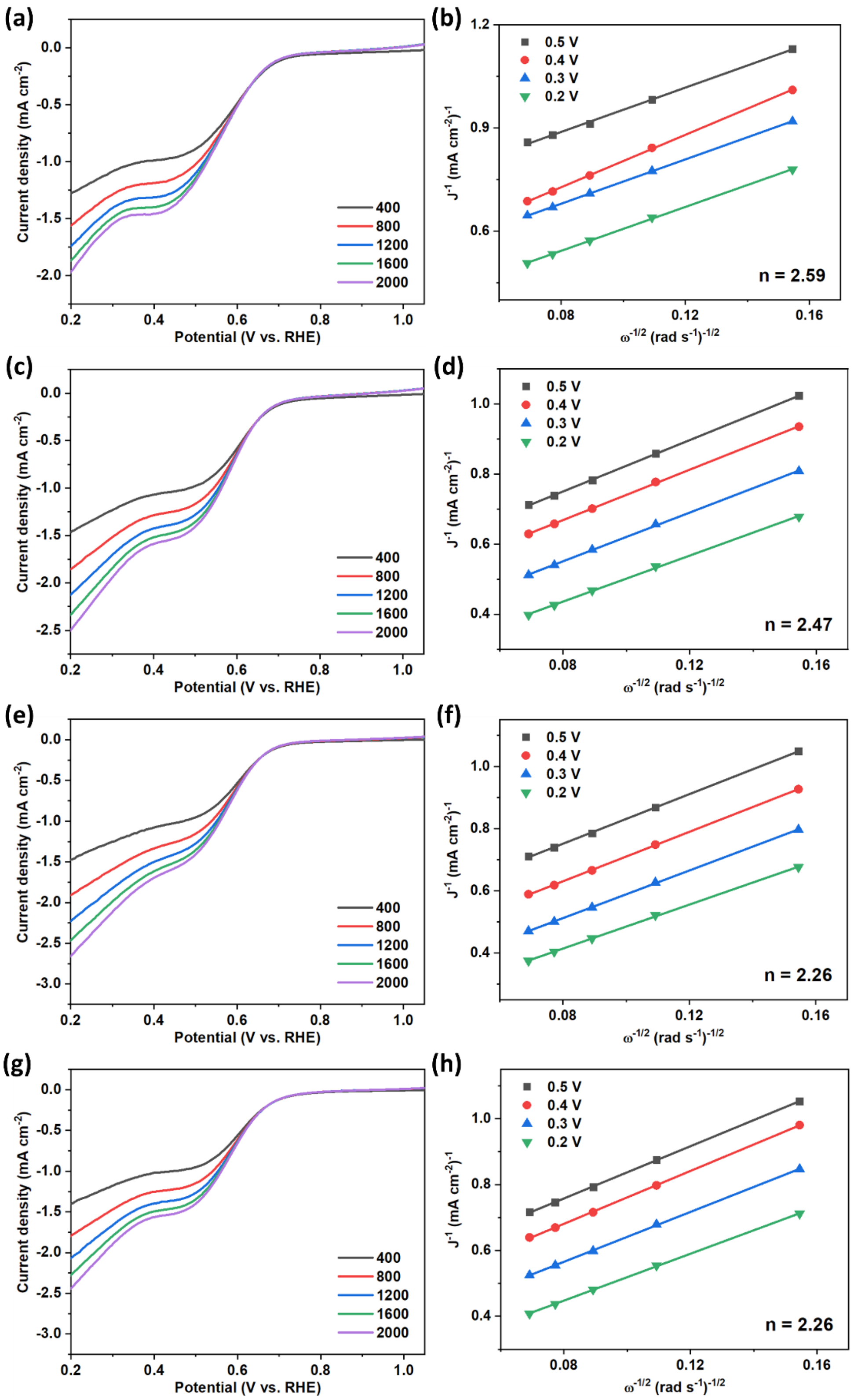

Figure 3.14 ORR LSV curves recorded at different rotation speeds (rpm) and the K-L plots of (a),(b) GDC_700, (c),(d) GDC_800, (e),(f) GDC_900, and (g),(h) GDC_1000.

The correlation of varied rotation speed to measured current and potential is calculated using Koutecky-Levich (K-L) equations[206]. LSV curves at different rotation speeds and corresponding K-L relations of all samples are shown in Figure 3.14. Calculating, using the equations provided in the experimental section, an estimated calculation of the number of electron transfer (*n*) in the associated oxygen electrocatalytic reaction can be obtained. Although the measured current densities of GDC_800, GDC_900, and GDC_1000, at any rotation speeds, were higher than GDC_700 sample, the electron transfer number of GDC_700 was the highest, with the value of 2.59 (closest to theoretical 4-electron transfer oxygen reactions). The difference between measured current densities at 0.2 V to 0.5 V for GDC_800, GDC_900, GDC_1000 is greater than that of GDC_700 with increased gradient. As the K-L relation is calculated from the inverse of the measured current density at a given potential, a steep drop in measured current in LSV lead to lower value of *n*, as shown in GDC_800, GDC_900, and GDC_1000. However, larger current densities observed in this region suggest better oxygen diffusion mechanisms[207, 208] with carbonisation temperature above 800 °C. Also, the first observed steep gradient of LSV curves of GDC_800, GDC_900, and GDC_1000, at the region between 0.41-0.72 V, imply faster oxygen reduction kinetics than GDC_700. It can be assumed that the improved oxygen permeability is achieved with the increase in surface area and pore volume resulting in more efficient oxygen conversion at the same measured cell potential.

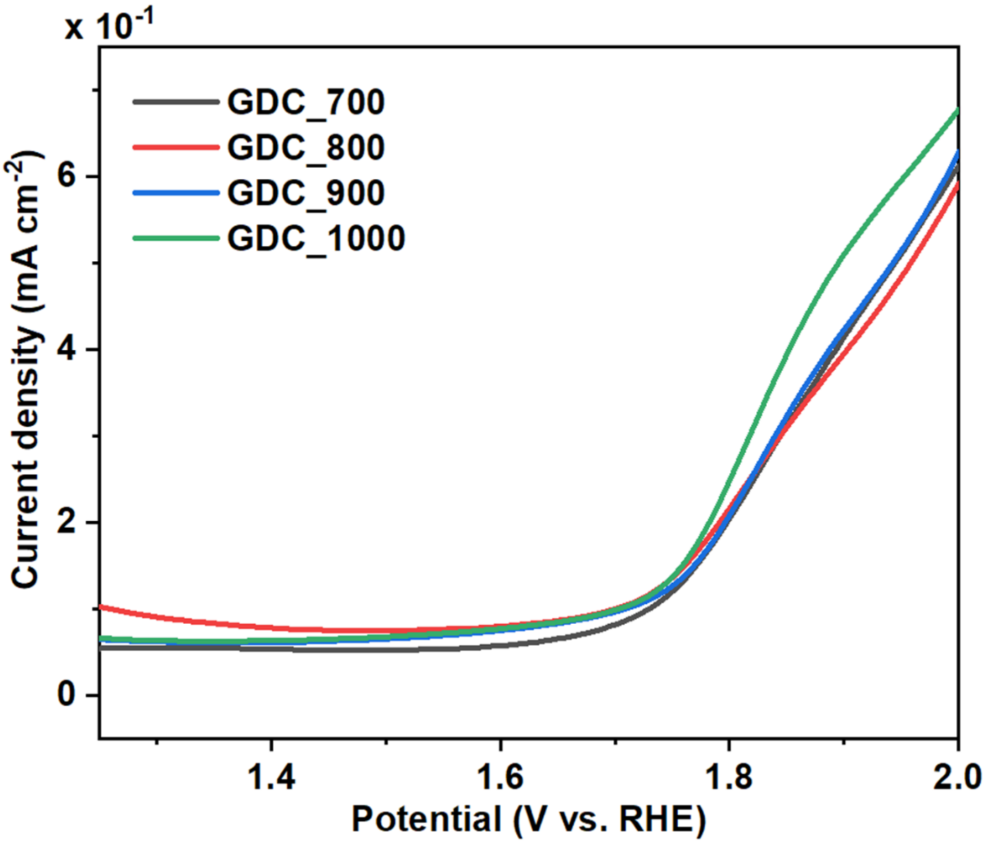

Figure 3.15 LSV curves in the OER region for all samples in 0.1 M KOH with rotation speed of 1600 rpm.

OER LSV curves of all samples were measured between 1.2 to 2.0 V vs. RHE in 0.1 M KOH with 10 mV s^{-1} at 1600 rpm (shown in Figure 3.15). GDC_1000 displayed the largest current density of 0.68 mA cm^{-2} however the OER capabilities of GDC polymers were significantly lower compared to conventional OER materials such as RuO_2[90] exhibiting E_{onset} at 1.4 V vs. RHE with current density greater than 10 mA cm^{-2}. Other reported N-doped graphene/carbon materials[209, 210] reached the same current density of 10 mA cm^{-2} with less than 420 mV required overpotential.

In N-doped carbon, it is reported that the most OER active sites are pyridinic N sites with the electron-withdrawing ability[119, 211]. As revealed in the XPS analyses, the high temperature carbonisation has decreased the concentration of the pyridinic N the most in all GDC samples, leading to reduced OER performances with low measured current density. Also, the high OER potential may often lead to oxidation of N-doped carbon/graphene materials which can reduce the long-term stability[212].

3.3 Conclusion

In summary, a simple carbonisation of glucose and DCDA, widely available organic monomers, can result in the formation of 2D N-doped carbon polymers, as active oxygen electrocatalysts for metal-air batteries and fuel cells applications. Combined structural and chemical characteristic features typical of both GO and AGO were observed in GDC polymers using techniques such as TEM and XPS. Increased carbonisation temperature resulted in increase in surface roughness of GDC polymers, to provide more oxygen accessible surface area and pores. Furthermore, the carbonisation degree and the ratio of the concentration of graphitic N, the most ORR active site in N-doped carbon substrates, grew with the annealing temperature. Out of all GDC samples, GDC_900 exhibited the highest current density of 2.47 mA cm^{-2} in the ORR region, which could be a result of the balance between surface disorder and the carbonisation/graphitic N concentration. GDC samples still lack in conversion efficiency and kinetics, compared against the Pt/C benchmark for ORR with around 5.7 mA cm^{-2} measured current density and less than 250 mV overpotential. Also, GDC polymers demonstrated insufficient OER performances (current densities less than 1 mA cm^{-2}, where most OER electrocatalysts reach more than

100 mA cm^{-2} at 2 V vs. RHE and 10 mA cm^{-2} at the overpotential of only around 350-400 mV) to be utilised as a bi-functional oxygen electrocatalyst which might be due to eliminations of electron-withdrawing groups at high carbonisation temperatures and the instability of materials at the high measured potential. If more active centres are introduced to the annealed carbon polymers via heteroatoms co-doping as well as the stable structure to maintain the functional groups, both ORR and OER capabilities could enhance. With the right selection of reagents, temperature-programmed annealing process can be very useful to easily prepare 2D electrocatalysts.

Chapter 4 : Utilising functionalised carbon dots as non-metal bi-functional electrocatalyst

4.1 Introduction

Electrification of transport and the development of smart electricity grids have led to significant advancement in electrochemical energy storage systems, both in volume and in capacity, to reduce the environmental impact associated with the combustion of fossil fuels. Electrocatalysts are key components in clean energy conversion/storage devices including fuel cells, electrolysers, and metal-air batteries[213]. Depending on the choice of metal, theoretical specific energy of a Zn-air battery can reach at least five times more than of LIB technology, to be the next-generation high-energy source[53].

Recently, many studies have focused on utilising metal-free carbon-based materials, with N, S, P, and B heteroatom doping, to replace existing transition metal species, and even noble metals, in low-cost systems showing good cyclability[149, 214]. In particular, carbon dots (CDs), a few nanometre scale 0-dimensional derivatives of carbon, have emerged as potential transition/noble metal substitute for many applications[215, 216]. CDs consist of a mixture of sp^2 graphite-like and amorphous carbon in quasi-spherical morphology[217] and are synthesised either via top-down or bottom-up approaches with varied sizes (width up to 20 nm and height ranging from few to multiple layers[218]). Size and edge effects are vital in catalysis as the reaction generally happens near newly introduced functional groups, which result in the formation of electron-rich and/or structural defect sites around the edge planes[219, 220]. CDs can provide more catalytically active sites by both surrounding edges and multiple layers, along with many functional groups[221, 222]. However, despite the attempts of utilising CDs in electrocatalysis, the performance of CD-containing ORR electrocatalysts has not reached the level of noble-metal catalysts and there are no reports exploiting OER with CDs[223-227]. It is unclear whether this unsatisfactory performance is due to the undefined CD syntheses, binding of CDs to the substrate, substrate pore blockage, or the functional groups around CDs.

In this chapter, heteroatom-doped CDs embedded on graphene substrates, which were synthesised from a simple hydrothermal approach followed by heat treatment, were used to clarify the compatibility of CDs and the substrate, and to examine the effect of different functional groups in CDs. Different combinations of heteroatom (N and N-S) doped CDs were prepared by a hydrothermal process using carefully selected reagents in order to exclude any undesirable elements from the reaction. Obtained catalysts all showed considerable improvement in performance, as metal-free catalysts, simply by the addition of CDs to the reaction mixture. After thermal treatment optimisation, electrocatalytic activities in both ORR and OER regions were comparable to conventional Pt/C and Ir/C with extremely high current densities for a given catalyst loading.

4.2 Results and discussion

4.2.1 Embedding of CDs on porous graphene framework

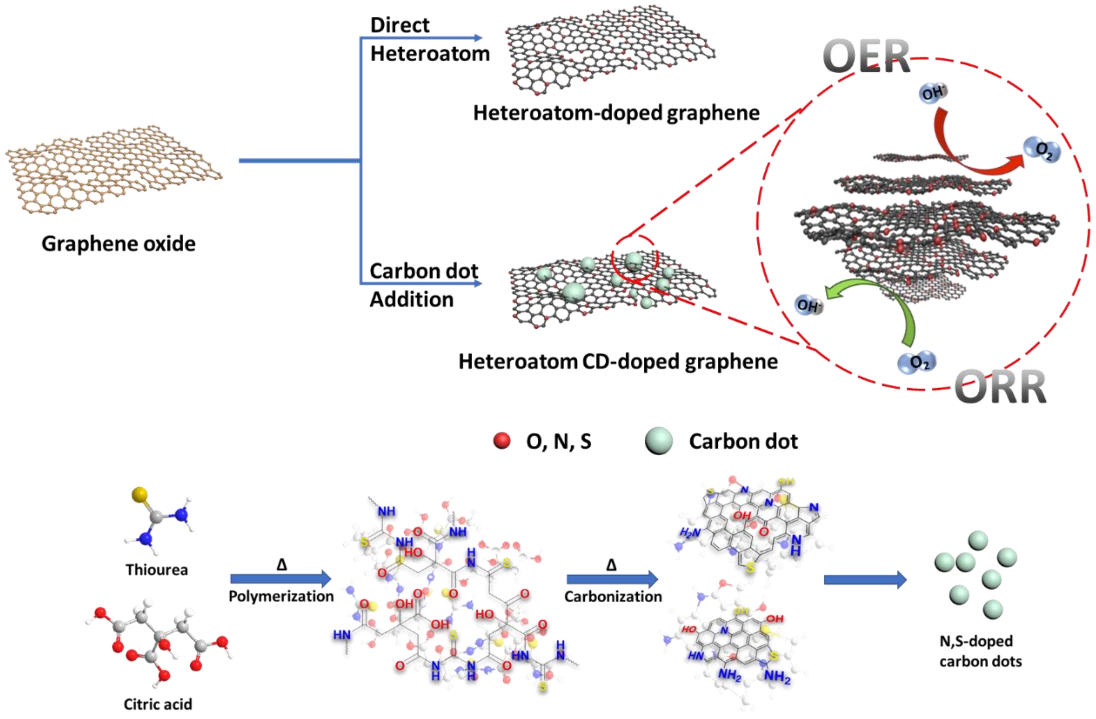

Figure 4.1 Schematic illustration of the CD-embedded porous carbon (CD@gf) preparation where green spheres represent carbon dots (N or N, S-doped) and red spheres represent heteroatom dopants (either O, N or S). Reaction scheme of CD fabrication is shown below.

The schematic synthesis procedure of heteroatom-doped CD-embedded porous graphene (CD@gf) is illustrated in Figure 4.1. Heteroatom co-doped CDs and highly porous CD@gf samples were both prepared in bulk by a simple hydrothermal approach and the highly exfoliated graphene oxide (GO) sheets with abundant oxygen-containing functional groups were synthesised by an improved Hummers' method[156]. Hydrothermal processes are often used to prepare and modify sizes, and structural/chemical properties of CDs by simply varying the reaction conditions (e.g. types of reagents, concentration, reaction temperature)[228]. Effective isolation of single- to few-layered GO was achieved by providing sufficient time for the oxidising agent to diffuse fully into water (TEM image as shown in Figure 4.2a-b)[229]. Many oxygen-containing groups, such as hydroxyl, carbonyl, and carboxyl (XPS results in Figure 4.2c-d), not only allow sufficient GO dispersion in water[230], but also the oxygen sites may interact with functionalised heteroatoms of CDs. Under hydrothermal conditions, reduced graphene oxides are formed via random reassembling (folded, twisted, and wrinkled manner) and pores/defects of the hydrogel are occupied by CDs to generate many catalytically active sites[231]. The overall carbon to oxygen (C/O) ratio of GO was 1.96 and observed XPS peaks at energy of 285.1, 287.2, and 288.4 eV correspond to C-C/C=C, C-O, and C=O/O-C=O bonds.

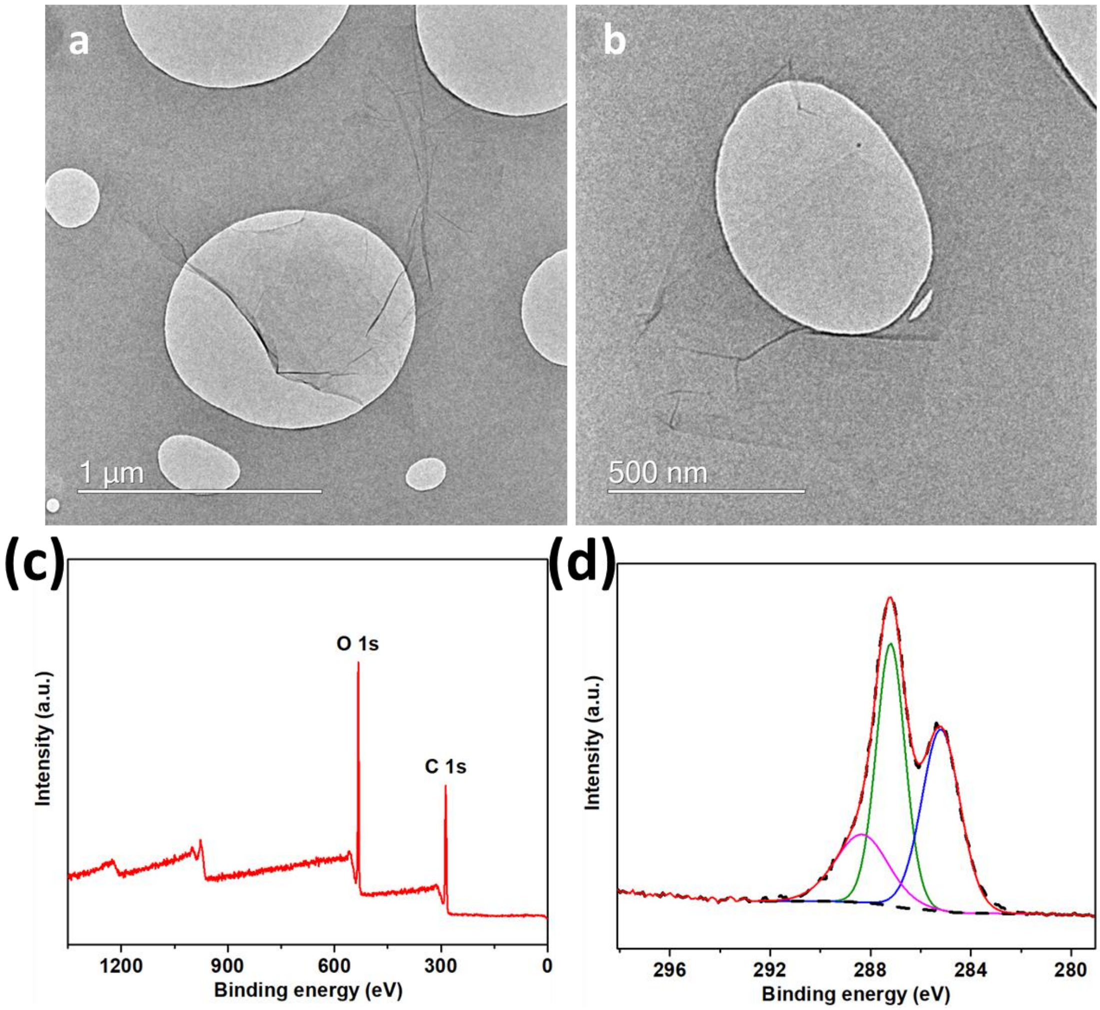

Figure 4.2 (a),(b) TEM images of few layers GO, (c) XPS survey spectrum of GO, and (d) High-resolution C 1s spectrum of GO.

4.2.2 Heteroatom-doped CDs

Heteroatom-doped CDs were successfully synthesised via simple hydrothermal-assisted condensation polymerisation reactions. CDs were measured to be in the range of 3-20 nm in diameter, evidenced by AFM (Figure 4.3a-b) and TEM images (Figure 4.3c-d). Heights of CDs differ from few layers to multiple layers/clumps of carbon as shown by the diversity in the AFM height profile.

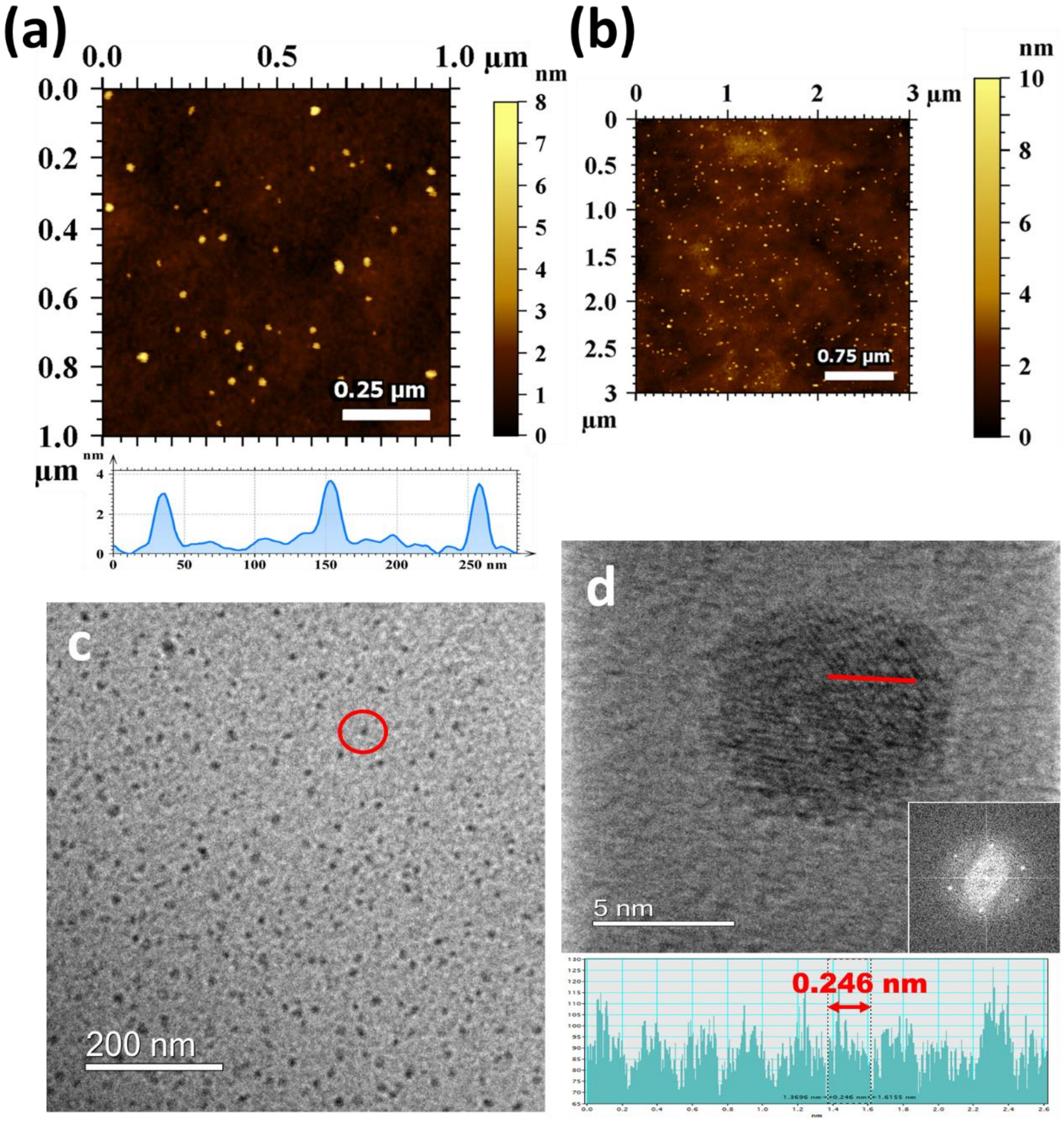

Figure 4.3 (a) AFM topology of well-dispersed NS-CD with height profile at high magnification. (b) Low magnification AFM topology of NS-CD. (c) TEM images of NS-CDs in low magnification. (d) High magnification TEM image of NS-CD with recorded height and interlayer spacing; inset is the corresponding reduced-FFT image.

TEM particle size distribution of NS-CD is shown in Figure 4.4 with average particle size of 8.5 nm. As shown in TEM images in Figure 4.3, the observed interlayer spacing of (100) of 0.24 nm and the (002) lattice fringe of graphene of 0.34 nm (reduced-FFT image showing the six-fold symmetry)[232-234], the structures of CDs are defined to be a mixture of amorphous and graphitic-like phases. The presence of D and G bands in Raman spectra[235-237] (properties described in the previous chapter) and broad observable peaks in XRD around 22°, slightly lower than (002) plane[196], were observed for all CD samples (Figure 4.5). Incorporation of heteroatoms (both N and S being bigger atoms than C with more available valence electrons) can lead to increase in amorphous nature of graphitic substrates and increases the number of defect sites in the given structure.

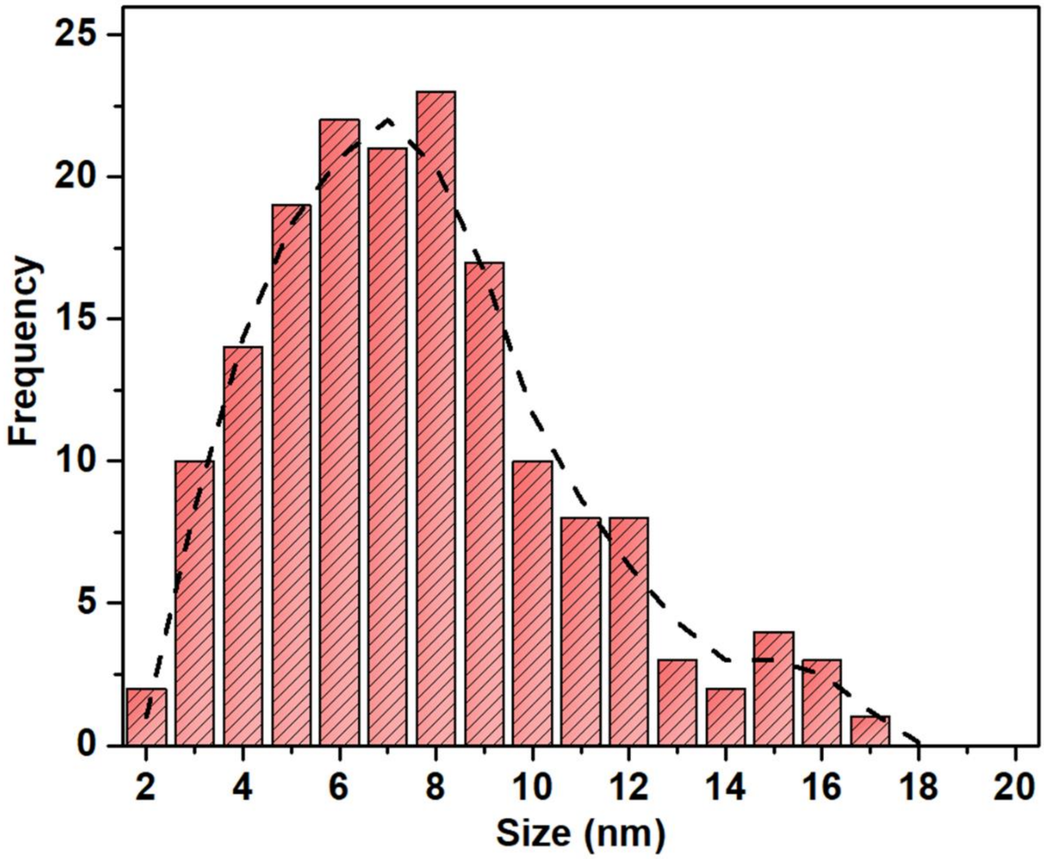

Figure 4.4 Particle size distribution of NS-CD obtained from low-magnification TEM image; the average particle size is 8.5 nm.

XPS results provided the chemical properties of heteroatom-doped CDs (Figure 4.6); C 1s spectrum of NS-CD exhibited C-C, C-O/C-N/C-S, and C=O bonds at binding energies of 284.8, 285.8, and 288.4 eV, respectively[237-239]. Binding energies of heteroatom to carbon bonds (of N and S) overlap with the energies of both single and double carbon-to-oxygen bonds showing increase in fitted peak intensities. The N 1s spectrum demonstrates the presence of pyridinic N (≈398.1 eV), pyrrolic N (≈400.0 eV), and graphitic N (401.2 eV), suggesting that sp^2/sp^3 nitrogen species are generated during the reaction. The energy of amine groups ($-NH_2$) overlap with those of pyrrole groups and is conflated[240-242]. Binding energies of sulphur are around 162.3 and 163.5 eV for the thiol group (S-H) on the surface, 163.7 and 164.9 eV for the thiophene-S (C-S, C=S, spin–orbit coupling of S 2p), and 167.1 eV for the sulphur oxide (SO_X)[240, 242]. O 1s high-resolution spectrum indicates C=O, C-O, O-C=O, and S=O bonds at 530.8, 531.5, 532.1, and 533.6 eV, respectively[238, 240]. Similar binding energies were observed for N-CD as NS-CD. Surface heteroatoms (either N or N/S) are revealed by the survey scans and the contribution of sulphur reduced the C=O bond contribution in NS-CD sample which is shown in Figure 4.7. N and S bonds of N-CD and NS-CD are also evidenced by the ATR results (Figure 4.8) and observed heteroatom stretching vibrations (1655, 1384/1172 cm^{-1} of C=N/C-N, and 1179, 644 cm^{-1} of C=S/C-S)[243-246] suggest the existence of the heteroatoms within carbon structures in accordance with the XPS results. Increased formation of carbon saturated N species, pyridinic N and graphitic N, was found with NS-CD compared to N-CD sample (shown in Table 4.1). Other precise elemental analyses of CDs are difficult to obtain due to the hygroscopic nature of prepared CDs.

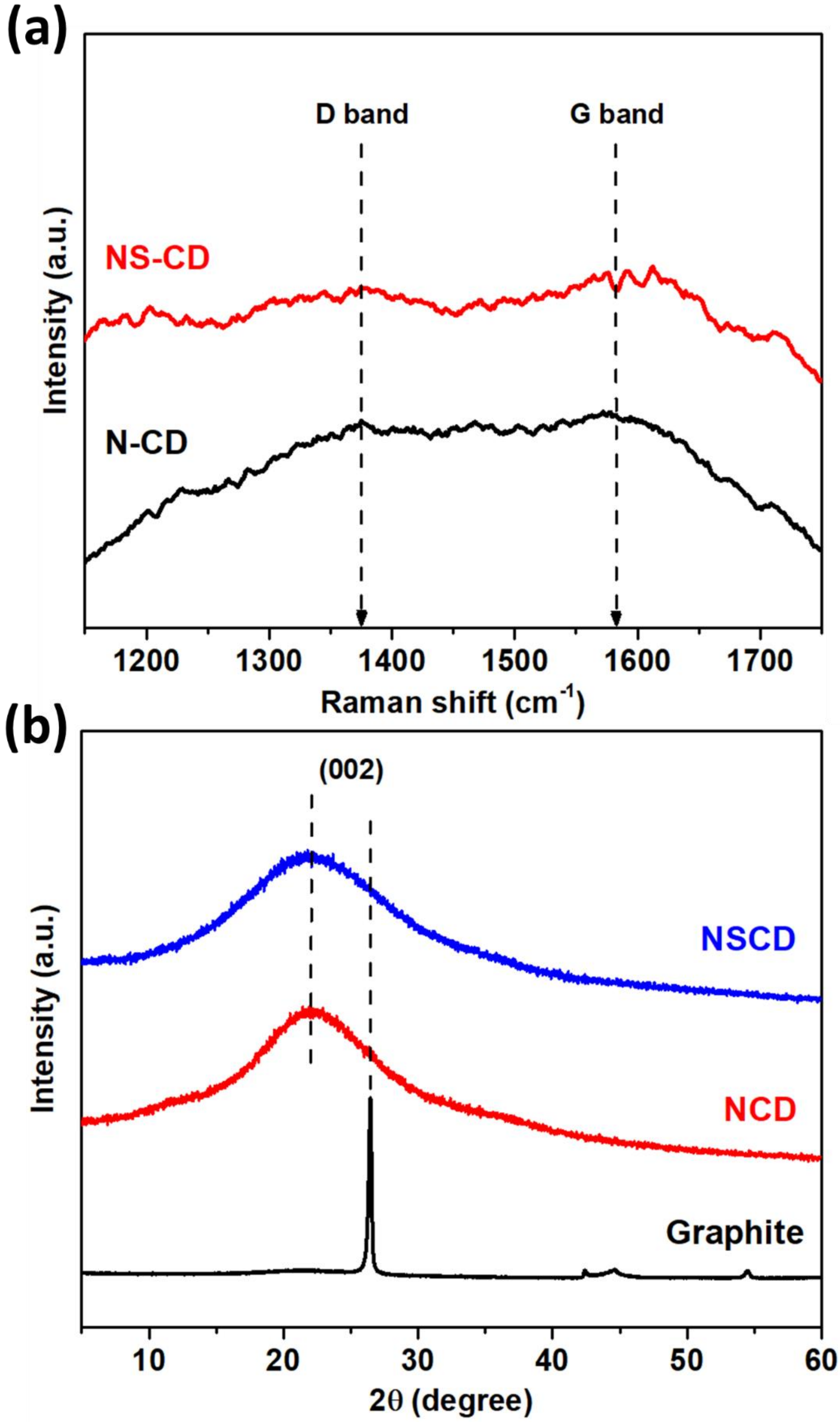

Figure 4.5 (a) Raman spectra of N-CD and NS-CD between 1200-1700 cm^{-1} region, and (b) XRD patterns of N-CD and NS-CD, exhibiting (002) graphitic plane.

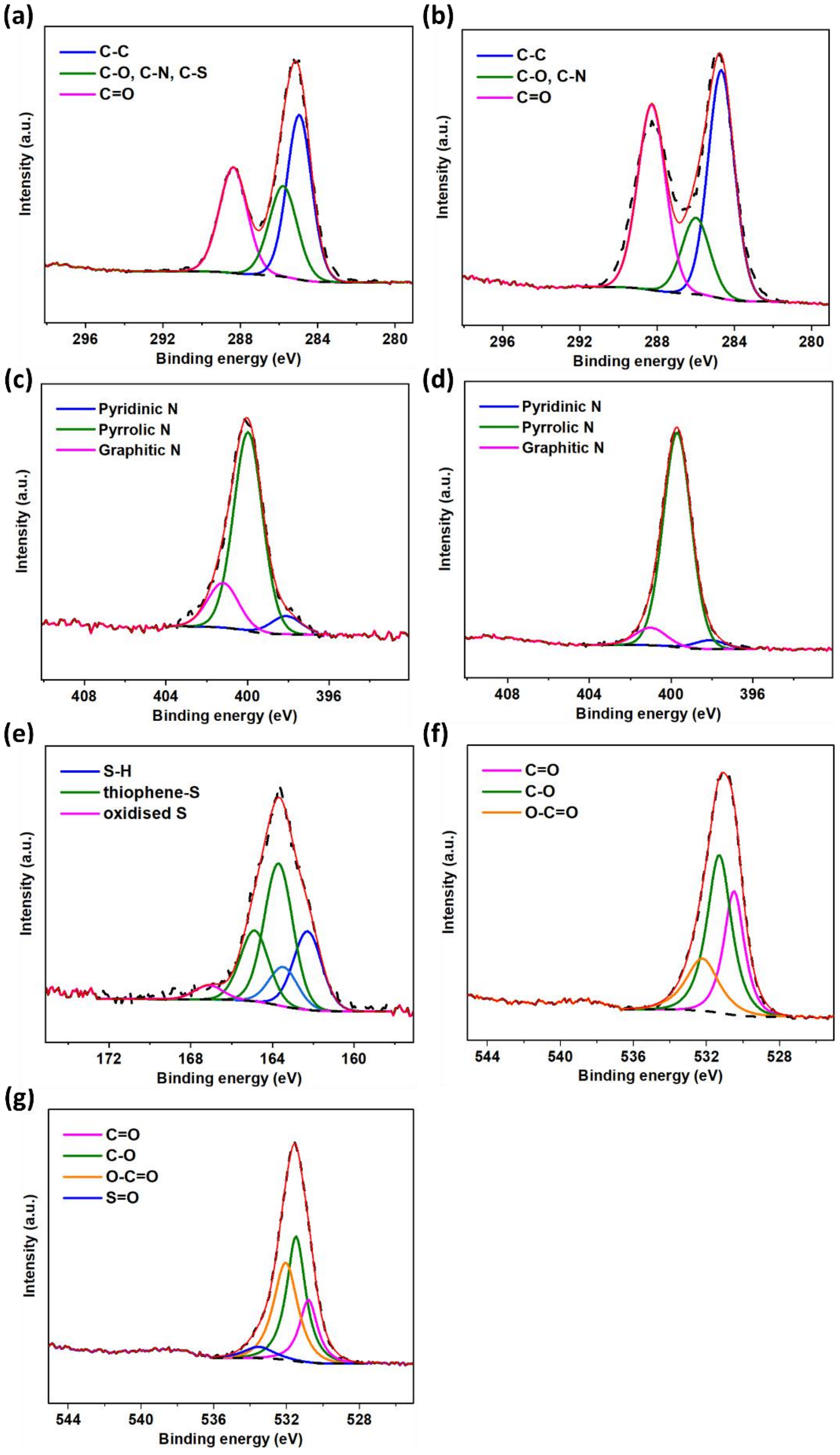

Figure 4.6 XPS spectra of NS-CD; (a) C 1s, (c) N 1s, (e) S 2p, and (g) O 1s. N-CD XPS spectra corresponding to (b) C 1s, (d) N 1s, and (f) O 1s.

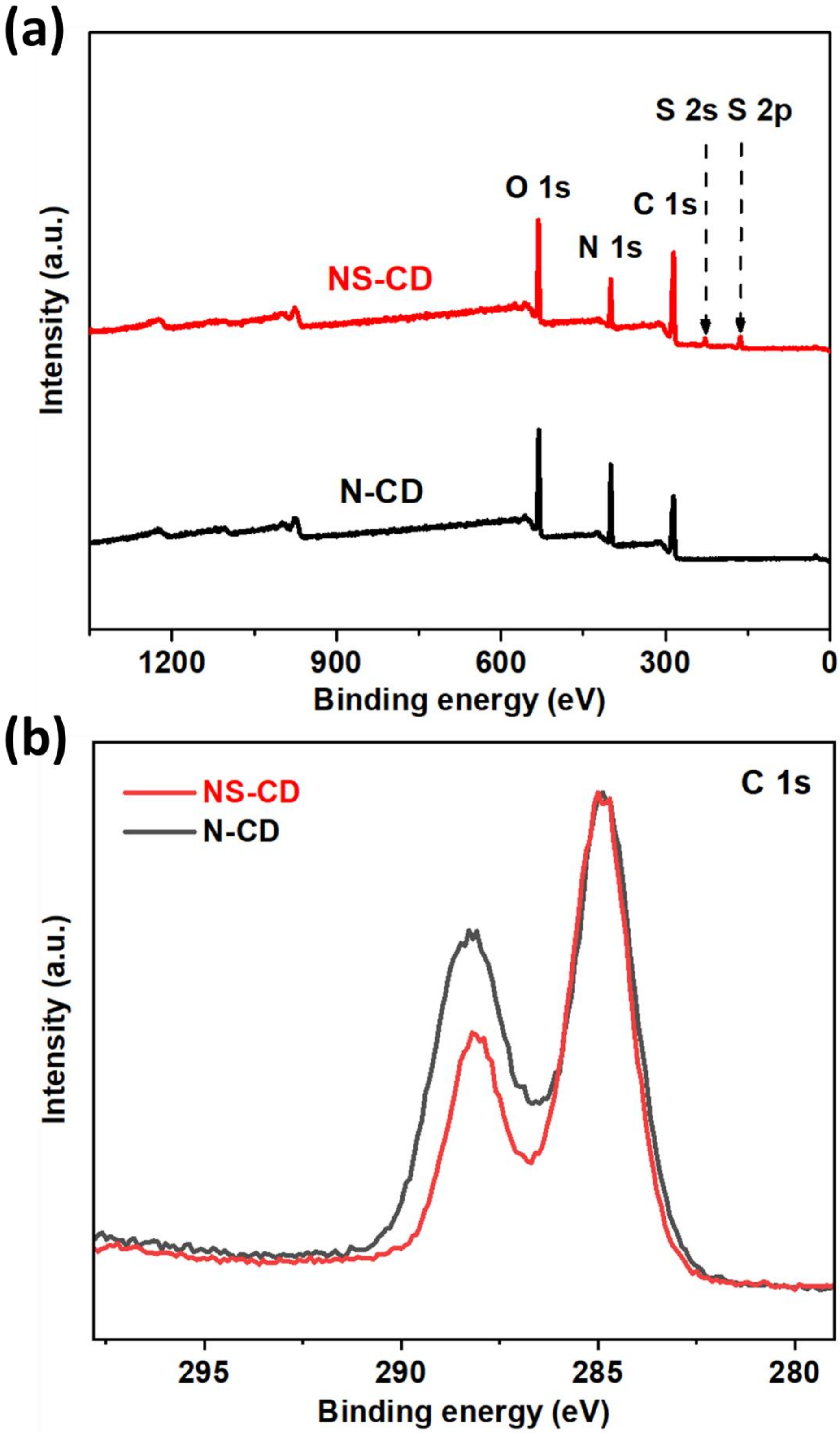

Figure 4.7 (a) XPS survey spectra of N-CD and NS-CD, and (b) Overlay of C 1s spectra of N-CD and NS-CD.

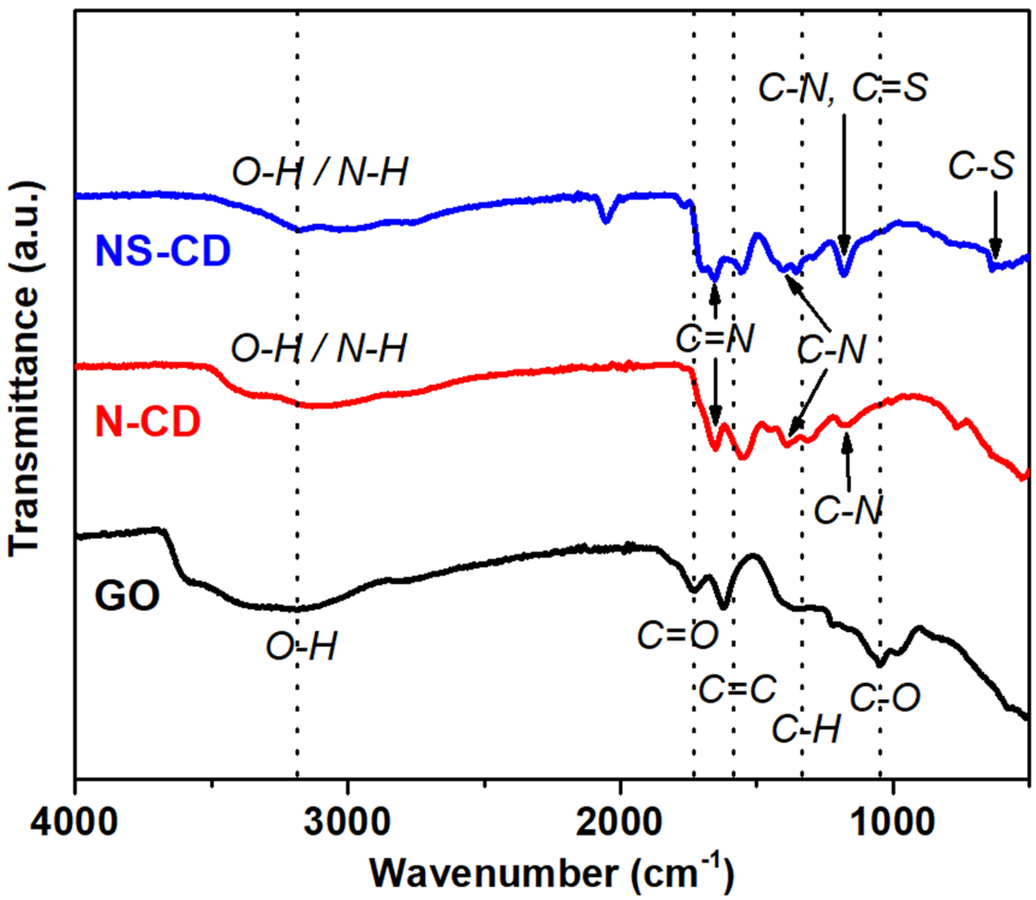

Figure 4.8 ATR-IR spectra of GO, N-CD, and NS-CD between 4000-400 cm^{-1}.

Table 4.1 Elemental quantification of N-CD and NS-CD obtained from XPS; percentage of pyridinic N, pyrrolic N, and graphitic N of the nitrogen fitting contribution shown.

	C (at. %)	N (at. %)	S (at. %)	O (at. %)	Pyrid N (%)	Pyrrol N (%)	G-N (%)
N-CD	62.7	10.4	—	26.9	4.1	87.9	8.0
NS-CD	65.9	8.9	3.4	21.8	7.5	74.5	18.0

4.2.3 Heteroatom-doped CD embedment on graphene

Heteroatoms-doped CD embedded graphene samples were synthesised by mixing the two in DI water followed by the hydrothermal process – reactions between heteroatom functional groups in CDs and oxygen functional groups around edges/defect sites in graphene oxide. The (001) plane of carbon appears with increased interlayer spacing of graphene/graphite (typically from the introduction of oxygen functional groups on the surface of each graphene/graphite layer during the chemical oxidation process); the higher oxidation degree of GO, the lower the (001) diffraction peak location. Upon thermal reduction (hydrothermally or via annealing), many oxygen functional groups are removed resulting in restoration of graphene/graphite layer-to-layer interactions close to (002) plane. Distinct peaks of (001) plane at around 11.1° of GO and (002) plane of graphitic carbon are shown for all samples in the XRD results (Figure 4.9a). All hydrothermally reduced graphitic framework samples, RGel, NS-CD@gf, and NS-CD@gf_a900, exhibited broad (002) peaks at around 21.0°, indicating an overall amorphous nature but varied short-range order of the reassembled graphene sheets. The effect of incorporated CDs broadened the (002) peak compared to the sample without CDs. Further broadening of (002) peak can be seen with annealing as additional fragmentation and defect formation take place. The (100) plane is shown for all samples at roughly 42.0°. Raman spectra show 0.86, 0.93, and 1.08 I_D/I_G ratio of RGel, NS-CD@gf, and NS-CD@gf_a900, respectively (Figure 4.9b). Close I_D/I_G values of RGel and NS-CD@gf suggest that there are no major changes in defect chemistry with the embedded CDs. However, the observable increase in the I_D/I_G ratio, compared to the untreated one, is seen with the annealed sample, which can be attributed to the formation of hierarchical porous structures of carbon with more defect sites available[247, 248]. From

N_2 adsorption-desorption isotherm (Figure 4.9c), the BET surface areas of for NS-CD@gf and NS-CD@gf_a900 were 264.66 and 559.59 m^2 g^{-1} with micro- and mesopores present[249]. Both isotherms exhibited type IV isotherm shape meaning that the general pore width is larger than the critical width for gas adsorption[179, 180]. Gereneral increase in pore diameter across the complete range for NS-CD@gf_a900 was displayed compared to the one without annealing step (Figure 4.9d). All BET specific surface areas and pore volumes are represented in Table 4.2.

Hydrothermally reduced graphene oxide hydrogels can vary in size only by altering the pH conditions; more dense and electrically conductive structure formed in the acidic condition[250]. However, sizes of hydrogels formed at different pH do not differ significantly when the concentration of GO suspension used for hydrothermal synthesis remains the same. Embedment of CDs in graphene is demonstrated by direct comparison of the physical size of hydrogels obtained from the hydrothermal process: NS-CD@gf shows significantly larger dimensions than that of RGel sample as shown in the photo in Figure 4.10. Both SEM and TEM images (Figure 4.11) reveal highly porous and fragmented carbon frameworks which are expected to facilitate easy penetration of oxygen molecules during electrocatalytic processes.

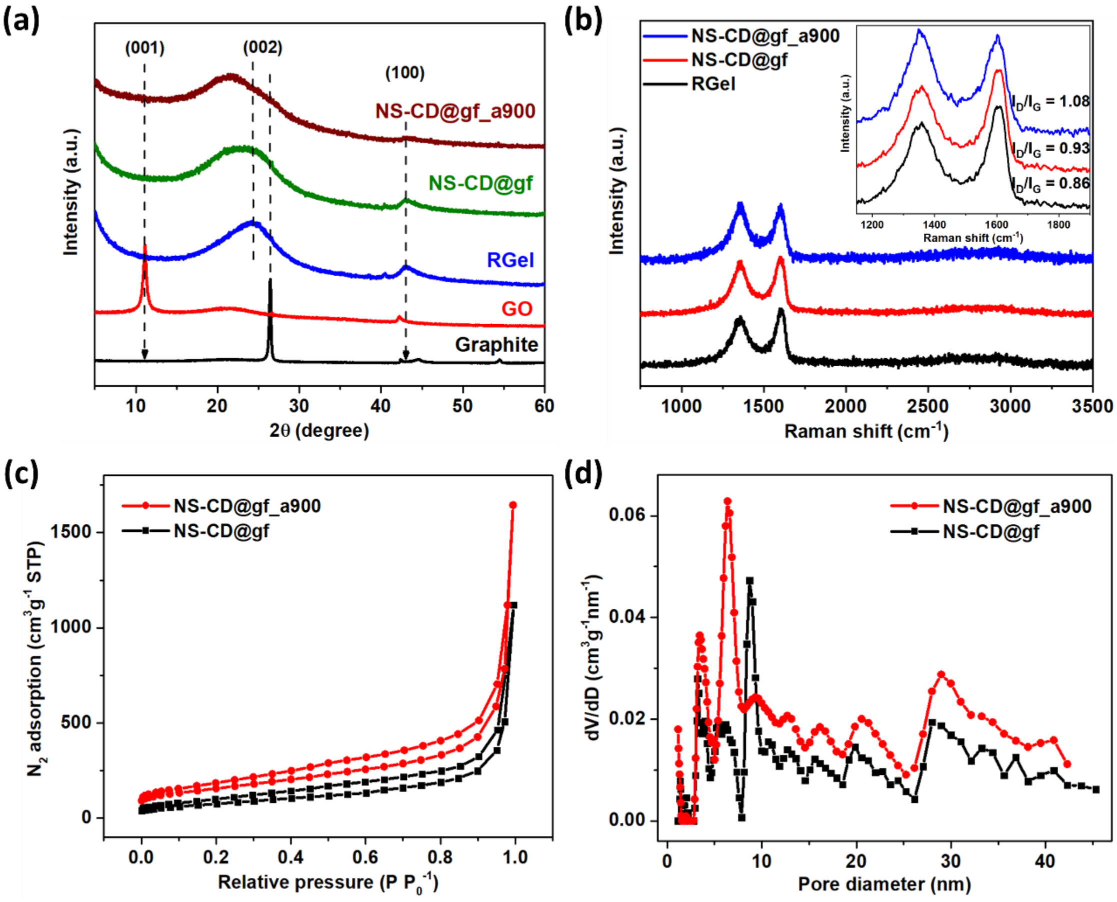

Figure 4.9 (a) XRD patterns of graphite, GO, RGel, NS-CD@gf, and NS-CD@gf_a900. (b) Raman spectra of RGel, NS-CD@gf, and NS-CD@gf_a900; the inset is a close-up of D and G band with calculated I_D/I_G ratio. (c) N_2 adsorption-desorption isotherm of NS-CD@gf and NS-CD@gf_a900, and (d) BET pore size distribution curves obtained using QSDFT and BJH methods for calculations.

Table 4.2 The total BET specific surface area and pore volume of all samples.

	Specific surface area (m^2 g^{-1})	**Pore volume (cm^3 g^{-1})**
RGel	345.02	1.82
N-CD@gf	255.88	1.76
NS-CD@gf	264.66	1.73
N-CD@gf_a900	550.20	3.19
NS-CD@gf_a900	559.59	2.54

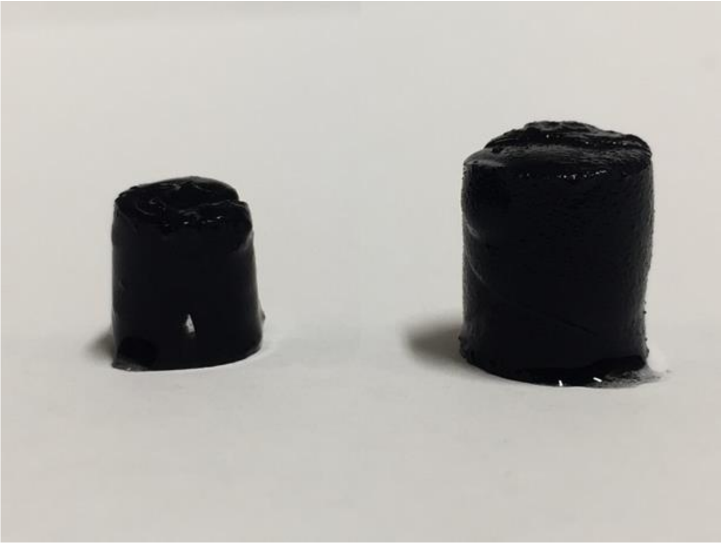

Figure 4.10 Photo of hydrothermally prepared RGel sample (left) and NS-CD@gf sample (right).

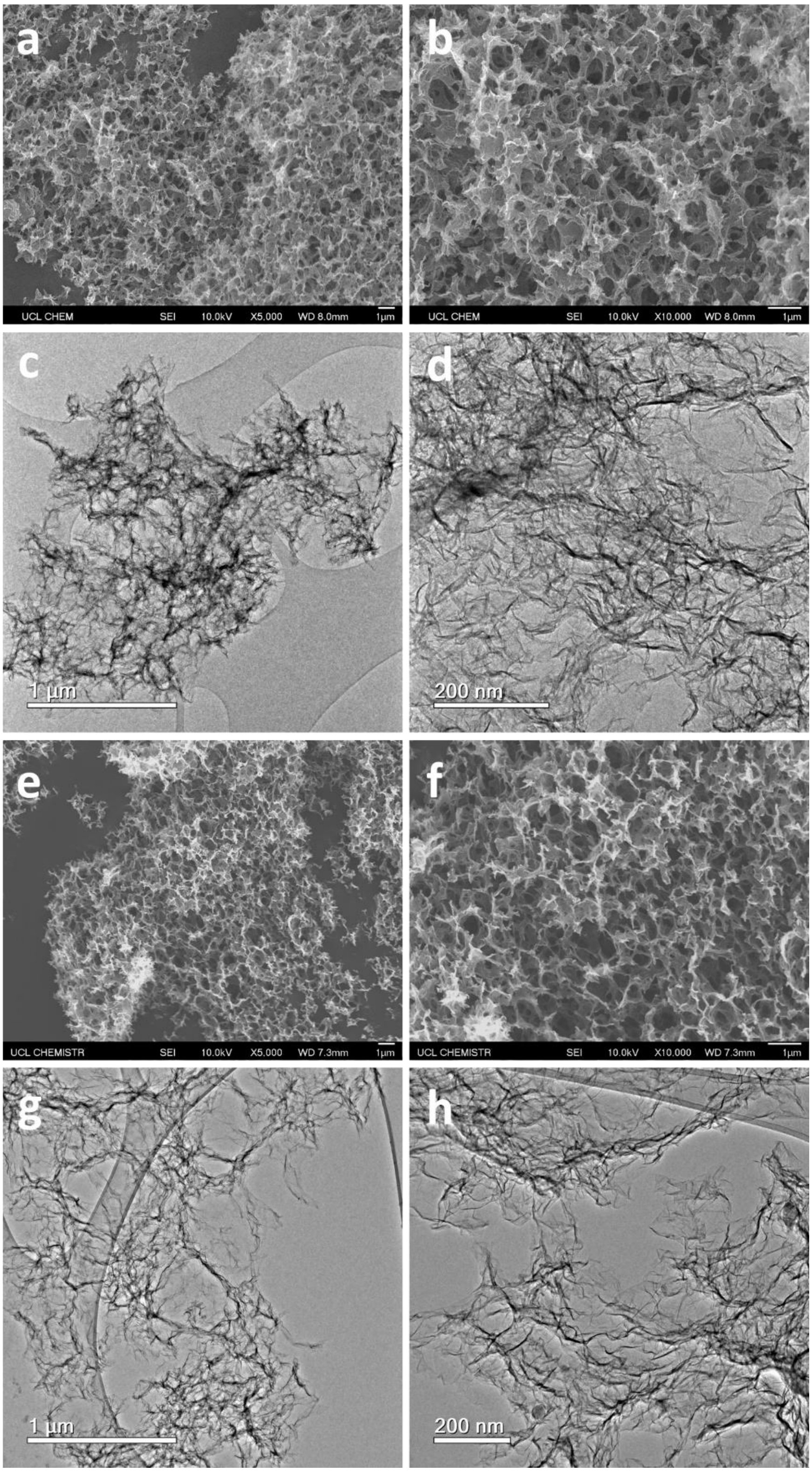

Figure 4.11 SEM images in (a) low, (b) high, and TEM images in (c) low, (d) high magnification of N-CD@gf_a900. SEM images in (e) low, (f) high, and TEM images in (g) low, (h) high magnification of NS-CD@gf_a900.

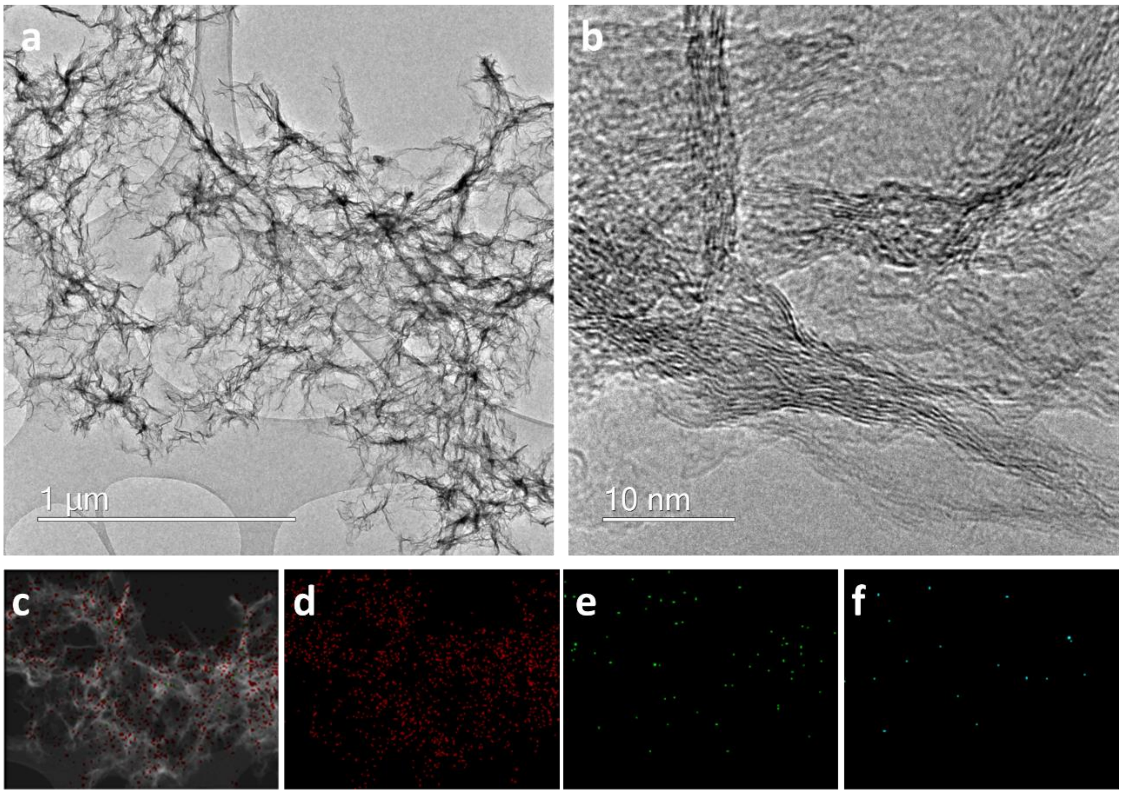

Figure 4.12 TEM images of NS-CD@gf_a900 at (a) low and (b) high magnification illustrating the embedment of NS-CDs. Same region EDS mapping images showing different elements of the NS-CD@gf_a900 framework; (c) overlap, (d) C, (e) N, and (f) S.

Generally, to prepare a hierarchically porous carbon, a template material is used which then requires an additional non-environmentally-friendly etching process[150, 251]. Instead, use of highly exfoliated graphene leads to a simple effective way of preparing porous substrates. Embedment of CDs to a graphene substrate is confirmed in low- and high-magnification TEM images (Figure 4.12); CDs can be observed as particles with darker contrast around either the edges or the voids on the plane of the graphene layer. Same region TEM-EDS elemental mapping of nitrogen and sulphur further illustrates the presence of heteroatoms from NS-CDs on carbon as the only origin of heteroatoms embedded to the graphene framework is from the CDs.

Table 4.3 Quantification of elements obtained from XPS for all CD-embedded graphene samples.

	C (at. %)	N (at. %)	S (at. %)	O (at. %)
N-CD@gf	83.7	1.6	—	14.7
N-CD@gf_a900	94.9	1.0	—	4.1
NS-CD@gf	87.4	5.2	0.7	6.7
NS-CD@gf_a900	95.4	1.4	0.4	2.8

XPS results of the CD-embedded graphene and thermally treated samples show change in overall composition of elements (Table 4.3). Atomic weight percentages of both N and S decrease for annealed samples as thermally unstable/weak bonds (-NH_2 and -SH) break at high temperature. XPS elemental scans of NS-CD embedded graphene samples (Figure 4.13) and N-CD embedded graphene samples (Figure 4.14) are shown. Noticeable conversion of N groups to graphitic N is achieved via high temperature annealing processes of CD-embedded graphene hydrogels[189]. Although the concentration of graphitic N (most responsible for lowering the overall free energy of ORR) and the total amount of heteroatoms coming from the CD-embedment are not significantly high compared to some reported literature (at. % of N usually greater than 5%)[167, 252, 253], effective embedment of CDs together with the effects of dual-heteroatom doping (N and S) boosts the overall catalytic performance.

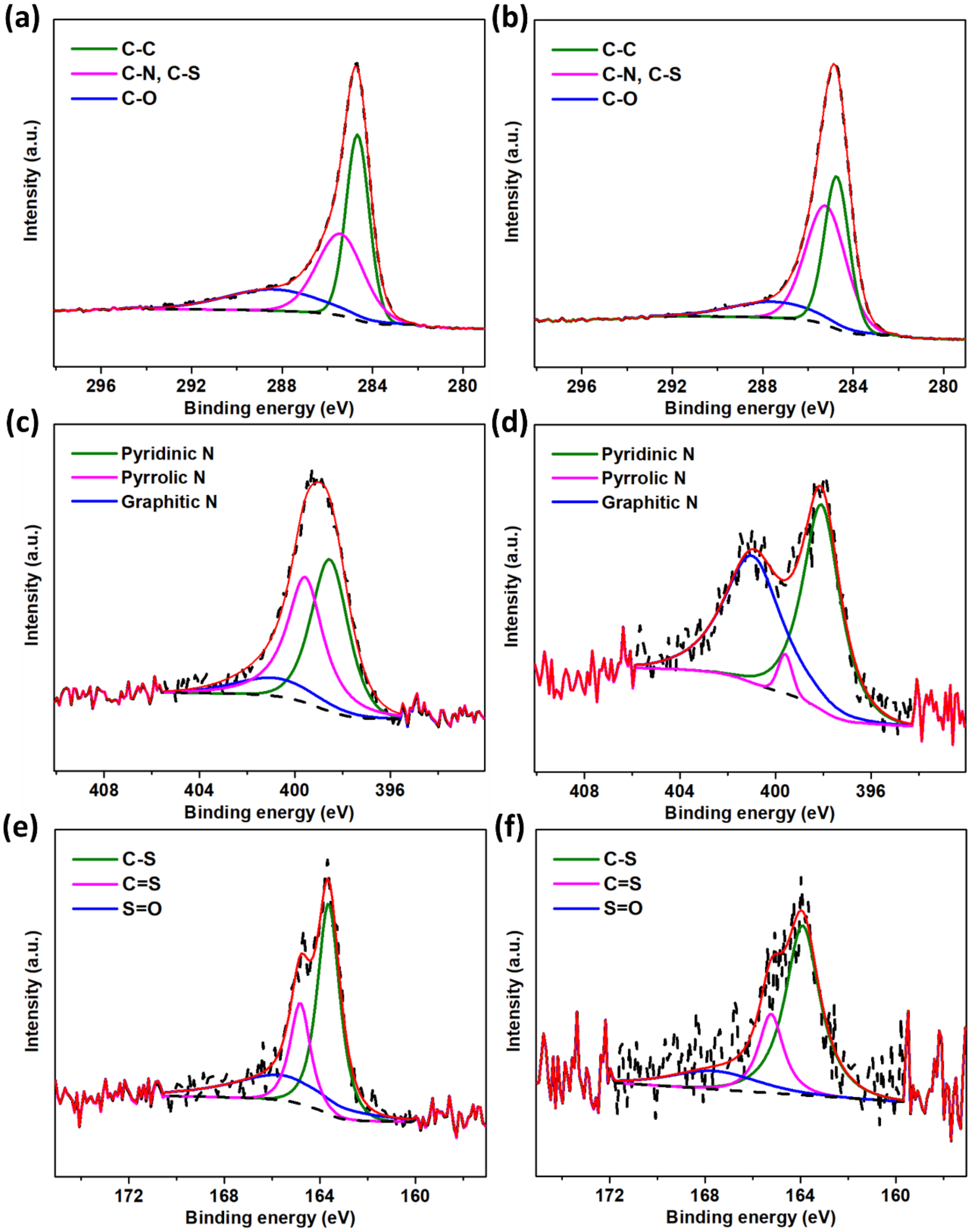

Figure 4.13 High resolution elemental scans of NS-CD@gf; (a) C 1s, (c) N 1s, and (e) S 2p. Spectra for NS-CD@gf_a900 are shown; (b) C 1s, (d) N 1s, and (f) S 2p.

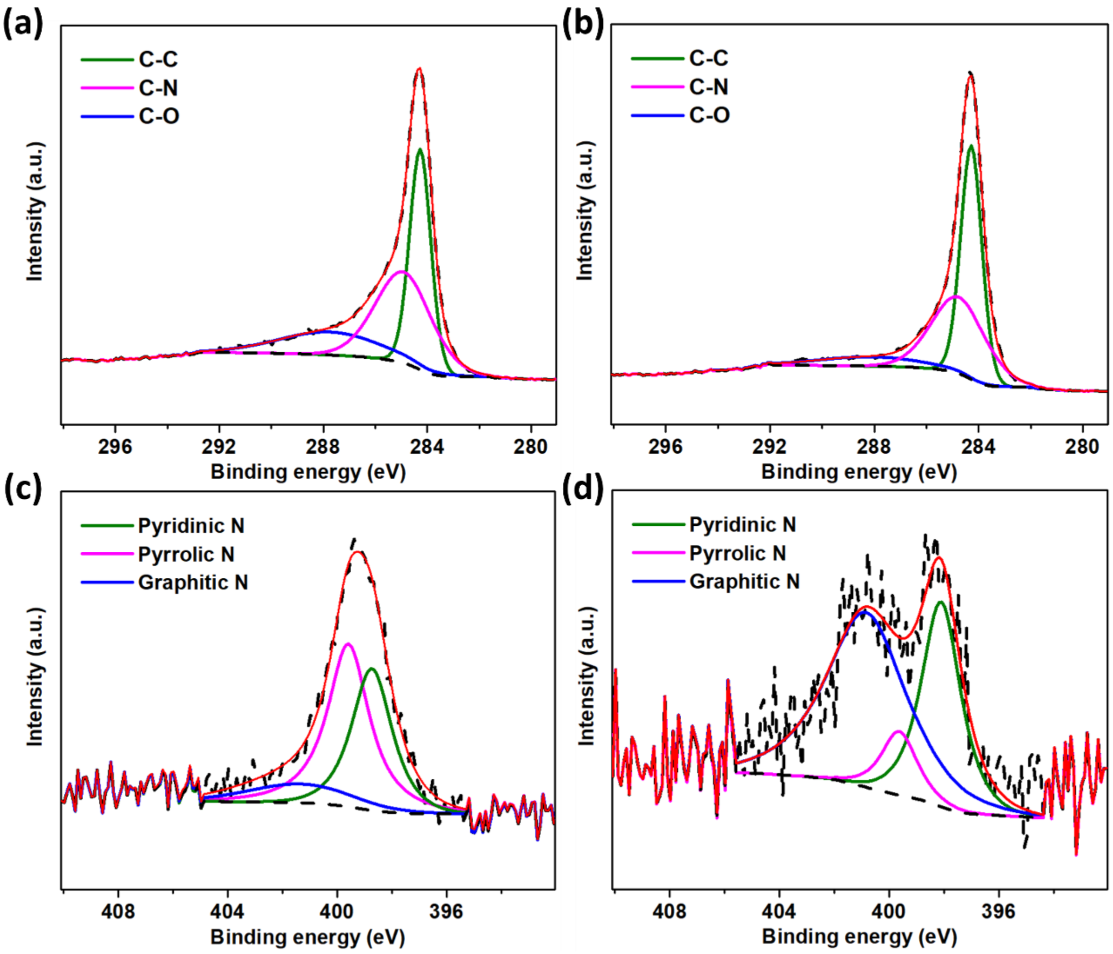

Figure 4.14 High resolution elemental scans of N-CD@gf; (a) C 1s, and (c) N 1s. Spectra for N-CD@gf_a900 are shown; (b) C 1s, and (d) N 1s.

4.2.4 Oxygen electrocatalysis of CD-embedded graphene

All samples are used directly as synthesised and electrochemically tested to understand the materials' potential as cathodes for metal-air batteries. The ohmic potential drop has not been applied to any of the tests (not iR-corrected). Initially, CV scans are measured in N_2/O_2-saturated 0.1 M KOH electrolyte. Distinct oxygen reduction peaks are shown only when oxygen is purged to the electrolyte solution suggesting a successful oxygen redox reaction (Figure 4.15).

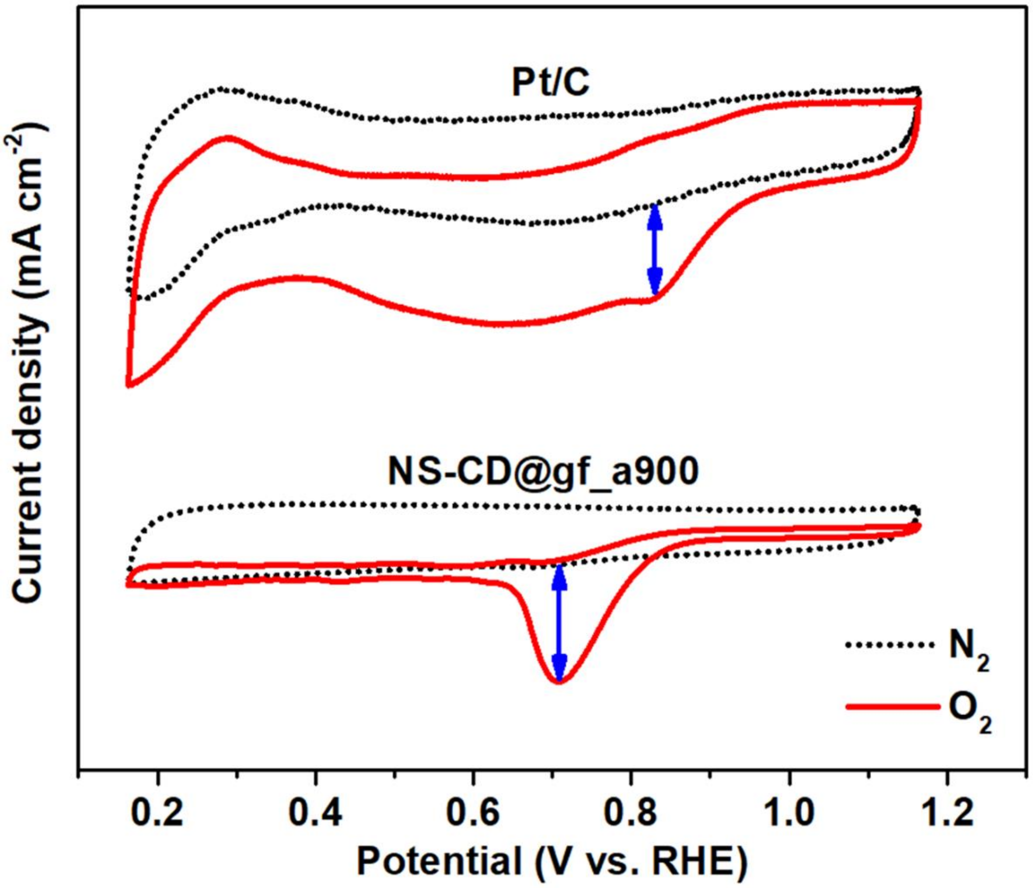

Figure 4.15 CV curves of NS-CD@gf_a900 and Pt/C obtained in N_2/O_2 *saturated 0.1 M KOH with the scan rate of 10 mV* s^{-1}.

Reduction peak current of the Pt/C sample is at 0.82 V vs. RHE whereas the peak of the NS-CD@gf_a900 sample is around 0.71 V. Differences in current densities (of O_2 and N_2) from CV scans are 1.25 and 1.53 mA cm^{-2} for Pt/C and NS-CD@gf_a900, respectively, suggesting that the NS-CD embedded graphene has better electrical response than Pt/C in the O_2-saturated alkaline condition. LSV curves of N-CD@gf, NS-CD@gf, N-CD@gf_a900, and NS-CD@gf_a900 samples exhibit outstanding electrocatalytic activities in an alkaline solution, with current responses either similar to or greater than Pt/C, despite being metal-free (Figure 4.16a). The performance of the NS-

CD sample is as expected with possible poor conductivity from high oxygen functionalities[254]. Onset potential (E_{onset}) of a sample is determined by extrapolating the point at which the change in electrical response occurs at the ORR condition. Although the E_{onset} and the half-wave potential (half of the total measured current density, $E_{1/2}$) of NS-CD@gf_a900 are around 0.93 and 0.75 V (slightly lower potentials than those of Pt/C at 0.98 and 0.84 V), the limiting current density reaches 7.71 mA cm^{-2} at 1600 rpm in 0.1 M KOH electrolyte, surpassing all CD-embedded samples and even higher than 5.55 mA cm^{-2} of Pt/C current response by approximately 38% - current measured at $E_{1/2}$ is also greater. Note that both thermally treated CD (N and NS) embedded samples exceed the limiting current density of Pt/C; performance enhancement of catalysts is realised by the intrinsic catalytic activities of CDs. The same trend is observed for the ORR results of CD@gf and CD@gf_a900 samples; N, S dual doping exhibits the highest activity followed by the single N-doping. Tafel slopes of all samples were obtained to study the relationship of the rate of ORRs with the attained overpotentials (Figure 4.16b). The value for the Pt/C (76.1 mV per decade) is smaller than the rest suggesting that the oxygen adsorption process is fast on the surface of the Pt/C. Still, the values of N-CD@gf_a900 and NS-CD@gf_a900 are 83.3 and 83.2 mV per decade, very close to that of Pt/C. The Tafel values of N-CD@gf and NS-CD@gf were 93.1 and 82.4 mV per decade, respectively. RDE–LSV measurements were collected at different rotation speeds (ranging from 400 to 2000) as shown in Figure 4.17 and Figure 4.18. NS-CD@gf_a900 outperformed all counterparts at any rotation speed, and the performance was comparable to the benchmark, Pt/C. K–L relations can be extrapolated from measured current densities of different rotations. Steady linear slopes suggest that the reaction kinetics is of first order with respect to the dissolved oxygen concentration in the electrolyte system.

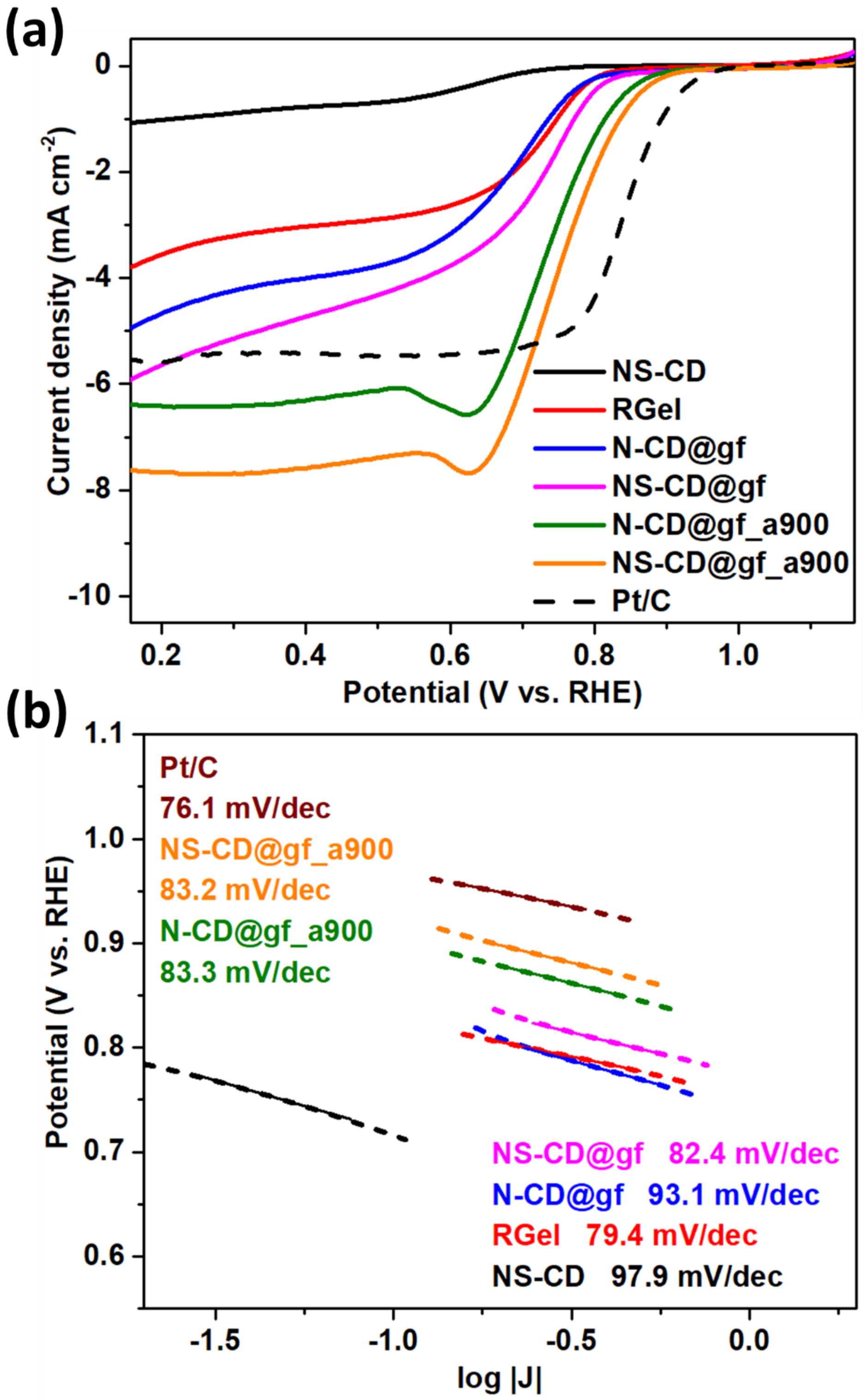

Figure 4.16 (a) Combined LSV curves for ORR of all prepared samples in O_2-saturated 0.1 M KOH at 1600 rpm. (b) Tafel plots of all samples obtained from LSV curves.

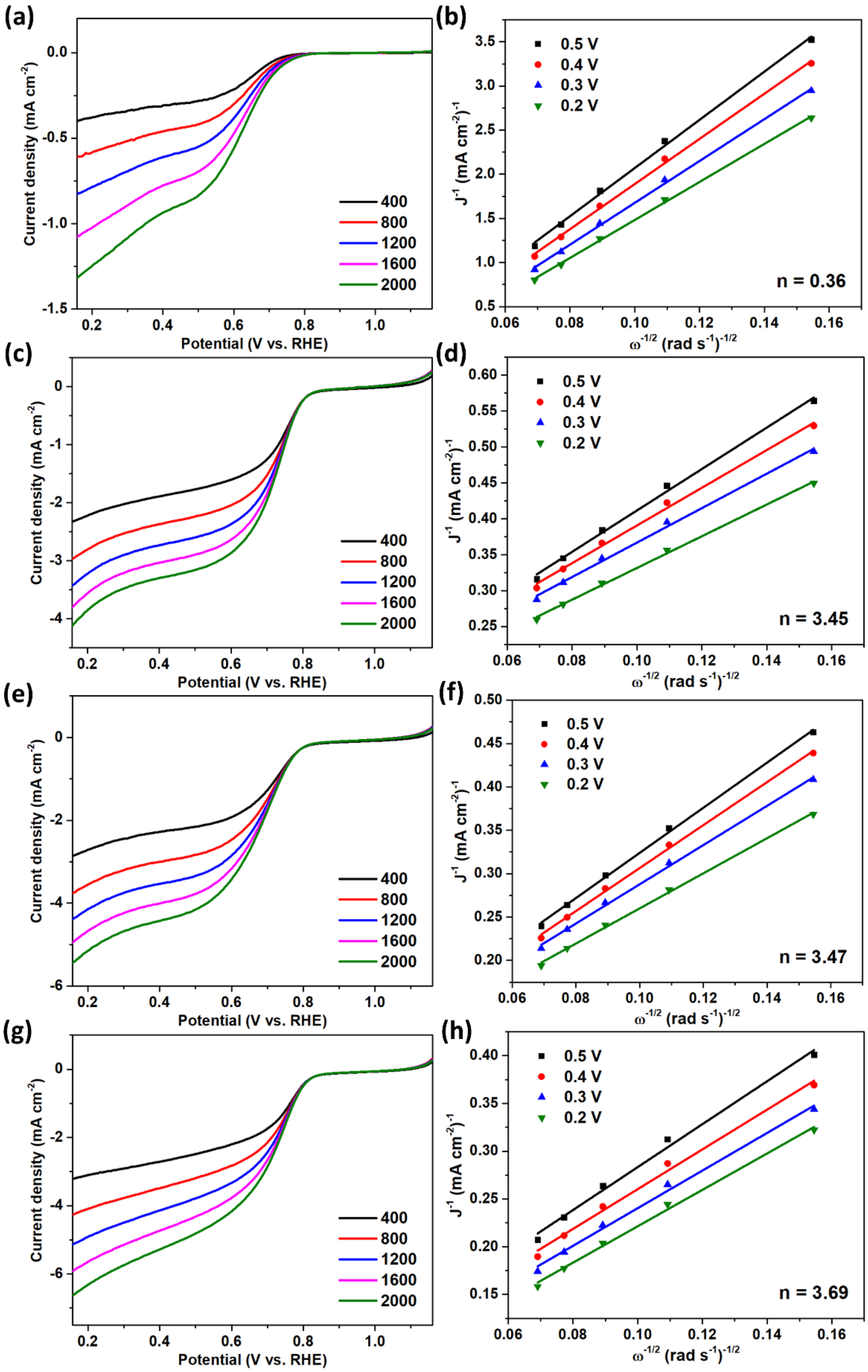

Figure 4.17 LSV curves at different rotation speeds and corresponding K-L plots for (a),(b) NS-CD, (c),(d) RGel, (e),(f) N-CD@gf, and (g),(h) NS-CD@gf.

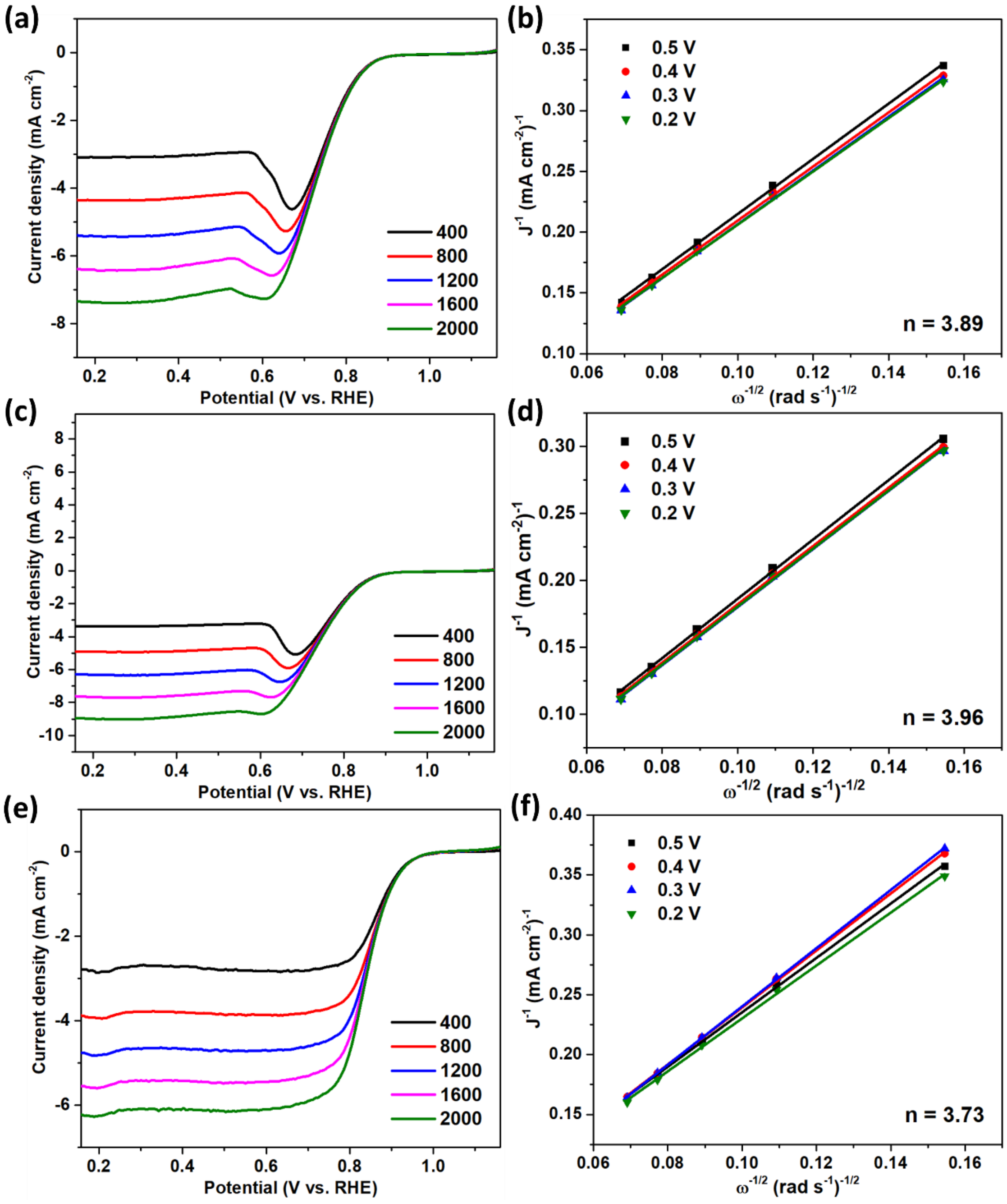

Figure 4.18 LSV curves at different rotation speeds and corresponding K-L plots for (a),(b) N-CD@gf_a900, (c),(d) NS-CD@gf_a900, and (e),(f) Pt/C.

The n value, electron transfer number, of NS-CD@gf_a900 is calculated to be around 3.96 (approaching 4, theoretical value at a successive 4e⁻ reduction pathway) for the potential range of 0.2–0.5 V versus RHE, implying effective oxygen reduction reactions. K–L values of N-CD@gf_a900 and Pt/C are 3.89 and 3.73, respectively; again, a high electron transfer number is obtained by the annealed N-CD carbon sample. The initial small hump in the ORR at low rotation suggests the peroxide formation; however, it gradually decreases with the increase of oxygen feed - approaching stable 4e⁻ processes[255].

To validate the effect of CD embedment on catalysis, the RDE result of NS-CD@gf_a900 is compared to the NS-Gel_a900, annealed-direct-heteroatom-doped graphene gel samples with no CDs (Figure 4.19). The observed ORR overpotential of the direct heteroatom-doped sample (E_{onset} = 0.94 V) is only slightly smaller than the CD-containing samples, but the measured current density is only about half (≈4.46 mA cm^{-2}) of the latter, which in fact is even lower than that of the untreated N-CD@gf and NS-CD@gf. It can be presumed that the direct heteroatom-doped defect sites are more accessible for the bulk oxygen migration and hence lead to a low overpotential[256]. Yet, a high number of vacant active sites can be provided by rich core/edge doping of heteroatoms in CD-embedded graphene framework resulting in improved ORR activity. Also, to understand the influence of annealing temperature, the RDE results of NS-CD@gf_a800, NS-CD@gf_a900, and NS-CD@gf_a1000 were studied. Slight increase in the activity is shown at carbonisation temperature of 800 °C with improved diffusion properties compared to the untreated sample. However, it can be assumed that at 800 °C there are still some oxygen functionalities interfering with the performance as well as the low conversion ratio of graphitic N[257].

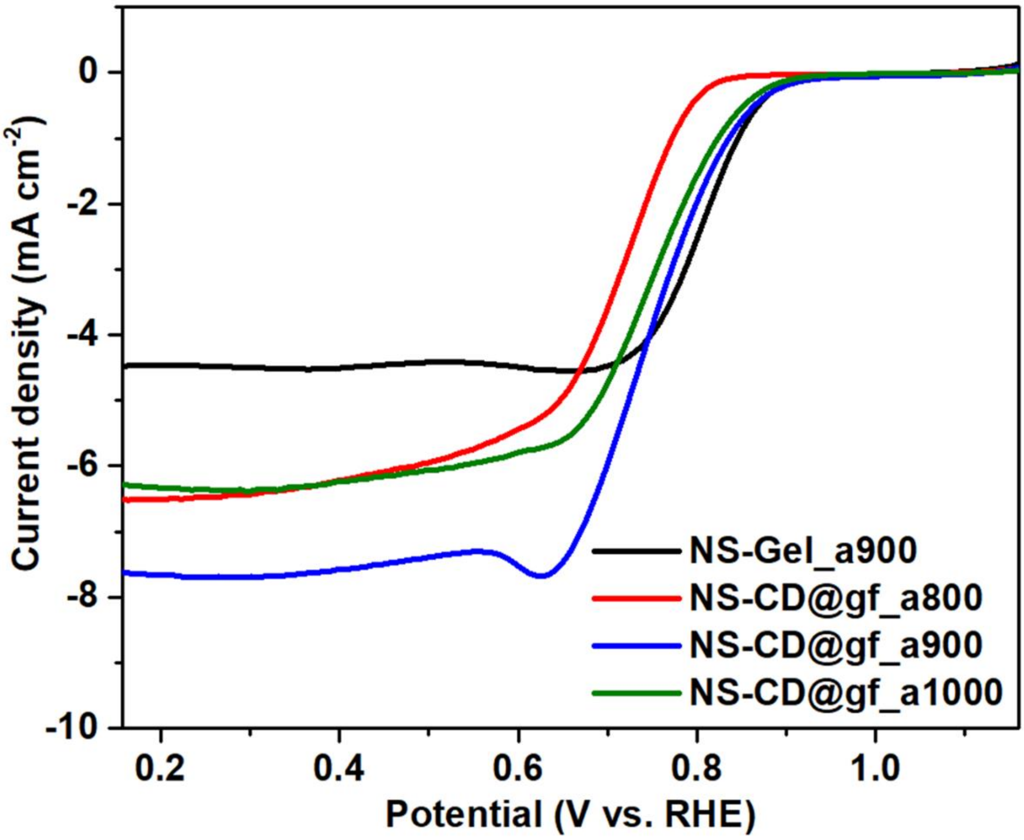

Figure 4.19 LSV curves of NS-Gel_a900 (without the CD embedment), and temperature controlled NS-CD embedded graphene samples in 0.1 M KOH with 1600 rpm.

Table 4.4 XPS elemental quantification of temperature controlled NS-CD embedded graphene samples.

	C (at. %)	**N (at. %)**	**S (at. %)**	**O (at. %)**	**Pyrid N (%)**	**Pyrrol N (%)**	**G-N (%)**
NS-CD @gf_a800	92.5	2.1	0.7	4.7	59.1	22.2	18.7
NS-CD @gf_a900	95.4	1.4	0.4	2.8	33.7	5.9	60.4
NS-CD @gf_a1000	96.2	1.2	0.3	2.3	35.4	16.4	48.2

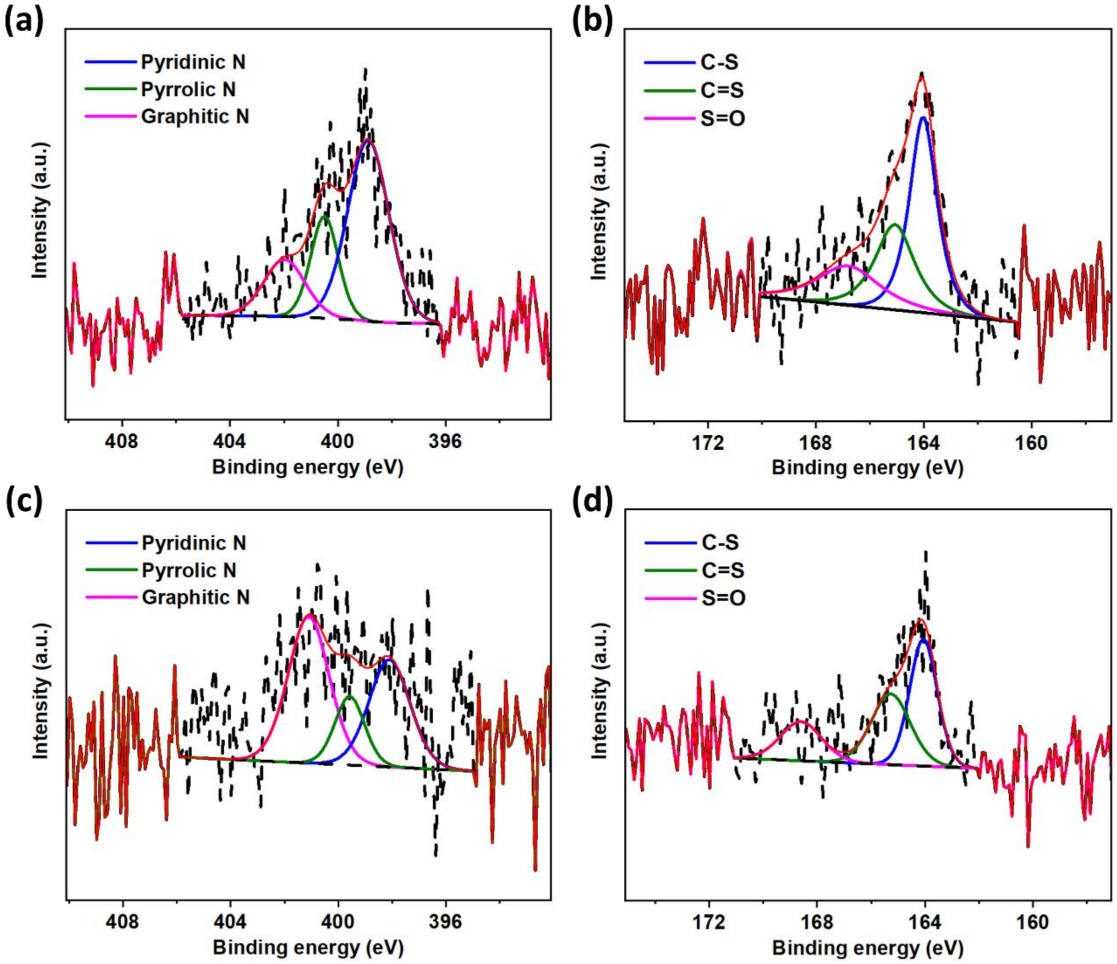

Figure 4.20 High resolution XPS spectra of NS-CD@gf_a800 (a) N 1s and (b) S 2p, and of NS-CD@gf_a1000 (c) N 1s and (d) S 2p.

At 1000 °C, on the other hand, despite the increase in rate of conversion with 60 mV reduction in overpotential (improved kinetics with low oxygen and high graphitic N), the loss of sulphur-containing groups (Table 4.4 and Figure 4.20) results in no change in limiting current density[258], compared with 800 °C. The optimum temperature of annealing is 900 °C with the oxygen level low enough to give rise to good conductivity and high graphitic N concentration while preserving sulphur components in CD-graphene materials.

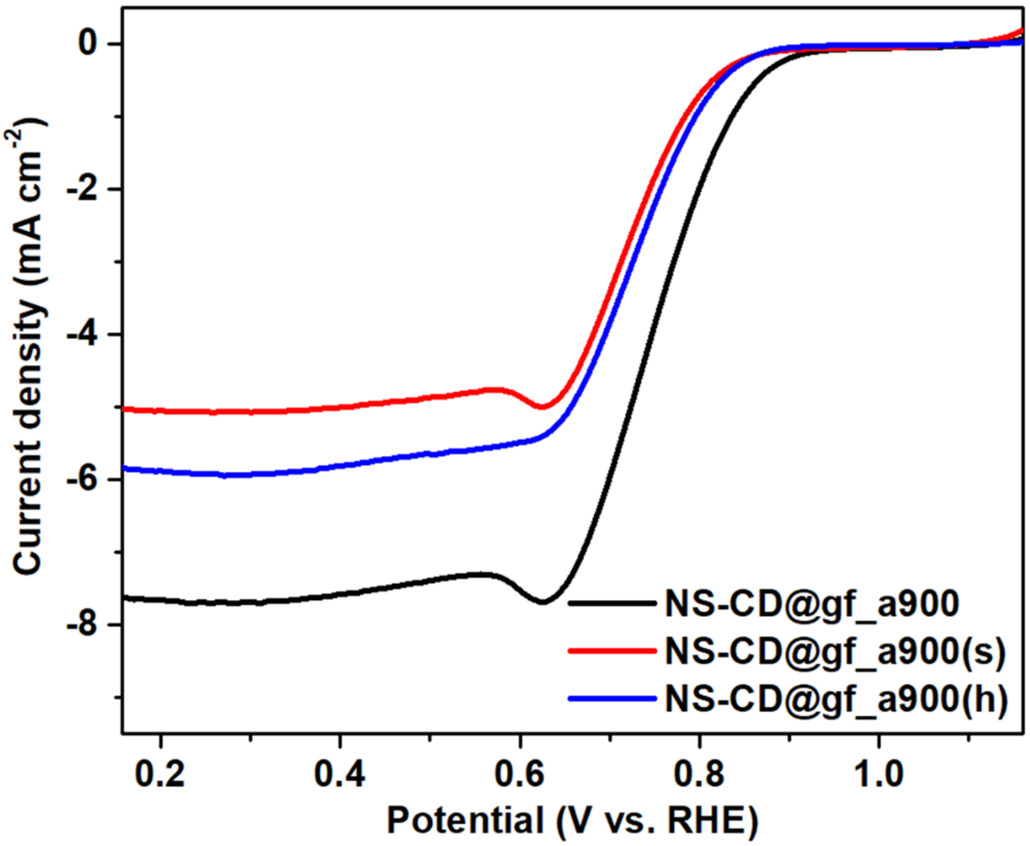

Figure 4.21 ORR LSV curves of NS-CD@gf_a900, NS-CD@gf_a900(s) with halved CD amount, and NS-CD@gf_a900(h) with doubled CD concentration.

The amount of CD embedment was varied in order to clarify the effect of the active site densities provided by the CDs. As shown in Figure 4.21, when the amount of NS-CD used is halved in the NS-CD@gf_a900(s) sample, the current response is significantly reduced with E_{onset} at 0.86 V compared to the original sample (NS-CD@gf_a900). As the addition of NS-CD is doubled in the sample, NS-CD@gf_a900(h), the current density and E_{onset} increase slightly to ≈5 mV cm^{-2} and 0.88 V, respectively. The SEM images of the following samples (Figure 4.21) show that the morphologies of the graphene substrate are more or less the same when the CD amount is halved.

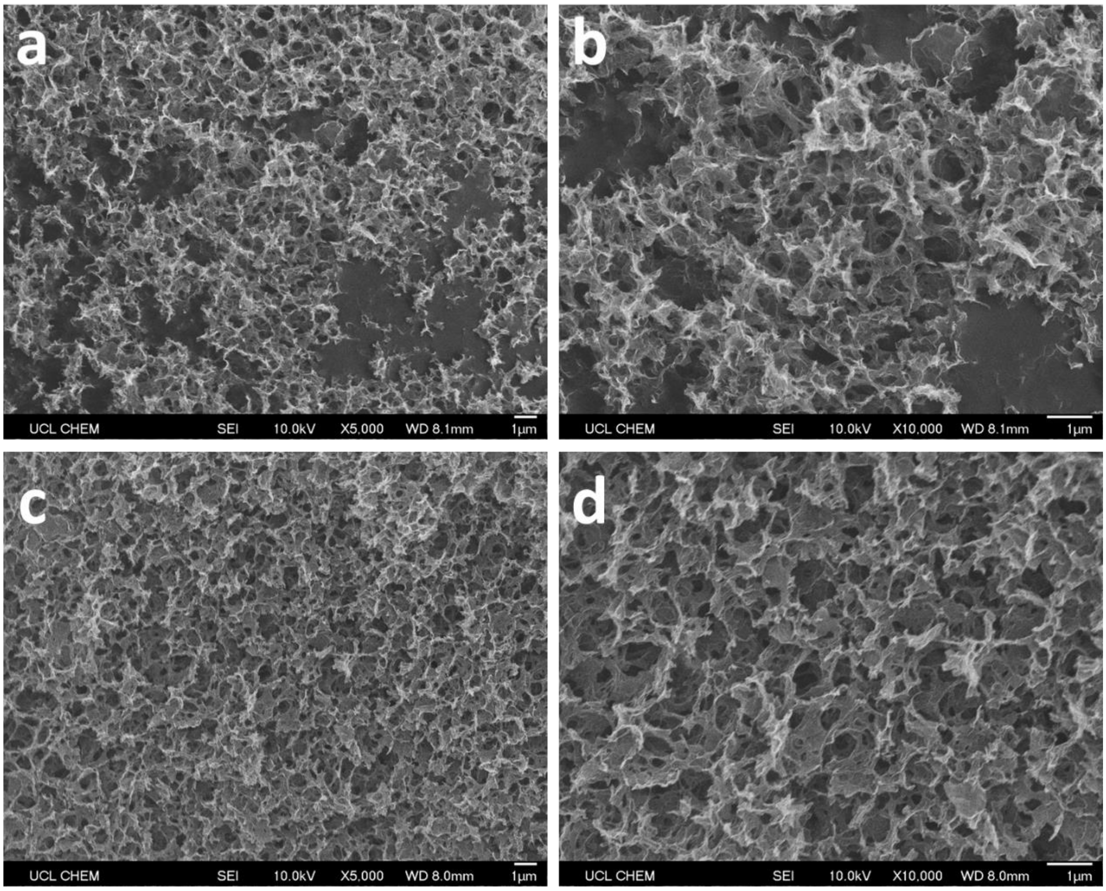

Figure 4.22 SEM images of NS-CD@gf_a900(s) in (a) low and (b) high, and NS-CD@gf_a900(h) in (c) low and (d) high magnification.

This suggests that the reduction of electrocatalytic performance for the halved sample is governed by the decreased number of active sites; for the same reason, the E_{onset} of NS-CD@gf_a900(h) is slightly higher than that of NS-CD@gf_a900(s) sample. However, as the amount is doubled, the pores of the graphene start to close up, as noted in the high-magnification image of NS-CD@gf_a900(h) as shown by the BET surface area and pore volume (Table 4.5). This may be due to agglomeration of CDs around the pores and edges of graphene sheet, hence restricting the access to some of the active sites within.

Table 4.5 BET specific surface area and pore volume for CD amount controlled samples.

	Specific surface area (m^2 g^{-1})	**Pore volume (cm^3 g^{-1})**
NS-CD@gf_a900(s)	545.12	3.07
NS-CD@gf_a900(h)	428.34	2.15

To evaluate the OER feasibility, all CD-containing samples were tested for OER activity in an alkaline solution - in the potential range of 1.2–2.0 V versus RHE at a rotation speed of 1600 rpm (Figure 4.23). Ir/C activity is obtained from literature[259] . E_{onset} values are all either very close to or less than 1.6 V. It is clear that NS-CD@gf_a900 sample has the lowest overpotential and the highest current response over the tested potential range, compared with other catalysts. E_{onset} and the potential at 10 mA cm^{-2} for a given catalyst (E_{10}) of NS-CD@gf_a900 are 1.52 and 1.68 V, respectively, compared to 1.48 and 1.58 V of Ir/C in 0.1 M KOH. Interestingly, the contribution of sulphur is apparent toward the OER performance. In CD@gf samples, the minor influence of sulphur only increases the activity of NS-CD@gf by a small amount, compared with N-CD@gf. However, after thermal treatments of the gel samples, a notable enhancement of NS-CD@gf_a900 OER activity is realised (30 and 60 mV difference in E_{onset} and E_{j10} compared to N-CD@gf_a900). The corresponding Tafel slope of NS-CD@gf_a900 (87.5 mV per decade) also confirms the best rate of OER against 460, 448, 208, 126, and 106 mV per decade of NS-CD, RGel, N-CD@gf, NS-CD@gf, and N-CD@gf_a900 catalysts, respectively.

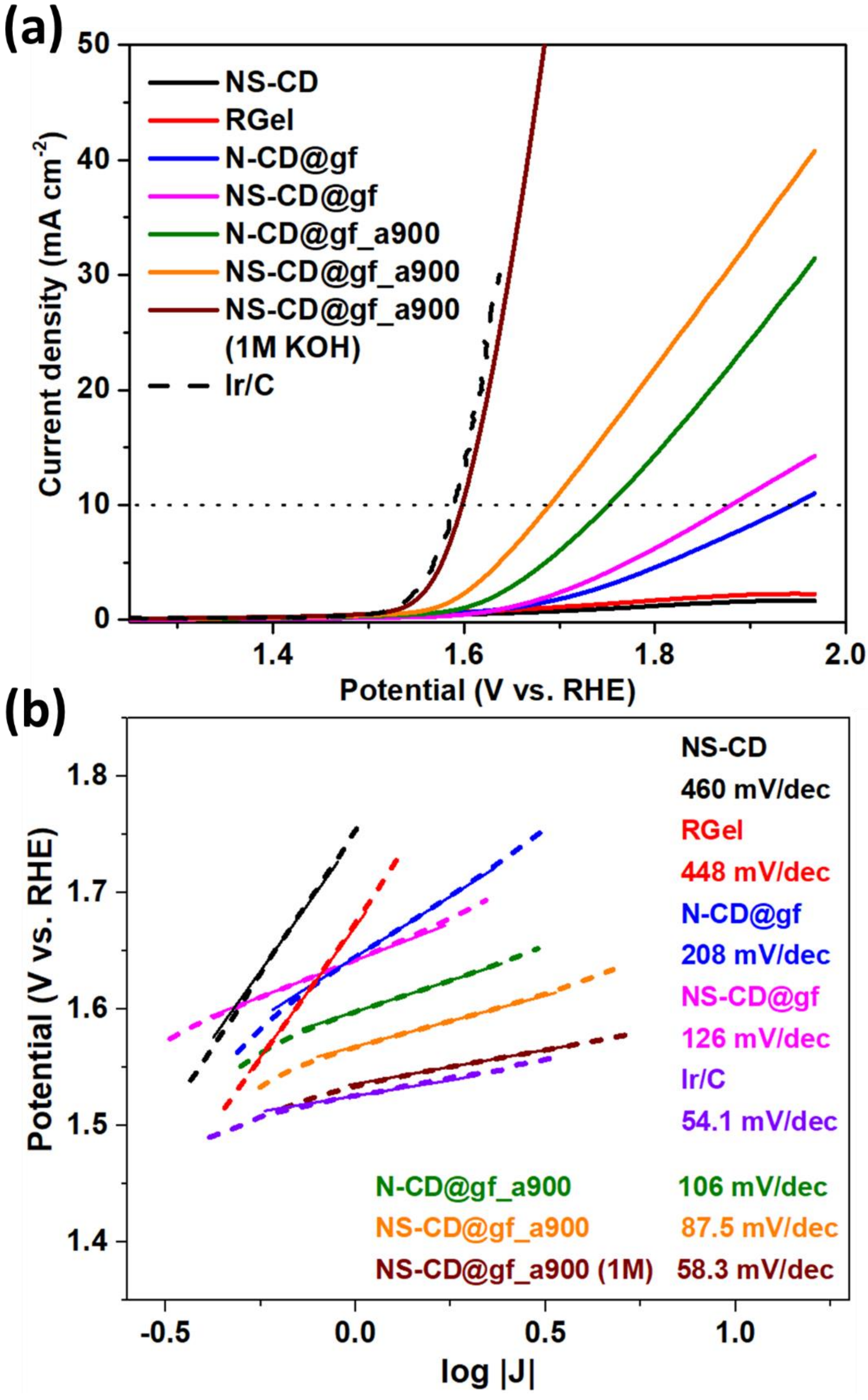

Figure 4.23 (a) Combined LSV curves for OER of all samples in O_2-saturated 0.1 M KOH at 1600 rpm. (b) Tafel plots for OER of all samples obtained from LSV curves.

A high-concentration alkaline electrolyte can promote OER processes as the concentration of hydroxyl ions increases. In 1.0 M KOH, NS-CD@gf_a900 exhibits exceptional OER activity with 1.49 V (E_{onset}) and 1.59 V (E_{10}), ≈100 mV less overpotential than at 0.1 M KOH solution, and comparable OER performance to that of Ir/C - also, very close Tafel value (58.3-54.1 mV per decade of Ir/C).

The influence of CDs and the dopant elements, N and S, has been investigated. Substituting heteroatoms (slightly different electronegativity compared to carbon) alters the surface charge densities of graphene. With higher electronegativity than carbon, nitrogen groups can draw charge density toward them from neighbouring carbons. The effect of the electron lone pairs on the graphitic and pyrrolic nitrogen (electron donating) together with slightly positive carbon sites makes oxygen adsorption more viable. In the case of sulphur, similar electronegativity to carbon leads to imbalanced orbital states, which contributes to high spin density of surrounding carbons[260]; leads to increase in the ORR activity compared to a pristine graphene. Other studies also suggest further reduction in adsorption energies for N, S dual doping where carbons located adjacent to graphitic N and thiophene S exhibit the maximum spin density - responsible for ORR activity. In contrast, OER activities are facilitated by pyridinic nitrogen (electron-withdrawing group) together with edge thiophene groups; the rate of adsorption of the negatively charged water oxidation intermediates (OH- and OOH-) is favoured[261, 262]. Heteroatom functional groups in CDs provide many catalytically active centres in given defect sites.

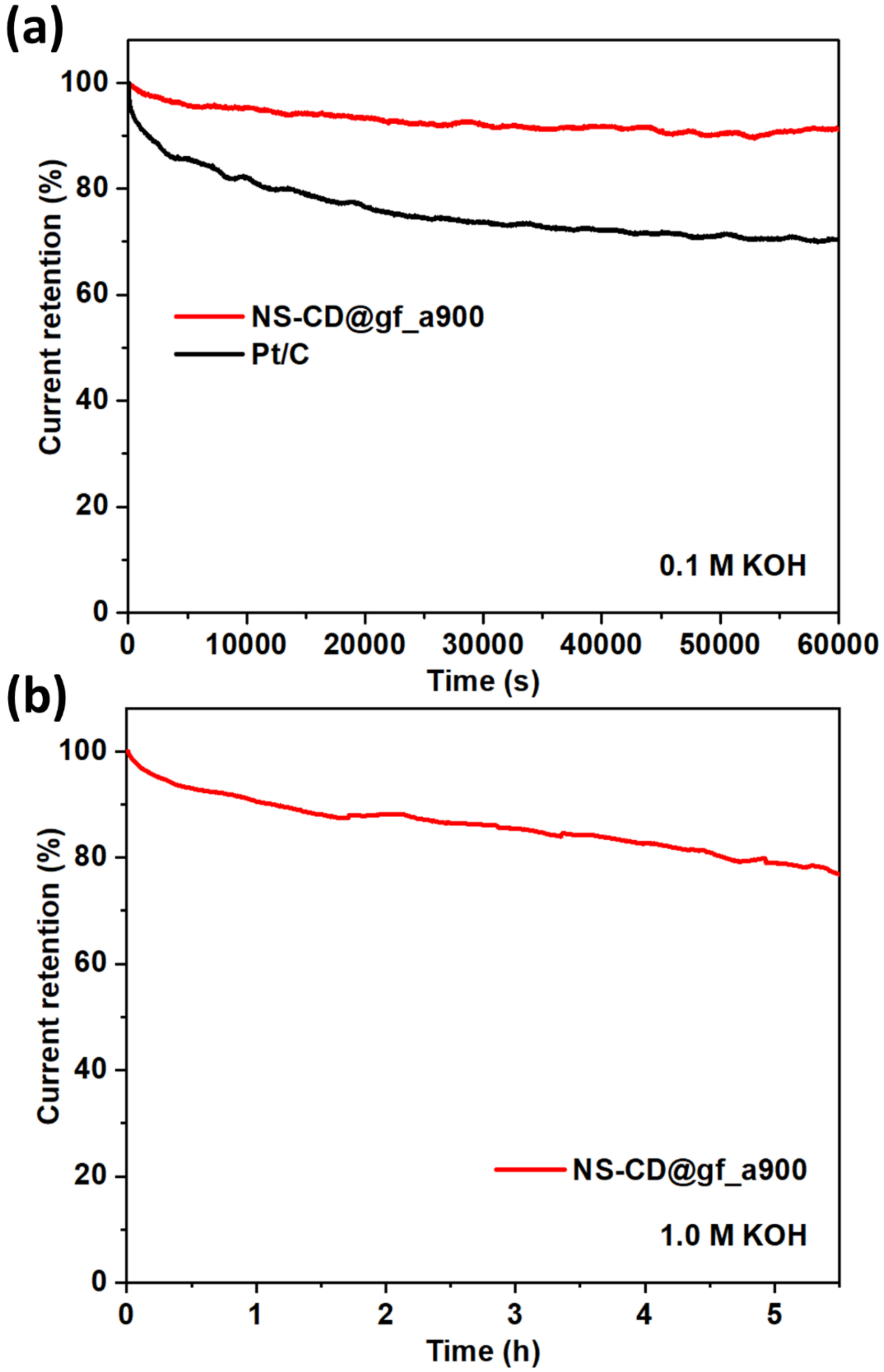

Figure 4.24 Chronoamperometric stability plot (current vs. time) of NS-CD@gf_a900 in (a) ORR, and (b) OER region at rotation speed of 1600 rpm.

Long-term ORR and OER current responses of the NS-CD@gf_a900 are obtained from chronoamperometric curves in Figure 4.24; NS-CD@gf_a900 is more stable than Pt/C with current retention kept to 88% compared to 73% after 60 000 s. This further suggests that CD embedment induces ORR capabilities with good regeneration of electrocatalysts under constant oxygen reduction - this is also the case for the stability of OER. However, at the higher OER potential region, oxidation of the carbon catalyst is inevitable with stability decrease to around 75% only after 5 h.

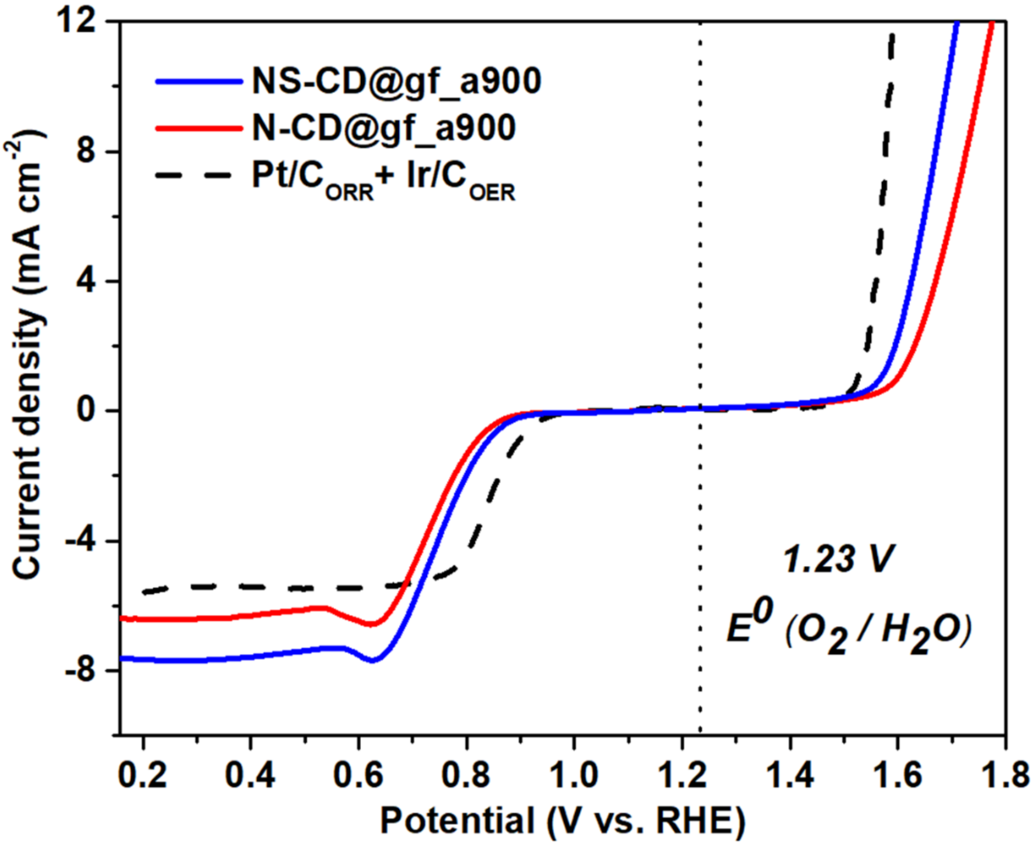

Figure 4.25 Combined LSV curves of N-CD@gf_a900, NS-CD@gf_a900, and conventional catalysts displaying the bi-functionality in water splitting (ORR/OER) region.

In Figure 4.25, the oxygen bi-functionalities of N-CD@gf_a900 and NS-CD@gf_a900 samples are evaluated against the results of the Pt/C + Ir/C pair. Overall performances of CD-embedded samples are slightly low on both ORR and OER compared to the combined noble catalyst. However, the ΔE values (potential difference between 3 mA cm^{-2}, ORR, and 10 mA cm^{-2}, OER) obtained are 0.99 V (N-CD@gf_a900) and 0.91 V (NS-CD@gf_a900) against the Pt/C + Ir/C (0.77 V). The value is further reduced to 0.82 V for NS-CD@gf_a900 if the OER result is from 1.0 M KOH.

4.3 Conclusion

In summary, an outstanding metal-free porous graphene framework with the embedment of heteroatom-doped carbon dots as bi-functional oxygen electrocatalysts for metal–air batteries has been developed via a facile and scalable hydrothermal approach and subsequent annealing process. The prepared sample, NS-CD@gf_a900, exhibited substantial increase in the catalytic behaviour (38% increase in current density) and stability (current attenuation of 12%) compared to the performances of benchmark oxygen electrocatalysts (Pt/C + Ir/C). The synergistic integration of dual N,S doping lowers the activation barrier for oxygen molecule adsorption on carbon for conversion processes to take place (evidenced by the difference between N-doped sample and N,S-doped sample). However, rather than occupying defect sites of highly porous graphene with a few number of dopants, embedding carbon dots provides numerous active centres, generated by nitrogen and sulphur species. This strategy of controlling the size/functional groups of carbon can be readily scaled up and applied to improve and develop cost-effective metal-free oxygen electrocatalysts to replace noble-metal catalysts for large-scale energy storage and conversion systems.

Chapter 5 : Two-dimensional carbon substrate as sole bi-functional electrocatalyst; Friedel-Craft assisted polymerisation of pyrene

5.1 Introduction

Oxygen electrocatalysis is an essential part of these technologies, such as fuel cells, electrolysers, metal-air batteries, and has been predominantly delivered by noble-metal-containing catalysts despite their inherent drawbacks (scarcity, cost, dissolution, leaching, and deactivation of catalyst)[263]. Transition-metal containing compounds (e.g. oxides, nitrides, sulphides, and carbides) have been widely investigated as replacements however, metal-based catalysts suffer from low selectivity, active-site poisoning, poor stability, and require carbon substrates[101, 264].

Graphene has been exploited in many electrochemical systems, in both non-precious metal-containing materials and metal-free frameworks, due to its chemical, electronic, thermal, and electrocatalytic properties[265, 266]. Typically, preparation involves harsh chemical oxidation of graphite to graphene oxide using concentrated acids followed by heteroatom doping via either hydrothermal or thermal reduction[156]. Although the procedure is widely carried out, non-selective oxidation reactions on the surface lead to random oxidation/doping sites, and defect/pore formation which cannot be controlled. Often, silica templates are used together with graphene oxide to create porous frameworks with micro-, meso-, and macro-pores, however post treatment processes possess environmental issues associated with HF acid etching to obtain the desired porosity[150, 267, 268].

Preparations of aromatic carbons via catalyst-assisted polymerisation is common with well-known procedures, such as Suzuki-coupling reactions, where organoboron species and halide species are polymerised assisted by palladium complexes. R. Fasel, K. Müllen, and their co-workers explored various bottom-up fabrications of atomically precise graphene nanoribbons and carbon allotropes using small aromatic monomers[269-271]; any sizes or iteration of graphitic carbon structures are synthesised varying the monomers used. Reagents for such reactions are widely available with mild reaction conditions and with a less toxic nature. However, palladium is scarce[272] and traces of metal species remain even after extensive work-up/removal processes[273-275]. Syntheses also involve multiple complex organic reactions. Recently, covalent organic frameworks (COFs), ordered 2D materials with controllable channels of pores throughout the structure, have been studied as a possible candidate for many energy applications including oxygen electrocatalysis[276-278]. This control of assembling desired frameworks can be achieved by varying precursors and linkers – molecules act as building blocks to generate specific sizes and pore dimensions. Despite the structure fine-tuning, catalysts preparations in inert conditions followed by complicated further treatments can restrict possible scale-up of catalyst syntheses. Thus, modification to the covalent link formation is necessary[279, 280]. Friedel-craft acylation processes are also capable of preparing macro-polymers using anhydrous aluminium chloride[281-283]. Use of $AlCl_3$ is simple, facile, and cheap as well as aluminium being a non-ORR/OER active catalyst[284, 285], unlike many precious metal catalysts.

In this chapter, ordered 2D metal-free carbon sheets were successfully synthesised via Friedel-craft assisted polymerisation followed by heat treatments. The monomer, pyrene, was carefully selected to form an aromatic carbon polymer with repeated domains and pores. Use of precious metals was avoided and the number of reactions involved was minimised to reduce the complication of materials syntheses. The properties of the as-prepared substrate were physically and chemically analysed to determine its potential to replace graphene/graphene oxide. Polymers were then annealed with dopants (N and S containing) to fabricate heteroatoms-doped aromatic polymers as possible oxygen electrocatalysts for cathode materials in metal-air batteries and fuel cells.

5.2 Results and discussion

5.2.1 Formation of 2D pyrene polymer

A possible/expected overall reaction scheme is illustrated in Figure 5.1. Following the literature reaction scheme[286], chlorination of pyrene was carried out by bubbling Cl_2 gas slowly to the pyrene and DCE mixture and then heated to 60 °C for 8 h with steady supply of Cl_2. The obtained CPy and pyrene were subjected to Friedel-Craft assisted polymerisation process assisted by the anhydrous aluminium chloride as a catalyst. As polymerisation occurs, the macro-polymeric nature of pyrene carbon polymer darkens the colour appearance of the powder (dark reddish brown/black shown in Figure 5.2). Fluffiness of the powder also illustrates the air pockets of the polymer formed by the repeated pores/defects.

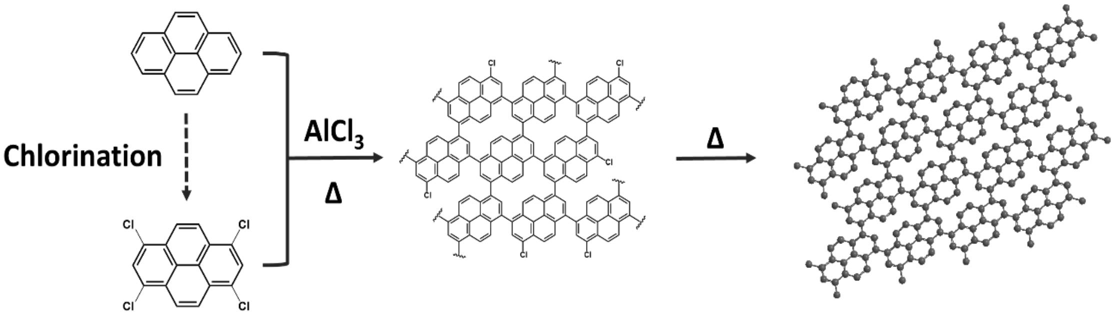

Figure 5.1 Schematic illustration of the formation of 2D porous pyrene polymer via thermal treatment (rPyG).

Figure 5.2 Photo of as prepared PyG with dark reddish brown/black colour.

5.2.2 Chlorinated-pyrene and pyrene polymer substrate

Tetra-chlorinated-pyrenes (CPys) were prepared in bulk and the chlorination process was first confirmed by ATR-IR (Figure 5.3). A strong peak, corresponding to C-Cl bond, was seen around 833 cm^{-1} to confirm a successful chlorination of pyrene[287]. Likewise, a weak C-H stretch signal just above 3000 cm^{-1} and a distinct single peak shown around 1940 cm^{-1} for C-H bending suggest that mainly the tetra-chlorinated CPy had been synthesised[288] – the intensity of the C-H stretch signal at around 3000 cm^{-1} will be higher for less Cl-substituted pyrenes (single-, bi-, or tri-chlorinated pyrenes) with more C-H groups in the structure and more characters of aromatic C-H bending/C=C stretching peaks will be present between 2000-1600 cm^{-1} with different C-Cl contribution[289]. However, since there are no additional separation or isolation processes involved, weak signals of less Cl-substituted pyrene[290] can be observed with characteristic peaks below

2000 cm^{-1} for CPy sample. Other observed peaks at ranges between 1600-1300 cm^{-1} and 1000-700 cm^{-1} correspond to C-H and C=C bending of alkanes/alkenes.

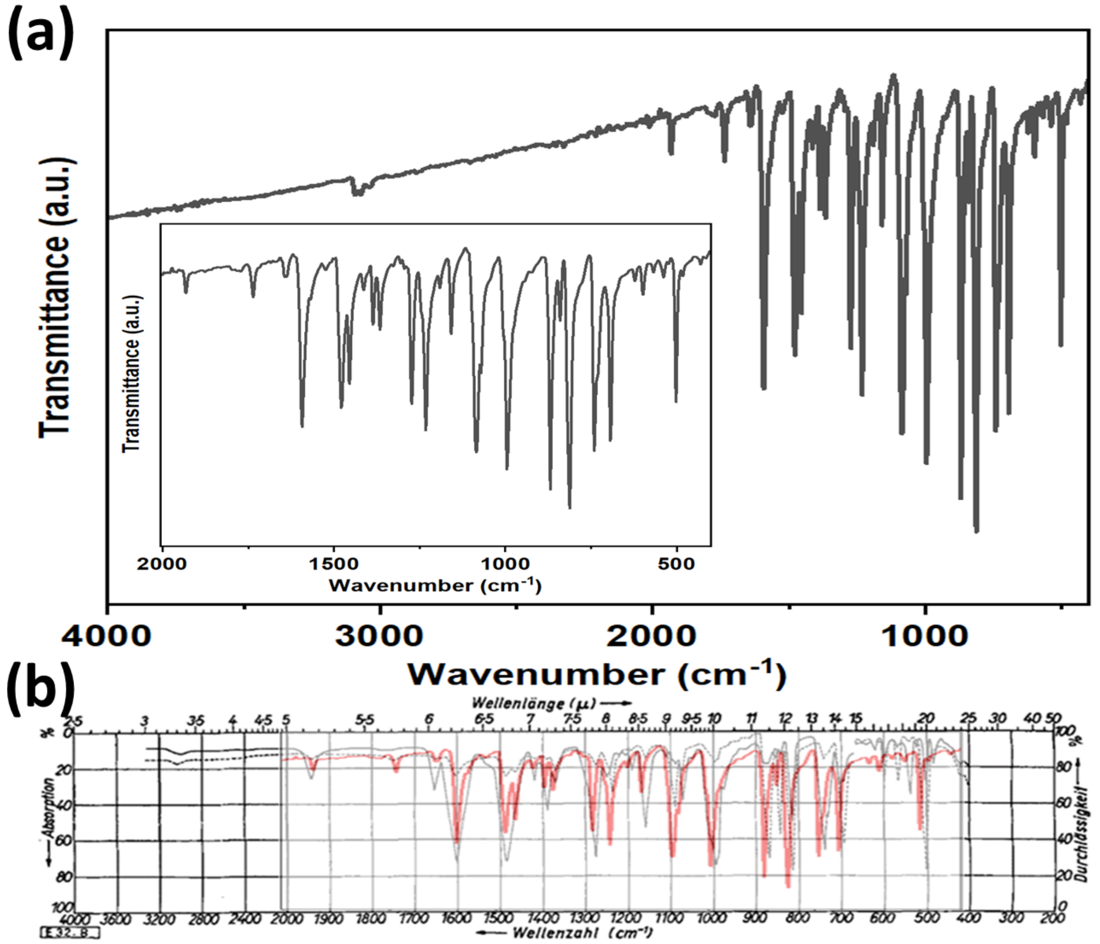

Figure 5.3 (a) ATR-IR spectra of CPy between 4000-400 cm^{-1}; the inset is a close-up between 2000-400 cm^{-1}. (b) Overlay of the CPy FT-IR spectra; the red line is the obtained experimental data and the black line is from the literature[289].

The tetra-chlorinated structure of CPy was further evidenced in the mass spectrum (Figure 5.4) where the main fragment peaks matched with the theoretical peaks of the tetra-chlorinated compound. Isotopic peaks of CPy were also observed with a small difference in m/z values – possibly from the presence of ^{13}C or ^{37}Cl isotopes. Traces of less-substituted pyrenes were also observed with different masses; the chlorination process is carried out in bulk which cannot be controlled in order to synthesise selective Cl-doped pyrene molecules. The m/z values of 190.92, 235.92, 307.85 may originate from chlorodimethyl-naphthalene (a fragment of pyrene), single-chloro pyrene, and tri-chloro pyrene. An additional separation step (such as column chromatography) can be considered here, however this will further complicate the overall process.

Morphologies of the pyrene polymer (PyG) and thermally reduced pyrene polymer (rPyG) were identified as 2D macroscopic sheets by TEM images (Figure 5.5). It is found that the flask used during the polymerisation is acting as a substrate for the polymer growth. The surfaces of both as prepared pyrene polymer samples were more rough and uneven compared to the smooth GO sheets. The thermal reduction process showed some degree of exfoliation of PyG to form rPyG with TEM images showing less contrast with fewer layers. High-resolution TEM images of rPyG at high magnification reveal the detailed surface morphology (Figure 5.6).

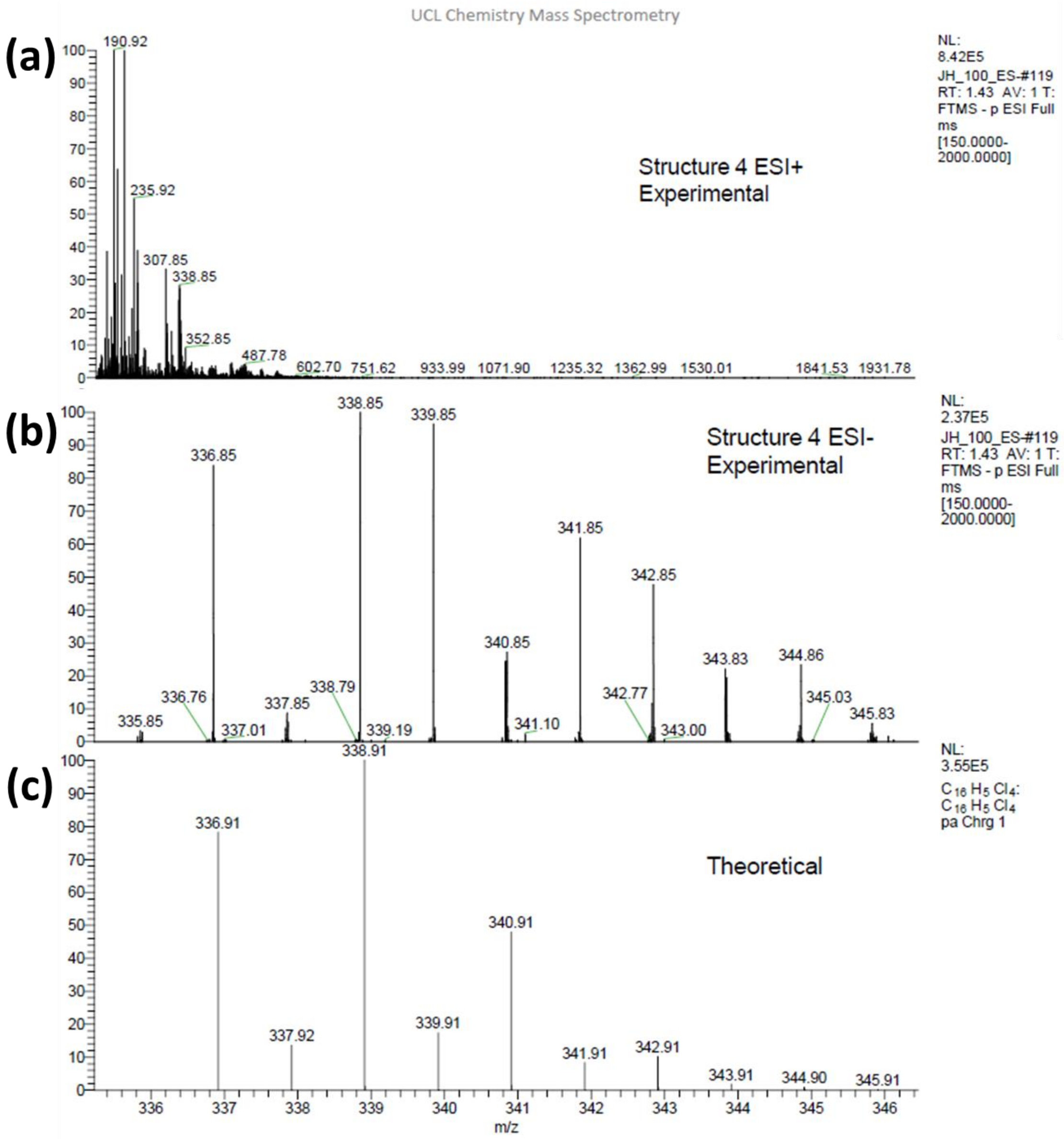

Figure 5.4 Obtained mass spectrum of CPy in (a) full range, and (b) close-up between 335-345 m/z. (c) Theoretical mass spectrum with expected mass.

During the polymerisation, a pyrene unit is bound to the neighbouring pyrene with a single sp^3 bond which is free to rotate about the axis. The formation of in-plane bonds leads to the expected 2D substrate however the out-of-plane linkage can result in domains/islands of interconnected pyrene structure, hence the roughness and unevenness of PyG and rPyG observed. Many pores in both PyG and rPyG stacked layers contribute towards the uneven surfaces as well. Steric hinderances of hydrogens may lead to slightly tilted chair or fan conformation of the polymer[291]. At high atomic-scale magnification, honeycomb structures, arising from fused aromatic carbon rings in pyrene, are found with empty voids (possibly repeated pores formed between pyrene units) suggesting successful Friedel-Craft assisted polymerisation of pyrene and CPy. As mentioned earlier, less chlorinated-pyrene (single-, bi-, and tri-chlorinated) monomers exist[290] from the synthesis of CPy, and these less-substituted variants lead to incomplete polymerisations contributing to the roughness of the substrate. With incomplete/termination of polymerisation processes with less Cl-substituted pyrenes, some of the observed pore sizes are larger than expected and may also have out-of-plane linkage around them. Possible variations of pyrene units are shown in Figure 5.7a. Note that larger units of pyrene (greater than 6, following similar patterns as in Figure 5.7a) may also exist and contribute to the surface roughness. In Figure 5.7b, possible locations of different sized pyrene units have been identified from the observed domains/islands of the rPyG substrate in the high-resolution TEM image and they are in close match with the dimensions of different pyrene units – dimensions of a single pyrene unit are displayed in Figure 5.7c. Domains/islands identification is only an assumption based on the dimensions of pyrene units and may not be the exact size or the orientation of pyrene units.

BET N_2 adsorption-desorption measurements of PyG and rPyG were obtained (Figure 5.8). BET specific surface area were calculated to be 154.17 and 257.15 m^2 g^{-1} and the total pore volume of 0.231 and 0.875 cm^3 g^{-1} for PyG and rPyG, respectively. For a 2D-sheet polymer, the measured surface area is reasonable (compared to CD-embedded graphene in Chapter 4) however, since there are no extreme structural changes via wrinkles/folding/twisting mechanism of the substrate, the obtained total pore volume is small compared to high temperature treated materials. Large extent of the pore volume contribution for rPyG is coming from pores sized around 5 nm or less in diameter and the value is much higher than the values seen with CD-embedded graphene samples. Small pores in PyG are not accessible (as seen in the pore-size distribution curve in Figure 5.8b) without the additional thermal reduction/exfoliation step. There was a very small contribution of meso-pores, sized >10 nm, for PyG sample.

XRD patterns of PyG and rPyG were compared against GO and rGO samples (Figure 5.9a). Except from GO with (001) plane at 10.2°, all displayed a broad peak around 22° corresponding to the (002) plane of reassembled graphitic sheets (graphite XRD reference shown in Chapter 3 and 4). Broad low intensity peaks were observed at lower angle, around 7° and 12°, for both PyG and rPyG. These peaks may represent a small fraction of irregular/amorphous pyrene units in a partially polymerised pyrene polymer (similar to reported heptazine units[292]). ATR-IR of PyG and rPyG, against CPy, is shown in Figure 5.9b. Compared to CPy, after the Friedel-Craft polymerisation and the thermal treatment, the intensity of the main C-Cl peak decreased as chlorine groups were removed from the substrate. Many aromatic and alkane/alkene C-C, C=C, and C-H contributions also decreased as meso- and/or macro-polymers of monomers were formed.

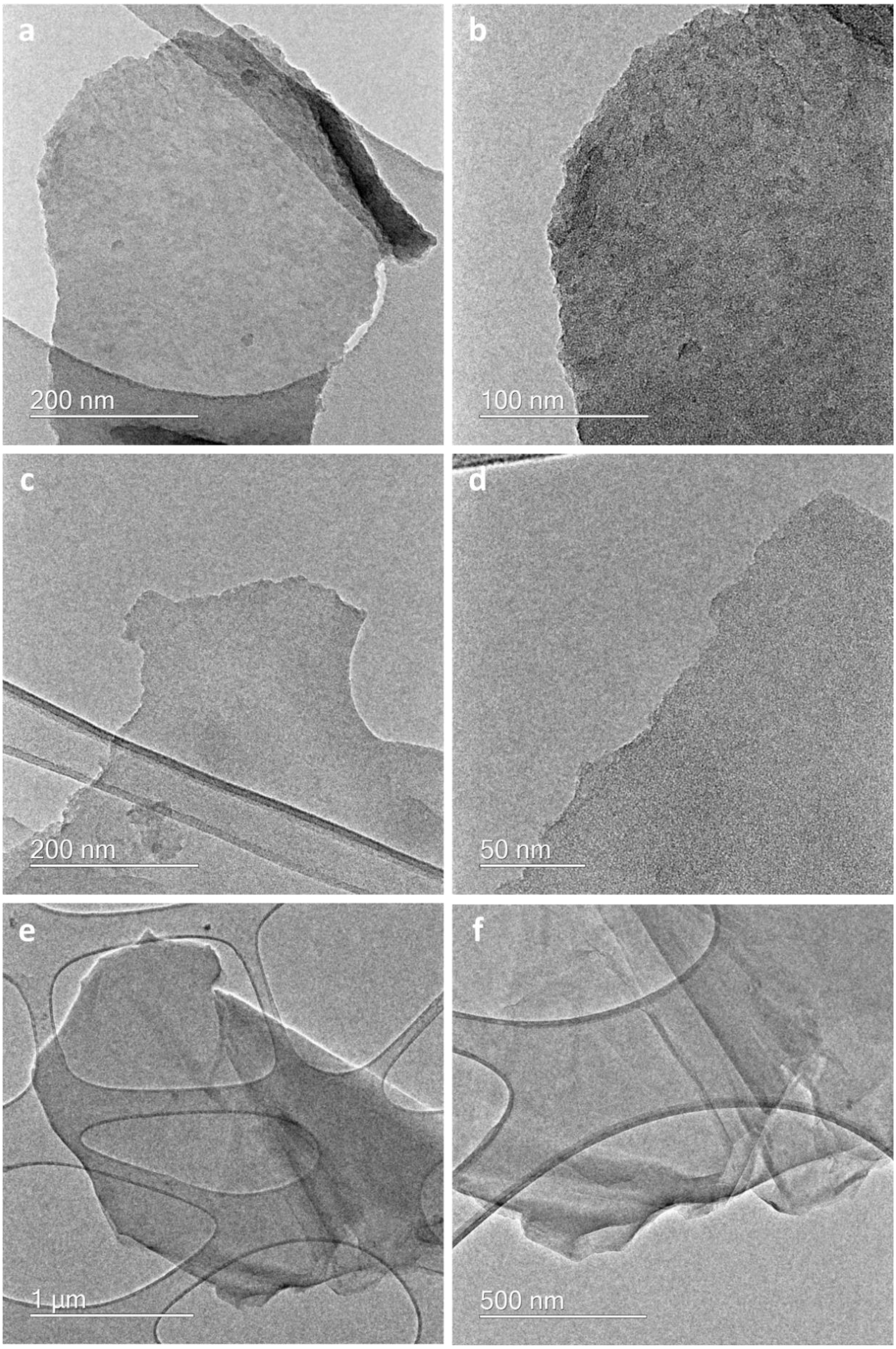

Figure 5.5 TEM images of (a),(b) PyG, (c),(d) rPyG, and (e),(f) GO at low and high magnifications showing different surface morphologies.

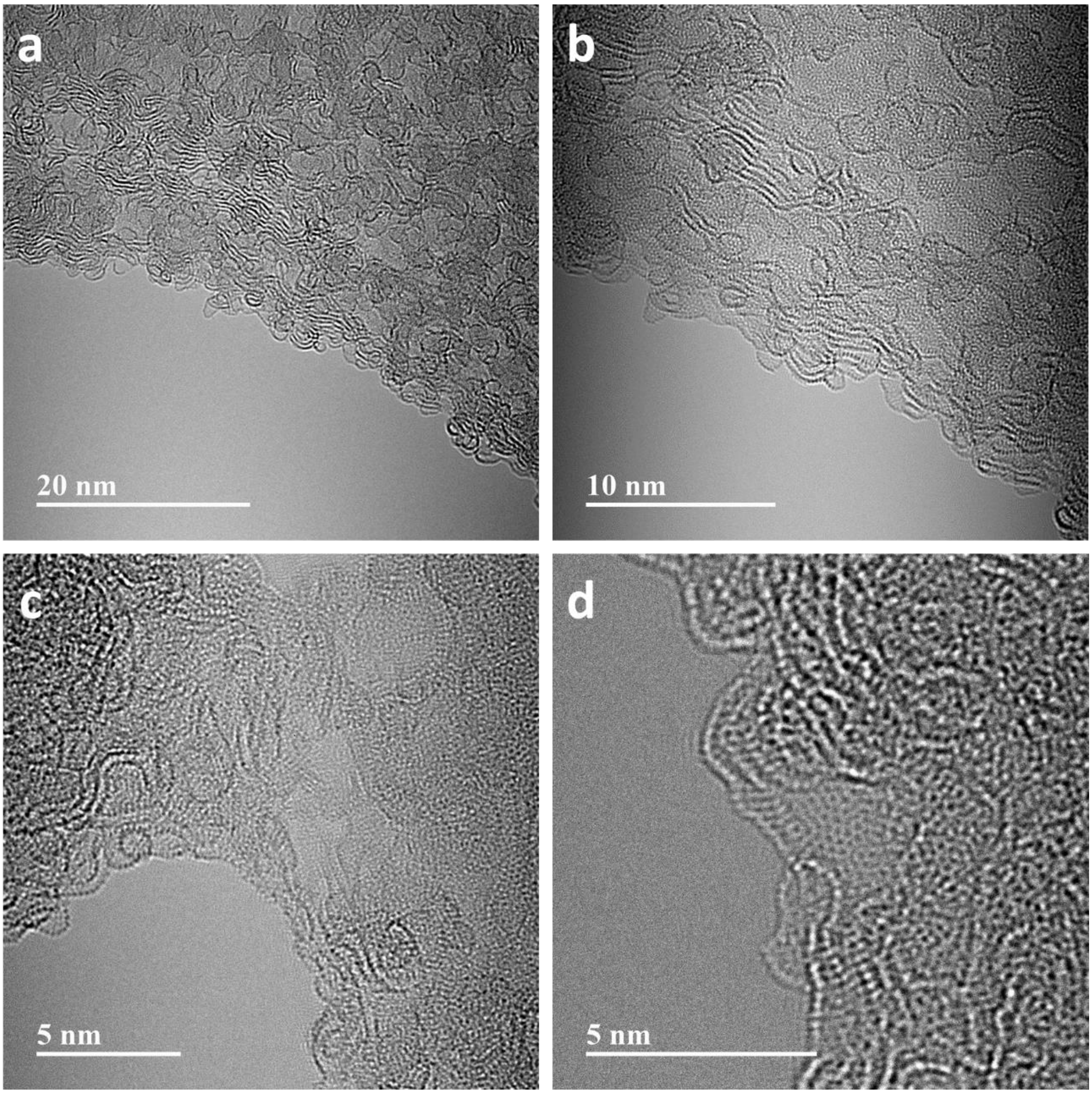

Figure 5.6 High resolution TEM images of rPyG at high magnifications showing surface roughness with islands/domains of pyrene units. Atomic resolution of rPyG shows honeycomb structures of pyrene units with voids (pores).

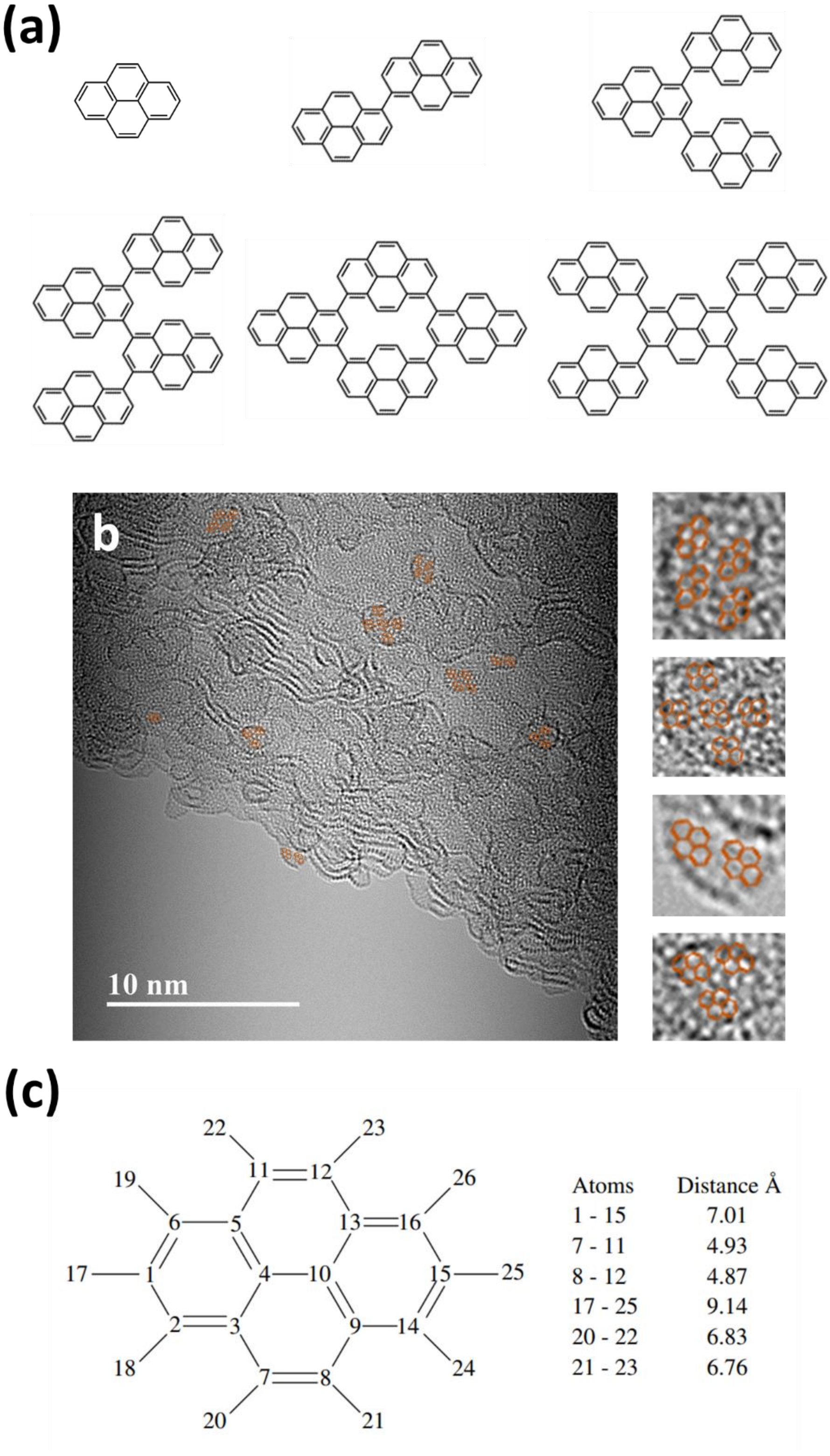

Atoms	Distance Å
1 - 15	7.01
7 - 11	4.93
8 - 12	4.87
17 - 25	9.14
20 - 22	6.83
21 - 23	6.76

Figure 5.7 (a) Molecular variations of possible pyrene units. (b) High resolution TEM image of rPyG with possible locations of pyrene units (inserted). (c) Dimensions of a single pyrene molecule.

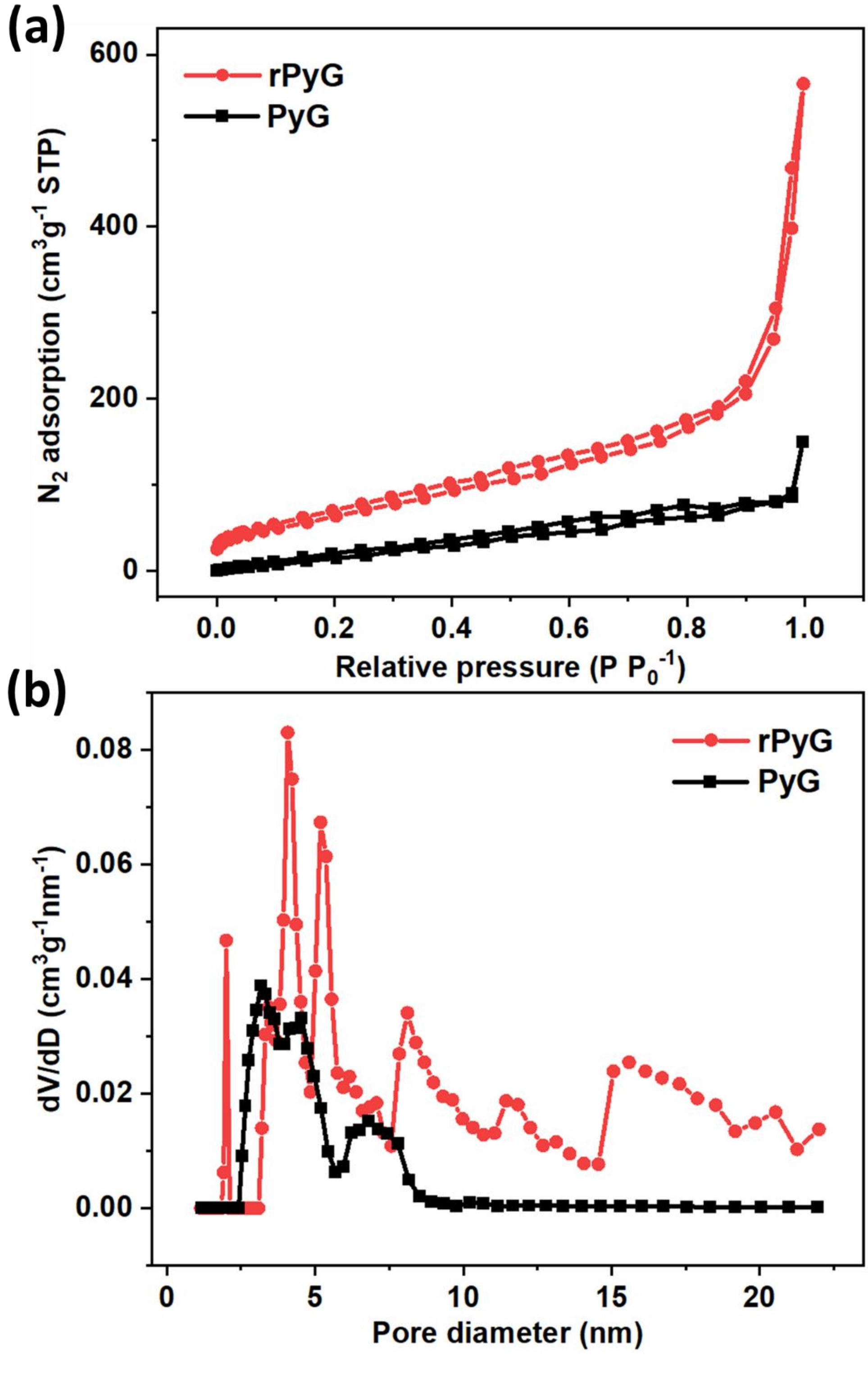

Figure 5.8 (a) BET N_2 adsorption-desorption isotherm of PyG and rPyG. (b) BET pore size distribution curve obtained using QSDFT and BJH methods for calculations.

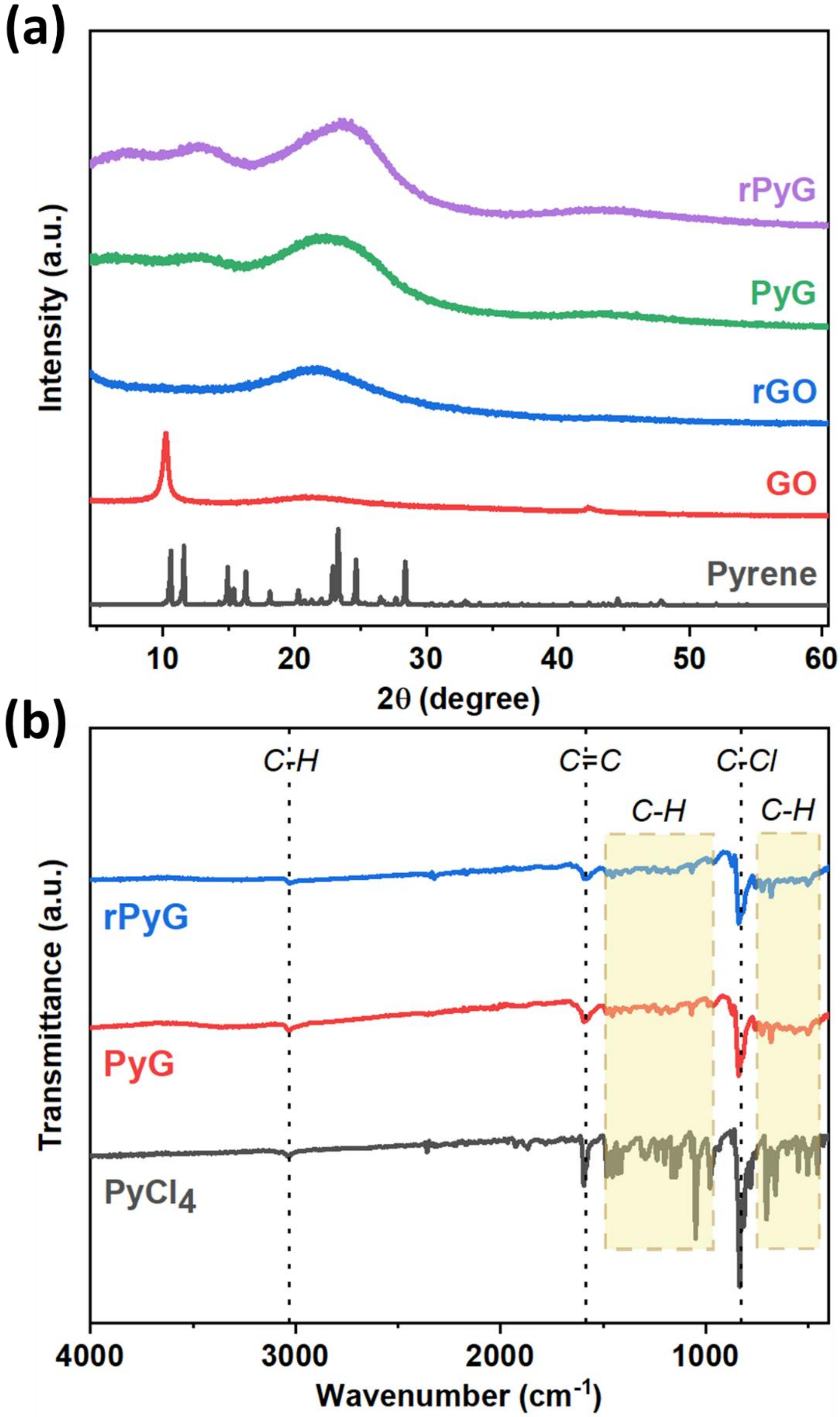

Figure 5.9 (a) XRD patterns of pyrene, GO, rGO, PyG, and rPyG.. (b) ATR-IR spectra of CPy, PyG, and rPyG between 4000-400 cm^{-1}.

Investigation of the defect chemistry was carried out using Raman spectroscopy in the D and G band regions between 1000-2000 cm^{-1} (Figure 5.10). As expected, rGO exhibited D and G band[184, 293] at around 1357 and 1593 cm^{-1} with I_D/I_G ratio of 0.86. Raman spectra of PyG and rPyG were almost identical to one another and displayed different distinctive bands – 1208, 1241, 1365, 1395, 1479,1580, and 1616 cm^{-1}, respectively.

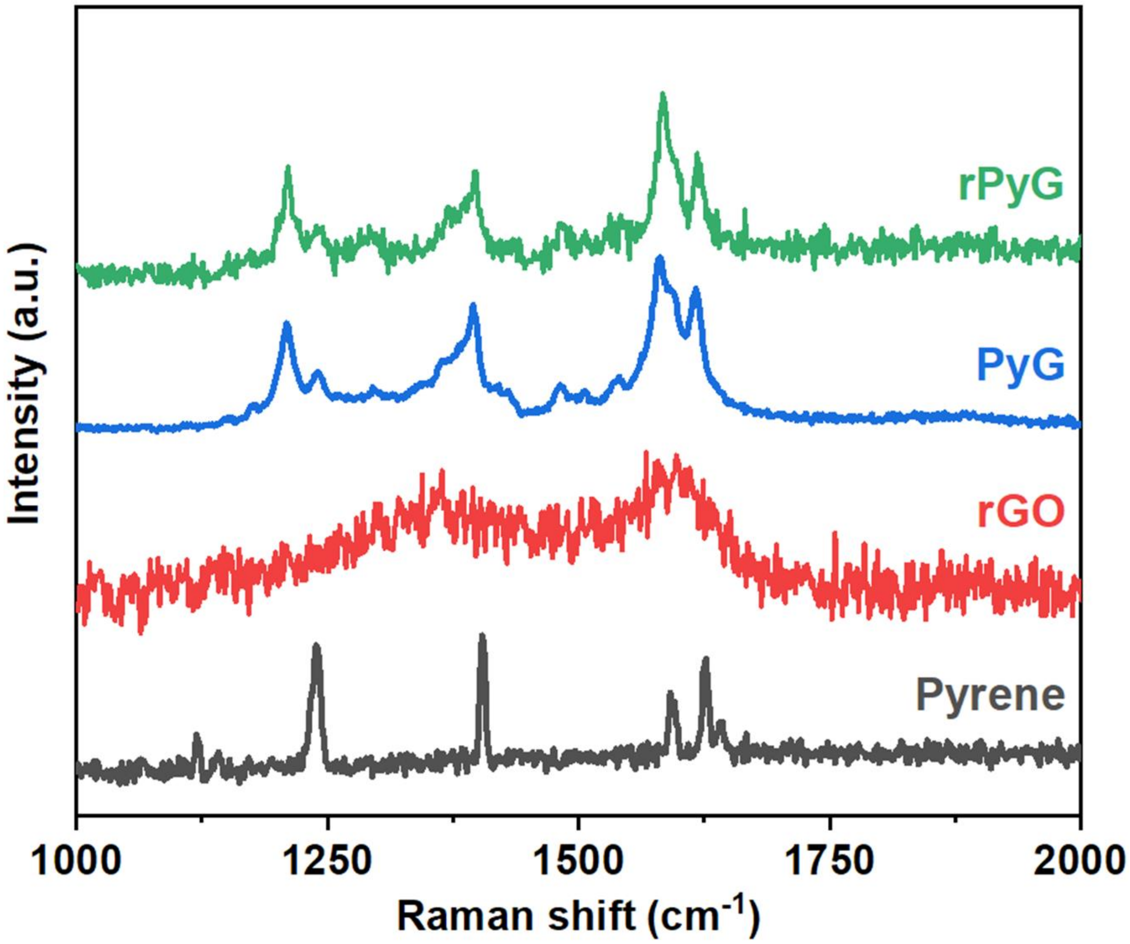

Figure 5.10 Raman spectra of rGO, PyG, and rPyG against pyrene in the region between 1000-2000 cm^{-1}.

Locations of these peaks matched with the pyrene reference sample but were broader, resulting from bulk polymerisation of pyrene and CPy. Bands between 1350-1500 cm^{-1} and 1500-1650 cm^{-1} can be identified as C-C stretching modes, similar to D and G bands of the rGO material as shown. The region between 1000-1300 cm^{-1} is attributed to the C-H in-plane bending vibrations, present in pyrene units with many interconnected sp^3 bonds[294-296].

XPS analysis provided the chemical composition of GO, rGO, PyG, and rPyG. Survey scans for all samples are shown in Figure 5.11 and the summary of all elemental composition of PyG and rPyG is tabulated in Table 5.1. After polymerisation process of PyG, there were still some Cl moieties seen, as expected. The concentration of Cl was approximately 2 at. % which dropped to 0.8 at. % after thermal treatment for rPyG. There were no traces of aluminium detected by the survey scans, hence there would be minimal contribution of Al to as-prepared PyG and rPyG samples – 0.1 at. % XPS sensitivity expected to have little influence on chemical and electrochemical properties of samples. A small increase in the concentration of O is observed for rPyG – the high resolution XPS scan of C 1s (Figure 5.12) exhibits a small round shoulder formed at higher binding energies (≥288 eV) which correlates to oxygen functional groups bound to carbon[297, 298]. It is assumed that the oxygen functionalities were introduced while Cl-groups were thermally removed during pyrolysis of the polymer.

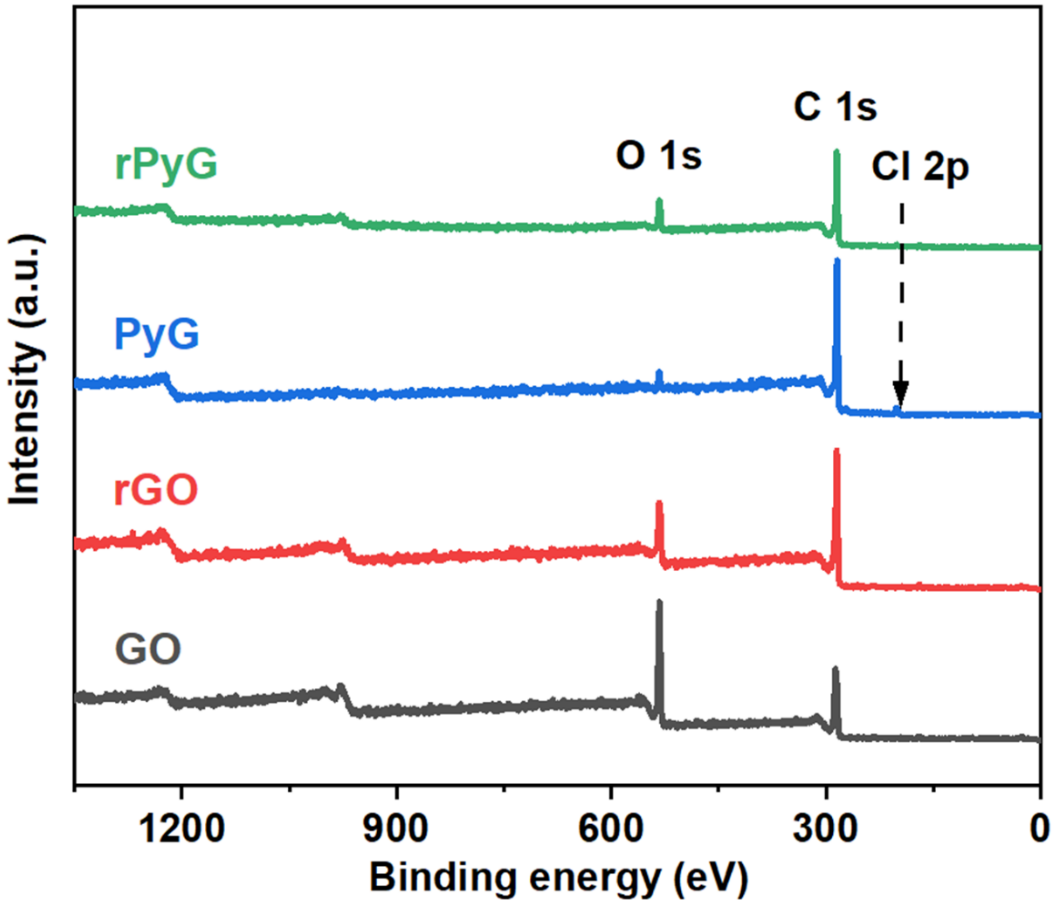

Figure 5.11 XPS survey spectra of GO, rGO, PyG, and rPyG samples.

Table 5.1 XPS elemental quantification of PyG and rPyG.

	C (at. %)	**Cl (at. %)**	**O (at. %)**
PyG	93.3	2.4	4.3
rPyG	88.1	0.8	11.1

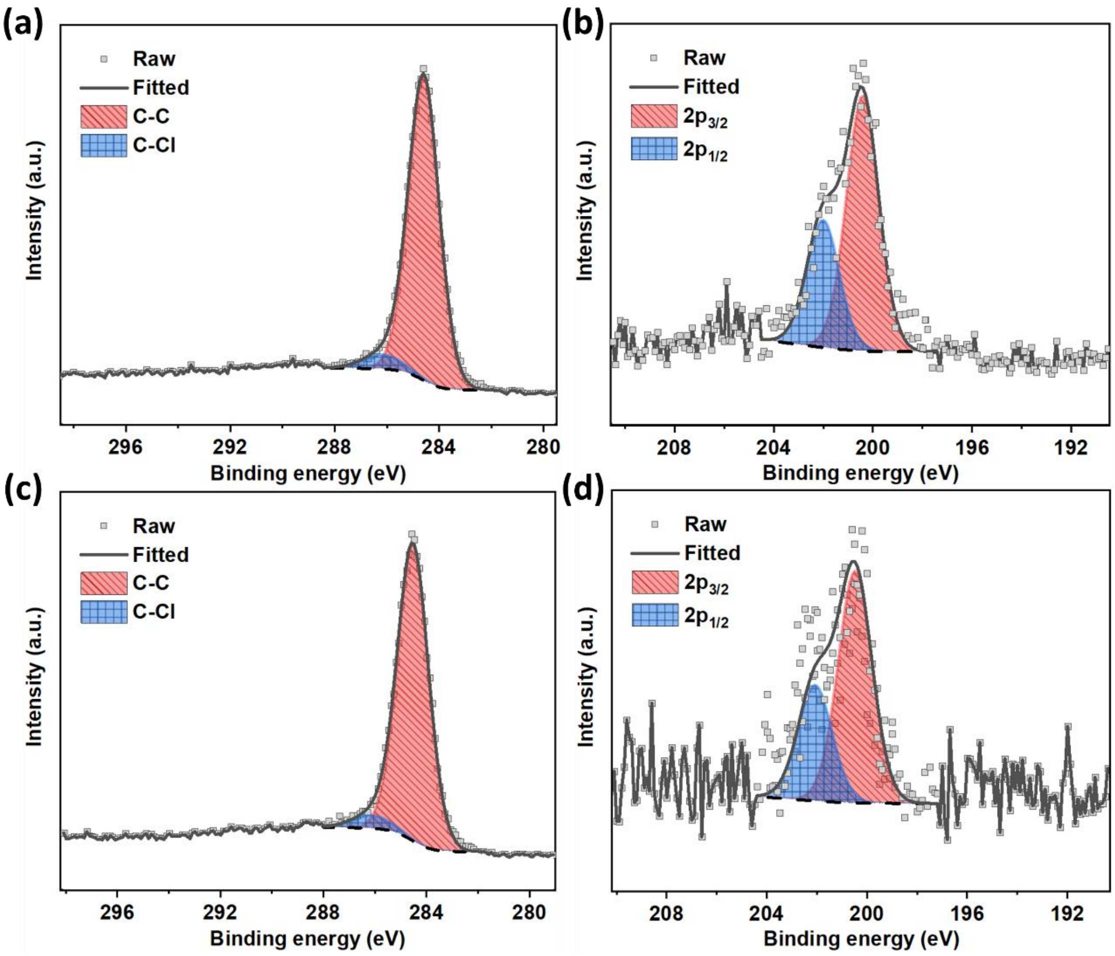

Figure 5.12 High resolution XPS spectra of PyG (a) C 1s, (b) Cl 2p. Spectra corresponding to (c) C 1s, and (d) Cl 2p of rPyG.

High resolution XPS C 1s scans of PyG and rPyG were identical with peaks at 284.7 and 286.1 eV attributed to C-C (combined carbon energy for aromatic rings) and C-Cl bonds. There were no obvious differences between the fitting of C-Cl contribution in both PyG and rPyG however, Cl 2p scans exhibited different binding energies.

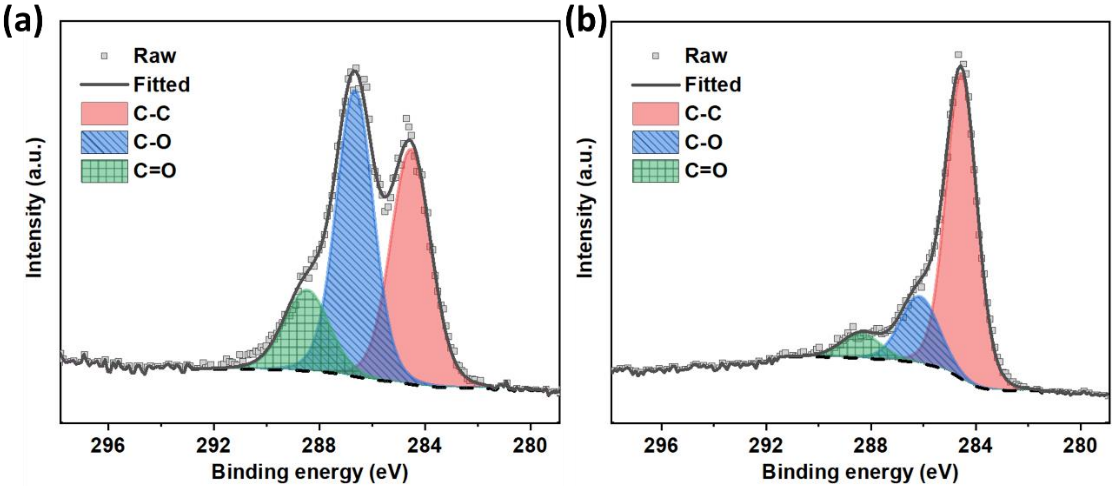

Figure 5.13 High resolution XPS C 1s spectra of (a) GO, and (b) rGO.

With the harsh oxidation step for GO, strong carbon-to-oxygen peaks were observed in the C 1s scan (Figure 5.13). The majority of the oxygen functional groups were removed after deploying thermal reduction to form rGO; C-O bonds and C=O bonds eliminated and released as CO and CO_2 gases[200]. As seen from the C 1s of PyG and rPyG, there were no oxygen species present; this may be either the oxygen gas in the instrument chamber or entrapped in pyrene polymers given off during the XPS measurement.

5.2.3 Oxidation of pyrene polymer to form porous substrate

Structural and chemical modifications of PyG are necessary to utilise pyrene polymers as a potential oxygen electrocatalyst – the remaining concentration of Cl and bulk structures of polymers reduce overall conductivity[299] and limit oxygen diffusion[300]; an increase in porosity and highly active electrocatalytic centres are required. Figure 5.14 illustrates the preparation of highly porous pyrene polymers via harsh acid oxidation of the substrate followed by high temperature annealing.

As prepared PyG was oxidised in concentrated nitric acid and was heated to 80 °C for 8 h. After neutralisation to obtain the etched pyrene polymer, it was subjected to annealing/doping process at 900 °C under N_2 gas flow for 3 h.

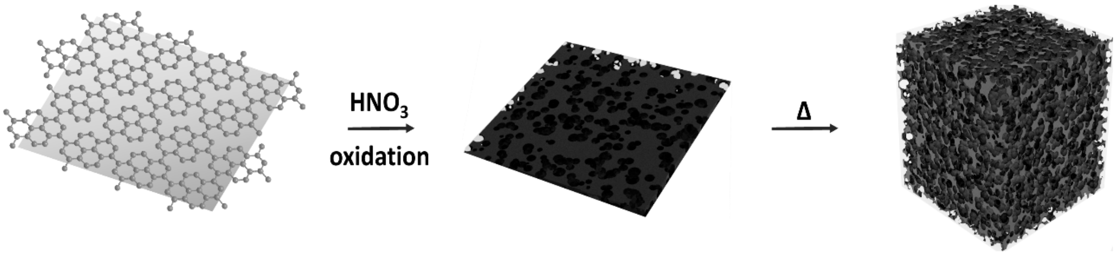

Figure 5.14 Schematic diagram illustrating the preparation of oxidised pyrene polymer (PyGO) and annealed highly porous pyrene polymer (NSPyGO).

From the obtained TEM images of PyGO (Figure 5.15), the strong acid etching of the polymer substrate is apparent with randomly formed rips and tears. The surface morphology of PyGO is completely different to those of PyG and rPyG (previously shown in Figure 5.5). As a conductive substrate, rips and tears of PyGO may not be desirable as structure defects will undeniably influence the electronic/electrical conductivity and resistance (important for some certain applications) however, in electrocatalysis, especially with metal-free carbon materials, some degree of structural imperfections (in both micro and macro-scale) is necessary to promote electron donations/withdrawals for catalytic reactions as well as diffusion of gas molecules/ions[65, 301]. Harsh oxidation with concentrated acid damages the carbon sheets and form defect sites.

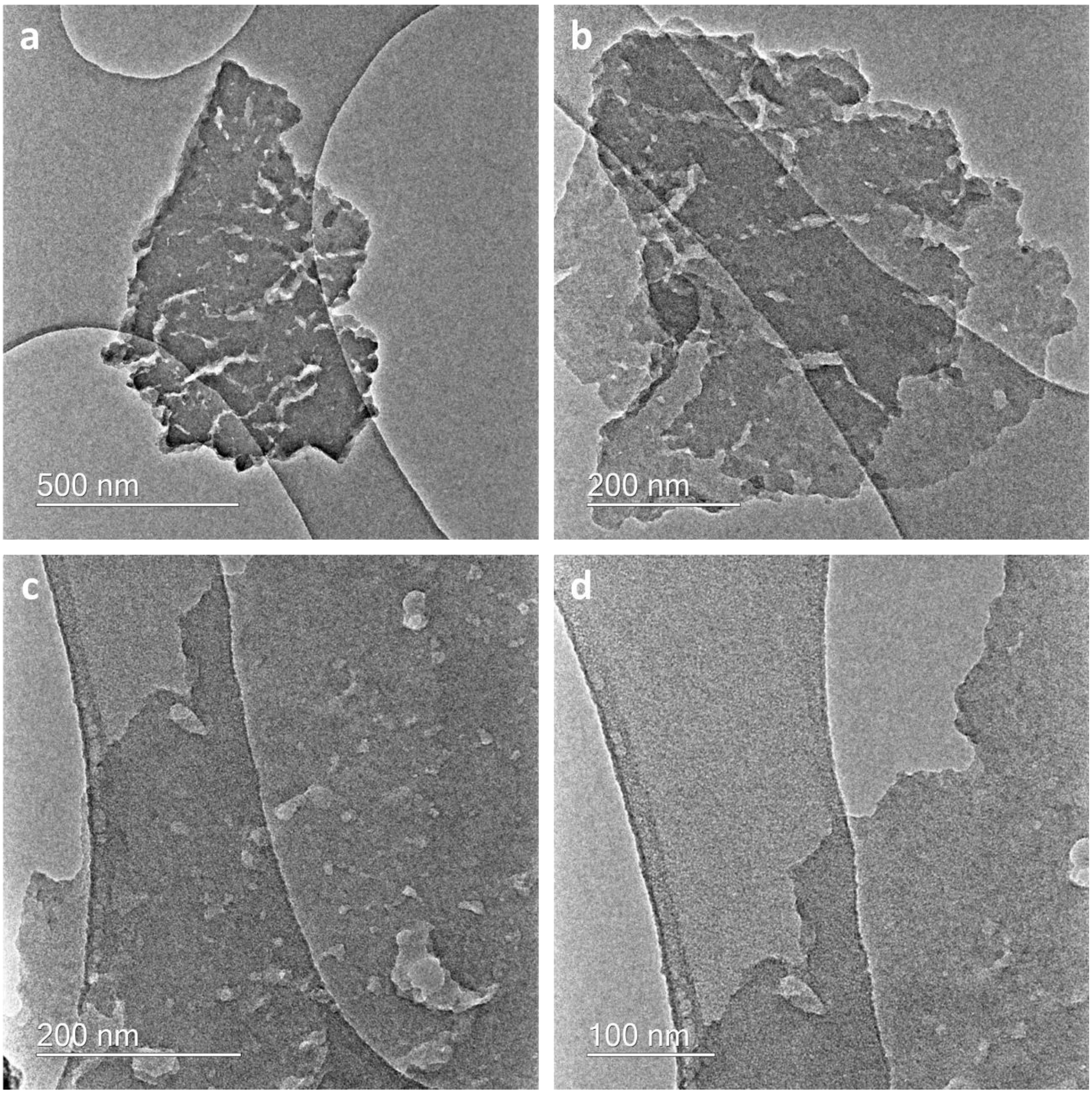

Figure 5.15 TEM images of PyGO at different magnifications.

Substantial differences are observed after structural transformations of pyrene polymers via high temperature annealing (NSPyGO shown in Figure 5.16); an extremely porous morphology was seen in the TEM images of NSPyGO sample. A honeycomb structure, observed in the high magnification images, implies that the polymer still retained its graphitic-like nature. Low contrast of the substrate also suggests that the folded and twisted structure of pyrene polymer is only a few layers. Visible pore sizes are considerably smaller than the pores revealed in NSPyG and NS-CD@gf_a900 samples (from Chapter 4) in the TEM images in Figure 5.17. The ordinary folding/twisting mechanism of smooth 2D carbon sheets lead to relatively porous substrate with removal of unstable functional groups and breakage of some weak sp^3 bonds[302, 303]. At high carbonisation temperature, as a result of harsh oxidation process, the exhibited rips and tears of PyGO fragment to generate a much-refined microporous media. When the substrate is bulky (with multiple layers), it is difficult to promote folding/twisting mechanisms to form porous media; NSPyG exhibits a less porous nature, prepared from bulk polymer, PyG (compared to using oxidised PyGO sample). Harsh oxidation step may assist the formation of highly porous substrate. Many macro-pores are observed in the NS-CD@gf_a900 sample due to thermal assisted structural alterations of exfoliated graphene oxide.

Carbon phases of annealed and heteroatom-doped samples, NPyG, NSPyG, NPyGO, and NSPyGO, were confirmed by XRD with observable (002) peaks at around 22.3° (Figure 5.18a). Compared to bulk untreated (PyG) and low temperature treated polymers (rPyG) as seen in Figure 5.9a, high carbonisation pyrene samples do not display the broad, low intensity peaks at the lower angle (7-12°). Most of the irregular pyrene units and partially polymerised regions may have reassembled at high temperature into an ordered graphitic-like structure. The graphitic nature was also verified by the presence of distinct D and G band in Raman spectra (Figure 5.18b). The bending and stretching modes of C-H, observed in the pyrene reference, disappeared and only D and G bands were detected[235] just like the rGO sample shown in Figure 5.10. The I_D/I_G ratio of NPyGO and NSPyGO were calculated to be 0.92 and 0.93; as a result of porosity and defect sites in the structure.

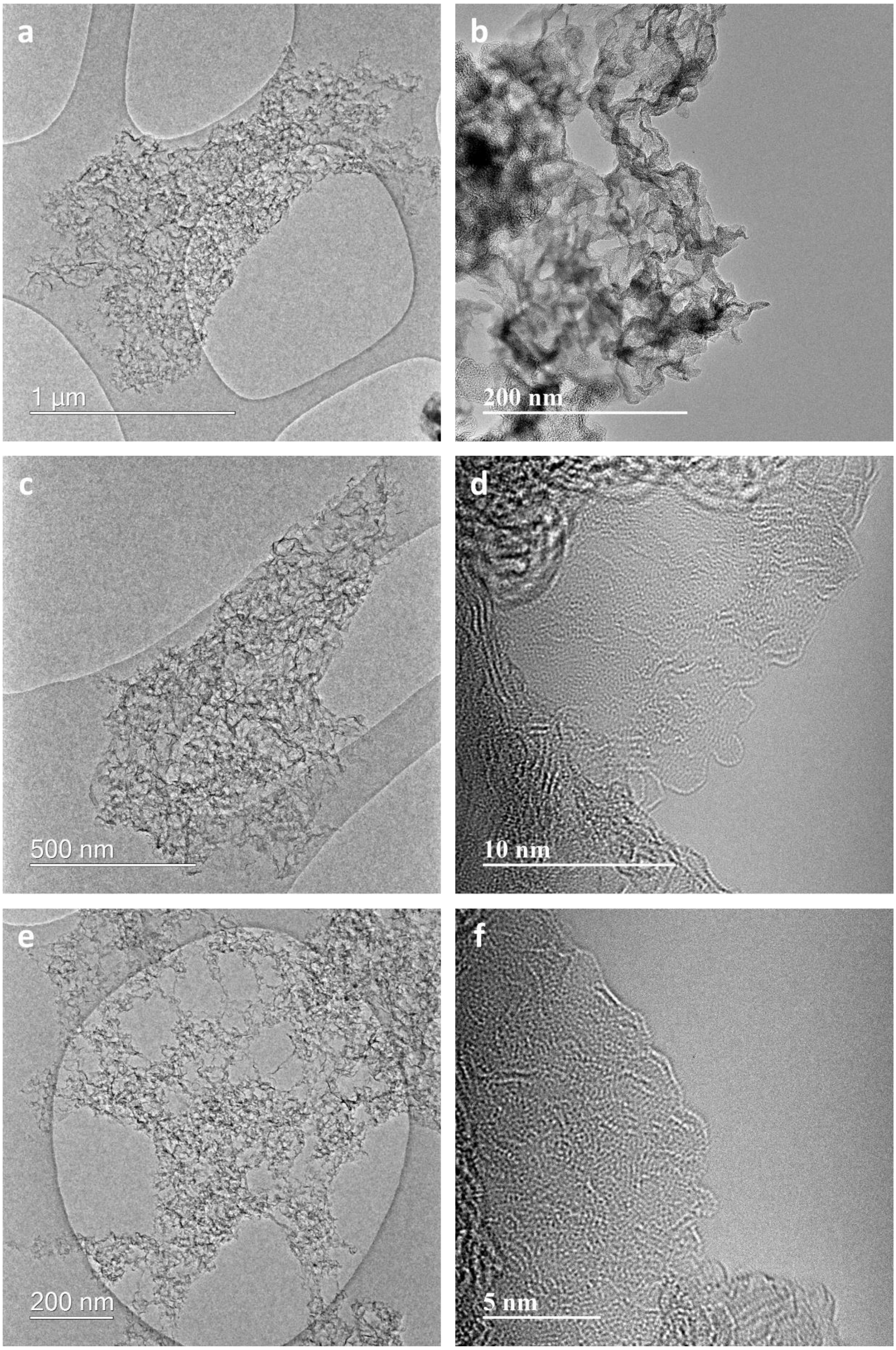

Figure 5.16 TEM images of NSPyGO at various low magnifications (a),(c),(e) and high-resolution TEM images at high-atomic resolution magnifications (b),(d),(f).

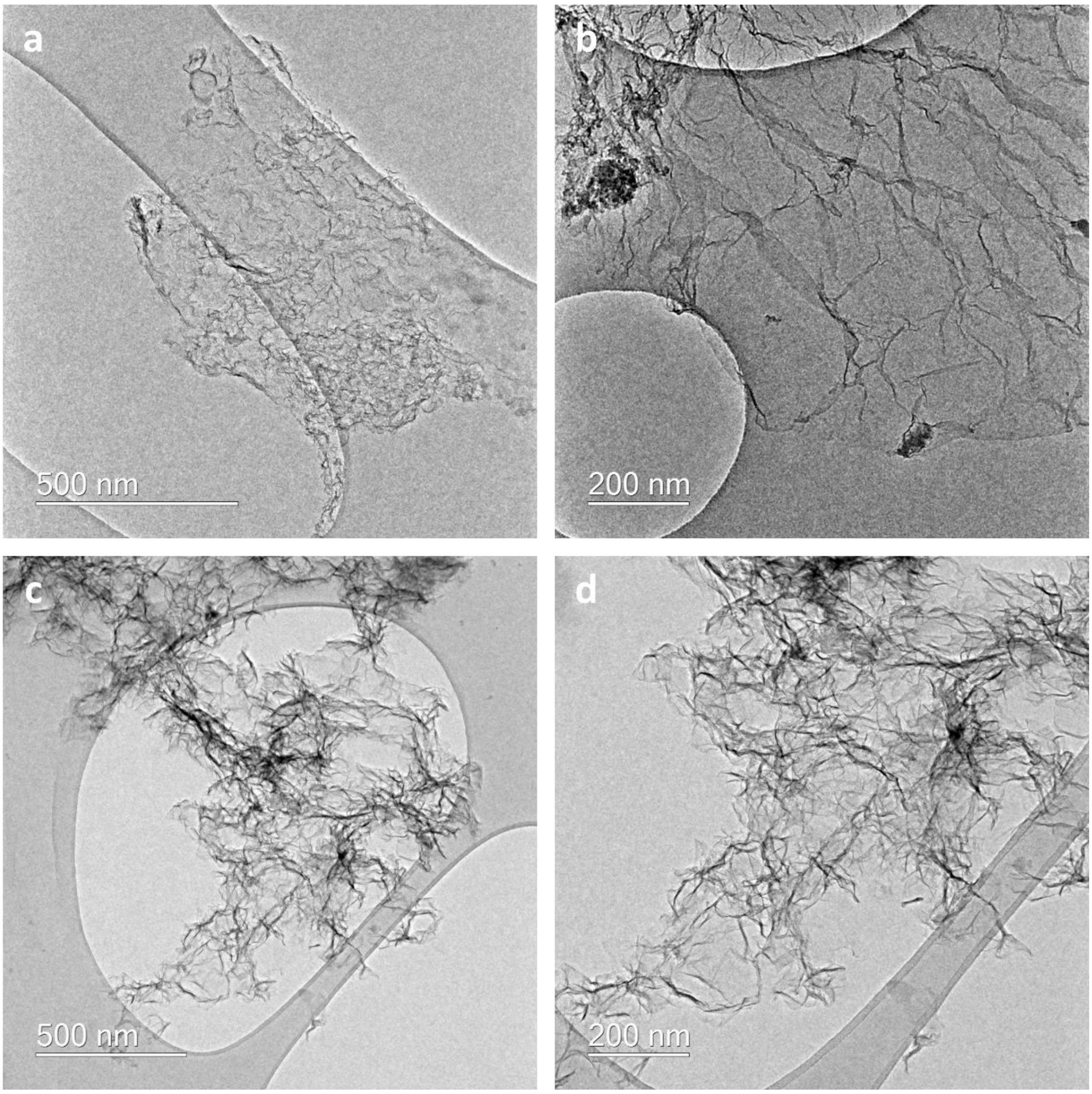

Figure 5.17 TEM images of NSPyG at (a) low and (b) high magnifications. TEM images of NS-CD@gf_a900 sample (prepared as mentioned in Chapter 3) at (c) low and (d) high magnifications.

Very low intensity D and G characters were shown with PyGO sample, suggesting the oxidation/etching process removes a lot of sp^3 contribution of the formed pyrene polymer. NPyG and NSPyG samples also exhibited similar Raman spectra with only D and G bands; ratios were 0.88 and 0.91, again slightly higher with N and S doping.

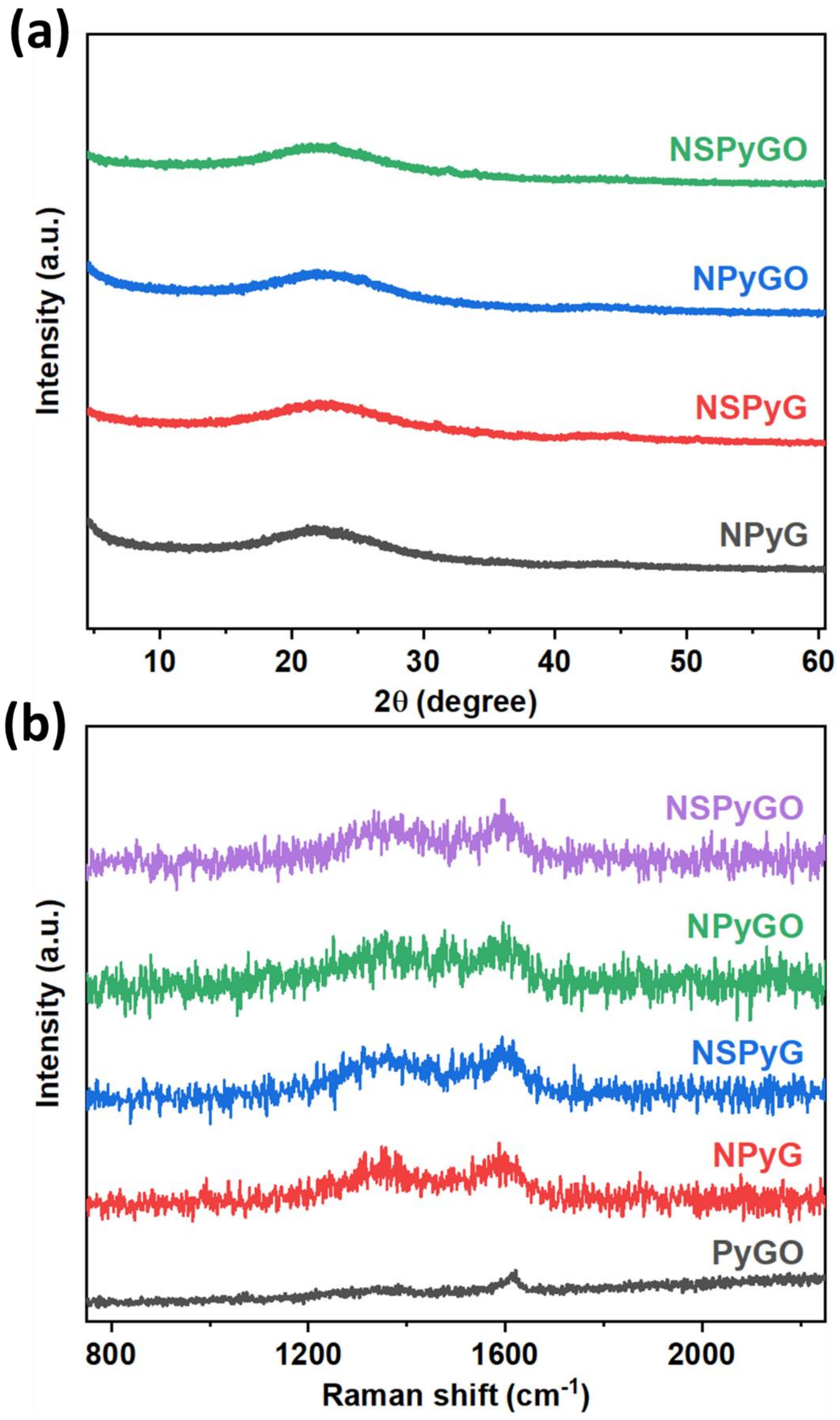

Figure 5.18 (a) XRD patterns of NPyG, NSPyG, NPyGO, and NSPyGO, the carbonised/heteroatom-doped samples. (b) Raman spectra of PyGO, NPyGO, and NSPyGO.

No Cl was detected for all sample in both XPS survey and in high-resolution Cl scans (Figure 5.19). Hence almost all Cl moieties have been removed either by thermal cleavage or N-, S- dopants substitution reactions during annealing which can also increase the conductivity of the substrate. The summary of all elemental composition of annealed/doped samples is presented in Table 5.2. Unlike the hydrothermal syntheses where reagents are efficiently mixed in-situ with solvents, polymers and dopants are dry-mixed prior to the thermal/doping process. This was to minimise/prevent the formation of oxygen functional groups. Doping concentrations of N and S in pyrene samples are not high; particularly, doping on bulk polymers, NPyG and NSPyG, less than 1 at. % of the nitrogen are observed. A higher observed concentration, around 4-5 at. %, of exhibited heteroatoms for annealed oxidised polymers (NPyGO and NSPyGO) may be due to more reactive sites provided by the polymer oxidation. Nitric acid assisted polymer oxidation not only provide fragmented substrate for improved gas diffusion, but also more reactive centres to promote heteroatom doping.

High-resolution C 1s spectra of NSPyG, NSPyGO (Figure 5.20), NPyG, and NPyGO (Figure 5.21) all exhibited similar peak shape; dominant C-C/C=C peak for aromaticity followed by C-to-heteroatom peak, and oxidised carbon (C=O) peak. Again, the same trend in peak shape was observed for N 1s spectra for all samples. Due to high temperature carbonisation/doping process, contribution of graphitic-N was higher than the pyridinic-N. In some cases, pyrrolic-N peaks were found but the energy mostly overlapped with both pyridinic- and graphitic-N and were omitted.

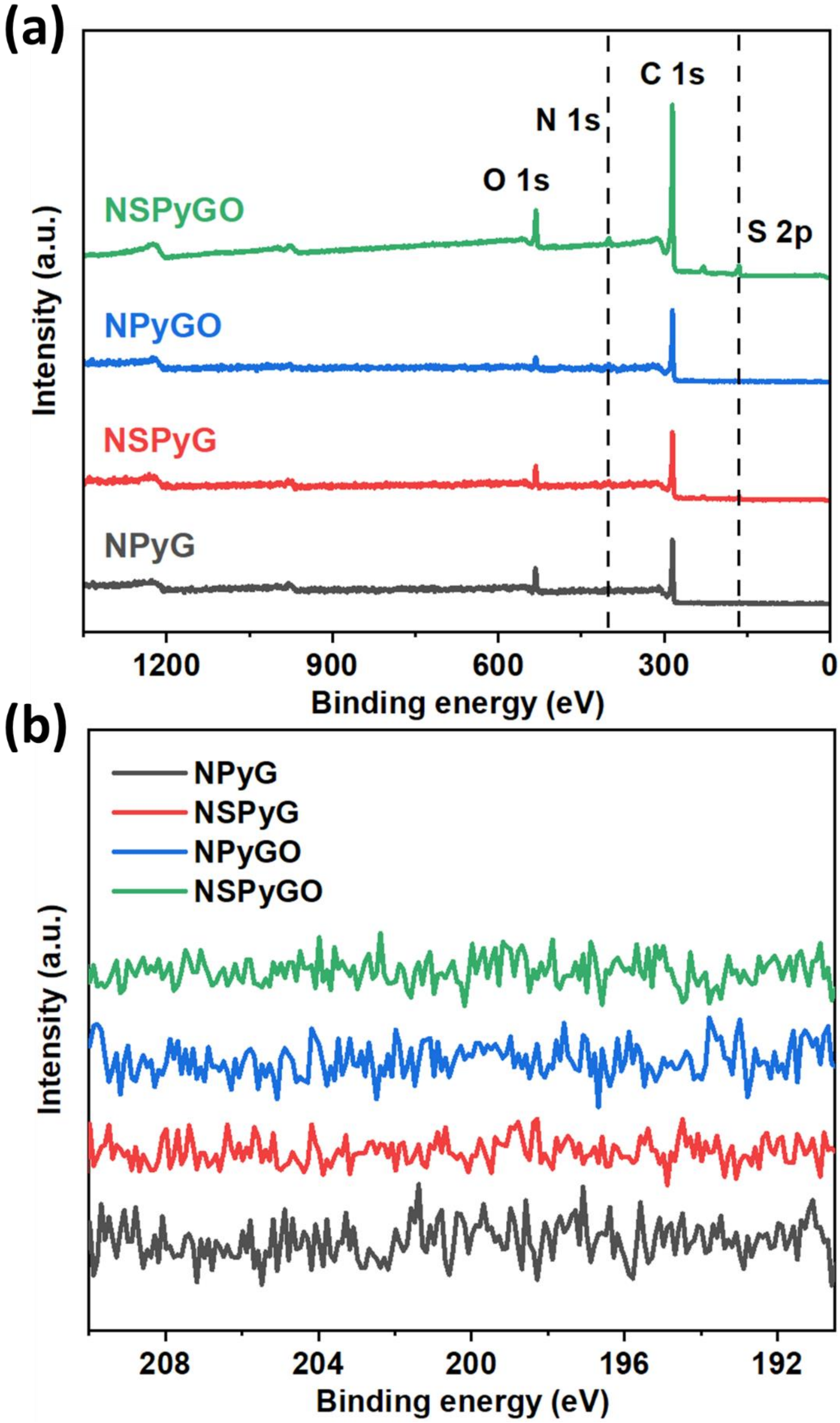

Figure 5.19 (a) XPS survey spectra of NPyG. NPyGO, NSPyG, and NSPyGO. (b) High-resolution Cl 2p scans of all annealed samples showing no signal.

Table 5.2 Obtained XPS elemental quantification for all annealed doped-pyrene polymers.

	C (at. %)	**N (at. %)**	**S (at. %)**	**O (at. %)**
NPyG	88.9	0.5	—	10.6
NSPyG	88.4	0.8	2.0	8.8
NPyGO	89.3	4.7	—	6.0
NSPyGO	85.8	4.3	4.1	5.8

Energies of the observed oxidised-N for all samples were not fitted to the high-resolution analyses as it is difficult to distinguish the low contribution of oxidised-N against the background signal. Sulphur scans of NSPyG and NSPyGO displayed 2 environments: aromatic 5-membered-ring thiophenic S and oxidised sulphonic S groups[240, 242].

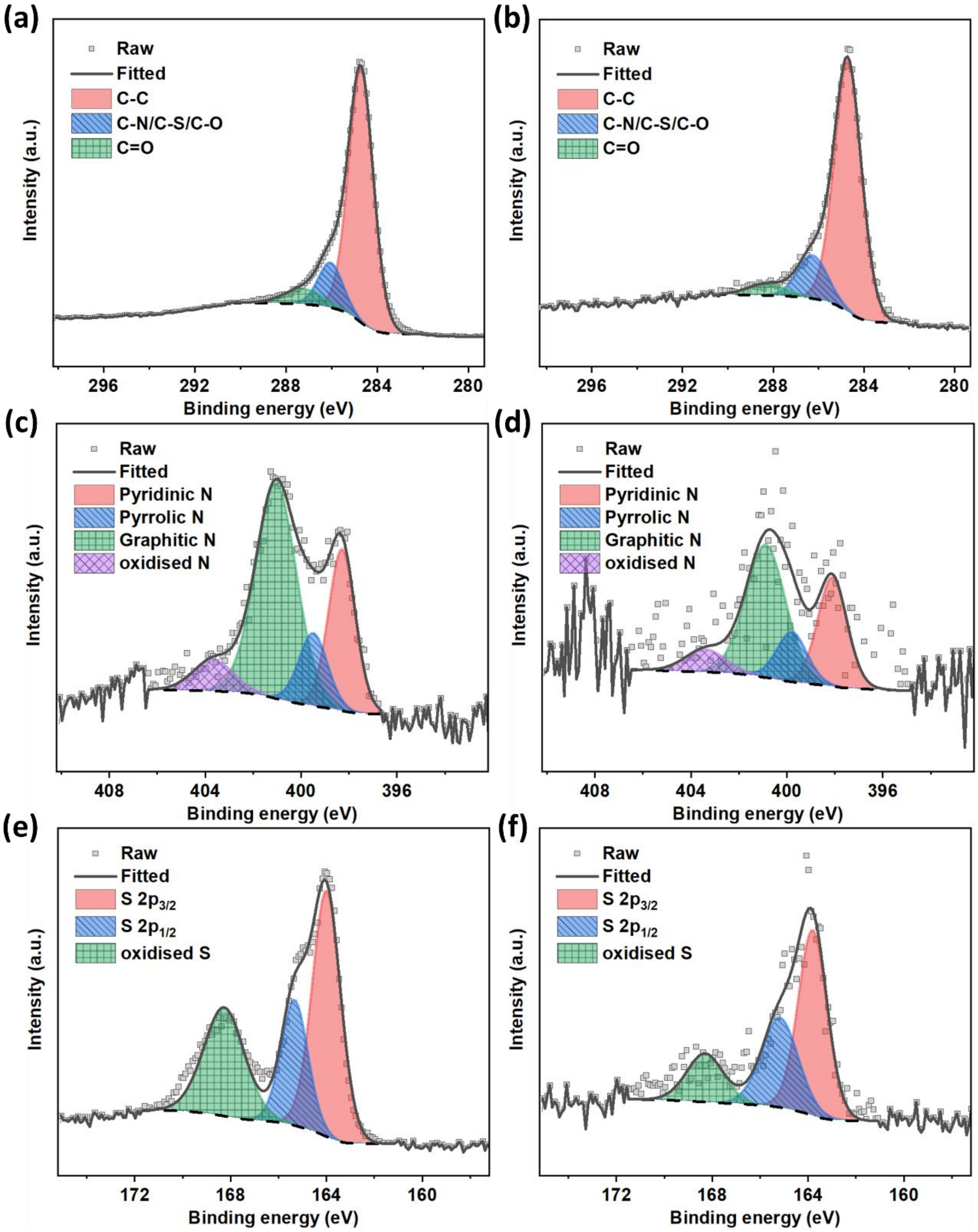

Figure 5.20 High resolution XPS spectra of (a) C 1s, (c) N 1s, and (e) S 2p of NSPyG and (b) C 1s, (d) N 1s, and (f) S 2p of NSPyGO.

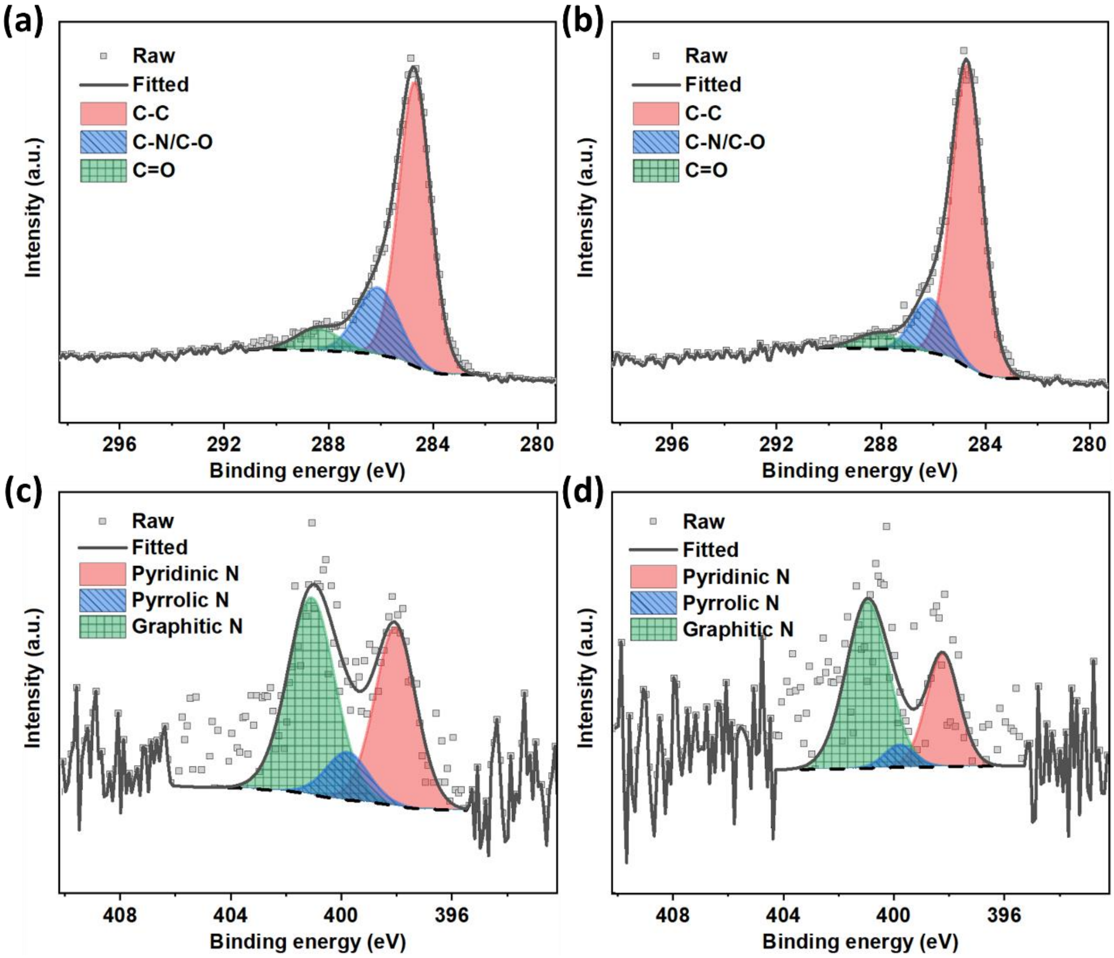

Figure 5.21 High resolution XPS spectra of (a) C 1s, and (c) N 1s of NPyG and (b) C 1s, and (d) N 1s of NPyGO.

5.2.4 Oxygen reduction reactions of highly porous pyrene polymers

All samples are used directly as synthesised and electrochemically tested to understand the potential as the ORR catalyst. The ohmic potential drop of the system has not been applied to any of the test results (not iR-corrected)[201]. CV scans of all samples are measured in O_2-saturated 0.1 M KOH electrolyte (Figure 5.22). Oxygen reduction peaks were shown at 0.69, 0.78, 0.79, 0.84, and 0.88 V vs. RHE for PyGO, NPyG, NSPyG, NPyGO, and NSPyGO, respectively. Compared to the CV oxygen reduction peak of Pt/C at 0.82 V (displayed in Chapter 4), there is roughly 60 mV reduction in overpotential for NSPyGO sample which implies better kinetics[304]. NSPyG and NPyGO also exhibited higher reduction potential than the Pt/C sample. The LSV curves of NPyG and NSPyG (Figure 5.23a) exhibited highest current densities of 2.92 and 3.40 mA cm^{-2}, which are slightly lower than 4.48 mA cm^{-2} of N, S-doped graphene hydrogel annealed at 900 (NS-Gel_a900 sample in Chapter 4). The half-wave potentials ($E_{1/2}$) were 0.66 and 0.70 V for NPyG and NSPyG. Lower potentials of doped PyG samples suggest that the electronic conductivities are not as good as in graphene samples. However, even with doped-PyG samples, dual doping of N and S enhanced current responses of the NSPyG sample (increased onset potential, half-wave potential and the total current density) compared to single-heteroatom-doped NPyG. For the oxidation process, NPyGO exhibited 0.8 V $E_{1/2}$ value (100 mV reduction compared with the un-oxidised samples) and a slight increase in maximum current density to 3.68 mA cm^{-2}. The reduction in overpotential suggests that with oxidation of pyrene polymers, the active sites are easier to access for oxygen molecules, hence providing improved kinetics. The NSPyGO sample exhibited outstanding electrocatalytic oxygen reduction activity in 0.1 M KOH with both the current density and kinetic responses (E_{onset} and $E_{1/2}$) very close to Pt/C. Kinetics in electrocatalysis is governed by the adsorption ability of the electrode material, usually greatest with metallic species. Despite being metal-free, NSPyGO exhibits E_{onset} of 0.98 V and 5.08 mA cm^{-2} current density (compared to 0.98 V and 5.55 mA cm^{-2} of Pt/C) – only 8.5% difference in observed current densities and very close to the maximum theoretical current density of 5.71 mA cm^{-2} at 1600 rpm (using K-L relations in the Experimental section). $E_{1/2}$ of NSPyGO and Pt/C are 0.86 V and 0.84 V vs. RHE.

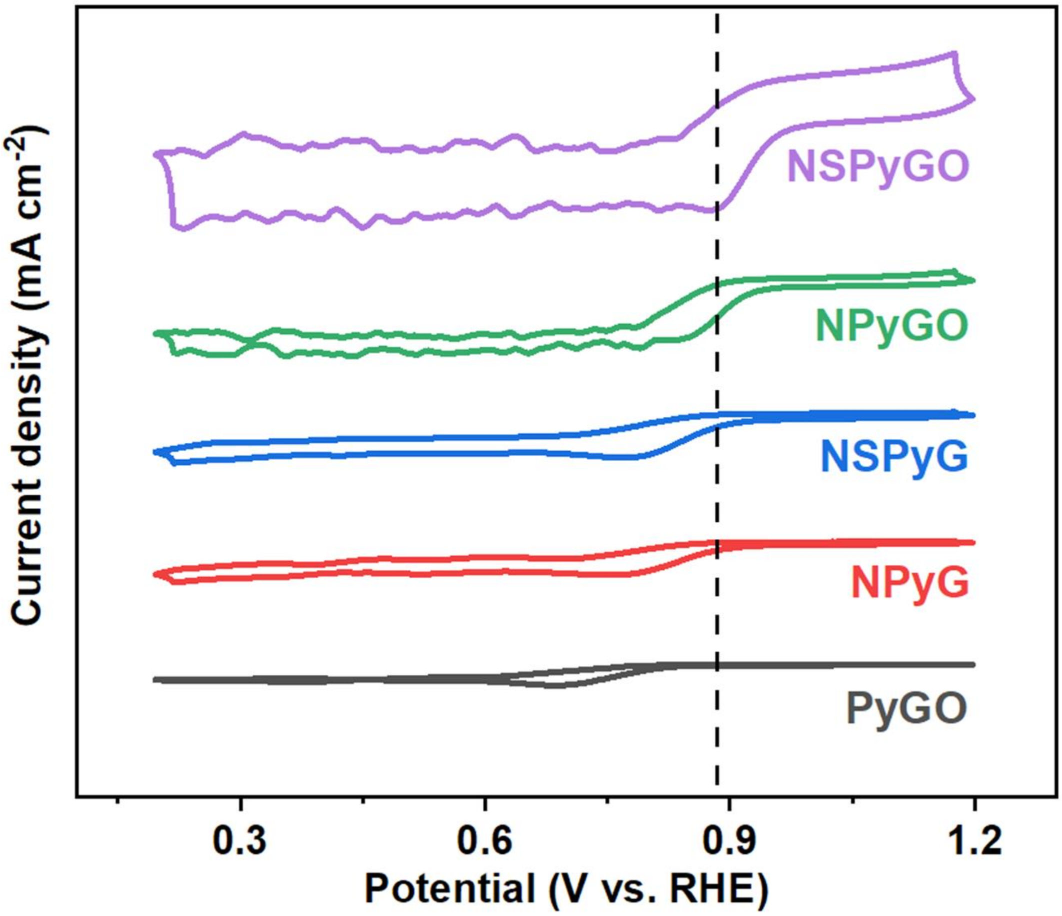

Figure 5.22 CV curves of PyGO, NPyG, NSPyG, NPyGO, and NSPyGO samples obtained in O_2-saturated 0.1 M KOH with the scan rate of 10 mV s^{-1}.

The synergistic effect of N and S noticeably increase the electrocatalytic abilities as shown by the differences in NPyGO and NSPyGO. Tafel slopes of all samples were extrapolated at the intersection between the linear kinetic region (around 1.0-1.2 V) and the linear kinetic/diffusion drop region from the ORR-LSV measurement (Figure 5.23b). Both highly porous annealed pyrene polymers, NPyGO and NSPyGO, exhibit exceptional Tafel values of 63.1 and 61.8 mV dec^{-1} which are lower than of 76.0 mV dec^{-1} of Pt/C. The low Tafel value, together with good E_{onset} and $E_{1/2}$, demonstrate efficient ORR kinetics realised by the highly porous pyrene matrix with N and S active sites[305].

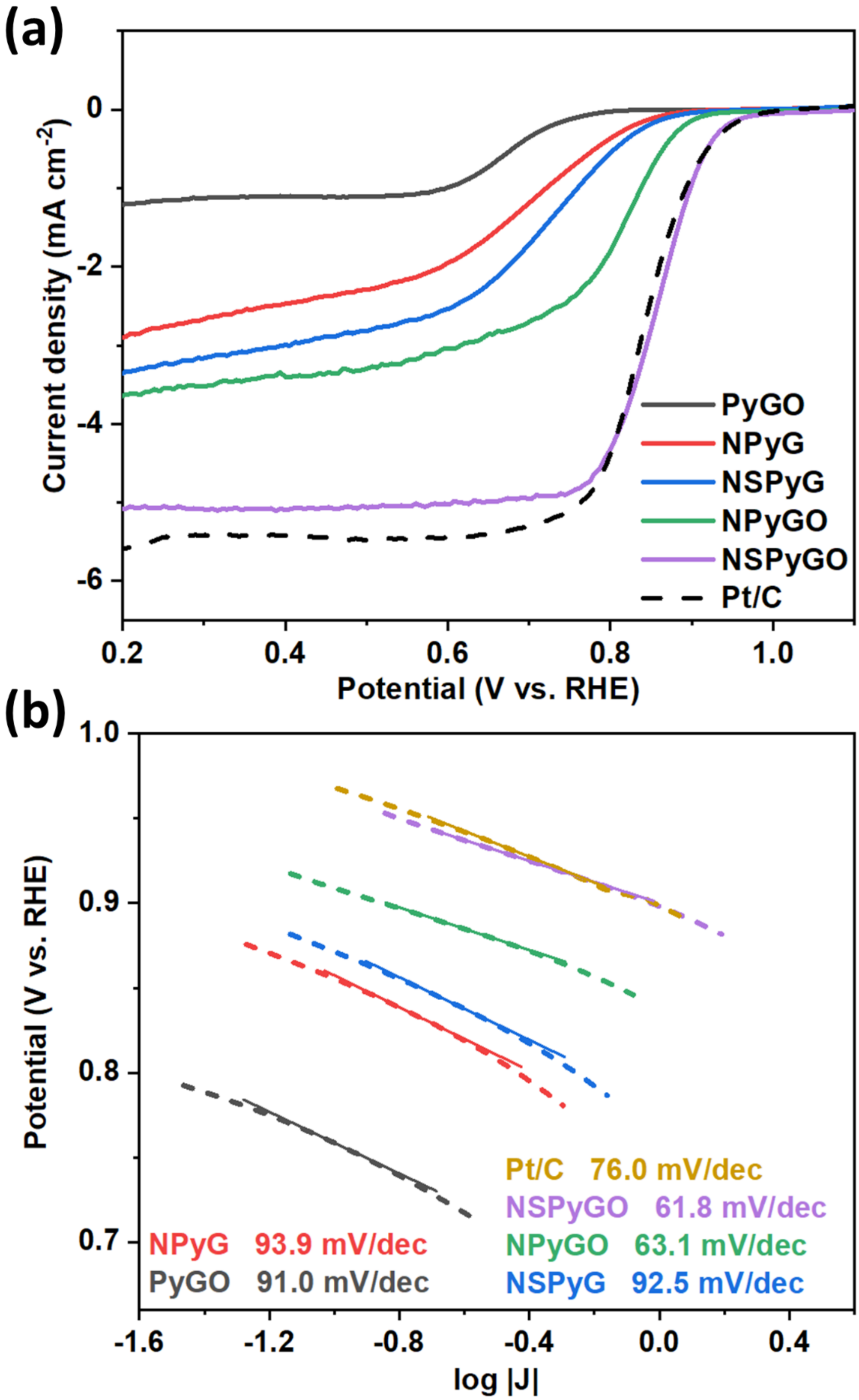

Figure 5.23 (a) Combined ORR-LSV curves for all prepared samples in O_2-saturated KOH at 1600 rpm. (b) Tafel plots of all samples calculated from the above LSV curves.

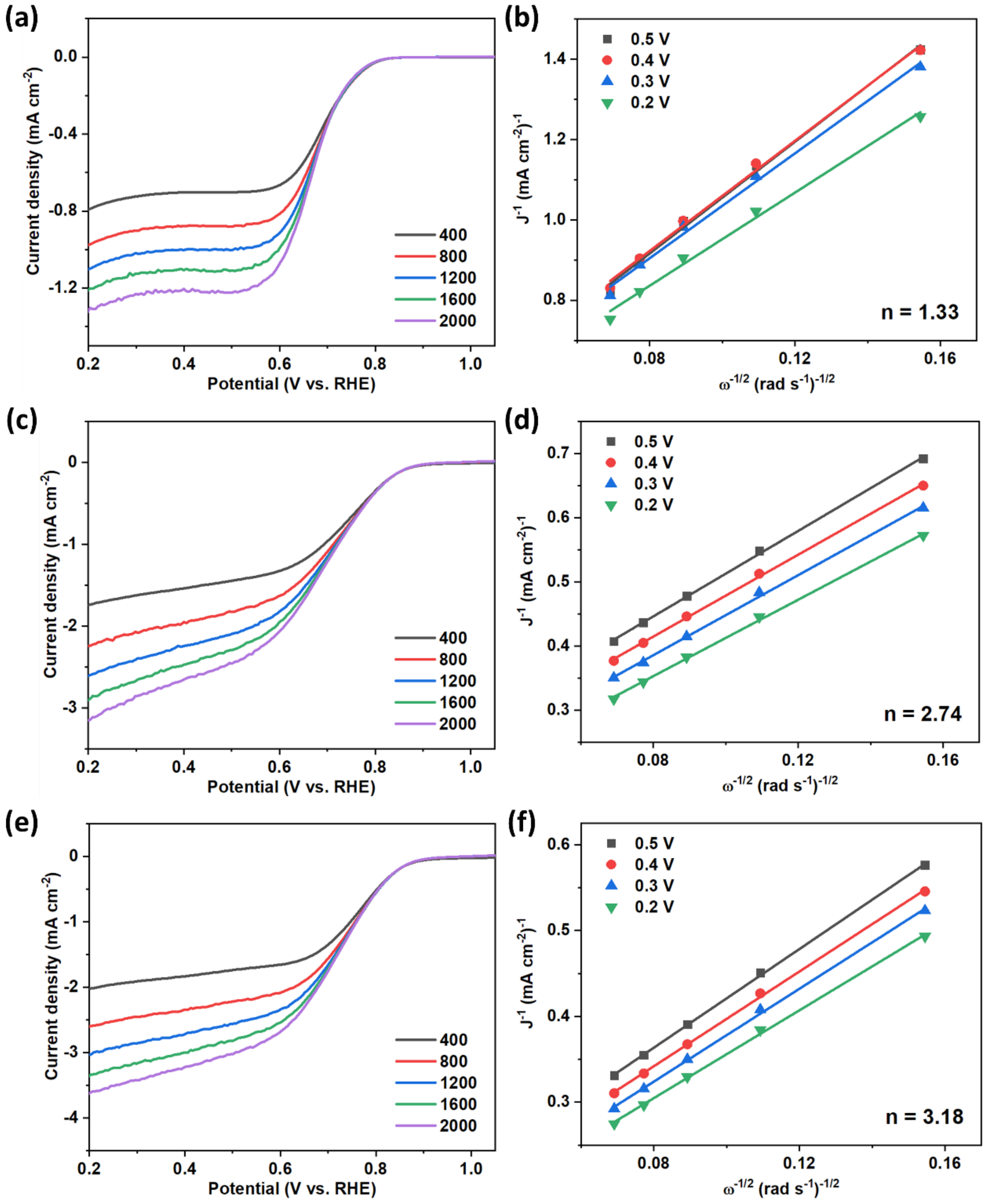

Figure 5.24 LSV curves at different rotation speeds (400-2000 rpm) and corresponding K-L plots for (a),(b) PyGO, (c),(d) NPyG, and (e),(f) NSPyG.

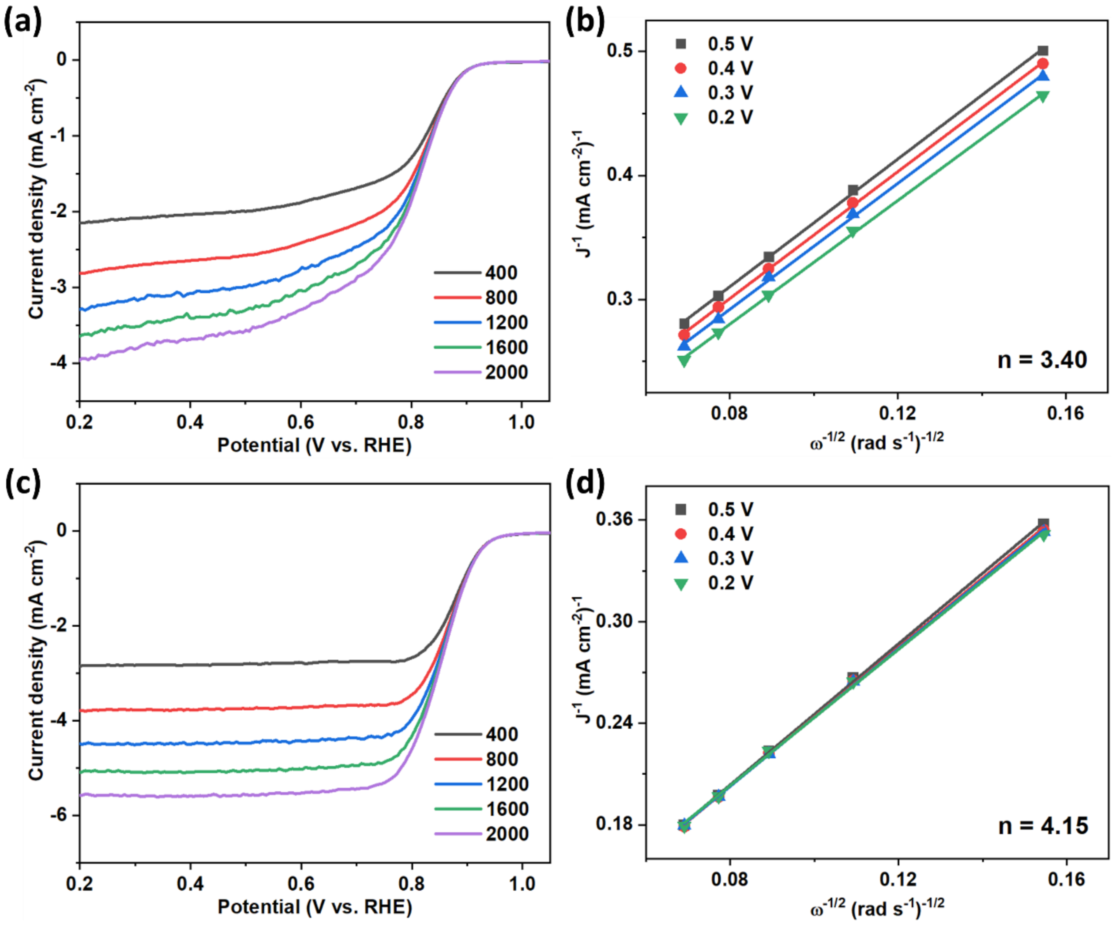

Figure 5.25 LSV curves at different rotation speeds (400-2000 rpm) and corresponding K-L plots for (a),(b) NPyGO, and (c),(d) NSPyGO.

Tafel values of NSPyG, NPyG, and PyGO were 92.5, 93.9, and 91.0 mV dec^{-1}, respectively. These values are comparable to hydrothermally prepared CD-embedded graphene samples (in Chapter 4).

Figure 5.24-5.25 show LSV curves and corresponding K-L plots for all samples. The electron transfer number, n, was calculated to be 4.15 for NSPyGO – a value close to 4 suggests that very effective catalytic reaction kinetics and diffusion take place. However, a value, greater than the theoretical successive 4 electron reduction pathway for oxygen reactions, suggests that there are small amount of side reactions taking place during the ORR-LSV measurement contributing to the higher electron transfer number. The n values were not high for NPyGO and NSPyG however, due to high porosity in the NPyGO sample and the co-doping of N and S in NSPyG sample, they both displayed reasonable values, 3.40 and 3.18 respectively, despite being non-metal substrates. However, the K-L relation applies with the assumption that the process is homogeneous (the same activation and diffusion areas) and that there are no errors obtained from the surface area, concentrations, and applied potentials[306]. Therefore, calculated n values, from the LSV curves with K-L equation, are approximation with intrinsic errors.

A long-term ORR stability test of NSPyGO was conducted by repeating the LSV measurement 1000 times in O_2-saturated 0.1 M KOH with constant rotation at1600 rpm (Figure 5.26). LSV cycling method is selected as the long-term stability test to observe the changes in LSV curves with respect to increase in number of LSV cycles – associated kinetics and diffusion. The current retention after 1000th was around 89% with increase in overpotential by only 7.7 mV at measured $E_{1/2}$ – stability measurement duration was approximately 95 000 s. Stable ORR capabilities of NSPyGO was achieved with minimum kinetic reduction; only a small decrease in current density was observed as a result of continuous rotation of the RDE. The ORR-stability of NSPyGO is similar to CD-embedded graphene samples in Chapter 4, and better than the Pt/C.

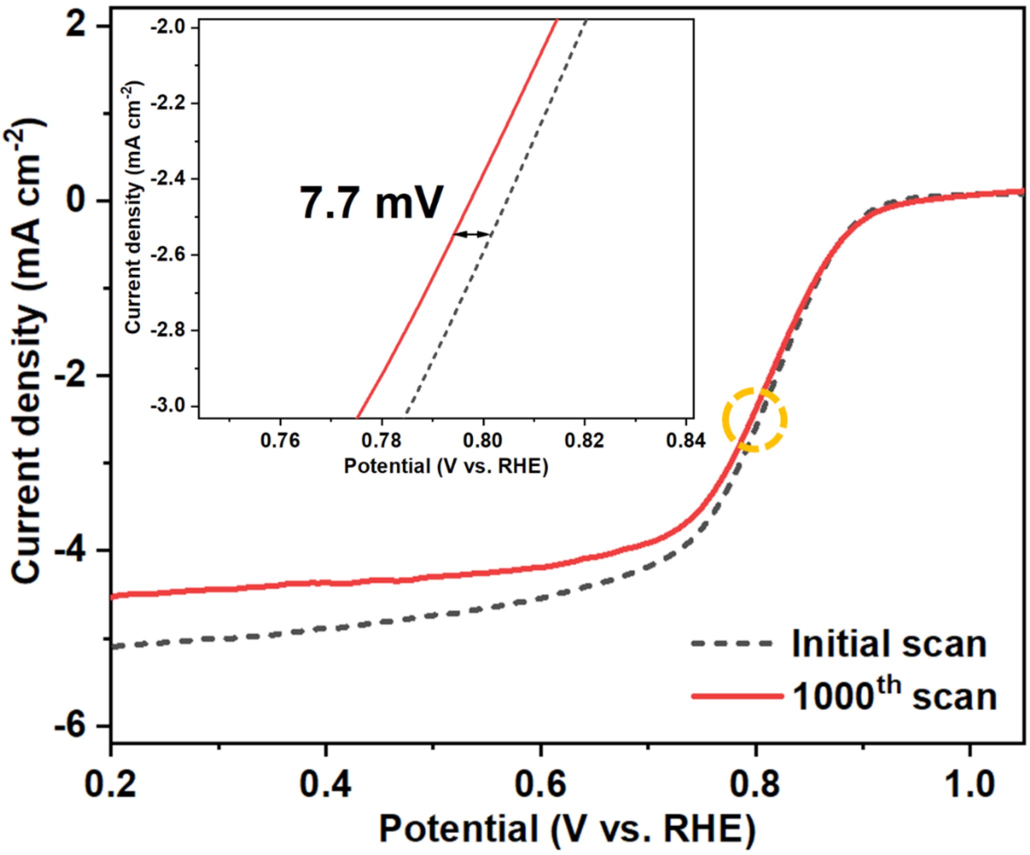

Figure 5.26 1000-cycles stability test of NSPyGO with constant rotation at 1600 rpm.

5.3 Conclusion

In summary, a desirable 2D porous pyrene polymer has been successfully synthesised via a Friedel-Craft polymerisation process. The choice of catalyst, anhydrous aluminium chloride, can be easily removed after the reaction and is not catalytically active (for ORR/OER) therefore does not contribute to the performance of energy application devices. The as-prepared polymer exhibited surface roughness with domains/islands (observed in high-resolution TEM images) due to free rotation movements around the sp^3 linkage of monomers and possible allotropes/fragments of the pyrene units. Repeated pores and defects from the pyrene polymer, PyG, was fragmented further with rips and tears after acid oxidation to form PyGO which was then subjected to an annealing/doping process to form a highly porous annealed pyrene polymer. The N and S dual doped sample, NSPyGO, exhibited substantial improvements in the kinetics associated with electrocatalysis, with E_{onset} and $E_{1/2}$, 0.98 V and 0.86 V of NSPyGO, and 0.98 V and 0.84 V of Pt/C, being either the same or surpassing the potential of Pt/C, despite being a metal-free carbon catalyst. The observed current density of NSPyGO was also very high (5.07 mA cm^{-2}), only 8.5% lower than Pt/C. From the K-L relations, the electron transfer number, n, was found to be 4.23 (slightly higher than 4), suggesting the successive 4 electron transfer process leading to efficient ORR. The exceptional catalytic performance of NSPyGO is realised by the highly porous pyrene polymer structure providing effective oxygen diffusion pathway as well as many catalytically active sites. N and S co-doping also exhibited a synergistic effect shown in both oxidised and non-oxidised samples, compared to single-heteroatom-doping. With separation of desired chlorinated monomers for controlled polymerisation, Friedel-Craft acylation polymerisation processes offer simple and facile syntheses of carbon substrate that can be scaled up. Monomer selections can also be changed to modify pore sizes of the substrate.

Chapter 6 : Conclusion and future work

Advancement of technologies as well as global environmental challenges have increased the public awareness and have accelerated the growth of energy sectors. LIBs have dominated the consumer electronics and the electric vehicle markets however they are gradually reaching the maturity stage with limitations on energy/power densities. Oxygen electrocatalysis, for metal-air batteries and fuel cells, is promising as it offers higher energy density with enhanced safety features provided by the aqueous electrolyte setup. Replacing noble-metal counterparts, Pt/C and Ir/C or RuO_2 catalysts, in ORR and OER is imperative to implement wide commercialisation of devices utilising electrocatalysis. With electrocatalytic performances and cost in mind, this thesis outlined various bottom-up carbon preparation methods to carefully design and synthesise desired morphologies of carbon substrates.

In many preparations of non-metal oxygen electrocatalysts, overall performances greatly depend on the deployed annealing/doping temperature - especially, when materials are synthesised via a single temperature-controlled carbonisation process, as described in Chapter 3. Widely available organic monomers, such as glucose and DCDA, can undergo a thermally assisted polymerisation process to form 2D N-doped annealed carbon polymers (GDCs). An initial low-temperature polymerisation step was necessary to preserve the carbon matrix prior to high temperature treatments. Varying the annealing temperature of GDC polymers (from 700-1000 °C), it was found that 900 °C generated optimum surface roughness with accessible pores/defects for efficient oxygen diffusion into the structure as well as the concentration of graphitic N to provide many ORR active sites. There is a fine balance between surface disorder and the graphitisation degree of the polymer (oxygen activity vs. electronic conductivity).

In electrocatalysis, the number of accessible active sites governs the kinetics and overall measured current densities of materials. Chapter 4 introduces the utilisation of heteroatoms-doped carbon dots embedded on a graphene substrate as a possible bi-functional oxygen electrocatalyst. Carbon dots, nano-sized derivatives of carbon with multiple layers, provide many exposed functional groups which, after heat treatments, become ORR active centres. Rather than occupying a single defect site within graphene (or carbon) matrix with only a couple heteroatoms as active sites, heteroatoms-doped CD embedment offer numerous active sites; the number of active sites to defect/edge sites is multiplied by a few factors. Embedment of CDs were carried out via hydrothermal process followed by high temperature carbonisation. As shown in Chapter 3, the sample prepared at 900 °C, NS-CD@gf_a900, exhibited the highest electrocatalytic performances with the limiting current density reaching 7.71 mA cm^{-2} at 1600 rpm (surpassing 5.55 mA cm^{-2} of Pt/C). Even the single N-doped CD embedded graphene sample, N-CD@gf_a900, exhibited 6.40 mA cm^{-2}, 15% increase from the Pt/C ORR current density. Direct heteroatom doping of N and S on graphene exhibited almost halved ORR performance compared to NS-CD@gf_a900, suggesting the enhancement with decorated CDs. Oxygen reduction kinetics was not as fast as the precious metal Pt/C catalyst with the observed E_{onset}, $E_{1/2}$, and measured Tafel slope, however the CD-embedded graphene samples managed to retain 88% of the current after the long-term ORR test with constant rotation. OER performances were also comparable to the Ir/C reference. Also, it was found that the co-doping of N and S significantly increased the oxygen electrocatalytic reactions in both ORR and OER conditions compared against the single N-doped samples.

Graphene and other carbon allotropes are excellent electric/electronic conductors for many applications. For electrocatalysis, graphene, in particular, is prepared via the oxidation of graphite for many reasons: oxidation exfoliations and abundant surface functional groups to be chemically modified. However, the oxidation process (preparation of GO) involves uncontrollable fragmentations of layers which lead to random pore and defect formations. In Chapter 5, the pyrene carbon polymer was prepared via bottom-up Friedel-Craft polymerisation process. The catalyst used, anhydrous aluminium chloride, was all washed out after polymerisation process – no contribution of Al metal to the electrocatalysis of the prepared carbon. High-resolution TEM images revealed uneven surfaces of the pyrene polymer with domains/islands of smaller pyrene units. After acid oxidation, the polymer formed rips and tears due to many sp^3 bonds breakage. High temperature carbonisation/heteroatoms doping led to formation of highly porous pyrene polymers – the observed micropores were in much smaller pore sizes than the pores seen with annealed graphene in chapter 4. Along with N and S dual doping (proved to be efficient in chapter 4), the porous NSPyGO sample displayed E_{onset} and $E_{1/2}$ of 0.98 V and 0.86 V which is either the same or surpassing the observed potentials of Pt/C (0.98 V and 0.84 V), despite being a metal-free carbon electrocatalyst. The measured current density was 5.07 mA cm^{-2}, very close to the value of Pt/C and the corresponding electron transfer number, n, was calculated to be over 4. Although the limiting current density was not as high as CD-embedded graphene samples with many active sites provided by CDs, the high ratio of micropores resulted in improved oxygen diffusion and conversion kinetics throughout the porous pyrene polymers.

Carbon materials, whether soft/hard carbons, can be modified structurally or chemically to be more efficient oxygen electrocatalysts. Although all materials outlined in this thesis are synthesised in bulk without any complex setups or treatments, still lack in product selectivity when formed. It is necessary to propose new controllable syntheses with high product conversion rate. For instance, readily available organic compounds can be used in polymerisation processes to reduce number of reaction steps and to minimise by-product formations. Preparations of graphitic substrates must also consider increased but accurate formations of active sites and accessibility to improve overall kinetics and the total number of associated conversion reactions (as illustrated in chapter 4 and 5). Analytically, in-situ Raman, in-situ/real-time liquid TEM, simultaneous thermal analysis and mass spectrometry, and other techniques can be utilised to further understand correlations between structural/phase changes and electrocatalytic performances.

Numerous as-prepared carbon substrates are subjected to additional high-temperature annealing to increase the carbonisation degree but also to increase stability of the material (either by the removal of unstable species or phase changes) and electronic conductivity. Both polymeric reactions and electrocatalytic conversion reactions occur around the heteroatom/metal-centred functional groups – however, not all functional groups present in polymers are favourable toward ORR and OER. Use of deposition methods, such as chemical vapour or atomic layer, can be explored to synthesise precise graphitic-like few-layered polymers with repeating ORR/OER active centres.

It is still challenging to fine-tune the oxygen electrocatalysts to be bi-functional (ORR and OER capable) as both electron donating and withdrawing properties need to be efficient. Especially, OER processes are difficult to achieve with non-metal carbon catalysts. Many metallic species have variable oxidation states demonstrating different chemical behaviours depending on the changes made to systems. With better understanding of carbon substrates and careful selections of metals and metallic compounds, including Fe, Co, Ni, Mn, the switch in ORR and OER systems in metal-anchored carbon electrocatalysts can be achieved with good conductivity (from the carbon) and conversions (from the metal centres). Minimal metal loading, together with high porosity, can offer efficient oxygen electrocatalyst materials that can outperform Pt/C and Ir/C.

There are also limitations to understanding the oxygen conversion mechanism only from experimental results; computational methods (first principle calculations, density functional theory methods, molecular dynamics simulations) should be strongly considered for future works to clarify molecular properties of catalysts and associated free-energies for electrochemical/electrocatalytic storage/conversion mechanisms.

For energy storage/conversion applications, stability of different scaled-up syntheses, casting of electrode materials, and fabrication of cells need to be scrutinised as well as being cost-effective, safe, and environmentally-friendly. Thus, further work is needed to revise and minimise risks associated from the very first step, electrocatalysts/electrode preparations, to the long-term conditions in devices.

Appendix

Comparison of ORR/OER activities of reported metal-free carbon-based oxygen electrocatalysts (V vs. RHE).

	ORR		OER	Bi-functional	Mass loading	Electrolyte	Ref
	E_{onset}	E_{-3}	E_{10}	ΔE	mg cm^{-2}	KOH	
GDC_900	0.75	—	—	—	0.28	0.1 M	This work
NS-CD@gf_a900	0.93	0.77	1.68	0.91	0.28	0.1 M	This work
NSPyGO	0.98	0.84	—	—	0.28	0.1 M	This work
N, S- porous carbon	0.99	0.85	1.69	0.81	0.42	0.1 M	[150]
N-doped graphene	0.92	0.84	1.66	0.82	0.30	0.1 M	[262]
N, S- carbon nanosheet	0.92	0.77	1.65	0.88	0.20	0.1 M	[307]
P, S- carbon nitride sponge	0.97	0.87	1.56	0.69	0.15	0.1 M	[308]
P- graphitic carbon nitride /carbon paper	0.94	0.67	1.63	0.96	0.20	0.1	[309]
N, P- carbon foam	0.94	0.85	>2.0	>1.15	0.15	0.1	[148]
N-doped graphdiyne	0.99	0.87	—	—	0.60	0.1	[151]

N, P, F- carbon nanosphere	0.93	0.81	1.57	0.76	0.29	0.1 (1 M OER)	310
N, P- covalent polymer	0.97	0.84	1.69	0.85	0.25	0.1	311
N- carbon network	0.88	0.79	1.77	0.98	0.21	0.1	312
N- carbon nanofiber film	0.97	0.80	1.84	1.04	0.10	0.1	313
C_{60}-SWCNTs	0.91	0.84	1.69	0.75	—	0.1	314
N, P, F- carbon nanofiber	0.95	0.80	2.00	1.20	0.20	0.1	315
N- carbon nanosphere	0.96	0.85	1.62	0.77	0.26	0.1 (1 M OER)	316
N- graphene /CNT	0.88	0.63	1.63	1.00	0.25	0.1	209
H- substituted N- graphdiyne	1.02	0.85	—	—	0.40	0.1	317
N, S- graphitic sheet with holes	1.01	0.87	1.56	0.69	0.64	0.1	318
N, S, P- graphene	0.95	0.82	1.76	0.94	0.20	0.1	319
N, O- porous carbon	0.90	0.78	1.58	0.80	0.26	0.1	320
N, S- carbon nanosheet	0.96	0.78	1.67	0.89	0.13	0.1	321
SWCNT in N, P- carbon	0.96	0.85	1.68	0.83	0.40	0.1	322
CNT/boron nitride	0.86	0.72	1.81	1.09	0.85	0.1	323

* $E_{1/2}$ values were compared when E_{-3} not available

List of publications

Juhun Shin, Jian Guo, Tingting Zhao and Zhengxiao Guo, Functionalized Carbon Dots on Graphene as Outstanding Non-Metal Bifunctional Oxygen Electrocatalyst, ***Small*, 2019, 15, 1900296**

Gi Byoung Hwang, He Huang, Gaowei Wu, **Juhun Shin**, Andreas Kafizas, Kersti Karu, Hendrik Du Toit, Abdullah M. Alotaibi, Layla Mohammad-Hadi, Elaine Allan, Alexander J. MacRobert, Asterios Gavriilidis and Ivan P. Parkin, Photobactericidal activity activated by thiolated gold nanoclusters at low flux levels of white light, ***Nature Communications*, 11, 1207 (2020)**

Gi Byoung Hwang, Gaowei Wu, **Juhun Shin**, Luca Panariello, Victor Sebastian, Kersti Karu, Elaine Allan, Asterios Gavriilidis and Ivan P. Parkin, Continuous Single-Phase Synthesis of [$Au_{25}(Cys)_{18}$] Nanoclusters and their Photobactericidal Enhancement, ***ACS Applied Material Interfaces*, 2020, 12, 43, 49021-49029**

Baldassarre Venezia, Luca Panariello, Daniel Biri, **Juhun Shin**, Spyridon Damilos, Anand N.P.Radhakrishnan, Chris Blackman and Asterios Gavriilidis, Catalytic Teflon AF-2400 membrane reactor with adsorbed ex situ synthesized Pd-based nanoparticles for nitrobenzene hydrogenation, ***Catalysis Today*, 362, 2021, 104-112**

Ki Joon Heo, Sang Bin Jeong, **Juhun Shin**, Gi Byoung Hwang, Hyun Sik Ko, Yeonsang Kim, Dong Yun Choi and Jae Hee Jung, Water-Repellent TiO_2-Organic

Dye-Based Air Filters for Efficient Visible-Light-Activated Photochemical Inactivation against Bioaerosols, ***Nano Letters*****, 2021, 21, 4, 1576-1583**

Seonghyeok Park, Jiatong Huo, **Juhun Shin**, Ki Joon Heo, Julie Jalila Kalmoni, Sanjayan Sathasivam, Gi Byoung Hwang, and Claire J. Carmalt, Production of an EP/PDMS/SA/AlZnO Coated Superhydrophobic Surface through an Aerosol-Assisted Chemical Vapor Deposition Process, ***Langmuir*****, 2022, 38, 25, 7825-7832**

References

1. Ritchie H, Roser M. "Energy" OurWorldInData.org: OurWorldInData; 2020 [Available from: https://ourworldindata.org/energy.

2. Council WE. World Energy Resources 2016 Full Report 2016 [Available from: https://www.worldenergy.org/publications/2016/world-energy-resources-2016/.

3. Schipper F, Aurbach D. A brief review: Past, present and future of lithium ion batteries. Russian Journal of Electrochemistry. 2016;52(12):1095-121.

4. Etacheri V, Marom R, Elazari R, Salitra G, Aurbach D. Challenges in the development of advanced Li-ion batteries: a review. Energy & Environmental Science. 2011;4(9):3243-62.

5. The Nobel Prize in Chemistry 2019 [press release]. NobelPrize.org, Fri. 18 Feb 2022 2019.

6. Manthiram A. A reflection on lithium-ion battery cathode chemistry. Nat Commun. 2020;11(1):1550.

7. Manthiram A. An Outlook on Lithium Ion Battery Technology. ACS Cent Sci. 2017;3(10):1063-9.

8. Liu K, Liu Y, Lin D, Pei A, Cui Y. Materials for lithium-ion battery safety. Science Advances.4(6):eaas9820.

9. Zubi G, Dufo-López R, Carvalho M, Pasaoglu G. The lithium-ion battery: State of the art and future perspectives. Renewable and Sustainable Energy Reviews. 2018;89:292-308.

10. An SJ, Li J, Daniel C, Mohanty D, Nagpure S, Wood DL. The state of understanding of the lithium-ion-battery graphite solid electrolyte interphase (SEI) and its relationship to formation cycling. Carbon. 2016;105:52-76.

11. Chan CK, Ruffo R, Hong SS, Cui Y. Surface chemistry and morphology of the solid electrolyte interphase on silicon nanowire lithium-ion battery anodes. Journal of Power Sources. 2009;189(2):1132-40.

12. Zhou Y, Su M, Yu X, Zhang Y, Wang JG, Ren X, et al. Real-time mass spectrometric characterization of the solid-electrolyte interphase of a lithium-ion battery. Nat Nanotechnol. 2020;15(3):224-30.

13. Contestabile M, Panero S, Scrosati B. A laboratory-scale lithium-ion battery recycling process. Journal of Power Sources. 2001;92(1):65-9.

14. Broussely M, Planchat JP, Rigobert G, Virey D, Sarre G. Lithium-ion batteries for electric vehicles: performances of 100 Ah cells. Journal of Power Sources. 1997;68(1):8-12.

15. Fang X, Shen C, Ge M, Rong J, Liu Y, Zhang A, et al. High-power lithium ion batteries based on flexible and light-weight cathode of LiNi 0.5 Mn 1.5 O 4 /carbon nanotube film. Nano Energy. 2015;12:43-51.

16. Zhang LL, Zhao XS. Carbon-based materials as supercapacitor electrodes. Chem Soc Rev. 2009;38(9):2520-31.

17. Frackowiak E. Carbon materials for supercapacitor application. Phys Chem Chem Phys. 2007;9(15):1774-85.

18. Raza W, Ali F, Raza N, Luo Y, Kim K-H, Yang J, et al. Recent advancements in supercapacitor technology. Nano Energy. 2018;52:441-73.

19. Wang Y, Shi Z, Huang Y, Ma Y, Wang C, Chen M, et al. Supercapacitor Devices Based on Graphene Materials. The Journal of Physical Chemistry C. 2009;113(30):13103-7.

20. Zhang L, Hu X, Wang Z, Sun F, Dorrell DG. A review of supercapacitor modeling, estimation, and applications: A control/management perspective. Renewable and Sustainable Energy Reviews. 2018;81:1868-78.

21. Yu Z, Tetard L, Zhai L, Thomas J. Supercapacitor electrode materials: nanostructures from 0 to 3 dimensions. Energy & Environmental Science. 2015;8(3):702-30.

22. Zuo W, Li R, Zhou C, Li Y, Xia J, Liu J. Battery-Supercapacitor Hybrid Devices: Recent Progress and Future Prospects. Adv Sci (Weinh). 2017;4(7):1600539.

23. Wang Q, Wen ZH, Li JH. A Hybrid Supercapacitor Fabricated with a Carbon Nanotube Cathode and a TiO2–B Nanowire Anode. Advanced Functional Materials. 2006;16(16):2141-6.

24. Vlad A, Singh N, Rolland J, Melinte S, Ajayan PM, Gohy JF. Hybrid supercapacitor-battery materials for fast electrochemical charge storage. Sci Rep. 2014;4:4315.

25. Li B, Dai F, Xiao Q, Yang L, Shen J, Zhang C, et al. Nitrogen-doped activated carbon for a high energy hybrid supercapacitor. Energy & Environmental Science. 2016;9(1):102-6.

26. Blurton KF, Sammells AF. Metal/air batteries: Their status and potential — a review. Journal of Power Sources. 1979;4(4):263-79.

27. Rahman MA, Wang X, Wen C. High Energy Density Metal-Air Batteries: A Review. Journal of The Electrochemical Society. 2013;160(10):A1759-A71.

28. Cheng F, Chen J. Metal-air batteries: from oxygen reduction electrochemistry to cathode catalysts. Chem Soc Rev. 2012;41(6):2172-92.

29. Li Y, Lu J. Metal–Air Batteries: Will They Be the Future Electrochemical Energy Storage Device of Choice? ACS Energy Letters. 2017;2(6):1370-7.

30. Lee DU, Xu P, Cano ZP, Kashkooli AG, Park MG, Chen Z. Recent progress and perspectives on bi-functional oxygen electrocatalysts for advanced rechargeable metal–air batteries. Journal of Materials Chemistry A. 2016;4(19):7107-34.

31. Heise GW, Cahoon NC. Dry Cells of the Leclanché Type, 1902-1952—A Review. Journal of Electrochemical Society. 1952;99(8):179C-87C.

32. Lee J-S, Tai Kim S, Cao R, Choi N-S, Liu M, Lee KT, et al. Metal-Air Batteries with High Energy Density: Li-Air versus Zn-Air. Advanced Energy Materials. 2011;1(1):34-50.

33. Koscher G, Kordesch K. Can refillable alkaline methanol–air systems replace metal–air cells? Journal of Power Sources. 2004;136(2):215-9.

34. Liu Q, Pan Z, Wang E, An L, Sun G. Aqueous metal-air batteries: Fundamentals and applications. Energy Storage Materials. 2020;27:478-505.

35. Xu K, Loh A, Wang B, Li X. Enhancement of Oxygen Transfer by Design Nickel Foam Electrode for Zinc−Air Battery. Journal of The Electrochemical Society. 2018;165(5):A809-A18.

36. Tran C, Yang X-Q, Qu D. Investigation of the gas-diffusion-electrode used as lithium/air cathode in non-aqueous electrolyte and the importance of carbon material porosity. Journal of Power Sources. 2010;195(7):2057-63.

37. Sandhu SS, Fellner JP, Brutchen GW. Diffusion-limited model for a lithium/air battery with an organic electrolyte. Journal of Power Sources. 2007;164(1):365-71.

38. Wang H-F, Xu Q. Materials Design for Rechargeable Metal-Air Batteries. Matter. 2019;1(3):565-95.

39. Harting K, Kunz U, Turek T. Zinc-air Batteries: Prospects and Challenges for Future Improvement. Zeitschrift für Physikalische Chemie. 2012;226(2):151-66.

40. Wang Z-L, Xu D, Xu J-J, Zhang X-B. Oxygen electrocatalysts in metal–air batteries: from aqueous to nonaqueous electrolytes. Chemical Society Reviews. 2014;43(22):7746-86.

41. Fang Y, Xiao L, Chen Z, Ai X, Cao Y, Yang H. Recent Advances in Sodium-Ion Battery Materials. Electrochemical Energy Reviews. 2018;1(3):294-323.

42. Ji B, Zhang F, Song X, Tang Y. A Novel Potassium-Ion-Based Dual-Ion Battery. Adv Mater. 2017;29(19).

43. Zhang X, Yang D, Rui X, Yu Y, Huang S. Advanced cathodes for potassium-ion battery. Current Opinion in Electrochemistry. 2019;18:24-30.

44. Sun H, Wang W, Yu Z, Yuan Y, Wang S, Jiao S. A new aluminium-ion battery with high voltage, high safety and low cost. Chem Commun (Camb). 2015;51(59):11892-5.

45. Das SK, Mahapatra S, Lahan H. Aluminium-ion batteries: developments and challenges. Journal of Materials Chemistry A. 2017;5(14):6347-67.

46. Chayambuka K, Mulder G, Danilov DL, Notten PHL. Sodium-Ion Battery Materials and Electrochemical Properties Reviewed. Advanced Energy Materials. 2018;8(16).

47. Conte FV. Battery and battery management for hybrid electric vehicles: a review. e & i Elektrotechnik und Informationstechnik. 2006;123(10):424-31.

48. Rudnik E, Nikiel M. Hydrometallurgical recovery of cadmium and nickel from spent Ni–Cd batteries. Hydrometallurgy. 2007;89(1-2):61-71.

49. Ikoma M, Hoshina Y, Matsumoto I, Iwakura C. Self-Discharge Mechanism of Sealed-Type Nickel/Metal-Hydride Battery. Journal of The Electrochemical Society. 1996;143(6):1904-7.

50. Appleby AJ. Fuel cell handbook. United States: New York, NY; Van Nostrand Reinhold Co. Inc.; 1988 1988-01-01.

51. Steele BCH, Heinzel A. Materials for fuel-cell technologies. Materials for Sustainable Energy: Co-Published with Macmillan Publishers Ltd, UK; 2010. p. 224-31.

52. Haile SM. Fuel cell materials and components☆☆☆The Golden Jubilee Issue—Selected topics in Materials Science and Engineering: Past, Present and Future, edited by S. Suresh. Acta Materialia. 2003;51(19):5981-6000.

53. Girishkumar G, McCloskey B, Luntz AC, Swanson S, Wilcke W. Lithium−Air Battery: Promise and Challenges. The Journal of Physical Chemistry Letters. 2010;1(14):2193-203.

54. Kalaiselvam S, Parameshwaran R. Thermal Energy Storage Technologies for Sustainability: Systems Design, Assessment and Applications: Elsevier Science; 2014.

55. Jayanti S. Regenerative Fuel Cells. In: Cabeza LF, editor. Encyclopedia of Energy Storage. Oxford: Elsevier; 2022. p. 329-37.

56. Zhu AL, Wilkinson DP, Zhang X, Xing Y, Rozhin AG, Kulinich SA. Zinc regeneration in rechargeable zinc-air fuel cells—A review. Journal of Energy Storage. 2016;8:35-50.

57. Du Pasquier A, Plitz I, Menocal S, Amatucci G. A comparative study of Li-ion battery, supercapacitor and nonaqueous asymmetric hybrid devices for automotive applications. Journal of Power Sources. 2003;115(1):171-8.

58. Fetcenko MA, Ovshinsky SR, Reichman B, Young K, Fierro C, Koch J, et al. Recent advances in NiMH battery technology. Journal of Power Sources. 2007;165(2):544-51.

59. Pan J, Xu YY, Yang H, Dong Z, Liu H, Xia BY. Advanced Architectures and Relatives of Air Electrodes in Zn–Air Batteries. Advanced Science. 2018;5(4):1700691.

60. Sapkota P, Kim H. Zinc–air fuel cell, a potential candidate for alternative energy. Journal of Industrial and Engineering Chemistry. 2009;15(4):445-50.

61. Adams LA, Poynton SD, Tamain C, Slade RCT, Varcoe JR. A Carbon Dioxide Tolerant Aqueous-Electrolyte-Free Anion-Exchange Membrane Alkaline Fuel Cell. ChemSusChem. 2008;1(1-2):79-81.

62. Xu M, Ivey DG, Xie Z, Qu W. Rechargeable Zn-air batteries: Progress in electrolyte development and cell configuration advancement. Journal of Power Sources. 2015;283:358-71.

63. Katsounaros I, Schneider WB, Meier JC, Benedikt U, Biedermann PU, Auer AA, et al. Hydrogen peroxide electrochemistry on platinum: towards understanding the oxygen reduction reaction mechanism. Physical Chemistry Chemical Physics. 2012;14(20):7384-91.

64. Ganyecz Á, Kállay M. Oxygen Reduction Reaction on N-Doped Graphene: Effect of Positions and Scaling Relations of Adsorption Energies. The Journal of Physical Chemistry C. 2021;125(16):8551-61.

65. Li Y, Zhou W, Wang H, Xie L, Liang Y, Wei F, et al. An oxygen reduction electrocatalyst based on carbon nanotube–graphene complexes. Nature Nanotechnology. 2012;7(6):394-400.

66. Calle-Vallejo F, Martínez JI, Rossmeisl J. Density functional studies of functionalized graphitic materials with late transition metals for oxygen reduction reactions. Physical Chemistry Chemical Physics. 2011;13(34):15639-43.

67. Dau H, Limberg C, Reier T, Risch M, Roggan S, Strasser P. The Mechanism of Water Oxidation: From Electrolysis via Homogeneous to Biological Catalysis. ChemCatChem. 2010;2(7):724-61.

68. Svane KL, Reda M, Vegge T, Hansen HA. Improving the Activity of M−N4 Catalysts for the Oxygen Reduction Reaction by Electrolyte Adsorption. ChemSusChem. 2019;12(23):5133-41.

69. Wang Y, Balbuena PB. Potential Energy Surface Profile of the Oxygen Reduction Reaction on a Pt Cluster: Adsorption and Decomposition of OOH and H2O2. Journal of Chemical Theory and Computation. 2005;1(5):935-43.

70. Rossmeisl J, Qu ZW, Zhu H, Kroes GJ, Nørskov JK. Electrolysis of water on oxide surfaces. Journal of Electroanalytical Chemistry. 2007;607(1):83-9.

71. Stock D, Dongmo S, Janek J, Schröder D. Benchmarking Anode Concepts: The Future of Electrically Rechargeable Zinc–Air Batteries. ACS Energy Letters. 2019;4(6):1287-300.

72. Lee CW, Sathiyanarayanan K, Eom SW, Yun MS. Novel alloys to improve the electrochemical behavior of zinc anodes for zinc/air battery. Journal of Power Sources. 2006;160(2):1436-41.

73. Zhang J, Zhou Q, Tang Y, Zhang L, Li Y. Zinc–air batteries: are they ready for prime time? Chemical Science. 2019;10(39):8924-9.

74. Siahrostami S, Tripković V, Lundgaard KT, Jensen KE, Hansen HA, Hummelshøj JS, et al. First principles investigation of zinc-anode dissolution in zinc–air batteries. Physical Chemistry Chemical Physics. 2013;15(17):6416-21.

75. Zhao K, Wang C, Yu Y, Yan M, Wei Q, He P, et al. Ultrathin Surface Coating Enables Stabilized Zinc Metal Anode. Advanced Materials Interfaces. 2018;5(16):1800848.

76. Naveed A, Yang H, Yang J, Nuli Y, Wang J. Highly Reversible and Rechargeable Safe Zn Batteries Based on a Triethyl Phosphate Electrolyte. Angewandte Chemie International Edition. 2019;58(9):2760-4.

77. Krichevski O, Singh RK, Bormashenko E, Bormashenko Y, Multanen V, Schechter A. Bioinspired oxygen selective membrane for Zn–air batteries. Journal of Materials Science. 2021;56(15):9382-94.

78. Wu GM, Lin SJ, Yang CC. Alkaline Zn-air and Al-air cells based on novel solid PVA/PAA polymer electrolyte membranes. Journal of Membrane Science. 2006;280(1):802-8.

79. Liu T, Chang Z, Yin Y, Chen K, Zhang Y, Zhang X. The PVDF-HFP gel polymer electrolyte for Li-O2 battery. Solid State Ionics. 2018;318:88-94.

80. Ye H, Huang J, Xu JJ, Khalfan A, Greenbaum SG. Li Ion Conducting Polymer Gel Electrolytes Based on Ionic Liquid/PVDF-HFP Blends. Journal of The Electrochemical Society. 2007;154(11):A1048.

81. Duan H, Fan M, Chen W-P, Li J-Y, Wang P-F, Wang W-P, et al. Extended Electrochemical Window of Solid Electrolytes via Heterogeneous Multilayered Structure for High-Voltage Lithium Metal Batteries. Advanced Materials. 2019;31(12):1807789.

82. Wang D, Li H, Liu Z, Tang Z, Liang G, Mo F, et al. A Nanofibrillated Cellulose/Polyacrylamide Electrolyte-Based Flexible and Sewable High-Performance Zn–MnO2 Battery with Superior Shear Resistance. Small. 2018;14(51):1803978.

83. Liu S, Wang H, Imanishi N, Zhang T, Hirano A, Takeda Y, et al. Effect of co-doping nano-silica filler and N-methyl-N-propylpiperidinium bis(trifluoromethanesulfonyl)imide into polymer electrolyte on Li dendrite formation in Li/poly(ethylene oxide)-Li(CF3SO2)2N/Li. Journal of Power Sources. 2011;196(18):7681-6.

84. Gilliam RJ, Graydon JW, Kirk DW, Thorpe SJ. A review of specific conductivities of potassium hydroxide solutions for various concentrations and temperatures. International Journal of Hydrogen Energy. 2007;32(3):359-64.

85. Muthiah P, Hsu S-H, Sigmund W. Coaxially Electrospun PVDF−Teflon AF and Teflon AF−PVDF Core−Sheath Nanofiber Mats with Superhydrophobic Properties. Langmuir. 2010;26(15):12483-7.

86. Zhang J, Xu W, Liu W. Oxygen-selective immobilized liquid membranes for operation of lithium-air batteries in ambient air. Journal of Power Sources. 2010;195(21):7438-44.

87. Li Y, Huang K, MacGregor JD, Xing Y. The Role of PTFE in Cathode Transition Layer in Aqueous Electrolyte Li-Air Battery. Electrochimica Acta. 2016;191:996-1000.

88. Wang Y, Zhou H. A lithium-air battery with a potential to continuously reduce O2 from air for delivering energy. Journal of Power Sources. 2010;195(1):358-61.

89. Xu Y, Zhang Y, Guo Z, Ren J, Wang Y, Peng H. Flexible, Stretchable, and Rechargeable Fiber-Shaped Zinc–Air Battery Based on Cross-Stacked Carbon Nanotube Sheets. Angewandte Chemie International Edition. 2015;54(51):15390-4.

90. Lee Y, Suntivich J, May KJ, Perry EE, Shao-Horn Y. Synthesis and Activities of Rutile IrO2 and RuO2 Nanoparticles for Oxygen Evolution in Acid and Alkaline Solutions. The Journal of Physical Chemistry Letters. 2012;3(3):399-404.

91. da Silva GC, Mayrhofer KJJ, Ticianelli EA, Cherevko S. Dissolution Stability: The Major Challenge in the Regenerative Fuel Cells Bifunctional Catalysis. Journal of The Electrochemical Society. 2018;165(16):F1376-F84.

92. Neergat M, Rahul R. Unsupported Cu-Pt Core-Shell Nanoparticles: Oxygen Reduction Reaction (ORR) Catalyst with Better Activity and Reduced Precious Metal Content. Journal of The Electrochemical Society. 2012;159(7):F234-F41.

93. Liu Q, Li Y, Zheng L, Shang J, Liu X, Yu R, et al. Sequential Synthesis and Active-Site Coordination Principle of Precious Metal Single-Atom Catalysts for Oxygen Reduction Reaction and PEM Fuel Cells. Advanced Energy Materials. 2020;10(20):2000689.

94. Sheng W, Lee SW, Crumlin EJ, Chen S, Shao-Horn Y. Synthesis, Activity and Durability of Pt Nanoparticles Supported on Multi-walled Carbon Nanotubes for Oxygen Reduction. Journal of The Electrochemical Society. 2011;158(11):B1398.

95. Hoshi N, Nakamura M, Hitotsuyanagi A. Active sites for the oxygen reduction reaction on the high index planes of Pt. Electrochimica Acta. 2013;112:899-904.

96. Cho KY, Yeom YS, Seo HY, Kumar P, Lee AS, Baek K-Y, et al. Molybdenum-Doped PdPt@Pt Core–Shell Octahedra Supported by Ionic Block Copolymer-Functionalized Graphene as a Highly Active and Durable Oxygen Reduction Electrocatalyst. ACS Applied Materials & Interfaces. 2017;9(2):1524-35.

97. Zhang L, Iyyamperumal R, Yancey DF, Crooks RM, Henkelman G. Design of Pt-Shell Nanoparticles with Alloy Cores for the Oxygen Reduction Reaction. ACS Nano. 2013;7(10):9168-72.

98. Čolić V, Bandarenka AS. Pt Alloy Electrocatalysts for the Oxygen Reduction Reaction: From Model Surfaces to Nanostructured Systems. ACS Catalysis. 2016;6(8):5378-85.

99. Nair AS, Pathak B. Computational Screening for ORR Activity of 3d Transition Metal Based M@Pt Core–Shell Clusters. The Journal of Physical Chemistry C. 2019;123(6):3634-44.

100. Kim Y-T, Lopes PP, Park S-A, Lee AY, Lim J, Lee H, et al. Balancing activity, stability and conductivity of nanoporous core-shell iridium/iridium oxide oxygen evolution catalysts. Nature Communications. 2017;8(1):1449.

101. Chen Z, Higgins D, Yu A, Zhang L, Zhang J. A review on non-precious metal electrocatalysts for PEM fuel cells. Energy & Environmental Science. 2011;4(9):3167-92.

102. Liu D, Tao L, Yan D, Zou Y, Wang S. Recent Advances on Non-precious Metal Porous Carbon-based Electrocatalysts for Oxygen Reduction Reaction. ChemElectroChem. 2018;5(14):1775-85.

103. Bashyam R, Zelenay P. A class of non-precious metal composite catalysts for fuel cells. Nature. 2006;443(7107):63-6.

104. Wang Y, Li J, Wei Z. Transition-metal-oxide-based catalysts for the oxygen reduction reaction. Journal of Materials Chemistry A. 2018;6(18):8194-209.

105. Wang Q, Shang L, Shi R, Zhang X, Zhao Y, Waterhouse GIN, et al. NiFe Layered Double Hydroxide Nanoparticles on Co,N-Codoped Carbon Nanoframes as Efficient Bifunctional Catalysts for Rechargeable Zinc–Air Batteries. Advanced Energy Materials. 2017;7(21):1700467.

106. Dong Y, Deng Y, Zeng J, Song H, Liao S. A high-performance composite ORR catalyst based on the synergy between binary transition metal nitride and nitrogen-doped reduced graphene oxide. Journal of Materials Chemistry A. 2017;5(12):5829-37.

107. Wu Z-Y, Xu X-X, Hu B-C, Liang H-W, Lin Y, Chen L-F, et al. Iron Carbide Nanoparticles Encapsulated in Mesoporous Fe-N-Doped Carbon Nanofibers for Efficient Electrocatalysis. Angewandte Chemie International Edition. 2015;54(28):8179-83.

108. Guo S, Zhang S, Wu L, Sun S. Co/CoO Nanoparticles Assembled on Graphene for Electrochemical Reduction of Oxygen. Angewandte Chemie International Edition. 2012;51(47):11770-3.

109. Yu M, Wang Z, Hou C, Wang Z, Liang C, Zhao C, et al. Nitrogen-Doped Co3O4 Mesoporous Nanowire Arrays as an Additive-Free Air-Cathode for Flexible Solid-State Zinc–Air Batteries. Advanced Materials. 2017;29(15):1602868.

110. Wu Z, Wang J, Song M, Zhao G, Zhu Y, Fu G, et al. Boosting Oxygen Reduction Catalysis with N-doped Carbon Coated Co9S8 Microtubes. ACS Applied Materials & Interfaces. 2018;10(30):25415-21.

111. Lin Y, Yang L, Zhang Y, Jiang H, Xiao Z, Wu C, et al. Defective Carbon–CoP Nanoparticles Hybrids with Interfacial Charges Polarization for Efficient Bifunctional Oxygen Electrocatalysis. Advanced Energy Materials. 2018;8(18):1703623.

112. Wang J, Lin L, He Y, Qin H, Yan S, Yang K, et al. Vacancy-assisted oxygen reduction reaction on cobalt-based catalysts in direct borohydride fuel cell revealed by in-situ XAFS and XRD. Electrochimica Acta. 2017;254:72-8.

113. Yin J, Li Y, Lv F, Lu M, Sun K, Wang W, et al. Oxygen Vacancies Dominated NiS2/CoS2 Interface Porous Nanowires for Portable Zn–Air Batteries Driven Water Splitting Devices. Advanced Materials. 2017;29(47):1704681.

114. Görlin M, Chernev P, Ferreira de Araújo J, Reier T, Dresp S, Paul B, et al. Oxygen Evolution Reaction Dynamics, Faradaic Charge Efficiency, and the Active Metal Redox States of Ni–Fe Oxide Water Splitting Electrocatalysts. Journal of the American Chemical Society. 2016;138(17):5603-14.

115. Zhu Z, Yin H, Wang Y, Chuang C-H, Xing L, Dong M, et al. Coexisting Single-Atomic Fe and Ni Sites on Hierarchically Ordered Porous Carbon as a Highly Efficient ORR Electrocatalyst. Advanced Materials. 2020;32(42):2004670.

116. Zhang Z, Sun J, Wang F, Dai L. Efficient Oxygen Reduction Reaction (ORR) Catalysts Based on Single Iron Atoms Dispersed on a Hierarchically Structured Porous Carbon Framework. Angewandte Chemie International Edition. 2018;57(29):9038-43.

117. Lee K, Zhang L, Lui H, Hui R, Shi Z, Zhang J. Oxygen reduction reaction (ORR) catalyzed by carbon-supported cobalt polypyrrole (Co-PPy/C) electrocatalysts. Electrochimica Acta. 2009;54(20):4704-11.

118. Yang Z, Zhao C, Qu Y, Zhou H, Zhou F, Wang J, et al. Trifunctional Self-Supporting Cobalt-Embedded Carbon Nanotube Films for ORR, OER, and HER Triggered by Solid Diffusion from Bulk Metal. Advanced Materials. 2019;31(12):1808043.

119. Wang X-R, Liu J-Y, Liu Z-W, Wang W-C, Luo J, Han X-P, et al. Identifying the Key Role of Pyridinic-N–Co Bonding in Synergistic Electrocatalysis for Reversible ORR/OER. Advanced Materials. 2018;30(23):1800005.

120. Xiao J, Xia Y, Hu C, Xi J, Wang S. Raisin bread-like iron sulfides/nitrogen and sulfur dual-doped mesoporous graphitic carbon spheres: a promising electrocatalyst for the oxygen reduction reaction in alkaline and acidic media. Journal of Materials Chemistry A. 2017;5(22):11114-23.

121. Tong Y, Chen P, Zhou T, Xu K, Chu W, Wu C, et al. A Bifunctional Hybrid Electrocatalyst for Oxygen Reduction and Evolution: Cobalt Oxide Nanoparticles Strongly Coupled to B,N-Decorated Graphene. Angewandte Chemie International Edition. 2017;56(25):7121-5.

122. He Y, Liu S, Priest C, Shi Q, Wu G. Atomically dispersed metal–nitrogen–carbon catalysts for fuel cells: advances in catalyst design, electrode performance, and durability improvement. Chemical Society Reviews. 2020;49(11):3484-524.

123. Zhang N, Zhou T, Chen M, Feng H, Yuan R, Zhong Ca, et al. High-purity pyrrole-type FeN4 sites as a superior oxygen reduction electrocatalyst. Energy & Environmental Science. 2020;13(1):111-8.

124. Chen Z, Higgins D, Tao H, Hsu RS, Chen Z. Highly Active Nitrogen-Doped Carbon Nanotubes for Oxygen Reduction Reaction in Fuel Cell Applications. The Journal of Physical Chemistry C. 2009;113(49):21008-13.

125. Zhao A, Masa J, Schuhmann W, Xia W. Activation and Stabilization of Nitrogen-Doped Carbon Nanotubes as Electrocatalysts in the Oxygen Reduction Reaction at Strongly Alkaline Conditions. The Journal of Physical Chemistry C. 2013;117(46):24283-91.

126. Li W, Yu A, Higgins DC, Llanos BG, Chen Z. Biologically Inspired Highly Durable Iron Phthalocyanine Catalysts for Oxygen Reduction Reaction in Polymer Electrolyte Membrane Fuel Cells. Journal of the American Chemical Society. 2010;132(48):17056-8.

127. Ziegelbauer JM, Olson TS, Pylypenko S, Alamgir F, Jaye C, Atanassov P, et al. Direct Spectroscopic Observation of the Structural Origin of Peroxide Generation from Co-Based Pyrolyzed Porphyrins for ORR Applications. The Journal of Physical Chemistry C. 2008;112(24):8839-49.

128. Kim H, Kim Y, Noh Y, Lee S, Sung J, Kim WB. Thermally Converted CoO Nanoparticles Embedded into N-Doped Carbon Layers as Highly Efficient Bifunctional Electrocatalysts for Oxygen Reduction and Oxygen Evolution Reactions. ChemCatChem. 2017;9(8):1503-10.

129. Wan G, Yang C, Zhao W, Li Q, Wang N, Li T, et al. Anion-Regulated Selective Generation of Cobalt Sites in Carbon: Toward Superior Bifunctional Electrocatalysis. Advanced Materials. 2017;29(47):1703436.

130. Fu X, Zamani P, Choi J-Y, Hassan FM, Jiang G, Higgins DC, et al. In Situ Polymer Graphenization Ingrained with Nanoporosity in a Nitrogenous Electrocatalyst Boosting the Performance of Polymer-Electrolyte-Membrane Fuel Cells. Advanced Materials. 2017;29(7):1604456.

131. Lee J, Farha OK, Roberts J, Scheidt KA, Nguyen ST, Hupp JT. Metal–organic framework materials as catalysts. Chemical Society Reviews. 2009;38(5):1450-9.

132. Gadipelli S, Guo ZX. Tuning of ZIF-Derived Carbon with High Activity, Nitrogen Functionality, and Yield – A Case for Superior CO2 Capture. ChemSusChem. 2015;8(12):2123-32.

133. He P, Yu X-Y, Lou XW. Carbon-Incorporated Nickel–Cobalt Mixed Metal Phosphide Nanoboxes with Enhanced Electrocatalytic Activity for Oxygen Evolution. Angewandte Chemie International Edition. 2017;56(14):3897-900.

134. Gadipelli S, Zhao T, Shevlin SA, Guo Z. Switching effective oxygen reduction and evolution performance by controlled graphitization of a cobalt–nitrogen–carbon framework system. Energy & Environmental Science. 2016;9(5):1661-7.

135. Jia G, Zhang W, Fan G, Li Z, Fu D, Hao W, et al. Three-Dimensional Hierarchical Architectures Derived from Surface-Mounted Metal–Organic Framework Membranes for Enhanced Electrocatalysis. Angewandte Chemie International Edition. 2017;56(44):13781-5.

136. Ma R, Lin G, Zhou Y, Liu Q, Zhang T, Shan G, et al. A review of oxygen reduction mechanisms for metal-free carbon-based electrocatalysts. npj Computational Materials. 2019;5(1):78.

137. Daems N, Sheng X, Vankelecom IFJ, Pescarmona PP. Metal-free doped carbon materials as electrocatalysts for the oxygen reduction reaction. Journal of Materials Chemistry A. 2014;2(12):4085-110.

138. Zhang J, Xia Z, Dai L. Carbon-based electrocatalysts for advanced energy conversion and storage. Science Advances.1(7):e1500564.

139. Chai G-L, Qiu K, Qiao M, Titirici M-M, Shang C, Guo Z. Active sites engineering leads to exceptional ORR and OER bifunctionality in P,N Co-doped graphene frameworks. Energy & Environmental Science. 2017;10(5):1186-95.

140. Du R, Zhang N, Zhu J, Wang Y, Xu C, Hu Y, et al. Nitrogen-Doped Carbon Nanotube Aerogels for High-Performance ORR Catalysts. Small. 2015;11(32):3903-8.

141. Zhang S, Cai Y, He H, Zhang Y, Liu R, Cao H, et al. Heteroatom doped graphdiyne as efficient metal-free electrocatalyst for oxygen reduction reaction in alkaline medium. Journal of Materials Chemistry A. 2016;4(13):4738-44.

142. Yang S, Feng X, Wang X, Müllen K. Graphene-Based Carbon Nitride Nanosheets as Efficient Metal-Free Electrocatalysts for Oxygen Reduction Reactions. Angewandte Chemie International Edition. 2011;50(23):5339-43.

143. Quílez-Bermejo J, Morallón E, Cazorla-Amorós D. Metal-free heteroatom-doped carbon-based catalysts for ORR: A critical assessment about the role of heteroatoms. Carbon. 2020;165:434-54.

144. Yang L, Shui J, Du L, Shao Y, Liu J, Dai L, et al. Carbon-Based Metal-Free ORR Electrocatalysts for Fuel Cells: Past, Present, and Future. Advanced Materials. 2019;31(13):1804799.

145. Hu C, Dai L. Carbon-Based Metal-Free Catalysts for Electrocatalysis beyond the ORR. Angewandte Chemie International Edition. 2016;55(39):11736-58.

146. Dai L, Xue Y, Qu L, Choi H-J, Baek J-B. Metal-Free Catalysts for Oxygen Reduction Reaction. Chemical Reviews. 2015;115(11):4823-92.

147. Jiang H, Gu J, Zheng X, Liu M, Qiu X, Wang L, et al. Defect-rich and ultrathin N doped carbon nanosheets as advanced trifunctional metal-free electrocatalysts for the ORR, OER and HER. Energy & Environmental Science. 2019;12(1):322-33.

148. Zhang J, Zhao Z, Xia Z, Dai L. A metal-free bifunctional electrocatalyst for oxygen reduction and oxygen evolution reactions. Nature Nanotechnology. 2015;10(5):444-52.

149. Jiao Y, Zheng Y, Jaroniec M, Qiao SZ. Origin of the Electrocatalytic Oxygen Reduction Activity of Graphene-Based Catalysts: A Roadmap to Achieve the Best Performance. Journal of the American Chemical Society. 2014;136(11):4394-403.

150. Pei Z, Li H, Huang Y, Xue Q, Huang Y, Zhu M, et al. Texturing in situ: N,S-enriched hierarchically porous carbon as a highly active reversible oxygen electrocatalyst. Energy & Environmental Science. 2017;10(3):742-9.

151. Zhao Y, Wan J, Yao H, Zhang L, Lin K, Wang L, et al. Few-layer graphdiyne doped with sp-hybridized nitrogen atoms at acetylenic sites for oxygen reduction electrocatalysis. Nature Chemistry. 2018;10(9):924-31.

152. Zhou S, Liu N, Wang Z, Zhao J. Nitrogen-Doped Graphene on Transition Metal Substrates as Efficient Bifunctional Catalysts for Oxygen Reduction and Oxygen Evolution Reactions. ACS Applied Materials & Interfaces. 2017;9(27):22578-87.

153. Feng X, Ding X, Jiang D. Covalent organic frameworks. Chemical Society Reviews. 2012;41(18):6010-22.

154. Ding S-Y, Wang W. Covalent organic frameworks (COFs): from design to applications. Chemical Society Reviews. 2013;42(2):548-68.

155. Xu Q, Tang Y, Zhang X, Oshima Y, Chen Q, Jiang D. Template Conversion of Covalent Organic Frameworks into 2D Conducting Nanocarbons for Catalyzing Oxygen Reduction Reaction. Advanced Materials. 2018;30(15):1706330.

156. Marcano DC, Kosynkin DV, Berlin JM, Sinitskii A, Sun Z, Slesarev A, et al. Improved Synthesis of Graphene Oxide. ACS Nano. 2010;4(8):4806-14.

157. Suryanto BHR, Fang T, Cheong S, Tilley RD, Zhao C. From the inside-out: leached metal impurities in multiwall carbon nanotubes for purification or electrocatalysis. Journal of Materials Chemistry A. 2018;6(11):4686-94.

158. Yu L, Sun S, Li H, Xu ZJ. Effects of catalyst mass loading on electrocatalytic activity: An example of oxygen evolution reaction. Fundamental Research. 2021;1(4):448-52.

159. Treimer S, Tang A, Johnson DC. A Consideration of the Application of Koutecký-Levich Plots in the Diagnoses of Charge-Transfer Mechanisms at Rotated Disk Electrodes. Electroanalysis. 2002;14(3):165-71.

160. Min X, Chen Y, Kanan MW. Alkaline O2 reduction on oxide-derived Au: high activity and 4e− selectivity without (100) facets. Physical Chemistry Chemical Physics. 2014;16(27):13601-4.

161. Lipkowski J, Ross PN. Electrocatalysis: Wiley; 1998.

162. Seh Zhi W, Kibsgaard J, Dickens Colin F, Chorkendorff I, Nørskov Jens K, Jaramillo Thomas F. Combining theory and experiment in electrocatalysis: Insights into materials design. Science. 2017;355(6321):eaad4998.

163. Higgins D, Zamani P, Yu A, Chen Z. The application of graphene and its composites in oxygen reduction electrocatalysis: a perspective and review of recent progress. Energy & Environmental Science. 2016;9(2):357-90.

164. Zhu C, Dong S. Recent progress in graphene-based nanomaterials as advanced electrocatalysts towards oxygen reduction reaction. Nanoscale. 2013;5(5):1753-67.

165. Waki K, Wong RA, Oktaviano HS, Fujio T, Nagai T, Kimoto K, et al. Non-nitrogen doped and non-metal oxygen reduction electrocatalysts based on carbon nanotubes: mechanism and origin of ORR activity. Energy & Environmental Science. 2014;7(6):1950-8.

166. Hong WT, Risch M, Stoerzinger KA, Grimaud A, Suntivich J, Shao-Horn Y. Toward the rational design of non-precious transition metal oxides for oxygen electrocatalysis. Energy & Environmental Science. 2015;8(5):1404-27.

167. Zheng B, Wang J, Wang F-B, Xia X-H. Synthesis of nitrogen doped graphene with high electrocatalytic activity toward oxygen reduction reaction. Electrochemistry Communications. 2013;28:24-6.

168. Lin Z, Waller G, Liu Y, Liu M, Wong C-P. Facile Synthesis of Nitrogen-Doped Graphene via Pyrolysis of Graphene Oxide and Urea, and its Electrocatalytic Activity toward the Oxygen-Reduction Reaction. Advanced Energy Materials. 2012;2(7):884-8.

169. Oberlin A. Carbonization and graphitization. Carbon. 1984;22(6):521-41.

170. Moon IK, Lee J, Ruoff RS, Lee H. Reduced graphene oxide by chemical graphitization. Nature Communications. 2010;1(1):73.

171. Zhu H, Wang X, Liu X, Yang X. Integrated Synthesis of Poly(o-phenylenediamine)-Derived Carbon Materials for High Performance Supercapacitors. Advanced Materials. 2012;24(48):6524-9.

172. Kuhn P, Thomas A, Antonietti M. Toward Tailorable Porous Organic Polymer Networks: A High-Temperature Dynamic Polymerization Scheme Based on Aromatic Nitriles. Macromolecules. 2009;42(1):319-26.

173. Benzigar MR, Joseph S, Ilbeygi H, Park D-H, Sarkar S, Chandra G, et al. Highly Crystalline Mesoporous C60 with Ordered Pores: A Class of Nanomaterials for Energy Applications. Angewandte Chemie International Edition. 2018;57(2):569-73.

174. Kandambeth S, Mallick A, Lukose B, Mane MV, Heine T, Banerjee R. Construction of Crystalline 2D Covalent Organic Frameworks with Remarkable Chemical (Acid/Base) Stability via a Combined Reversible and Irreversible Route. Journal of the American Chemical Society. 2012;134(48):19524-7.

175. Tsubouchi N, Mochizuki Y, Naganuma R, Kamiya K, Nishio M, Ono Y, et al. Influence of Inherent Oxygen Species on the Fluidity of Coal during Carbonization. Energy & Fuels. 2016;30(3):2095-101.

176. Fanjul F, Granda M, Santamaría R, Menéndez R. On the chemistry of the oxidative stabilization and carbonization of carbonaceous mesophase. Fuel. 2002;81(16):2061-70.

177. Bardestani R, Patience GS, Kaliaguine S. Experimental methods in chemical engineering: specific surface area and pore size distribution measurements—BET, BJH, and DFT. The Canadian Journal of Chemical Engineering. 2019;97(11):2781-91.

178. Chmiola J, Yushin G, Dash R, Gogotsi Y. Effect of pore size and surface area of carbide derived carbons on specific capacitance. Journal of Power Sources. 2006;158(1):765-72.

179. Brunauer S, Emmett PH, Teller E. Adsorption of Gases in Multimolecular Layers. Journal of the American Chemical Society. 1938;60(2):309-19.

180. Thommes M, Kaneko K, Neimark AV, Olivier JP, Rodriguez-Reinoso F, Rouquerol J, et al. Physisorption of gases, with special reference to the evaluation of surface area and pore size distribution (IUPAC Technical Report). Pure and Applied Chemistry. 2015;87(9-10):1051-69.

181. Chen L, Shi G, Shen J, Peng B, Zhang B, Wang Y, et al. Ion sieving in graphene oxide membranes via cationic control of interlayer spacing. Nature. 2017;550(7676):380-3.

182. Liu Y, Wei H, Zhai X, Wang F, Ren X, Xiong Y, et al. Graphene-based interlayer for high-performance lithium–sulfur batteries: A review. Materials & Design. 2021;211:110171.

183. Liu J, Zhang Y, Zhang L, Xie F, Vasileff A, Qiao S-Z. Graphitic Carbon Nitride (g-C3N4)-Derived N-Rich Graphene with Tuneable Interlayer Distance as a High-Rate Anode for Sodium-Ion Batteries. Advanced Materials. 2019;31(24):1901261.

184. Malard LM, Pimenta MA, Dresselhaus G, Dresselhaus MS. Raman spectroscopy in graphene. Physics Reports. 2009;473(5):51-87.

185. Ferrari AC, Meyer JC, Scardaci V, Casiraghi C, Lazzeri M, Mauri F, et al. Raman Spectrum of Graphene and Graphene Layers. Physical Review Letters. 2006;97(18):187401.

186. Eigler S, Dotzer C, Hirsch A. Visualization of defect densities in reduced graphene oxide. Carbon. 2012;50(10):3666-73.

187. Jorio A, Lucchese MM, Stavale F, Martins Ferreira EH, Moutinho MVO, Capaz RB, et al. Raman study of ion-induced defects inN-layer graphene. Journal of Physics: Condensed Matter. 2010;22(33):334204.

188. M. D P, S CF, Gnanamani A. Preparation, characterization and reusability efficacy of amine-functionalized graphene oxide-polyphenol oxidase complex for removal of phenol from aqueous phase. RSC Advances. 2018;8(67):38416-24.

189. Arrigo R, Hävecker M, Schlögl R, Su DS. Dynamic surface rearrangement and thermal stability of nitrogen functional groups on carbon nanotubes. Chemical Communications. 2008(40):4891-3.

190. Shen L, Zhang L, Wang K, Miao L, Lan Q, Jiang K, et al. Analysis of oxidation degree of graphite oxide and chemical structure of corresponding reduced graphite oxide by selecting different-sized original graphite. RSC Advances. 2018;8(31):17209-17.

191. Chen C-H, Hu S, Shih J-F, Yang C-Y, Luo Y-W, Jhang R-H, et al. Effective Synthesis of Highly Oxidized Graphene Oxide That Enables Wafer-scale Nanopatterning: Preformed Acidic Oxidizing Medium Approach. Scientific Reports. 2017;7(1):3908.

192. Morimoto N, Kubo T, Nishina Y. Tailoring the Oxygen Content of Graphite and Reduced Graphene Oxide for Specific Applications. Scientific Reports. 2016;6(1):21715.

193. Chen Y, Xie B, Ren Y, Yu M, Qu Y, Xie T, et al. Designed nitrogen doping of few-layer graphene functionalized by selective oxygenic groups. Nanoscale Research Letters. 2014;9(1):646.

194. Zhang Y, Sun Z, Wang H, Wang Y, Liang M, Xue S. Nitrogen-doped graphene as a cathode material for dye-sensitized solar cells: effects of hydrothermal reaction and annealing on electrocatalytic performance. RSC Advances. 2015;5(14):10430-9.

195. Lin Z, Waller GH, Liu Y, Liu M, Wong C-p. 3D Nitrogen-doped graphene prepared by pyrolysis of graphene oxide with polypyrrole for electrocatalysis of oxygen reduction reaction. Nano Energy. 2013;2(2):241-8.

196. Sheng Z-H, Shao L, Chen J-J, Bao W-J, Wang F-B, Xia X-H. Catalyst-Free Synthesis of Nitrogen-Doped Graphene via Thermal Annealing Graphite Oxide with Melamine and Its Excellent Electrocatalysis. ACS Nano. 2011;5(6):4350-8.

197. Krishnamoorthy K, Veerapandian M, Yun K, Kim SJ. The chemical and structural analysis of graphene oxide with different degrees of oxidation. Carbon. 2013;53:38-49.

198. Torres D, Pinilla JL, Moliner R, Suelves I. On the oxidation degree of few-layer graphene oxide sheets obtained from chemically oxidized multiwall carbon nanotubes. Carbon. 2015;81:405-17.

199. Abid, Sehrawat P, Islam SS, Mishra P, Ahmad S. Reduced graphene oxide (rGO) based wideband optical sensor and the role of Temperature, Defect States and Quantum Efficiency. Scientific Reports. 2018;8(1):3537.

200. Acik M, Lee G, Mattevi C, Pirkle A, Wallace RM, Chhowalla M, et al. The Role of Oxygen during Thermal Reduction of Graphene Oxide Studied by Infrared Absorption Spectroscopy. The Journal of Physical Chemistry C. 2011;115(40):19761-81.

201. Čolić V, Tymoczko J, Maljusch A, Ganassin A, Schuhmann W, Bandarenka AS. Experimental Aspects in Benchmarking of the Electrocatalytic Activity. ChemElectroChem. 2015;2(1):143-9.

202. Anantharaj S, Kundu S. Do the Evaluation Parameters Reflect Intrinsic Activity of Electrocatalysts in Electrochemical Water Splitting? ACS Energy Letters. 2019;4(6):1260-4.

203. Liu J, Jiao M, Lu L, Barkholtz HM, Li Y, Wang Y, et al. High performance platinum single atom electrocatalyst for oxygen reduction reaction. Nature Communications. 2017;8(1):15938.

204. Morozan A, Jousselme B, Palacin S. Low-platinum and platinum-free catalysts for the oxygen reduction reaction at fuel cell cathodes. Energy & Environmental Science. 2011;4(4):1238-54.

205. Fang Y-H, Liu Z-P. Tafel Kinetics of Electrocatalytic Reactions: From Experiment to First-Principles. ACS Catalysis. 2014;4(12):4364-76.

206. Xu S, Kim Y, Higgins D, Yusuf M, Jaramillo TF, Prinz FB. Building upon the Koutecky-Levich Equation for Evaluation of Next-Generation Oxygen Reduction Reaction Catalysts. Electrochimica Acta. 2017;255:99-108.

207. Ramaswamy N, Mukerjee S. Influence of Inner- and Outer-Sphere Electron Transfer Mechanisms during Electrocatalysis of Oxygen Reduction in Alkaline Media. The Journal of Physical Chemistry C. 2011;115(36):18015-26.

208. Roche I, Chaînet E, Chatenet M, Vondrák J. Carbon-Supported Manganese Oxide Nanoparticles as Electrocatalysts for the Oxygen Reduction Reaction (ORR) in Alkaline Medium: Physical Characterizations and ORR Mechanism. The Journal of Physical Chemistry C. 2007;111(3):1434-43.

209. Tian G-L, Zhao M-Q, Yu D, Kong X-Y, Huang J-Q, Zhang Q, et al. Nitrogen-Doped Graphene/Carbon Nanotube Hybrids: In Situ Formation on Bifunctional Catalysts and Their Superior Electrocatalytic Activity for Oxygen Evolution/Reduction Reaction. Small. 2014;10(11):2251-9.

210. Li D, Ren B, Jin Q, Cui H, Wang C. Nitrogen-doped, oxygen-functionalized, edge- and defect-rich vertically aligned graphene for highly enhanced oxygen evolution reaction. Journal of Materials Chemistry A. 2018;6(5):2176-83.

211. Faisal SN, Haque E, Noorbehesht N, Zhang W, Harris AT, Church Tamara L, et al. Pyridinic and graphitic nitrogen-rich graphene for high-performance supercapacitors and metal-free bifunctional electrocatalysts for ORR and OER. RSC Advances. 2017;7(29):17950-8.

212. Stelmachowski PDJSDLMJAUKAC-BCaEfOERiAM. Materials [Internet]. 2021; 14(17).

213. Gao Q, Zhang W, Shi Z, Yang L, Tang Y. Structural Design and Electronic Modulation of Transition-Metal-Carbide Electrocatalysts toward Efficient Hydrogen Evolution. Advanced Materials. 2019;31(2):1802880.

214. Fei H, Ye R, Ye G, Gong Y, Peng Z, Fan X, et al. Boron- and Nitrogen-Doped Graphene Quantum Dots/Graphene Hybrid Nanoplatelets as Efficient Electrocatalysts for Oxygen Reduction. ACS Nano. 2014;8(10):10837-43.

215. Dong Y, Pang H, Yang HB, Guo C, Shao J, Chi Y, et al. Carbon-Based Dots Co-doped with Nitrogen and Sulfur for High Quantum Yield and Excitation-Independent Emission. Angewandte Chemie International Edition. 2013;52(30):7800-4.

216. Zhu S, Meng Q, Wang L, Zhang J, Song Y, Jin H, et al. Highly Photoluminescent Carbon Dots for Multicolor Patterning, Sensors, and Bioimaging. Angewandte Chemie International Edition. 2013;52(14):3953-7.

217. Martindale BCM, Hutton GAM, Caputo CA, Prantl S, Godin R, Durrant JR, et al. Enhancing Light Absorption and Charge Transfer Efficiency in Carbon Dots through Graphitization and Core Nitrogen Doping. Angewandte Chemie International Edition. 2017;56(23):6459-63.

218. Pan D, Zhang J, Li Z, Wu M. Hydrothermal Route for Cutting Graphene Sheets into Blue-Luminescent Graphene Quantum Dots. Advanced Materials. 2010;22(6):734-8.

219. De B, Karak N. Recent progress in carbon dot–metal based nanohybrids for photochemical and electrochemical applications. Journal of Materials Chemistry A. 2017;5(5):1826-59.

220. Jia Y, Zhang L, Du A, Gao G, Chen J, Yan X, et al. Defect Graphene as a Trifunctional Catalyst for Electrochemical Reactions. Advanced Materials. 2016;28(43):9532-8.

221. Baker SN, Baker GA. Luminescent Carbon Nanodots: Emergent Nanolights. Angewandte Chemie International Edition. 2010;49(38):6726-44.

222. Tang C, Zhang Q. Nanocarbon for Oxygen Reduction Electrocatalysis: Dopants, Edges, and Defects. Advanced Materials. 2017;29(13):1604103.

223. Zhou X, Tian Z, Li J, Ruan H, Ma Y, Yang Z, et al. Synergistically enhanced activity of graphene quantum dot/multi-walled carbon nanotube composites as metal-free catalysts for oxygen reduction reaction. Nanoscale. 2014;6(5):2603-7.

224. Hu C, Yu C, Li M, Wang X, Dong Q, Wang G, et al. Nitrogen-doped carbon dots decorated on graphene: a novel all-carbon hybrid electrocatalyst for enhanced oxygen reduction reaction. Chemical Communications. 2015;51(16):3419-22.

225. Niu W-J, Zhu R-H, Yan H, Zeng H-B, Cosnier S, Zhang X-J, et al. One-pot synthesis of nitrogen-rich carbon dots decorated graphene oxide as metal-free electrocatalyst for oxygen reduction reaction. Carbon. 2016;109:402-10.

226. Li Q, Zhang S, Dai L, Li L-s. Nitrogen-Doped Colloidal Graphene Quantum Dots and Their Size-Dependent Electrocatalytic Activity for the Oxygen Reduction Reaction. Journal of the American Chemical Society. 2012;134(46):18932-5.

227. Bhattacharyya S, Konkena B, Jayaramulu K, Schuhmann W, Maji TK. Synthesis of nano-porous carbon and nitrogen doped carbon dots from an anionic MOF: a trace cobalt metal residue in carbon dots promotes electrocatalytic ORR activity. Journal of Materials Chemistry A. 2017;5(26):13573-80.

228. Wang B, Yu J, Sui L, Zhu S, Tang Z, Yang B, et al. Rational Design of Multi-Color-Emissive Carbon Dots in a Single Reaction System by Hydrothermal. Advanced Science. 2021;8(1):2001453.

229. Dimiev AM, Tour JM. Mechanism of Graphene Oxide Formation. ACS Nano. 2014;8(3):3060-8.

230. Paredes JI, Villar-Rodil S, Martínez-Alonso A, Tascón JMD. Graphene Oxide Dispersions in Organic Solvents. Langmuir. 2008;24(19):10560-4.

231. Luan VH, Tien HN, Hoa LT, Hien NTM, Oh E-S, Chung J, et al. Synthesis of a highly conductive and large surface area graphene oxide hydrogel and its use in a supercapacitor. Journal of Materials Chemistry A. 2013;1(2):208-11.

232. Habiba K, Makarov VI, Avalos J, Guinel MJF, Weiner BR, Morell G. Luminescent graphene quantum dots fabricated by pulsed laser synthesis. Carbon. 2013;64:341-50.

233. Pandey DK, Chung TF, Prakash G, Piner R, Chen YP, Reifenberger R. Folding and cracking of graphene oxide sheets upon deposition. Surface Science. 2011;605(17):1669-75.

234. Yang S, Sun J, Zhu C, He P, Peng Z, Ding G. Supramolecular recognition control of polyethylene glycol modified N-doped graphene quantum dots: tunable selectivity for alkali and alkaline-earth metal ions. Analyst. 2016;141(3):1052-9.

235. Ferrari AC. Raman spectroscopy of graphene and graphite: Disorder, electron–phonon coupling, doping and nonadiabatic effects. Solid State Communications. 2007;143(1):47-57.

236. Ferrari AC, Basko DM. Raman spectroscopy as a versatile tool for studying the properties of graphene. Nature Nanotechnology. 2013;8(4):235-46.

237. Xue M, Zhang L, Zhan Z, Zou M, Huang Y, Zhao S. Sulfur and nitrogen binary doped carbon dots derived from ammonium thiocyanate for selective probing doxycycline in living cells and multicolor cell imaging. Talanta. 2016;150:324-30.

238. Wang Y, Kim S-H, Feng L. Highly luminescent N, S- Co-doped carbon dots and their direct use as mercury(II) sensor. Analytica Chimica Acta. 2015;890:134-42.

239. Zhang Y, Wang Y, Feng X, Zhang F, Yang Y, Liu X. Effect of reaction temperature on structure and fluorescence properties of nitrogen-doped carbon dots. Applied Surface Science. 2016;387:1236-46.

240. Luo Z, Yang D, Qi G, Shang J, Yang H, Wang Y, et al. Microwave-assisted solvothermal preparation of nitrogen and sulfur co-doped reduced graphene oxide and graphene quantum dots hybrids for highly efficient oxygen reduction. Journal of Materials Chemistry A. 2014;2(48):20605-11.

241. Yeh T-F, Chen S-J, Teng H. Synergistic effect of oxygen and nitrogen functionalities for graphene-based quantum dots used in photocatalytic H2 production from water decomposition. Nano Energy. 2015;12:476-85.

242. Zhou G, Paek E, Hwang GS, Manthiram A. Long-life Li/polysulphide batteries with high sulphur loading enabled by lightweight three-dimensional nitrogen/sulphur-codoped graphene sponge. Nature Communications. 2015;6(1):7760.

243. Ding H, Wei J-S, Xiong H-M. Nitrogen and sulfur co-doped carbon dots with strong blue luminescence. Nanoscale. 2014;6(22):13817-23.

244. Kundu S, Yadav RM, Narayanan TN, Shelke MV, Vajtai R, Ajayan PM, et al. Synthesis of N, F and S co-doped graphene quantum dots. Nanoscale. 2015;7(27):11515-9.

245. Zeng Y-W, Ma D-K, Wang W, Chen J-J, Zhou L, Zheng Y-Z, et al. N, S co-doped carbon dots with orange luminescence synthesized through polymerization and carbonization reaction of amino acids. Applied Surface Science. 2015;342:136-43.

246. Zhang Y, He J. Facile synthesis of S, N co-doped carbon dots and investigation of their photoluminescence properties. Physical Chemistry Chemical Physics. 2015;17(31):20154-9.

247. Beams R, Gustavo Cançado L, Novotny L. Raman characterization of defects and dopants in graphene. Journal of Physics: Condensed Matter. 2015;27(8):083002.

248. Tuinstra F, Koenig JL. Raman Spectrum of Graphite. The Journal of Chemical Physics. 1970;53(3):1126-30.

249. Geng D, Yang S, Zhang Y, Yang J, Liu J, Li R, et al. Nitrogen doping effects on the structure of graphene. Applied Surface Science. 2011;257(21):9193-8.

250. Hu K, Xie X, Szkopek T, Cerruti M. Understanding Hydrothermally Reduced Graphene Oxide Hydrogels: From Reaction Products to Hydrogel Properties. Chemistry of Materials. 2016;28(6):1756-68.

251. Kao L-H, Hsu T-C. Silica template synthesis of ordered mesoporous carbon thick films with 35-nm pore size from mesophase pitch solution. Materials Letters. 2008;62(4):695-8.

252. Zhang Y, Ge J, Wang L, Wang D, Ding F, Tao X, et al. Manageable N-doped Graphene for High Performance Oxygen Reduction Reaction. Scientific Reports. 2013;3(1):2771.

253. Parvez K, Yang S, Hernandez Y, Winter A, Turchanin A, Feng X, et al. Nitrogen-Doped Graphene and Its Iron-Based Composite As Efficient Electrocatalysts for Oxygen Reduction Reaction. ACS Nano. 2012;6(11):9541-50.

254. Li ZJ, Yang BC, Zhang SR, Zhao CM. Graphene oxide with improved electrical conductivity for supercapacitor electrodes. Applied Surface Science. 2012;258(8):3726-31.

255. Dong Q, Santhanagopalan S, White RE. Simulation of Polarization Curves for Oxygen Reduction Reaction in 0.5 M H[sub 2]SO[sub 4] at a Rotating Ring Disk Electrode. Journal of The Electrochemical Society. 2007;154(8):A816.

256. Liu Y, Wang H, Lin D, Zhao J, Liu C, Xie J, et al. A Prussian blue route to nitrogen-doped graphene aerogels as efficient electrocatalysts for oxygen reduction with enhanced active site accessibility. Nano Research. 2017;10(4):1213-22.

257. Marciano O, Gonen S, Levy N, Teblum E, Yemini R, Nessim GD, et al. Modulation of Oxygen Content in Graphene Surfaces Using Temperature-Programmed Reductive Annealing: Electron Paramagnetic Resonance and Electrochemical Study. Langmuir. 2016;32(44):11672-80.

258. You J-M, Ahmed MS, Han HS, Choe Je, Üstündağ Z, Jeon S. New approach of nitrogen and sulfur-doped graphene synthesis using dipyrrolemethane and their electrocatalytic activity for oxygen reduction in alkaline media. Journal of Power Sources. 2015;275:73-9.

259. Lu Z, Qian L, Tian Y, Li Y, Sun X, Duan X. Ternary NiFeMn layered double hydroxides as highly-efficient oxygen evolution catalysts. Chemical Communications. 2016;52(5):908-11.

260. Yang Z, Yao Z, Li G, Fang G, Nie H, Liu Z, et al. Sulfur-Doped Graphene as an Efficient Metal-free Cathode Catalyst for Oxygen Reduction. ACS Nano. 2012;6(1):205-11.

261. El-Sawy AM, Mosa IM, Su D, Guild CJ, Khalid S, Joesten R, et al. Controlling the Active Sites of Sulfur-Doped Carbon Nanotube–Graphene Nanolobes for Highly Efficient Oxygen Evolution and Reduction Catalysis. Advanced Energy Materials. 2016;6(5):1501966.

262. Yang Hong B, Miao J, Hung S-F, Chen J, Tao Hua B, Wang X, et al. Identification of catalytic sites for oxygen reduction and oxygen evolution in N-doped graphene materials: Development of highly efficient metal-free bifunctional electrocatalyst. Science Advances.2(4):e1501122.

263. Koenigsmann C, Wong SS. One-dimensional noble metal electrocatalysts: a promising structural paradigm for direct methanol fuel cells. Energy & Environmental Science. 2011;4(4):1161-76.

264. Wang L, Zeng Z, Gao W, Maxson T, Raciti D, Giroux M, et al. Tunable intrinsic strain in two-dimensional transition metal electrocatalysts. Science. 2019;363(6429):870-4.

265. Yan D, Li Y, Huo J, Chen R, Dai L, Wang S. Defect Chemistry of Nonprecious-Metal Electrocatalysts for Oxygen Reactions. Advanced Materials. 2017;29(48):1606459.

266. Paul R, Zhu L, Chen H, Qu J, Dai L. Recent Advances in Carbon-Based Metal-Free Electrocatalysts. Advanced Materials. 2019;31(31):1806403.

267. Li S, Cheng C, Zhao X, Schmidt J, Thomas A. Active Salt/Silica-Templated 2D Mesoporous FeCo-Nx-Carbon as Bifunctional Oxygen Electrodes for Zinc–Air Batteries. Angewandte Chemie International Edition. 2018;57(7):1856-62.

268. Silva R, Voiry D, Chhowalla M, Asefa T. Efficient Metal-Free Electrocatalysts for Oxygen Reduction: Polyaniline-Derived N- and O-Doped Mesoporous Carbons. Journal of the American Chemical Society. 2013;135(21):7823-6.

269. Cai J, Ruffieux P, Jaafar R, Bieri M, Braun T, Blankenburg S, et al. Atomically precise bottom-up fabrication of graphene nanoribbons. Nature. 2010;466(7305):470-3.

270. Rizzo DJ, Veber G, Cao T, Bronner C, Chen T, Zhao F, et al. Topological band engineering of graphene nanoribbons. Nature. 2018;560(7717):204-8.

271. Liu J, Mishra S, Pignedoli CA, Passerone D, Urgel JI, Fabrizio A, et al. Open-Shell Nonbenzenoid Nanographenes Containing Two Pairs of Pentagonal and Heptagonal Rings. Journal of the American Chemical Society. 2019;141(30):12011-20.

272. Nakamura E, Sato K. Managing the scarcity of chemical elements. Nature Materials. 2011;10(3):158-61.

273. Masa J, Zhao A, Xia W, Sun Z, Mei B, Muhler M, et al. Trace metal residues promote the activity of supposedly metal-free nitrogen-modified carbon catalysts for the oxygen reduction reaction. Electrochemistry Communications. 2013;34:113-6.

274. Bagheri A, Behbahani M, Amini MM, Sadeghi O, Tootoonchi A, Dahaghin Z. Preconcentration and separation of ultra-trace palladium ion using pyridine-functionalized magnetic nanoparticles. Microchimica Acta. 2012;178(3):261-8.

275. Nikiforov MP, Lai B, Chen W, Chen S, Schaller RD, Strzalka J, et al. Detection and role of trace impurities in high-performance organic solar cells. Energy & Environmental Science. 2013;6(5):1513-20.

276. Cui X, Lei S, Wang AC, Gao L, Zhang Q, Yang Y, et al. Emerging covalent organic frameworks tailored materials for electrocatalysis. Nano Energy. 2020;70:104525.

277. Zhao X, Pachfule P, Li S, Langenhahn T, Ye M, Schlesiger C, et al. Macro/Microporous Covalent Organic Frameworks for Efficient Electrocatalysis. Journal of the American Chemical Society. 2019;141(16):6623-30.

278. Yan Y, He T, Zhao B, Qi K, Liu H, Xia BY. Metal/covalent–organic frameworks-based electrocatalysts for water splitting. Journal of Materials Chemistry A. 2018;6(33):15905-26.

279. Zhang H, Zhu M, Schmidt OG, Chen S, Zhang K. Covalent Organic Frameworks for Efficient Energy Electrocatalysis: Rational Design and Progress. Advanced Energy and Sustainability Research. 2021;2(4):2000090.

280. Lin C-Y, Zhang L, Zhao Z, Xia Z. Design Principles for Covalent Organic Frameworks as Efficient Electrocatalysts in Clean Energy Conversion and Green Oxidizer Production. Advanced Materials. 2017;29(17):1606635.

281. Nayak RR, Shanmugharaj AM, Ryu SH. A Novel Route for Polystyrene Grafted Single-Walled Carbon Nanotubes and their Characterization. Macromolecular Chemistry and Physics. 2008;209(11):1137-44.

282. Lim H, Cha MC, Chang JY. Synthesis of microporous polymers by Friedel–Crafts reaction of 1-bromoadamantane with aromatic compounds and their surface modification. Polymer Chemistry. 2012;3(4):868-70.

283. Noh S, Jeon JY, Adhikari S, Kim YS, Bae C. Molecular Engineering of Hydroxide Conducting Polymers for Anion Exchange Membranes in Electrochemical Energy Conversion Technology. Accounts of Chemical Research. 2019;52(9):2745-55.

284. Baker JG, Schneider JR, Garrido Torres JA, Singh JA, Mackus AJM, Bajdich M, et al. The Role of Aluminum in Promoting Ni–Fe–OOH Electrocatalysts for the Oxygen Evolution Reaction. ACS Applied Energy Materials. 2019;2(5):3488-99.

285. Zheng Y, Jiao Y, Jaroniec M, Qiao SZ. Advancing the Electrochemistry of the Hydrogen-Evolution Reaction through Combining Experiment and Theory. Angewandte Chemie International Edition. 2015;54(1):52-65.

286. Yasutake M, Fujihara T, Nagasawa A, Moriya K, Hirose T. Synthesis and Phase Structures of Novel π-Acceptor Discotic Liquid Crystalline Compounds Having a Pyrenedione Core. European Journal of Organic Chemistry. 2008;2008(24):4120-5.

287. Tabb D, Koenig J. Fourier transform infrared study of plasticized and unplasticized poly (vinyl chloride). Macromolecules. 1975;8(6):929-34.

288. Mecke R, Klee W. Das Schwingungsspektrum des Pyren. Zeitschrift für Elektrochemie, Berichte der Bunsengesellschaft für physikalische Chemie. 2010;65:327-36.

289. Mecke R, Klee WE. Das Schwingungsspektrum des Pyren. Zeitschrift für Elektrochemie, Berichte der Bunsengesellschaft für physikalische Chemie. 1961;65(4):327-36.

290. Kohli J, Jones D, Safe S. The metabolism of higher chlorinated benzene isomers. Canadian Journal of Biochemistry. 1976;54(3):203-8.

291. Zwijnenburg MA, Cheng G, McDonald TO, Jelfs KE, Jiang J-X, Ren S, et al. Shedding Light on Structure–Property Relationships for Conjugated Microporous Polymers: The Importance of Rings and Strain. Macromolecules. 2013;46(19):7696-704.

292. Fina F, Callear SK, Carins GM, Irvine JTS. Structural Investigation of Graphitic Carbon Nitride via XRD and Neutron Diffraction. Chemistry of Materials. 2015;27(7):2612-8.

293. Eckmann A, Felten A, Mishchenko A, Britnell L, Krupke R, Novoselov KS, et al. Probing the Nature of Defects in Graphene by Raman Spectroscopy. Nano Letters. 2012;12(8):3925-30.

294. Shinohara H, Yamakita Y, Ohno K. Raman spectra of polycyclic aromatic hydrocarbons. Comparison of calculated Raman intensity distributions with observed spectra for naphthalene, anthracene, pyrene, and perylene. Journal of Molecular Structure. 1998;442(1):221-34.

295. Prabakaran P, Satapathy S, Prasad E, Sankararaman S. Architecting pyrediyne nanowalls with improved inter-molecular interactions, electronic features and transport characteristics. Journal of Materials Chemistry C. 2018;6(2):380-7.

296. Carrasco EA, Campos-Vallette M, Leyton P, Diaz G, Clavijo RE, García-Ramos JV, et al. Study of the Interaction of Pollutant Nitro Polycyclic Aromatic Hydrocarbons with Different Metallic Surfaces by Surface-Enhanced Vibrational Spectroscopy (SERS and SEIR). The Journal of Physical Chemistry A. 2003;107(45):9611-9.

297. Briggs D, Beamson G. XPS studies of the oxygen 1s and 2s levels in a wide range of functional polymers. Analytical chemistry. 1993;65(11):1517-23.

298. Kelemen SR, Rose KD, Kwiatek PJ. Carbon aromaticity based on XPS II to II∗ signal intensity. Applied Surface Science. 1993;64(2):167-74.

299. Kostuch A, Jarczewski S, Surówka MK, Kuśtrowski P, Sojka Z, Kruczała K. The joint effect of electrical conductivity and surface oxygen functionalities of carbon supports on the oxygen reduction reaction studied over bare supports and Mn–Co spinel/carbon catalysts in alkaline media. Catalysis Science & Technology. 2021;11(23):7578-91.

300. Liang H-W, Zhuang X, Brüller S, Feng X, Müllen K. Hierarchically porous carbons with optimized nitrogen doping as highly active electrocatalysts for oxygen reduction. Nature Communications. 2014;5(1):4973.

301. Zhang L, Niu J, Dai L, Xia Z. Effect of Microstructure of Nitrogen-Doped Graphene on Oxygen Reduction Activity in Fuel Cells. Langmuir. 2012;28(19):7542-50.

302. Zheng C, Zhou X, Cao H, Wang G, Liu Z. Synthesis of porous graphene/activated carbon composite with high packing density and large specific surface area for supercapacitor electrode material. Journal of Power Sources. 2014;258:290-6.

303. Han S, Wu D, Li S, Zhang F, Feng X. Porous Graphene Materials for Advanced Electrochemical Energy Storage and Conversion Devices. Advanced Materials. 2014;26(6):849-64.

304. Wang J, Zhao C-X, Liu J-N, Ren D, Li B-Q, Huang J-Q, et al. Quantitative kinetic analysis on oxygen reduction reaction: A perspective. Nano Materials Science. 2021;3(3):313-8.

305. Bag S, Mondal B, Das AK, Raj CR. Nitrogen and Sulfur Dual-Doped Reduced Graphene Oxide: Synergistic Effect of Dopants Towards Oxygen Reduction Reaction. Electrochimica Acta. 2015;163:16-23.

306. Vidal-Iglesias FJ, Solla-Gullón J, Montiel V, Aldaz A. Errors in the use of the Koutecky–Levich plots. Electrochemistry Communications. 2012;15(1):42-5.

307. Qu K, Zheng Y, Dai S, Qiao SZ. Graphene oxide-polydopamine derived N, S-codoped carbon nanosheets as superior bifunctional electrocatalysts for oxygen reduction and evolution. Nano Energy. 2016;19:373-81.

308. Shinde SS, Lee C-H, Sami A, Kim D-H, Lee S-U, Lee J-H. Scalable 3-D Carbon Nitride Sponge as an Efficient Metal-Free Bifunctional Oxygen Electrocatalyst for Rechargeable Zn–Air Batteries. ACS Nano. 2017;11(1):347-57.

309. Ma TY, Ran J, Dai S, Jaroniec M, Qiao SZ. Phosphorus-Doped Graphitic Carbon Nitrides Grown In Situ on Carbon-Fiber Paper: Flexible and Reversible Oxygen Electrodes. Angewandte Chemie International Edition. 2015;54(15):4646-50.

310. Zheng Y, Song H, Chen S, Yu X, Zhu J, Xu J, et al. Metal-Free Multi-Heteroatom-Doped Carbon Bifunctional Electrocatalysts Derived from a Covalent Triazine Polymer. Small. 2020;16(47):2004342.

311. Lin X, Peng P, Guo J, Xiang Z. Reaction milling for scalable synthesis of N, P-codoped covalent organic polymers for metal-free bifunctional electrocatalysts. Chemical Engineering Journal. 2019;358:427-34.

312. Zhang C, Zhang G, Li H, Chang Y, Chang Z, Liu J, et al. Interfacial dehalogenation-enabled hollow N-doped carbon network as bifunctional catalysts for rechargeable Zn-air battery. Electrochimica Acta. 2017;247:1044-51.

313. Liu Q, Wang Y, Dai L, Yao J. Scalable Fabrication of Nanoporous Carbon Fiber Films as Bifunctional Catalytic Electrodes for Flexible Zn-Air Batteries. Advanced Materials. 2016;28(15):3000-6.

314. Gao R, Dai Q, Du F, Yan D, Dai L. C60-Adsorbed Single-Walled Carbon Nanotubes as Metal-Free, pH-Universal, and Multifunctional Catalysts for Oxygen Reduction, Oxygen Evolution, and Hydrogen Evolution. Journal of the American Chemical Society. 2019;141(29):11658-66.

315. Wu M, Wang Y, Wei Z, Wang L, Zhuo M, Zhang J, et al. Ternary doped porous carbon nanofibers with excellent ORR and OER performance for zinc–air batteries. Journal of Materials Chemistry A. 2018;6(23):10918-25.

316. Zong L, Wu W, Liu S, Yin H, Chen Y, Liu C, et al. Metal-free, active nitrogen-enriched, efficient bifunctional oxygen electrocatalyst for ultrastable zinc-air batteries. Energy Storage Materials. 2020;27:514-21.

317. Lv Q, Si W, He J, Sun L, Zhang C, Wang N, et al. Selectively nitrogen-doped carbon materials as superior metal-free catalysts for oxygen reduction. Nature Communications. 2018;9(1):3376.

318. Hu C, Dai L. Multifunctional Carbon-Based Metal-Free Electrocatalysts for Simultaneous Oxygen Reduction, Oxygen Evolution, and Hydrogen Evolution. Advanced Materials. 2017;29(9):1604942.

319. Wang Y, Xu N, He R, Peng L, Cai D, Qiao J. Large-scale defect-engineering tailored tri-doped graphene as a metal-free bifunctional catalyst for superior electrocatalytic oxygen reaction in rechargeable Zn-air battery. Applied Catalysis B: Environmental. 2021;285:119811.

320. Xiao X, Li X, Wang Z, Yan G, Guo H, Hu Q, et al. Robust template-activator cooperated pyrolysis enabling hierarchically porous honeycombed defective carbon as highly-efficient metal-free bifunctional electrocatalyst for Zn-air batteries. Applied Catalysis B: Environmental. 2020;265:118603.

321. Guo Y, Yao S, Gao L, Chen A, Jiao M, Cui H, et al. Boosting bifunctional electrocatalytic activity in S and N co-doped carbon nanosheets for high-efficiency Zn–air batteries. Journal of Materials Chemistry A. 2020;8(8):4386-95.

322. Li J-C, Hou P-X, Cheng M, Liu C, Cheng H-M, Shao M. Carbon nanotube encapsulated in nitrogen and phosphorus co-doped carbon as a bifunctional electrocatalyst for oxygen reduction and evolution reactions. Carbon. 2018;139:156-63.

323. Patil IM, Lokanathan M, Ganesan B, Swami A, Kakade B. Carbon Nanotube/Boron Nitride Nanocomposite as a Significant Bifunctional Electrocatalyst for

Oxygen Reduction and Oxygen Evolution Reactions. Chemistry – A European Journal. 2017;23(3):676-83.